

NORTHWESTERN UNIVERSITY

Multi-scale Modeling of Polymer/Metal Interface

A DISSERTATION

SUBMITTED TO THE GRADUATE SCHOOL
IN PARTIAL FULFILLMENT OF THE REQUIREMENTS

for the degree of

DOCTOR OF PHILOSOPHY

Field of Mechanical Engineering

By

Shaorui Yang

EVANSTON, ILLINOIS

March 2014

UMI Number: 3615544

All rights reserved

INFORMATION TO ALL USERS

The quality of this reproduction is dependent upon the quality of the copy submitted.

In the unlikely event that the author did not send a complete manuscript and there are missing pages, these will be noted. Also, if material had to be removed, a note will indicate the deletion.



UMI 3615544

Published by ProQuest LLC (2014). Copyright in the Dissertation held by the Author.

Microform Edition © ProQuest LLC.

All rights reserved. This work is protected against unauthorized copying under Title 17, United States Code



ProQuest LLC.
789 East Eisenhower Parkway
P.O. Box 1346
Ann Arbor, MI 48106 - 1346

© Copyright by Shaorui Yang 2014

All Rights Reserved

ABSTRACT

Multi-scale Modeling of Polymer/Metal Interface

Shaorui Yang

High-density circuits which involve multi-material integration have been extensively adopted in electronic packaging designs, in order to meet the requirements by recent portable electronics: compact size, multi-functional and high speed operational system. Reliability concerns, including mechanical, thermal and moisture, naturally rise when materials with large mismatch in properties are assembled into extremely restricted volume. Among them, the one involving copper based lead frame and epoxy based molding compound is critical, since the interface (epoxy/Cu) is prone to delamination. In evaluating the performance of the interface, a predictive numerical simulation tool is highly desired to replace time/recourse-consuming destructive experimental tests. The current thesis focuses on molecular level modeling of epoxy/Cu interface to understand its response to mechanical loadings.

Full-atomic MD studies based on rigorously parameterized and validated force-fields are first conducted on bulk epoxy and epoxy/Cu bimaterial. The epoxy's chemically cross-linked network structure is modeled through a simulated polymerization process. A number of key properties of a commercially important epoxy molding compound, including thermal, mechanical, structural and dynamic, are computed using MD simulation and found in good agreement with experiment measurements. The epoxy/Cu bimaterial is modeled by applying the same simulated polymerization with the presence of Cu substrate. Its tensile deformation behavior and stress versus strain/displacement are investigated by non-equilibrium MD

simulation. It is found that the interfacial failure is brittle caused by simultaneous detachment of epoxy atoms from the copper substrate. Quantitative aspects, including failure strain and strength, are extracted for various loading and structural conditions.

The full-atomic MD simulation is severely limited on length and time scale, thus restricted from describing physical processes requiring larger temporal and spatial scales to correctly capture, e.g., localized plastic deformations (crazes/dilatation bands) developed in epoxies occur with the width of a few microns or lower (several hundred nanometers) and length of tens of microns. Therefore a meso-scale model is desired to fill the gap between atomic and continuous descriptions. The second part of this thesis fulfills this task by developing a coarse-grained model of the epoxy molding compound and the epoxy/Cu bimaterial, via fitting epoxy's key thermo-mechanical properties and epoxy/Cu interface's free energy landscape.

Investigations based on the coarse-grained model on the deformation/failure behavior of both bulk epoxy and epoxy/Cu bimaterial reveal valuable insights. These studies are conducted on the scale of $\sim 100\text{nm}$, approaching to the width of the zone of localized plastic deformations, thus effectively upscale the full-atomic MD length scale towards the continuum mechanics length scale.

In terms of engineering applications, accomplishments in the current dissertation provide useful guidance in material design for electronic packaging. Further development can lead to an atomic-to-continuous multi-scale simulation framework which enables modeling the interfacial failure at device level.

ACKNOWLEDGMENTS

Looking back to the challenging and rewarding journey towards the completion of my PhD study, the first person I would like to extend my sincerest gratitude to is my academic advisor, Dr. Jianmin Qu. Being supported and instructed by a mentor like him, who has masterful grasp of his field and is constantly inspiring his students towards success especially at moments when disappointment might have overcome enthusiasm, is my great pleasure. The memory of discussing research progress and exchanging ideas with him every week is still vivid as if it just happened. I truly appreciate all the resources and facilities he's been providing to me, without which I wouldn't be able to accomplish the work of my thesis. He's also been setting up a perfect role model: a decent gentleman who has long-lasting enthusiasm in his career and shows distinctive leadership. I have been and will always be benefited through learning from his unique characteristics.

I would like to thank Dr. L. Catherine Brinson and Dr. Sinan Keten for serving as my committee member. It is no easy task reading and reviewing a PhD thesis. Their constructive feedback and thoughtful comments give me the opportunity to revisit my dissertation and make it a better one.

My gratitude then goes to a few colleagues who have been very helpful during the course of completing my doctorate research. I would like to thank Dr. Feng Gao for helping me gain access to the computing facilities and get familiar with the system, also for the fruitful discussions about my research. Thank you to Dr. Zhiwei Cui and Dr. Ajing Cao for teaching me the knowledge of MD simulations and the use of LAMMPS software. I'm also grateful to Dr.

Ole Holck in Fraunhofer Institute and Dr. Stephen Todd in Accelrys Inc. for introducing me to the Material Studio software.

I appreciate the time spending with all the labmates and friends in both Georgia Tech and Northwestern University. Because of them this has turned into quite enjoyable experience that I will surely remember for years. Many thanks and gratitude to Guangxin Tang, Minghe Liu, Shan Huang, Xujun Zhao, Yuan Zhong, Honggang Zhou, Ying Li, Daniel Rogers, Hamed Haftbaradaran, Zimu Chen, Taeho Ju and Youxuan Zhao.

Finally, thanks from the bottom of my heart to my parents for their love and support. They raised me to who I am today and encouraged me to overcome every single obstacle during my study.

My wife, Wanxin, came into my life in the middle of this long journey and has been by my side ever since. My deepest appreciation goes to her. Without her patience and support, I would not be able to stick to the completion of my PhD study.

TABLE OF CONTENTS

ABSTRACT	3
ACKNOWLEDGMENTS	5
TABLE OF CONTENTS.....	7
LIST OF TABLES.....	10
LIST OF FIGURES	11
Chapter 1 INTRODUCTION.....	17
1.1 Motivation.....	17
1.2 Adhesion Mechanisms at Polymer/Metal Interface	20
1.3 Fracture at Interface	21
1.4 Thesis Objective and Structure	25
Chapter 2 MOLECULAR DYNAMICS SIMULATION	30
2.1 Introduction.....	30
2.2 Ingredients of MD simulation.....	31
2.2.1 Governing Equation and Time Integrator	31
2.2.2 Inter-atomic potentials	32
2.2.3 Ensembles and Thermo/Baro-Stat	37
2.2.4 Boundary Conditions	40
2.3 Summary of This Chapter	44
Chapter 3 ATOMISTIC STUDY OF BULK EPOXY	46
3.1 Introduction.....	46
3.2 MD Simulation Method	49
3.3 Results and Discussions.....	58
3.3.1 Local Structure Evolution	58
3.3.2 Cross-link Induced Shrinkage	61
3.3.3 Thermal Expansion and Glass Transition	62
3.3.4 Mechanical Properties.....	75
3.4 Summary of This Chapter	80

Chapter 4 ATOMISTIC STUDY OF EPOXY/COPPER BIMATERIAL	82
4.1 Introduction.....	82
4.2 MD Simulation Method	85
4.3 Results and Discussion	88
4.3.1 Effects of Simulation Cell Size and Strain Rates.....	88
4.3.2 Deformation Behavior	91
4.3.3 Bulk versus Interfacial Deformation.....	93
4.3.4 Unloading and Reloading Behavior.....	96
4.3.5 Effect of Temperature	98
4.3.6 Effect of Conversion	100
4.3.7 Effect of Epoxy Functionality.....	105
4.4 Summary of This Chapter.....	108
Chapter 5 COARSE-GRAINED MODEL FOR EPOXY	112
5.1 Introduction.....	112
5.2 Model and Interactions	117
5.2.1 Mapping	117
5.2.2 Inter-Bead Potential	118
5.2.3 Cross-linking Process.....	121
5.3 Parameter Optimization	122
5.3.1 Particle Swarm Optimization.....	122
5.3.2 Implementation	123
5.4 Results and Discussions.....	127
5.4.1 Glass Transition	128
5.4.2 Elastic Constants.....	130
5.4.3 Deformation and Failure Behavior of Bulk Epoxy.....	133
5.5 Summary of This Chapter.....	139
Chapter 6 APPLYING LARGE SCALE cgmd TO STUDY BULK EPOXY FRACTURE	141
6.1 Introduction.....	141
6.2 Simulation Method.....	144
6.3 Results and Discussions	145
6.3.1 Stress-strain Curve and Deformation Sequence	145
6.3.2 Stress Criterion for Cavitation	148

6.3.3 Cavity Formation and Growth	151
6.3.4 Network Strand Scission.....	154
6.3.5 Comparison to Thermoplastic Glassy Polymers.....	158
6.3.6 Comparison to Experimental Observations	159
6.4 Summary of This Chapter	160
Chapter 7 STUDY OF TENSILE DEFORMATION AND FAILURE MECHANISMS OF EPOXY/CU BIMATERIAL USING LARGE SCALE COARSE-GRAINED md SIMULATION	162
7.1 Introduction.....	163
7.2 Coarse-Grained Model Development	165
7.3 Coarse-Grained Study of Tensile Deformation of Bimaterial	170
7.4 Results and Discussions	172
7.4.1 Microstructure Near Surface.....	172
7.4.2 Stress-strain Curve and Deformation Behavior	174
7.4.3 Effects of Strain Rate and Temperature	180
7.4.4 Effects of Conversion	184
7.5 Conclusions.....	188
Chapter 8 CONCLUSIONS AND RECOMMENDATIONS.....	190
8.1 Summary of Contributions.....	190
8.2 Recommendations to Future Work	194
8.2.1 On the Atomic End	194
8.2.2 Transition From Atomic to Macroscopic Cohesive Law.....	194
REFERENCES	198

LIST OF TABLES

Table 2-1. Potential terms involved in typical Force Fields	33
Table 2-2. Computer code to calculate inter-atomic distance in periodic cell.....	43
Table 4-1. Dimensions of the simulation cells.....	89
Table 4-2. Failure strength and strains for bimaterials with different conversions	105
Table 4-3. Failure strength and strain for different functionalities	108
Table 5-1. The lower and upper guess of the parameters and their optimized values (r_c is given as in the unit of σ . $k_\theta^{(1)}$, $k_\theta^{(2)}$ and $k_\theta^{(3)}$ are given in the unit of ε/rad^2).....	126
Table 5-2. Comparison between material properties calculated by coarse-grained and all-atom MD simulations (Superscript “(90)” stands for 90% cross-linked epoxy. Superscript “(0)” stands for the non-cross-linked epoxy. Units for temperature, density, and modulus are Kelvin (K), g/cm ³ and GPa, respectively)	126

LIST OF FIGURES

Figure 1-1. Schematics of a 3D electronic package containing polymer/metal interfaces	18
Figure 1-2. Failure sites and mechanisms in plastic package [1]	19
Figure 1-3. Illustration of cohesive zone (left) and cohesive law (right).....	23
Figure 1-4. Tvergaard and Hutchinson's adhesive law for ductile adhesive joint. δ_n and δ_t stand for normal and tangential crack opening displacements.....	24
Figure 1-5. Illustration of atomic configuration used in MD simulation of crack propagation along interface.....	27
Figure 2-1. Illustration of Periodic Boundary Condition.....	42
Figure 2-2. Illustration of minimal image criterion	44
Figure 3-1. (a) Molecular Structure of BPA (left) and EPN (Right); (b) Curing reaction mechanism; (c) Impression of network structure of epoxy Novolac cured	51
Figure 3-2. Snapshot of atomistic configuration after crosslinking.....	56
Figure 3-3. Variation of molecular weight of the largest and second largest fragment with degree of curing	57
Figure 3-4. RDF's of reactive atoms at different conversion rates for (a) minus center-minus center pairs (b) plus center-plus center pairs	60
Figure 3-5. Contributions to the RDF from (a) reacted-reacted minus-center pairs, (b) unreacted-unreacted minus-center pairs, (c) reacted-reacted plus-center pairs and (d) unreacted-unreacted plus-center pairs	61
Figure 3-6. Volumetric shrinkage upon crosslinking	62
Figure 3-7. Volume versus temperature relationship for the 90% cured epoxy system, fitted by bilinear function. The intersection corresponds to T_g	64
Figure 3-8. Free volume versus temperature relationship for the 90% cured system, fitted by bi-linear function. The intersection corresponds to T_g	66
Figure 3-9. Temperature dependence of potential energy components for the system of 90% conversion. a). total non-bond energy, b) bond stretching energy, c) angle bending energy and d) dihedral torsion energy	67

Figure 3-10. Total radial distribution function for the 90% crosslinked system at temperature of 300K and 500K	69
Figure 3-11. Radial distribution function between hydroxyl oxygens within the 90% crosslinked system at temperature of 300K and 500K.....	69
Figure 3-12. Torsion distributions for dihedrals aligned along (a) epoxy backbones, and (b) newly created crosslinks.	70
Figure 3-13. Mean square displacement versus time curves for epoxy backbone atoms at different temperatures.	71
Figure 3-14. MSD at the time of 20ps at different temperatures.	72
Figure 3-15. Volume versus temperature relationship for systems with different conversions: black square: monomer mixture, red circle: 25%, blue triangle: 50%, cyan diamond: 75%, magenta pentagon: 90%.....	74
Figure 3-16. (a) Tg versus conversion relationship; (b) coefficient of thermal expansion (rubbery and glassy) versus conversion relationship.....	74
Figure 3-17. (a) Stress-strain response and (b) lateral versus longitudinal strain curve for the 90% cured epoxy model at 300K, using strain rate of 1×10^9 s ⁻¹	76
Figure 3-18. (a) Stress-strain response of the 90% cross-linked system at 300K under various loading rates. (b) Young's modulus derived under different loading rates for the 90% cross-linked system at the temperature of 300K	78
Figure 3-19. Young's modulus (a) and Poisson's ratio (b) at room temperature for structures with different conversion rates.....	79
Figure 3-20. Young's modulus (a) and Poisson's ratio (b) versus temperature measured from Tg (T-Tg) relationships.....	80
Figure 4-1. Schematic of the epoxy/Cu bi-material.....	86
Figure 4-2. Stress versus strains curves for cells #2 and #3	89
Figure 4-3. Stress versus strains curves for cells #2 using different strain rates	90
Figure 4-4. Variation of (a) total and non-bond, and (b) valence potential energies with respect to strain.....	91
Figure 4-5. Snapshots of atomic configurations during the tensile simulation. The different figures in a row represent strains (from left to right): 8.7%, 38.5%, 77.1% and 107.9%.....	92

Figure 4-6. Stress-strain curves for the epoxy/Cu interface and the epoxy slab alone, respectively.	95
Figure 4-7. Unloading-reloading behavior of the epoxy/Cu interface system	97
Figure 4-8. Variation of the (a) non-bond and (b) valence potential energy components during the unloading-reloading process	97
Figure 4-9. Stress-strain curves at different temperatures	99
Figure 4-10. Yield and failure strengths of the bimaterial versus temperature	99
Figure 4-11. Stress-strain curves for bimaterials with different epoxy conversions	103
Figure 4-12. Atomistic configurations during tensile deformation for bimaterials with lower conversions at different strains: (a) 50% crosslinked; (b) 82% crosslinked. The different figures in each row represent strains (from left to right): (a) 56.6% and 98.1%; (b) 130% and 185.7%	104
Figure 4-13. Number of epoxy atoms within the van der Waals cutoff distance from the epoxy/Cu	105
Figure 4-14. Stress-strain curves for models with different epoxy monomer functionalities	107
Figure 4-15. Deformed atomistic configurations for the $f_n = 6$ case. The different figures from left to right represent strains at 39.2% and 63.7%	108
Figure 5-1. Illustration of Coarse-Graining of a Polymer Chain into Beads	116
Figure 5-2. Bead-connector representations of monomers: (a). EPN-3mer; (b). EPN-4mer and (c). BPA	118
Figure 5-3. Bond Potential curves for different bond extension cutoffs	120
Figure 5-4. Demonstration of raw data from the phase of MD simulation in the optimization process and the derivation of material properties of the two systems (pre-cured and cross-linked with conversion of 90%): (a). T_g 's are obtained as the intersection of bi-linear functions used to fit volume versus temperature data; (b). Densities are obtained as the time averaged value over the time range [50,000~100,000]; (c). Elongation moduli are obtained as the slope of the linear function which fits the stress-strain data; (d). Poisson's ratios are obtained as the slope of the linear function fitting the lateral-longitudinal strain data	125
Figure 5-5. Specific volume versus temperature relationships for systems with different conversions using the optimized coarse-grained potential parameters	129

Figure 5-6. Glass transition temperature versus conversion relationships obtained from coarse-grained and all-atomistic simulations [140].....	130
Figure 5-7. (a) Moduli and (b) Poisson's ratio versus temperature relationships for the 90% cross-linked epoxy using coarse-grained model and potential	132
Figure 5-8. Young's modulus versus temperature relationships for epoxies with different conversion rates.	132
Figure 5-9. Stress-strain curves for the uni-axial tensile simulation using different strain rates.	136
Figure 5-10. Number fraction of broken bonds versus strain	137
Figure 5-11. Snapshots of deformed configurations during the uniaxial tension for strains of (from left to right): 259%, 348%, 372% and 394%. Beads are colored according to their virial stress along the loading direction. The color bar is shown right to the last snapshot.	138
Figure 5-12. Spatial distribution of percentage of broken bonds at different strain levels.....	139
Figure 6-1. (a) Carbon-platinum surface replicas of craze structure in DGEBA-DETA epoxy films that were strained on metal substrate [132]; (b) TEM micrograph of dilatation bands of CTBN-modified DGEBA/piperidine taken inside the fatigue crack propagated damage zone [133].....	144
Figure 6-2. Stress-strain curve of the tensile deformations	147
Figure 6-3. Snapshots of the deformation sequence. Strains are ((a) ~ (e)): 45%, 140%, 200%, 255% and 260%. (f) is the color bar. Snapshots are made by Atomeye [169].	148
Figure 6-4. Zoomed-in view of one cavity from the configuration with strain of 45%. Beads are colored according to coordination number and the color map is the same as in Figure 6-3	148
Figure 6-5. Some loading conditions for study of yield criterion.....	149
Figure 6-6. Relationship between the octahedral shear stress at yielding and the pressure	150
Figure 6-7. Visualization of clusters of beads with Voronoi cell volume larger than threshold volume. Beads are colored according to their Voronoi cell volumes.	153
Figure 6-8. Total cavity volume and the fraction over the simulation cell volume, at different strains	154
Figure 6-9. Illustration of one piece of cross-linked polymer network with linked two cross-links marked. Red beads are hardener molecule beads. Grey beads are epoxy molecule beads.....	156
Figure 6-10. Probability distribution of ra for different deformed configuration.....	156

Figure 6-11. Fraction of broken bonds versus strain	157
Figure 6-12. Atomic configurations with beads colored by their atomic stress along the loading direction. Corresponding strains are (a)~(c): 90%, 145% and 200%	158
Figure 7-1. (a) full-atomic and (b) coarse grained models of the representative molecule attached to the Cu substrate.....	167
Figure 7-2. Metadynamics calculated free energy surface for the full-atomic model.....	168
Figure 7-3. Free energy surfaces using different coarse-grained potential parameters, compared to the full-atomic free energy surface. ε and σ are LJ parameters for epoxy beads.	170
Figure 7-4. Zoomed-in view near the interface. Grey and red beads are EPN beads and BPA beads, respectively. Yellow beads are substrate beads.	173
Figure 7-5. Variation of (a) density and (b) end-to-end distance (projection to the normal axis) of network strands along the normal direction. The dashed line represents the bulk value.....	174
Figure 7-6. Stress-strain curves for the tensile simulation of epoxy/Cu bimaterial.....	176
Figure 7-7. Snapshots of the configurations of the 90% cross-linked epoxy/Cu bimaterial during the tensile deformation using the strain rate of 10^8 s^{-1}	177
Figure 7-8. (a) Displacement profile along the normal direction for the 90% cross-linked epoxy/Cu bimaterial, for two different overall strains. (b) The extracted traction-separation relationship based on the definition of the interfacial zone.	178
Figure 7-9. End-end distance (projection to the normal axis) of network strands along the normal direction for different overall strains.	180
Figure 7-10. Stress-strain curves for lower strain rate and higher temperature.....	182
Figure 7-11. Snapshots of the configurations of the 90% cross-linked epoxy/Cu bimaterial during the tensile deformation using the strain rate of $2 \times 10^7 \text{ s}^{-1}$	182
Figure 7-12. (a) Displacement profile for lower strain rate and higher temperature. (b) Traction-separation relationship for lower strain rate and higher temperature.	182
Figure 7-13. Number of broken bonds versus strain for different strain rates and temperatures	183
Figure 7-14. Stress-strain curve for bimaterial with lower epoxy conversion.....	186
Figure 7-15. Snapshots of the configurations of the 73% cross-linked epoxy/Cu bimaterial during the tensile deformation.....	187
Figure 7-16. Number of broken bonds versus strain for different conversions	187

Figure 7-17. Traction-separation relationship for different conversions	187
Figure 8-1. SEM images of Cu leadframe being oxidized [17]	194
Figure 8-2. schematic illustration of how a roughened interface is modeled and meshed in FEM [182].....	195

CHAPTER 1 INTRODUCTION

This chapter introduces the research presented this dissertation. We first discuss the motivations, then review the current state of understanding of adhesion mechanisms and fracture behaviors of polymer/metal interfaces. After that a synopsis of the current thesis's objectives and goals is given. Finally the organization of this dissertation is explained.

1.1 Motivation

The past few decades have witnessed the emergence and explosive development of portable electronic devices. Laptops, smart phones and tablets are heading fast towards the goal of smaller size, higher performance and lower power consumption. Behind the evolvement of in-market products, it is the advancement of electronic packaging technology that acts as the driving force. The emerging technology of 3D packaging, which exploits the third or height dimension to provide a volumetric packaging solution, has become critical in the current trend of miniaturization of electronic devices. It enables integrating multi-media features and diversified consumer demands into smaller, lighter products, and provides more design freedom and higher electrical performance. As demonstrated in Figure 1-1, 3D packaging technology involves stacking of numerous metal layers bonded by polymer dielectric adhesives. This naturally generates large amount interfaces between highly dissimilar materials, and in further, risk of failures occurring at the interfaces. Unfortunately, polymer/metal interfaces are often considered as the “weakest links”. They are prone to delamination due to the effects of 1) intrinsic lack of chemical bonding between polymer and metal, 2) thermal stresses caused by the large mismatch of thermal and mechanical properties, and 3) various other factors including surface treatment,

humidity and formation of metal oxides. Delamination occurs at a number of locations in plastic packages, including encapsulant versus leadframe/die, adhesive versus leadframe/die and so on (See Figure 1-2). Interfacial delamination may lead to malfunction of the entire electronic device, thus is a critical reliability concern in packaging designs and manufactures.

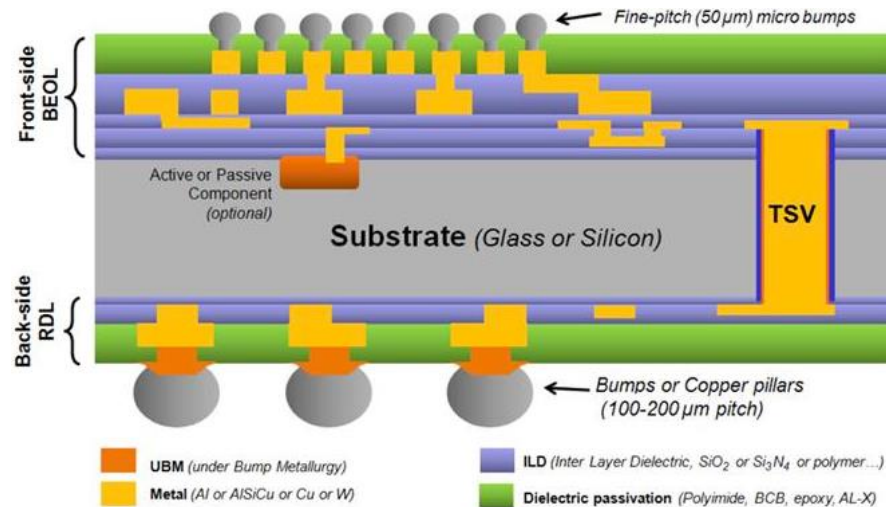


Figure 1-1. Schematics of a 3D electronic package containing polymer/metal interfaces

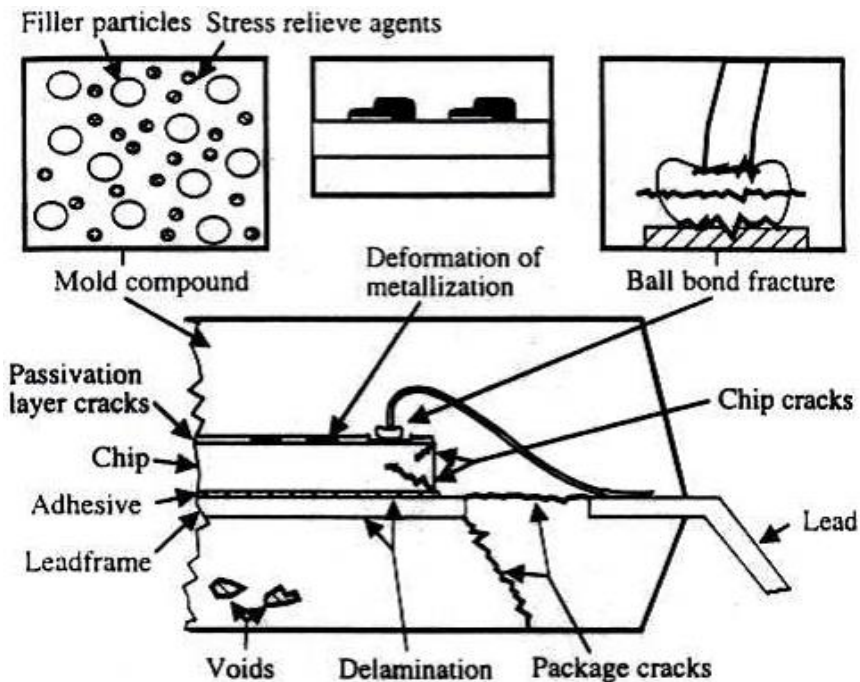


Figure 1-2. Failure sites and mechanisms in plastic package [1]

Of particular interests is the copper (Cu) based substrate versus epoxy based molding compound bimaterial. Because of Cu's excellent electrical/thermal conductivity and epoxy's superior mechanical/thermal integrity, they are prevalent among all the material systems in the current and near future electronic devices. However, the joint of the two components suffers from the same reliability concern as for other polymer/metal interfaces. Therefore, there has always been strong motivation to understand the fundamental physics of the interface, such as mechanisms of adhesion, strength and/or fracture toughness, and factors affecting these quantities. Based on these knowledge the interface can be engineered to gain better performances.

1.2 Adhesion Mechanisms at Polymer/Metal Interface

A number of different mechanisms are involved in the bonding of polymer and metal. By nature they can be chemical, physical or mechanical. These mechanisms often act in conjunction with each other on the same or different length scales, making the adhesion a multi-physics, multi-scale process. At molecular level, physical adsorption and chemical bonding are the mechanisms that operate. Physical adsorption refers to van der Waals forces or dipole-dipole interactions. Its intensity depends on density and proximity of interacting site pairs. The bonding energy associated with the types of interactions involved in physical adsorption is typically more than one order of magnitude lower than that of chemical bonding [2, 3]. However, studies [4, 5] have shown that the intrinsic strength of bimaterial bonded purely through physical adsorption can be as high as a few hundred MPa, due to the rather dense distribution of interacting site pairs in the vicinity of the interface. The chemical bonding is established through electron transfers which give rise to both covalent and ionic bonds. Hydrogen bond is another type of chemical bonding mechanism although it's relatively weaker. It should be pointed out that chemical bonding is generally lacked between epoxy and Cu [6], if no further surface treatment is applied, e.g., introducing coupling agents [7] and self-assembly monolayer (SAM) [8].

Mechanical adhesion originates from the irregularity of the geometry of the interface. In reality the contact surface between two solids is never perfectly planar. Instead they often penetrate one another by entering cavities and pores on the other side of the interface [9], resulting mechanical interlocking of the two phases. For instance, epoxy was found to be adsorbed to glass substrate to a depth of 3nm [10] and this contributes significantly to the intrinsic fracture toughness. Similar findings have been reported for polyurethane and glass [11,

12]. Another good example of interlocking between polymer and in-organic substrate is the roughed epoxy/Cu interface caused by the oxidation of copper. Copper substrate can be oxidized to form pebble like Cuprous Oxide (Cu_2O) and needle shaped Cupric Oxide (CuO) [13-15]. Oxides roughen the interface and change the failure path from purely interfacial to partially cohesive through the epoxy or the oxides [13-16]. Mechanical interlocking is thought to be an effective approach to improve adhesion between polymer and metal.

1.3 Fracture at Interface

The adhesion of interface between polymer and metal is often evaluated experimentally through destructive tests. Some of these tests aim to extract a single-parameter criterion, either strength based or energy based, to quantitatively describe the interface's performance. Strength based method includes pull-out test [17], peel test [17-19] and button shear test [20]. Energy based approach measures the fracture toughness, using setups such as four point bending [21] and sandwiched double cantilever beam [13, 14, 22]. In recent years it has been realized that the single-parameter criterion does not suffice to describe the non-linear behavior associated with fracture behaviors of some modern toughened adhesives, and the full constitutive relationship is desired. Based on the well-known J -integral [23], some researchers have developed methodologies to obtain the cohesive law for polymer metal adhesive joints [24-26].

The above described experimental approaches are time and money consuming. Thus people would like to develop “predictive” modeling/simulation techniques to avoid them. These techniques often find their roots in the theories of fracture mechanics. The linear elastic fracture mechanics (LEFM), based on the assumption of small-scale yielding ahead of the crack tip, has a long history of being applied to study failure of bonded joints made of polymer and metal.

LEFM uses the stress intensity factor (SIF) to describe the crack-tip stress field, and the critical condition of the crack (propagation) is related to the critical value of SIF, which defines interfacial fracture toughness. It is simple yet accurate enough for many polymer/metal interfaces of practical interest, especially those relatively brittle ones. However, LEFM's limitation is obvious: restricted to small-scale yielding, it is not applicable to scenarios where the plastic zone associated with the crack tip is comparable to a polymeric adhesive's thickness. Also, in numerical simulations such as Finite Element Method (FEM), modeling of fracture behavior based on LEFM requires pre-existing crack thus is not suitable to capture the entire crack initiation-growth process.

LEFM's drawback has long been recognized and more advanced theories have been developed to describe nonlinear fracture behavior. J.R. Rice proposed a new measure of energy release rate, i.e., the J -integral [23], to account for the situations where large-scale non-linear elastic or plastic (monotonic) deformation occurs ahead of the crack tip. On the other hand, the concept of cohesive zone ahead of the crack was introduced by Barenblatt [27] and Dugdale [28] proposed the mathematically similar but conceptually different model to discuss plane-stress yielding in sheets. As illustrated in Figure 1-3, the cohesive zone model considers a fracture processing zone ahead of the apparent crack tip, and stress across the processing zone, σ is a function of the separation distance δ . In other words a cohesive law in the form of traction-separation relationship, $\sigma = \sigma(\delta)$, can be used to describe the fracture initiation/extension process. The key parameters of the cohesive law include the cohesive strength, the critical separation distance at which traction vanishes, and the work of separation corresponding to the area under the traction-separation curve. A number of different cohesive laws have been

formulated. For instance, Needleman and Xu [29, 30] proposed a cohesive zone model for debonding of inclusion in ductile material. Regarding impact damage in brittle materials, a cohesive law was presented by Camacho and Ortiz [31]. For ductile adhesive, Tvergaard and Hutchinson [32, 33] used a trapezoidal shaped traction-separation relationship (see Figure 1-4) to model its delamination with elastic substrates. The cohesive zone model can be easily used with numerical simulations. In FEM a potential crack growing path is represented by a line or plane of zero-thickness cohesive elements that initially have zero thickness but open when stress is applied. Their constitutive behaviors are characterized by traction-separation laws, while the surrounding bulk is described by elastic-plastic continuum models. This method is particularly suitable for scenarios where crack propagation path is well-defined, e.g., delamination between two different materials.

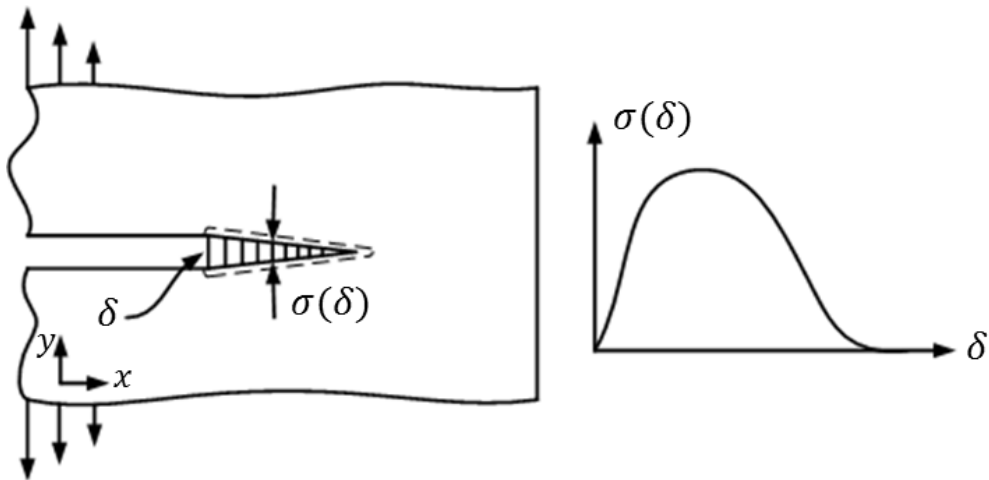


Figure 1-3. Illustration of cohesive zone (left) and cohesive law (right).

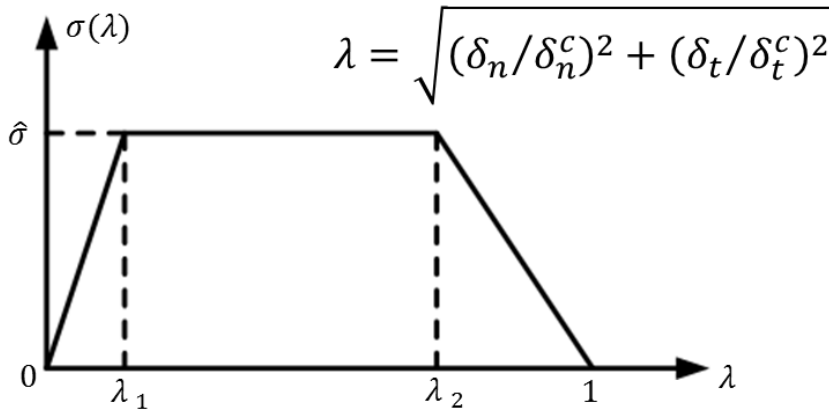


Figure 1-4. Tvergaard and Hutchinson's adhesive law for ductile adhesive joint. δ_n and δ_t stand for normal and tangential crack opening displacements.

Despite the success of cohesive zone model in simulating crack initiating/propagating within bulk and along interfaces, the parameters present in the model need to be determined beforehand. Wei and Anand [34] investigated inter-granular fracture in nano-crystalline Ni using cohesive elements in finite element (FE) simulation. The cohesive law used to characterize cohesive elements was parameterized based on experimental data regarding stress-strain curves of nano-crystalline Ni with large number of grains. The FE obtained stress-strain curves were compared and matched to measured ones so as to estimate the cohesive model parameters. In another study by Zavattieri et al. [35], cohesive parameters were determined based on the value of fracture toughness. These two works represent the method of indirectly finding parameters of cohesive laws. In recent years a number of researchers have developed the approach to directly extract cohesive laws. The methodology is based on obtaining the crack opening and J -integral in experiments and the deriving the traction-separation curve as [23]:

$$\sigma(\delta) = \frac{\partial J(\delta)}{\partial \delta} \quad (1.1)$$

Sorensen et al. [25, 26] and Ji et al. [24] have applied this method to determine cohesive laws for adhesive joints using double cantilever beam (DCB), for which the J -integral can be easily calculated [36].

1.4 Thesis Objective and Structure

The previous section has reviewed the fracture mechanics based numerical tools in modeling fracture occurring at interfaces, and pointed out that, either the single-parameter fracture related property or the full constitutive relationship (cohesive law) needs in turn to be determined through experimental testings, which can be time/resource consuming. Besides, cohesive laws obtained this way reflect the aggregate response of interfacial and bulk portion of the material thus does not reflect the intrinsic behavior of the interface where local failure occurs. In addition, the ongoing trend of miniaturization of electronic devices down to micron even nano scales is putting more challenges to experimental measuring techniques.

Motivated by these limitations, some researchers have considered using molecular simulations to extract fracture related properties. Molecular modeling techniques, such as Molecular Statics/Dynamics and Monte Carlo simulation, explicitly capture inter-atomic forces across the interface thus are suitable alternatives for such purposes. In addition, the micro-structure near the interface can be analyzed and tuned with great ease to explore structural-properties correlations, which can be formidable tasks in experiments. Farkas et al. [37] used atomistic simulation to study crack propagations in nanocrystalline Ni. The fracture toughness was calculated, as the slope of the system's excess energy versus the crack advance length. In [38] Yamakov et al. computed, in MD simulation, the stress intensity factor under the condition of steady-state crack propagation, by fitting the stress profile ahead of the crack tip to

$\sigma_{yy} = K_1 / \sqrt{2\pi(x - x_0)}$. Constitutive relationships used to describe the interface's response to mechanical loading, have also been studied by atomistic simulations. Gall et al. [39] investigated tensile debonding between aluminum and silicon using MD simulation with modified Embedded Atom Method (MEAM) potential. The traction versus local opening displacements relationship was extracted from atomistic simulation, and was found to have similar mathematical form with some continuum-based cohesive laws. Similar research was conducted for direct debonding of silicon wafer [40]. Spearot et al. [41] proposed a continuum interface separation constitutive laws, motivated by MD simulation of tensile and shear deformation of a grain boundary. A few internal state variables (ISV's) were used to describe interface attributes in the constitutive relation, whose evolutions were also determined by MD simulations. Instead of simulating direct debonding of pristine interface, a number of works have been done regarding MD simulation of crack propagation along the interface. Zhou et al. [42, 43] studied crack propagation between two BCC metals in order to derive the traction-separation curve under mixed-mode loading conditions. The MD simulations were conducted using the atomic configuration shown Figure 1-5, in which a pre-crack was introduced along the interface and the region in the vicinity of interface was divided into a row of cohesive zone volume elements (CZVE's). The statistical average over stress-opening displacement curves for a serial of CZVE's gives the interface's traction-separation law with mode-mixity accounted for, which was later used in FE analysis of brittle fracture [44]. The similar method was used by Yamakov et al. [38, 45] in their research regarding inter-granular fracture in aluminum and development of a FEM/MD-CZM multi-scale model for fracture modeling.

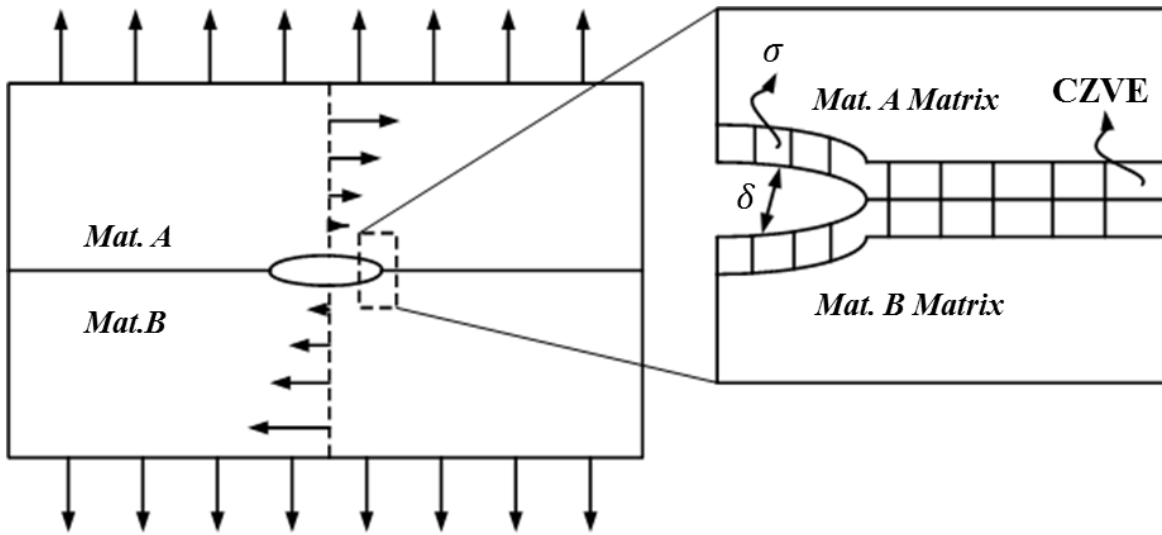


Figure 1-5. Illustration of atomic configuration used in MD simulation of crack propagation along interface

Indeed, molecular level simulations, if conducted correctly with accurate potential, can be a powerful tool in predicting fracture related properties of material interfaces. Therefore, for polymer/metal interfaces which have enormous amount of applications yet are so prone to delamination, there is strong thrust to apply molecular simulations to better understand their fundamental physics before engineering/modifying them to more favorable performances. However, unlike crystalline materials, such efforts can face serious challenges for the reasons listed below:

- 1). The complex amorphous structure of polymers rise the difficulty of building the correct atomistic (or coarse-grained) models upon which simulations will be conducted. Systems containing physically entangled polymer chains have been more thoroughly investigated for chain dynamics. Chemically cross-linked polymer such as epoxy based thermoset studied in the current thesis, however, remains a quite open area.

2). Inter-atomic interactions in polymers are rather sophisticated, involving forces of various different natures, and may require great amount of parameters to correctly describe. When in-organic second phase like a metal substrate kicks in, further complexity is brought into the picture, since additional potentials/parameters are needed for the interfacial interactions. Even such potentials are available they are often expensive to implement for large-scale simulations, as will be discussed in later parts of the thesis.

3). Length scale associated with fracture within polymers, either in bulk materials or along the interface, is beyond the length scale that molecular simulations deal with. Crack opening displacement can be a few microns or smaller (several hundred nano-meters), and length of fracture process zone is on the order of tens of microns. It is not possible to include the entire cohesive zone and the best thing one can do is to study a represent volume.

4). Time scale in molecular simulations is typically not exceeding the limit of hundreds of nano-seconds. Simulations with time span of micro-second are very rarely reported, and always use highly coarse-grained models and potentials. Therefore, constitutive stress-strain behaviors are for ultra-high strain rate situations in molecular simulations, as compared to the quasi-static conditions in experimental testings. One can foresee the obvious obstacle of applying them in continuum modeling.

The objective of the current dissertation is thus to meet these challenges. Using a commercially important epoxy molding compound, Epoxy Phenol Novolac (EPN), as an example, methodology will be explored to determine fracture related properties of its interface with copper substrate using molecular simulations. The properties of interest are strength and traction versus displacement relationship. The methodology developed will not be limited to this

specific material system but transferrable to other polymer/metal bimaterials, thus provide useful guidance for practical applications.

To achieve above stated goal, the dissertation starts with a brief introduction to the nuts and bolts of molecular dynamics simulation, in Chapter 2. After that, fully atomistic study of the epoxy molding compound and epoxy/Cu bimaterials will be firstly conducted, as presented in Chapter 3 and Chapter 4. A molecular dynamics simulated polymerization process is developed to build the permanently cross-linked polymer network, based upon which further MD studies to compute key thermo-mechanical properties. The successful reproduction of material properties, validated by good agreement with available experimental data, approves the use of the same method of modeling the epoxy in epoxy/Cu bimaterial. The bimaterial is investigated for its strength and stress-strain/displacement constitutive behavior using MD simulation. Several structural and loading-condition related affecting factors are studied for their effects.

From Chapter 5 to Chapter 7 we will be focused on developing meso-scale model to solve the stringent length/time scale limitation of fully atomistic simulations. The coarse-grained (CG) model and potentials designed for the epoxy modeling compound and epoxy/Cu bimaterial will be parameterized. Use of CG model enables simulation of deformation/failure behavior of bulk epoxy and epoxy/Cu bimaterial on the scale of $\sim 10^6$ nm³, which is not possible to access using fully atomistic simulations, thus will greatly enhance our understanding of the true mechanical behaviors of epoxies and their interfaces with substrate.

CHAPTER 2 MOLECULAR DYNAMICS SIMULATION

This chapter introduces the basics of molecular dynamics (MD) simulation. The fundamental assumption and scope of MD simulation are firstly discussed. The key ingredients, including governing equation, interatomic potentials, ensembles and thermal/baro-stat, and boundary conditions are explained. Focuses will be on issues specific to organic and/or polymeric materials.

2.1 Introduction

MD simulation tracks the movement of atoms, molecules or other generalized particles in the context of N-body system. Motions are governed by the Newton's equation and driven by interatomic interactions, described by interatomic potentials. Classical MD simulation uses empirical potential, predefined as a mathematical formulation. The fundamental assumption behind this is that, the electronic degrees of freedom are not explicitly incorporated in the picture of classical MD. Nevertheless, empirical potentials are carefully formulated and rigorously parameterized by fitting against Ab initio calculated or experimental measured physical properties, and thus are good approximations of interatomic interactions. After decades of efforts, classical MD with empirical potentials has achieved overwhelming success on various kinds of condensed matters for rather sophisticated physical processes. Due to the limitation of classical MD, events like chemical bond breaking and reactions cannot be modeled explicitly, unless the recently developed reactive force-field, e.g., ReaxFF [46] is used.

2.2 Ingredients of MD simulation

2.2.1 Governing Equation and Time Integrator

In MD simulations, an N-body system's configuration change with respect to time is governed by the equation of motion:

$$m_i \ddot{\mathbf{r}}_i = \mathbf{f}_i \quad \mathbf{f}_i = -\frac{\partial}{\partial \mathbf{r}_i} U(\mathbf{r}_1, \mathbf{r}_2, \dots, \mathbf{r}_N) \quad (2.1)$$

where U is the potential energy of the system and is a function of the vector $\mathbf{r}^N = (\mathbf{r}_1, \mathbf{r}_2, \dots, \mathbf{r}_N)$ which is the set of $3N$ particle coordinates. Given the initial positions and velocities of each particle, the subsequent evolution of the system is deterministic. Per-particle information, including positions, velocities and forces are sampled and used to obtain global observables, e.g., energy, temperature, pressure and (virial) stress tensor, to describe the system's state at any time.

To numerically solve Eq.(2.1), an integrator is needed. Several algorithms have been developed to meet the demand of efficiency, accuracy, robustness and memory saving. These include Verlet algorithm [47], its modified “leap-frog” form [48], the velocity Verlet algorithm [49], predictor-corrector algorithm [50], etc. The velocity Verlet algorithm, which is used as the standard integrator by a number of large scale, parallel MD codes, such as LAMMPS [51], GROMACS and AMBER, will be introduced here. Velocity Verlet splits a time increment δt into two halves, as is done in leap-frog method. However, unlike the leap-frog algorithm which computes velocities at $t + \frac{1}{2}\delta t$ and positions at $t + \delta t$, velocity Verlet manages to simultaneously calculate both the positions and velocities at time $t + \delta t$, thus is improved over leap-frog's disadvantage. The algorithm can be formulated as [52]:

$$\begin{aligned}
 \mathbf{p}_i(t + \frac{1}{2}\delta t) &= \mathbf{p}_i(t) + \frac{1}{2}\delta t\mathbf{f}_i(t) \\
 \mathbf{r}_i(t + \delta t) &= \mathbf{r}_i(t) + \delta t\mathbf{p}_i(t + \frac{1}{2}\delta t)/m_i \\
 \mathbf{p}_i(t + \delta t) &= \mathbf{p}_i(t + \frac{1}{2}\delta t) + \frac{1}{2}\delta t\mathbf{f}_i(t + \delta t)
 \end{aligned} \tag{2.2}$$

where \mathbf{p}_i is the i -th particle's linear momentum. Note that in step 3 of Eq.(2.2), the forces at time $t + \delta t$ are calculated from the positions at this moment obtained in step 2. Velocity Verlet algorithm obtains positions and velocities at the same time, thus is able to output the system's total energy (potential plus kinetic), which is not doable using leap-frog method. In addition, it is low order in time, thus allows use of relatively larger time-step [52]. However, the algorithm is expensive in terms of memory consumption during the inter-atomic force evaluation.

2.2.2 Inter-atomic potentials

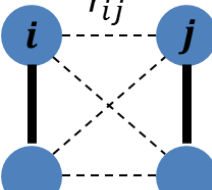
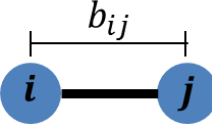
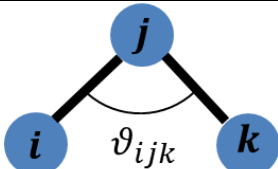
Whether a material system has suitable potential to describe its inter-atomic forces determines if it can be studied in molecular simulations. Therefore, developing/parameterizing potential has always been of central importance. Depending on the nature of the inter-atomic force, various types of potentials have been developed and successfully applied. These include:

- 1) the Lennard-Jones (LJ) potential [53] to describe van der Waals forces (dipole-dipole interactions, occurs in all chemical substances)
- 2) the Embedded Atom Method (EAM) [54], and its modified version MEAM [55, 56], to describe metallic systems (takes into account interactions of an atom with the whole environment thus is a many-body potential)
- 3) inter-ionic potentials for ionic solids, such as Born-Mayer-Huggins (BMH) [57, 58] and Michielsen-Woerlee-Graaf (MWG) potentials.

4) Angular-dependent many-body (Stillinger-Weber [59]) and Bond-Order (Tersoff [60]) potentials for semiconductor materials Si, GaAs, Ge, etc.

5) Force Fields (FF) for organic compounds, including AMBER [61], CHARMM [62], CVFF [63], PCFF [64-66], COMPASS [67], etc.

Table 2-1. Potential terms involved in typical Force Fields

Illustrative diagram	Description	Mathematical Formulation (may vary with different FF's)
	Lennard-Jones Coulombic Hydrogen Bonds ¹	$U(r_{ij}) = 4\epsilon_{ij} \left[\left(\frac{\sigma_{ij}}{r_{ij}} \right)^{12} - \left(\frac{\sigma_{ij}}{r_{ij}} \right)^6 \right]$ $U(r_{ij}) = 4\epsilon_{ij} \left[\left(\frac{\sigma_{ij}}{r_{ij}} \right)^9 - \left(\frac{\sigma_{ij}}{r_{ij}} \right)^6 \right]$ $U(r_{ij}) = \frac{q_i q_j}{\epsilon r_{ij}}$
	Bond Stretching	$U(b_{ij}) = \frac{1}{2} k_{ij} (b_{ij} - b_{ij}^0)^2$ $U(b_{ij}) = D_{ij} (1 - e^{-\alpha_{ij} (b_{ij} - b_{ij}^0)})$
	Angle Bending	$U(\vartheta_{ijk}) = \frac{1}{2} k_{ijk} (\vartheta_{ijk} - \vartheta_{ijk}^0)^2$

	Torsional Dihedral	$U(\varphi_{ijkl}) = k_{ijkl} [1 + \cos(n\varphi_{ijkl} - \varphi_{ijkl}^0)]$
	Improper Dihedral	$U(\psi_{ijkl}) = \frac{1}{2} k_{ijkl} (\psi_{ijkl} - \psi_{ijkl}^0)^2$

¹ Hydrogen Bonds are explicitly incorporated in Dreiding FF using a LJ-12-10 term [68]. In other FF's, Hydrogen Bonds are implicitly handled by optimizing LJ potential parameters.

The FF methods account for all different kinds of interactions in biological and polymeric materials. These interactions can be categorized into two classes: non-bonded and bonded. Non-bonded forces include van der Waals, electrostatic forces and hydrogen bonds. Bonded forces are related to covalent bonds, e.g., bond stretching, angle stretching and torsional/improper dihedrals. These interactions are demonstrated in Table 2-1. Each interaction has a corresponding term and a Force Field is a summation of the terms. In more recently developed Force Fields like PCFF and COMPASS, terms representing coupling between bond stretching, angle bending and torsional/improper dihedrals are introduced to more accurately describe structure and properties.

Among non-bonded FF terms, the Lennard-Jones potentials are short range interactions and thus computed based on direct truncation method, i.e., calculation of energy and forces is not conducted if distance is larger than a prescribed cutoff distance. The cutoff distance is used to build and update neighbor list during the MD simulation. Therefore, these forces can be fast

calculated without sacrificing accuracy. Another issue with using LJ potentials is assigning parameters for unlike species. Force Fields typically hold their own databases having parameters for each species (or atom types) and use mixing rules to compute the parameter for pairs of unlike atoms. Widely used mixing rules include arithmetic, geometric and sixth power rules. The sixth power rule, which is used by Class II FF's (PCFF, COMPASS), is written as [69]:

$$\epsilon_{ij} = \frac{2\sigma_i^3\sigma_j^3\sqrt{\epsilon_i\epsilon_j}}{\sigma_i^6 + \sigma_j^6} \quad \sigma_{ij} = \left(\frac{\sigma_i^6 + \sigma_j^6}{2} \right)^{1/6} \quad (2.3)$$

Unlike van der Waals interaction, the Coulombic or electrostatic forces are much more expensive to compute due to its long-range nature ($\propto r^{-1}$). Besides, in infinite lattices, e.g. in ionic solids, use of large cutoff distance does not lead to convergence of the summation (of Coulombic forces between pairs of ions), since the summation itself is conditionally convergent [70]. Therefore, calculation of electrostatic interactions requires special techniques to meet the demand of speed and accuracy. The Ewald method [71] is the earliest approach proposed to solve this difficulty. Its fundamental idea is decompose the electrostatic interaction into short range part, calculated in real space through truncation, and long range part, calculated in reciprocal space. The Ewald method calculates the total Coulombic energy as [72]:

$$\begin{aligned} E &= E^S + E^L - E^{\text{self}} \\ &= \frac{1}{4\pi\epsilon_0} \frac{1}{2} \sum_{\mathbf{n}} \sum_{i=1}^N \sum_{j=1}^N \frac{q_i q_j}{|r_i - r_j + \mathbf{n}L|} \operatorname{erfc}\left(\frac{|r_i - r_j + \mathbf{n}L|}{\sqrt{2}\sigma}\right) \\ &\quad + \frac{1}{2V\epsilon_0} \sum_{\mathbf{k} \neq 0} \frac{e^{-\sigma^2 k^2/2}}{k^2} |S(\mathbf{k})|^2 - \frac{1}{4\pi\epsilon_0} \frac{1}{\sqrt{2\pi}\sigma} \sum_{i=1}^N q_i^2 \end{aligned} \quad (2.4)$$

The detailed derivation can be found in [72]. In Eq.(2.4) E^S and E^L are summed in real space and reciprocal space, respectively, and both their summations are short ranged. Using Ewald method

the total Coulombic energy converges absolutely and rapidly. The method is not only used in periodic lattices of ions but also in amorphous materials such as polymers in which atoms are partially charged. However, it is still a relatively expensive computational technique ($O(N^{3/2})$) and is efficient only for small to moderately sized systems. For larger systems, the particle-particle particle-mesh (PPPM) method [73] is the better choice. In PPPM, “particle-particle” refers to calculating the real space contribution as pairwise interactions truncated at a certain cutoff, while “particle-mesh” means assigning the particle’s charge to a mesh and computing the electrostatic force on the particle as the particle’s charge multiplying the mesh’s electric field, in order to obtain the reciprocal space contribution. The PPPM method uses Fast Fourier Transformation (FFT) to solve the electric field on the mesh, thus gives better performance in terms of computation speed.

The non-bonded interactions are calculated only for pairs of atoms which are not bonded pairs, meaning that atom i, j in a bond, atom i, k in an angle, and atom i, l in a dihedral (see Table 2-1) will not interact through non-bonded potentials. In molecular simulations, information of bonds, angles, and dihedrals are written into the initial configurations. Their energies are computed per the potential functions, and forces on each atom involved are evaluated by conducting partial derivative of energy with respect to atom coordinate. As mentioned in Table 2-1, different Force Fields have different expressions for each kind of interactions. Take bond stretching term for example. In AMBER and CHARMM the simplest harmonic function is used, while in CVFF the Morse potential is applied. The Class II FF’s, PCFF and COMPASS use the more complicated 4th order polynomial to describe bonds. In Coarse-Grained (mentioned later in

the dissertation), the finite extensible nonlinear elastic (FENE) [74] and quartic potentials are the ones most suitable for description of bonds between coarse-grained beads rather than atoms.

In addition to the bond related terms described in Table 2-1, PCFF and COMPASS also introduced coupling terms or off-diagonal terms, such as bond-bond, angle-angle, bond-angle, bond-torsion, etc. These terms can be important when modeling some organic compounds with complex molecular structures.

2.2.3 Ensembles and Thermo/Baro-Stat

In statistical mechanics, a thermodynamic ensemble is known as a collection of a large number of possible microstates that the system might be in, each of which is subjected to the same set of constraints, such as fixed number of particle (N), volume (V), pressure (P), and energy (E). An ensemble corresponds to a partition function, defined as the weighted sum over all microstates, and the weight of a microstate is its probability of appearance in the ensemble. The purpose of introducing the concept of ensemble is that, it is practically not feasible to study all possible microstates. Instead, thermodynamic quantities of interests can be calculated by averaging over the entire ensemble using the appropriate partition function.

In MD simulations, it is one type of the thermodynamic ensembles to be realized through controlling the corresponding thermodynamic quantity: 1) the Microcanonical or constant NVE ensemble; 2) the Canonical or constant NVT ensemble; 3) the isothermal-isobaric or constant NPT ensemble; 4) the Grandcanonical or constant μVT ensemble (μ stands for chemical potential). The Microcanonical ensemble is the natural ensemble of MD simulation. If no external forces are applied, the system's Hamiltonian is constant [70]. To maintain Canonical

and isothermal-isobaric ensembles, thermo/baro-stats, i.e., adjustment of temperature and pressure, need to be applied. Below we will briefly review the most common temperature/pressure controlling methods.

In realizing the *NVT* ensemble, only the thermo-stat needs to be applied. The simplest controlling mechanism is the velocity scaling method. This method evaluates the actual temperature T and scales each particle's velocity by a factor $\sqrt{T_0/T}$ (T_0 is the target temperature). The drawback of the method is obvious: every adjustment brings in a discontinuity into the system's phase trajectory thus the time to reach equilibriums is expected to be longer. Another mechanism, originated from the same fundamental thought of scaling particles' momenta but allow for fluctuation of the temperature around the target value, was proposed by Berendsen et al. [75, 76]. The method scales velocities by a different factor $\lambda = \left[1 + \frac{\delta t}{\tau} \left(\frac{T_0}{T} - 1 \right) \right]^{\frac{1}{2}}$.

Neither velocity scaling nor Berendsen method generates the true Canonical ensemble. The method that indeed realizes the Canonical ensemble is the Nose-Hoover thermo-stat [77, 78]. The Nose-Hoover thermo-stat operates through introducing a virtual degree of freedom (DOF), s , to represent the interaction between the system and the external heat reservoir. s is a scaling factor that transforms real time to virtual time, i.e., $d\tau/dt = s$. The real system plus the additional DOF forms an extended system, and its Hamiltonian is expressed as:

$$H^*(p, q, s, p_s) = \sum_{i=1}^N \frac{\tilde{p}_i^2}{2m_i s^2} + U(q_1, q_2, \dots, q_N) + \frac{p_s^2}{2M_s} + (3N+1)k_B T \ln s \quad (2.5)$$

where $p_i = \tilde{p}_i/s$, $q_i = \tilde{q}_i$ are real system's momenta and coordinates, and p_s is the momentum of the additional degree of freedom. M_s is the effective mass of the additional degree of freedom.

By introducing a time-dependent frictional term ζ , the equations of motion drawn from the Hamiltonian (Eq. (2.5)) can be derived as:

$$\begin{aligned}\zeta &= \frac{\dot{s}}{s} = \frac{p_s}{M_s} \\ \dot{q}_i &= \frac{p_i}{m_i} \\ \dot{p}_i &= -\frac{\partial U}{\partial q_i} - \zeta p_i \\ \dot{\zeta} &= \frac{1}{M_s} \left(\sum_i \frac{\dot{p}_i}{m_i} - (3N+1)k_B T \right)\end{aligned}\tag{2.6}$$

which describes how Nose-Hoover thermo-stat tune each particle's velocity to each the target overall temperature.

In coarse-grained molecular simulations, the two thermo-stats that have been widely used are the Langevin thermo-stat [79] and Dissipative Particle Dynamics (DPD) thermostat [80]. The two mechanisms have in common that dissipative forces are introduced to damp the particles' velocity to maintain temperature. Each atom's force will have the form:

$$\mathbf{f} = \mathbf{f}^C + \mathbf{f}^D + \mathbf{f}^R\tag{2.7}$$

where \mathbf{f}^C , \mathbf{f}^D and \mathbf{f}^R represent for conservative, dissipative and random forces, respectively. The difference lies in that Langevin thermo-stat uses dissipative terms to describe interactions between particles and the background implicit solvent, while in DPD they stand for frictional forces between particles.

To maintain a *NPT* ensemble, both thermo- and baro-stat need to be applied. The mostly extensively used pressure controlling mechanisms include Berendsen method, Anderson method and Parrinello-Rahman algorithm. The Berendsen method [76] places the system in a virtual “bath” and adjust the system's pressure to be in balance with the bath's pressure, through

rescaling the simulation box length, and hence the particles' positions. As for Berendsen thermostat, the disadvantage of this approach is that it is unclear what statistical ensemble will be generated. The Anderson method [81] is based on the concept of introducing the simulation box's volume ($V = L^3$) as an additional degree of freedom. The system's Hamiltonian can then be written in a scaled way as:

$$H(\tilde{q}, \tilde{p}, V, p_V) = \sum_{i=1}^N \frac{\tilde{p}_i^2}{2m_i L^2} + U(L\tilde{q}) + \frac{p_V^2}{2Q} + P^{ext}V \quad (2.8)$$

where $\tilde{q}_i = q_i/L$ and $\tilde{p}_i = p_i L$ are the particle's scaled coordinate and linear momentum, and P^{ext} is the prescribed external pressure. An obvious drawback of Anderson method is that it keeps the box as cubic. Anisotropic and even shear deformation of the simulation box is not possible under Anderson baro-stat.

To overcome Anderson method's limitation, the Parrinello-Rahman [82] (PR) algorithm was proposed to make possible the change of both the volume and shape of the simulation box. The PR algorithm defines a matrix holding the three edge vectors of the simulation cell:

$\mathbf{h} = \{\mathbf{a}, \mathbf{b}, \mathbf{c}\}$, and the particles' coordinates can be expressed as $q_i = \mathbf{h}s_i$. The extended system's Lagrangian is written as:

$$L = \sum_{i=1}^N \frac{m_i \dot{s}_i^T \mathbf{G} \dot{s}_i}{2} - U(\mathbf{h}s) + \frac{1}{2} W \text{Tr}(\dot{\mathbf{h}}^T \dot{\mathbf{h}}) - P^{ext} \Omega - \frac{1}{2} \text{Tr}(\Sigma \Omega) \quad (2.9)$$

in which W is the mass the external bath and Σ is the external stress.

2.2.4 Boundary Conditions

Due to limitation of computational power, the number of atoms is quite limited in MD simulations. Although systems containing as many as billions of atoms have been simulated [83],

it is still almost negligible compared to the number of atoms in a tiny chunk within the condensed matters. This causes the “surface effect”, meaning that the fraction of atoms on the surfaces of the MD modeled volume over atoms within the bulk, is much bigger than on the macroscopic level. Therefore, what MD obtains does not represent true behavior/property of the material. To eliminate the surface effect, the Periodic Boundary Condition (PBC) is applied on all Cartesian directions of the cubic MD simulation cell. By using PBC, each atom within the simulation cell, together with its motion, is replicated to infinity. Mathematically, an atom (or a general particle) at position \mathbf{r} has images at locations:

$$\mathbf{r} + m\mathbf{a} + n\mathbf{b} + l\mathbf{c} \quad (2.10)$$

where m , n and c are integers from $-\infty$ to $+\infty$, and \mathbf{a} , \mathbf{b} , \mathbf{c} are edge vectors of the simulation cell. PBC is illustrated in Figure 2-1. In the figure the brown polyethylene chain is the original chain and all the surrounding chains are its images. Whenever a carbon/hydrogen atom on the chain has a velocity \mathbf{v} , the imagery atoms in the neighboring cells move with the exactly same velocity. The result of applying PBC is that, atoms that would otherwise sit on the surface now feel forces from imagery atoms. Therefore surface is effectively eliminated. The periodic boundary condition can be used three dimensionally to study properties/behaviors of bulk materials. When applied only one or two dimensionally, it helps to mimic geometries such as nanotube/wire and thin film.

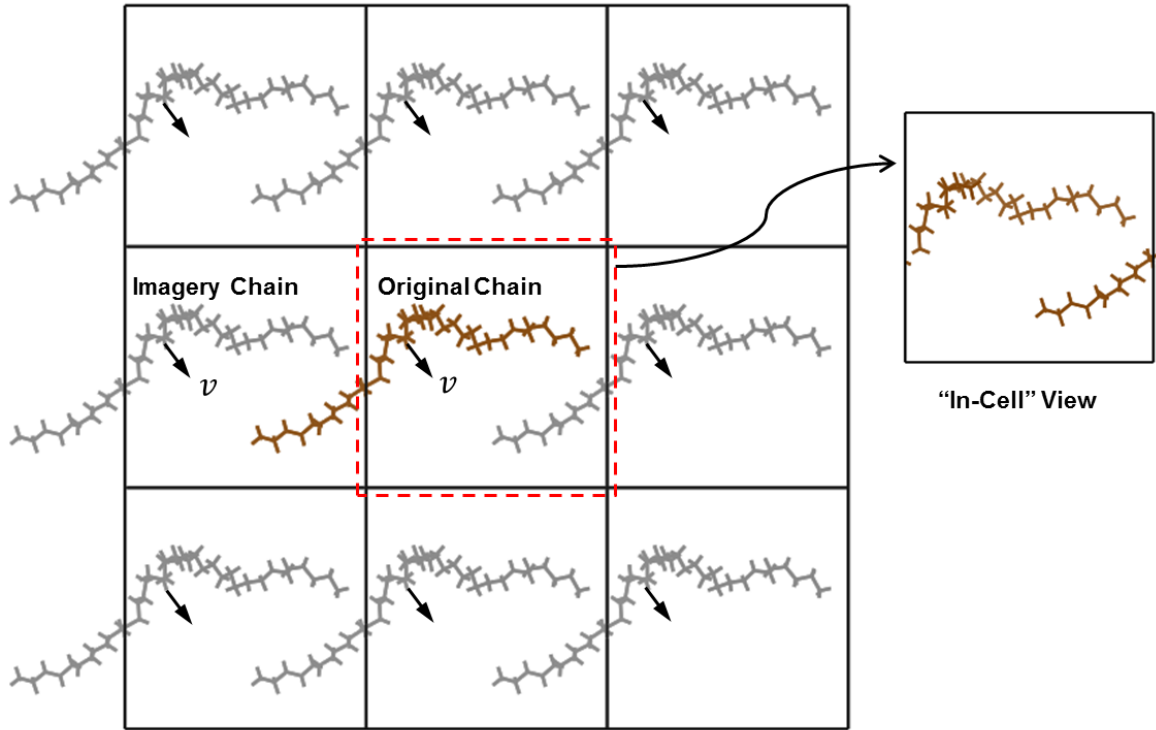


Figure 2-1. Illustration of Periodic Boundary Condition

As demonstrated in Figure 2-1, the original polyethylene chain is not fully contained in the original simulation cell. Instead, it extends into the neighboring cell, and as the result of PBC, its image enters the original cell from the opposite side (see “In-Cell” view in Figure 2-1). This is common for applying PBC to simulate polymer chains, that the original *atoms* may not all belong the original *molecule*. In order to correctly calculate quantities related to molecules, such as center of mass, radius of gyration and end-end distance, the original atoms need to be “unwrapped” to their locations on the original molecule, by using an attribute of atom called *image flag*, defined as:

$$\begin{aligned} i_x &= \left\lceil (x_{\alpha}^u - x_{\text{low}}) / (x_{\text{high}} - x_{\text{low}}) \right\rceil \\ i_y &= \left\lceil (y_{\alpha}^u - y_{\text{low}}) / (y_{\text{high}} - y_{\text{low}}) \right\rceil \\ i_z &= \left\lceil (z_{\alpha}^u - z_{\text{low}}) / (z_{\text{high}} - z_{\text{low}}) \right\rceil \end{aligned} \quad (2.11)$$

where subscripts “high” and “low” refer to the maximum and minimum boundaries along the certain direction, respectively, and $\lceil r \rceil$ denotes the largest integer that is smaller than the real number r . x_{α}^u , y_{α}^u and z_{α}^u are the unwrapped coordinates.

The use of PBC brings ambiguity into inter-atomic force evaluations. As is illustrated in Figure 2-2, an atom α can interact with both the atom β and its image β' if both $r_{\alpha\beta}$ and $r_{\alpha\beta'}$ are smaller than the cutoff distance r^c , which is unrealistic and introduces excessive computational load. To avoid this ambiguity, it is required that all three dimensions of the simulation cell are larger than $2r_c$, i.e. the so called *minimal image criterion* needs to be satisfied. This ensures that if one of $r_{\alpha\beta}$ and $r_{\alpha\beta'}$ is smaller than r^c , the other one is larger than r^c thus will not be considered for force evaluation. In real MD simulations the separation between two atoms is always pre-processed before it enters the potential function to calculate energy and forces. Such an action can be explained by a piece of computer code:

Table 2-2. Computer code to calculate inter-atomic distance in periodic cell

```
dx = x[i]-x[j]; // x coordinate difference of ith and jth atom
if (dx > lx/2) // lx = xhi-xlo
    dx -= lx;
if (dx < -lx/2)
    dx += lx;
```

```
// Similar actions done here for y and z coordinates
dr = sqrt(dx*dx + dy*dy + dz*dz); // calculate distance
```

This ensures that the distance between two atoms will always be the smallest among all possible values under the consideration of periodic boundary condition. Also it prevents the program from getting unrealistically long covalent bond when the bond crosses the periodic boundary, as is in the situation in shown in Figure 2-1.

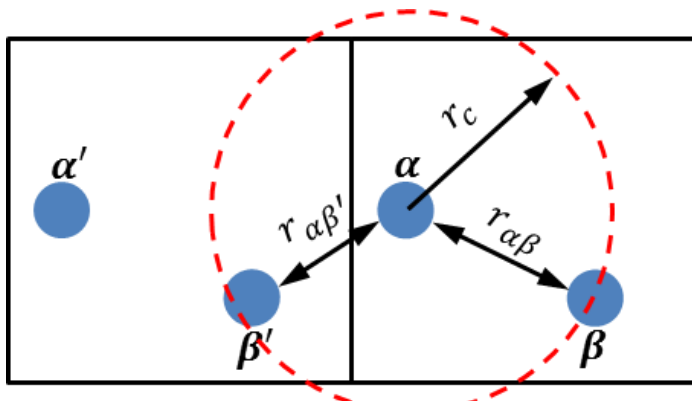


Figure 2-2. Illustration of minimal image criterion

As will be shown later in Chapter 3, the use of PBC to model epoxy molding compound is of special importance, since epoxy thermosetting polymers have the cross-linked network which percolates to infinity (or in reality, the inner wall of containers). PBC enables one to mimic such percolation of polymer network.

2.3 Summary of This Chapter

In this chapter, the fundamental concept and the key elements of realistic MD simulations, including governing equation, potential, ensemble and boundary conditions, are

introduced. Although these introductions are general and may not be directly related to the work in the current dissertation, they are crucial to understand the fundamental methodologies and technical details which will be presented in the following chapters.

CHAPTER 3 ATOMISTIC STUDY OF BULK EPOXY

In this chapter, the use of MD simulation to study the thermo-mechanical properties of the epoxy molding compound (EMC) is presented. The EMC is formed by curing tri/tetra-functionalized Epoxy Phenol Novolac (EPN). An iterative crosslinking-relaxation methodology is developed to construct the simulation cell. This crosslinking-relaxation methodology allows the construction of highly cross-linked polymer network from a given set of monomers. Based on this computational algorithm, three-dimensional simulation cells can be constructed. By using an existing polymer consistent force-field, several thermo-mechanical properties of the model epoxy are computed such as the curing induced shrinkage, gelation point, coefficient of thermal expansion, glass transition temperature, Young's modulus and Poisson's ratio. The dependence of these properties on crosslink density and temperature is also investigated. Simulated results are compared with existing theoretical or experimentally measured values when available. Good agreements are observed.

3.1 Introduction

Epoxy is a class of thermosetting polymers synthesized chemically by curing molecules containing epoxy groups and hardeners with active hydrogen atoms such as hydroxyls and amines. For its superior properties, including mechanical/thermal integrity and moisture/chemical resistance, epoxy has wide applications as matrix materials of composites, adhesives, encapsulants and molding compounds in consumer electronics, automobiles and aircrafts. Because of their ubiquitous nature, the thermo-mechanical behavior of these epoxy compounds plays critical roles in the efficiency and reliability of micro-electronics. Therefore it

is critical to know accurately their thermo-mechanical properties under various temperature and loading conditions.

The conventional approach to obtain the thermo-mechanical properties of engineering materials is to conduct experimental tests. However, experimental testing has its limitations. For example, most tests are typically very time-consuming and expensive. Such difficulties are further exasperated by the recent advances in the application of nano-materials, because direct testing of nano-size samples is nearly impossible with the existing testing capabilities. MD simulation offers a good alternative. If done appropriately, it is capable of predicting many thermo-mechanical properties of crystalline solids such as coefficient of thermal expansion (CTE) [84, 85], elastic modulus [84, 85], tensile strength [86, 87], etc.

Conducting MD simulations of polymeric materials is, however, rather challenging. Unlike in the crystalline solids, the molecules in polymeric materials are somewhat randomly connected. Such amorphous molecular nature makes it very difficult to construct the MD simulation model. This is particularly true for polymers with cross-linked network structures. Over the decades, extensive research has been conducted to construct the cross-linked network of polymeric molecules. Early works were mainly concentrated on the kinetic aspects of the network build-up process through Monte Carlo simulations on idealized models, without considering topological information and chemical details [88-90]. Prediction/reproduction of thermo-mechanical properties for realistic materials was, however, not intended in these investigations. In recent years, fully atomistic representations of polymer networks have been proposed along with realistic force-fields that have been extensively parameterized and validated. Some of these works follow the approach of manually connecting constituent

monomers into a fully cured network [91-94]. Such manual approaches are not only limited to rather small model size, but also somewhat unrealistic in that there is no reason to assume *a priori* how monomers are linked to each other. More advanced methodologies involve dynamic curing of network starting from physical mixture of monomers. For example, Komarov et al. [95] developed a mapping/reverse mapping procedure for epoxy network formation, where monomers were first coarse-grained to bead-springs models and placed on lattice sites. Covalent links were randomly created between reactive beads. Afterwards the cross-linked system was reverse-mapped to the atomistic level. Yarovsky et al. [96] applied a crosslinking scheme for epoxy resins (with cross-linker CYMEL 1172 and 1158). Both works performed chemical curing in a one-step fashion, i.e., all bonds between reactive bead/atoms were introduced simultaneously. Other authors have proposed multi-step procedures which create covalent bonds and equilibrate the structure iteratively. For instance, Wu and Xu [97] studied DGEBA-IPD epoxy system through MD simulations. Their atomistic model was constructed by repeatedly crosslinking and relaxing the system until the desired conversion rate was reached. Similarly, Varshney et al.[98] used cyclic crosslinking algorithm, which conducted multi-step topology relaxation, to construct epoxy-based polymer network.

Based on the molecular models built by the afore-described approaches, various MD simulation techniques have been used to simulate the dynamic [99], thermal [92-95, 98, 100-104], mechanical [93, 94, 97, 100, 102] and diffusion [91, 96, 105, 106] behavior of epoxies and epoxy-as-matrix composites. Simulation results were in reasonably good agreement with experimental measurements, indicating that MD simulation can be an efficient and accurate tool to study thermosetting polymers. Dependency of material properties on cross-link density, or the

degree of polymerization, has also been examined through molecular simulations [100, 102, 107, 108]. For example, Li and Strachan [102] studied EPON862/DETDA epoxy system and predicted significant increase in glass transition temperature (T_g), stiffness and yield stress with conversion. Bandyopadhyay et al. [108] investigated the same material system and reported increasing T_g and elastic constants but decreasing coefficient of thermal expansion (CTE) with respect to cross-link density. The authors also reported that the magnitude of property changes decrease above a threshold conversion (63%).

Work presented in this chapter aims at utilizing molecular dynamics simulation to study not only material properties of a Novel epoxy molding compound but also its structural-property relationship by varying the degree of curing of the molecular model. Conversion dependence of epoxy's properties is essential to material design thus worthy of thorough investigation. The rest of the paper is organized as follows. Crosslinking scheme and inter-atomic potentials are described in Section 3.2. Section 3.3 presents results on material properties and structural-property correlations, as well as related discussions. Finally some concluding remarks are summarized in Section 3.4.

3.2 MD Simulation Method

The epoxy molding compound studied in this dissertation is an epoxy phenol novolac (EPN). The EPN consists of EPN-1180 as epoxy and Bisphenol-A (BPA) as hardener [109]. Their chemical structures are illustrated in Figure 3-1 (a). The epoxy monomer is a mixture of 3mers and 4mers, and the number averaged length is 3.6. Benzene rings in the epoxy resin are connected through methylene groups. The distribution of ortho-, meta- and para-connections are considered to be trivial and thus followed an arbitrary arrangement in modeling epoxy

monomers. Figure 3-1 (b) elucidates the curing reaction mechanism. In the presence of catalyst, the carbon-oxygen bond in the epoxy monomers is broken, which opens the epoxy ring. The oxygen-end of the opened epoxy ring takes over the hydrogen atom from a nearby hydroxyl group in a BPA molecule, leaving a dangling oxygen in the BPA molecule. This dangling oxygen then forms a covalent bond with the carbon-end of the opened epoxy ring. This process links the epoxy monomer to a BPA molecule. Since each BPA has two hydroxyl groups, two epoxy monomers may be attached to the same BPA molecule. This process allows the formation of polymer chains. Furthermore, depending on the functionality of the epoxy monomers, multiple BPA molecules might be attached to the same epoxy monomer, which forms the crosslink between the polymer chains. Using the stoichiometric mixing ratio of tri-epoxy:tetra-epoxy:BPA = 2:3:9, the theoretical full conversion can be reached and the average epoxy functionality of $f = 3.6$ is maintained. In Figure 3-1 (c) the cured epoxy network is schematically illustrated.

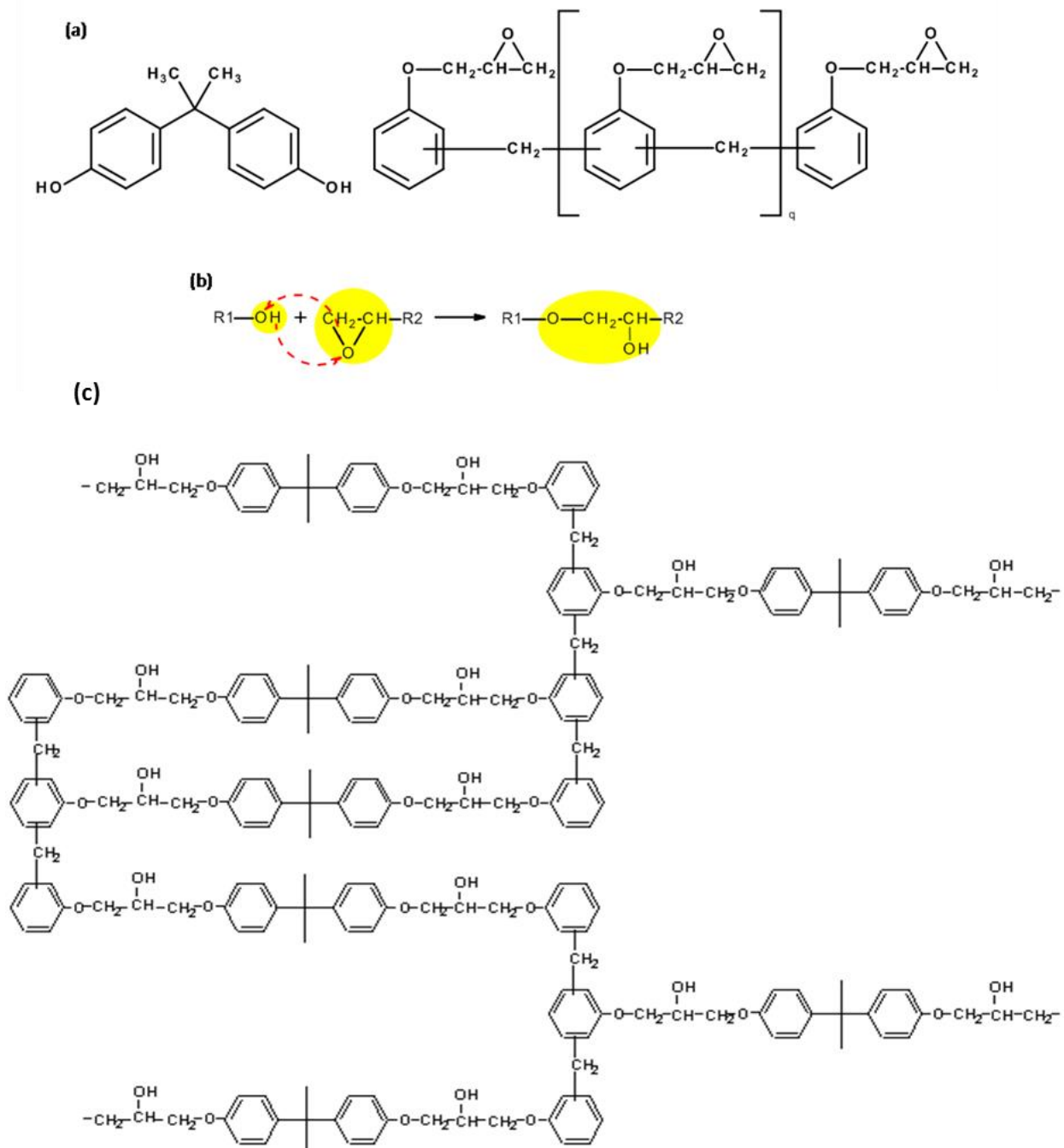


Figure 3-1. (a) Molecular Structure of BPA (left) and EPN (Right); (b) Curing reaction mechanism; (c) Impression of network structure of epoxy Novolac cured

The force-field used to describe the inter-atomic forces of EPN is the polymer consistent force-field (PCFF) [66]:

$$\begin{aligned}
 E_{total} = & \sum_b [k_2(b-b_0)^2 + k_3(b-b_0)^3 + k_4(b-b_0)^4] + \sum_\theta [H_2(\theta-\theta_0)^2 + H_3(\theta-\theta_0)^3 + H_4(\theta-\theta_0)^4] \\
 & + \sum_\phi [V_1(1-\cos\phi) + V_2(1-\cos 2\phi) + V_3(1-\cos 3\phi)] + \sum_\chi K_\chi \chi^2 \\
 & + \sum_{b,b'} F_{bb'}(b-b_0)(b'-b'_0) + \sum_{b,\theta} F_{b\theta}(b-b_0)(\theta-\theta_0) + \sum_{\theta,\theta'} F_{\theta\theta'}(\theta-\theta_0)(\theta'-\theta'_0) \\
 & + \sum_{b,\phi} (b-b_0)(V \cos\phi + V_2 \cos 2\phi + V_3 \cos 3\phi) + \sum_{\theta,\phi} (\theta-\theta_0)(V \cos\phi + V_2 \cos 2\phi + V_3 \cos 3\phi) \\
 & + \sum_{b,\theta,\phi} F_{b\theta\phi}(b-b_0)(\theta-\theta_0) \cos\phi + \sum_{i,j} \frac{q_i q_j}{r_{ij}} + \sum_{i,j} \epsilon_{i,j} \left[\frac{A_{ij}}{r_{ij}^9} - \frac{B_{ij}}{r_{ij}^6} \right]
 \end{aligned} \tag{3.1}$$

This PCFF has been parameterized and validated for various organic and in-organic species [66, 110-112]. It consists of valence and non-bond forces, as is seen from Eq. (3.1). The valence terms are for bond stretching, angle bending, dihedral and improper interactions, as well as coupling between them. The non-bond terms include the electrostatic and van der Waals forces. The latter is represented by the Lennard-Jones (LJ) 9-6 potential. In our calculations, a cut-off distance of 12.5 Å is used for the LJ potential, while the electrostatic force is calculated using the Ewald method with an accuracy of 1×10^{-6} to account for its long-range nature.

Once the force-field is available, the next step is to construct the initial molecular model for conducting the MD simulations. The most challenging aspect of constructing the model is how to accurately describe the cross-linked network of polymers. The actual curing process of thermosetting polymers, which results in the cross-linked network, is a complex quantum-chemical process involving the breakage/formation of covalent bonds and hydrogen transfers. Depending on the temperature, the curing time required to reach full conversion may range from tens of minutes to hours. Simulating the actual curing dynamics at the molecular level is beyond the capability of even the fastest computer in the world now. Instead, we have developed a

methodology that yields the final cross-linked structure without actually simulating the details of the chemistry of the curing process. The basic idea of this methodology is to use spatial proximity as a criterion for bond formation. When the hydroxyl oxygen of a BPA molecule is within a threshold distance to an epoxy monomer's epoxy carbon, which has been exposed as active sites by pre-opening the epoxy ring, they readily react with each other and form a chemical bond. The initial threshold distance used is 3Å. This distance is somewhat subjectively determined based on the van der Waals radii of the reacting atoms. As the crosslink density increases, formation of new bonds becomes more difficult. To speed up the process, the threshold distance is increased gradually to 10Å. The process described above is implemented in the following steps.

1. Create epoxy monomers and BPA molecules by using the sketch tool in the Material Studio Visualizer [46]. Epoxy rings were pre-opened for the convenience of forming chemical bonds, leaving the ending epoxy carbons and hydroxyl oxygens on BPA's as reactive sites. The geometries of these molecules are optimized by energy minimization.
2. Randomly seed epoxy monomers and BPA molecules into a cubic simulation box at the target density of 1.2g/cc with periodic boundary conditions in all three orthogonal directions. This is done by using the Amorphous Cell module in Material Studio based on the self-avoiding random-walk of Theodorou and Suter [113]. The mixture contains 8 tri-functionalized epoxies, 12 tetra-functionalized epoxies and 36 BPAs, corresponding to 2766 atoms and cell length of ~30Å. The stoichiometric mixing ratio of tri-epoxy:tetra-epoxy:BPA = 2:3:9 is maintained.
3. Conduct MD simulation in the NVT ensemble at 300K to relax the system from internal

stress built up during the formation of new chemical bonds in the previous steps, and to allow atoms to move around so reactive sites may get closer. Periodic boundary conditions (PBCs) are prescribed in all three orthogonal directions of the cubic simulation box. Further equilibration and removal of residual stress is performed by running long term MD simulation in NPT ensemble upon the completion of cross-linking process, as will be described later on. We believe that NVT versus NPT during the cross-linking process would not cause noticeable difference in structure and material properties to the resultant epoxy model. Several existing work, e.g., Wu and Xu [97] and Yarovsky and Evans [96] followed the same NVT ensemble MD in their equilibration phase of curing simulation.

4. Identify all the pairs of hydroxyl oxygen and ending epoxy carbons that are separated by a distance within the bond formation threshold. Each pair is marked as one “close contact” and is linked by newly formed covalent bond. If one ending epoxy carbon is involved in multiple close contacts, it will be bonded to one of hydroxyl oxygens in proximity. Both reactive atoms (epoxy carbon and hydroxyl oxygen) are then marked as reacted and forbidden from possible reaction to other reactive atoms.
5. Repeat steps 3 and 4 above until the desired conversion rate is reached.

We note that once a link is introduced between hydroxyl oxygen and epoxy carbon, the charge distribution around these atoms will be altered. Therefore, partial charges of the entire system need to be re-assigned upon the completion of crosslinking. This can be accomplished by using the bond increment charging algorithm of the PCFF force-field. The final step of the crosslinking process is to saturate the remaining reactive sites (unreacted epoxy carbons and BPA oxygens)

with hydrogens. Our cross-linking methodology is dynamic in nature since it involves molecular mechanics/dynamics equilibration in the intervals of bond formations. Compared to static approach, e.g. in the work by Bandyopadhyay et al. [108] which cures statically the EPON862-DETDA system based on root mean square (RMS) distance between reactive atoms and relates the conversion rate (or crosslink density) to the RMS distance being used, we believe the dynamic scheme introduces new covalent bonds more gradually and thus generates more energy favorable configurations.

In the end, in order to achieve a fully relaxed network, the crosslinked system is further equilibrated by MD simulations under the canonical (NVT) ensemble at 600K for 1ns, followed by NVT annealing to 300K at the cooling rate of 10K/10ps. Afterwards, another MD simulation is run under the NPT ensemble for 1ns at 300K and atmospheric pressure to bring the system to the correct density of 1.172g/cc. The Nose-Hoover thermo- and barostats are used to adjust temperature and pressure in all the MD simulations. An example of the crosslinked structure for the studied epoxy resin is shown in Figure 3-2. The conversion rate for this example is 90%.

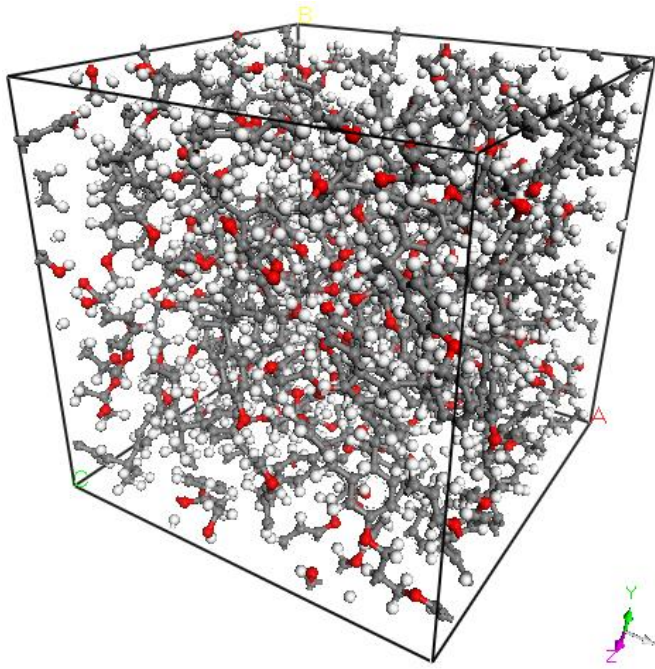


Figure 3-2. Snapshot of atomistic configuration after crosslinking

Before closing this section, we note that, because of the PBCs used, covalent bonds are formed not only among the original set of monomers but also between monomers and their virtual neighbors. Consequently, the crosslinked system is actually an infinitely percolating network. Ideally, the system should consist of one single macro molecule upon gelation as is the case for realistic thermosetting polymers. This can be confirmed by investigating the molecular weight of the largest and second largest group during the simulated curing process. At high degrees of polymerization (>80% conversion), molecular weight of the largest group builds up to its upper limit after increasing drastically while that of the second largest group drop to very low level from its peak value, indicating that a system-spanning cluster has formed and most of the subsequent reactions would occur within this cluster. Therefore, the peak of the second largest group represents the conversion at which gelation occurs, or the gel point. As seen from Figure 3-3, the gel point predicted by our MD simulation is around 74%. Following Miller and

Macosko's theory [114], the theoretical gel point for our epoxy system (tri/tetra-functionalized epoxy + bi-functionalized crosslinker) is 62%. The discrepancy between the MD and theoretical results are most likely due to the occurrence of intra-molecular curing reactions. There is a possibility that the two reactive sites of a crosslinker (BPA) connects to the same epoxy monomer in both simulation and reality while it is assumed in theory that no intra-molecular reaction occurs. In other words, the 74% predicted from our MD contains the intra-molecular reaction while the theoretical value of 62% does not.

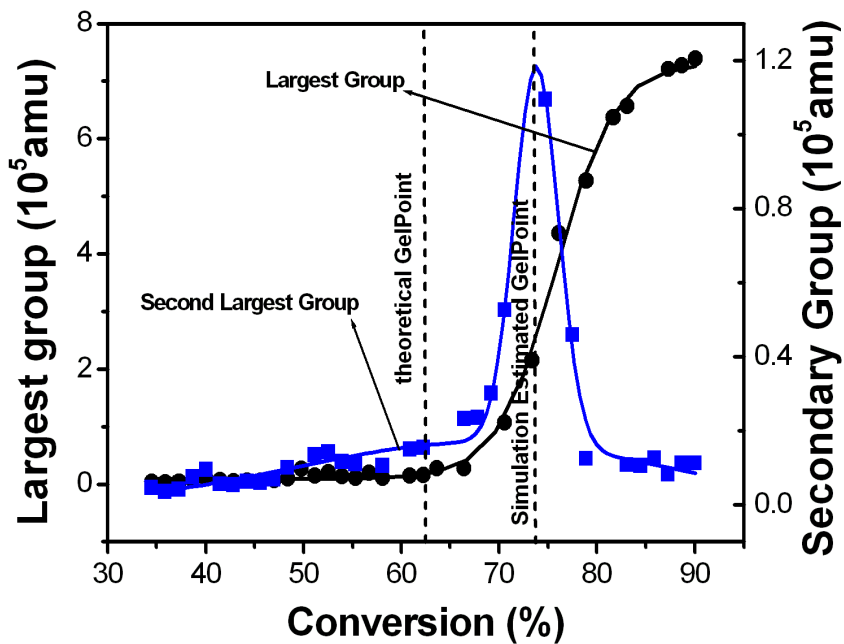


Figure 3-3. Variation of molecular weight of the largest and second largest fragment with degree of curing

3.3 Results and Discussions

3.3.1 Local Structure Evolution

The local structure evolution during the curing process was studied by investigating the radial distribution function (RDF) for specific groups of atoms. The RDF describes the probability of finding species α and β at a separation distance r :

$$g_{\alpha\beta}(r) = \frac{n_{\alpha\beta}(r)}{4\pi r^2 dr (N_\alpha N_\beta / V)} \quad (3.2)$$

where N_α and N_β are numbers of species α and β , V is the system volume. $n_{\alpha\beta}(r)$ is the number of α - β pairs within the range of $(r - \Delta r/2, r + \Delta r/2)$. The RDF converges to unity at large distances since spatial correlation no longer exists, and has a value of zero within short range due to excluded volume interaction. We here mark hydroxyl oxygens on BPAs as “minus centers” and the ending epoxy carbons on EPNs as “plus centers”. Figure 3-4 (a) and (b) plot RDFs for minus center-minus center pairs and plus center-plus center pairs, respectively. Minus center RDF’s for all conversions share a common peak at 9.5\AA , corresponding to the distance between the two hydroxyl oxygens on the same BPA molecule. Since hydroxyl oxygen atoms mark the two ends of a BPA molecule, the above observation indicates that the hardeners (BPA) do not experience significant stretch when crosslinking is completed. At 0% conversion, we see a noticeable peak at approximately 2.9\AA in the minus-minus RDF, which decreases in magnitude as the conversion becomes higher. Meanwhile the principal peak shifts to 6\AA . To understand this transition, we present the reacted-reacted (Figure 3-5 (a)) and unreacted-unreacted (Figure 3-5 (b)) components of the minus center RDF’s. It is clearly shown that the 2.9\AA peak corresponds to

the most probable inter-atomic separation between un-reacted minus centers while the 6Å peak is for reacted-reacted minus-center pairs. The reason why reacted-reacted minus centers show a different spatial distribution is that, each of the reacted minus centers is linked to one specific epoxy carbon thus has to re-position itself in accordance to the location of its connected epoxy carbon. When the curing reaction proceeds, the number fraction of unreacted-unreacted and reacted-reacted pairs decreases and increases, respectively, so does their contributions to the total minus-center RDF. As a result, the main feature shifts from 2.9 to 6Å. As for the plus-plus RDF (Figure 3-4 (b)), two peaks at approximately 4 and 5.6Å are observed. The former peak diminishes as the conversion approaches to 90%. The latter one roughly keeps its position but varies in magnitude. Figure 3-5 (c) and (d) indicate that the unreacted-unreacted component of the plus center RDF has peaks at both 4 and 5.6Å, while the reacted-reacted part has a single peak at 5.6Å which coincides that of the reacted-reacted minus-center RDF with difference of only 0.4Å, implying that reacted plus centers re-distributed themselves in accordance to their linked minus centers. It is again the change of relative contribution from unreacted and reacted parts that changes the overall radial distribution function.

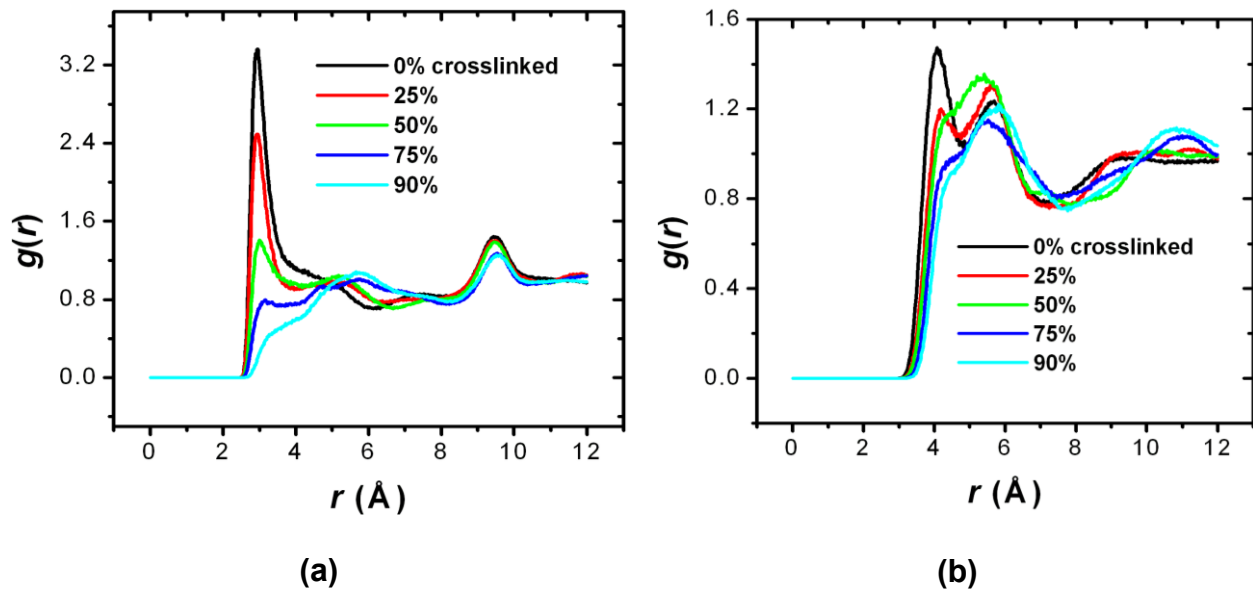
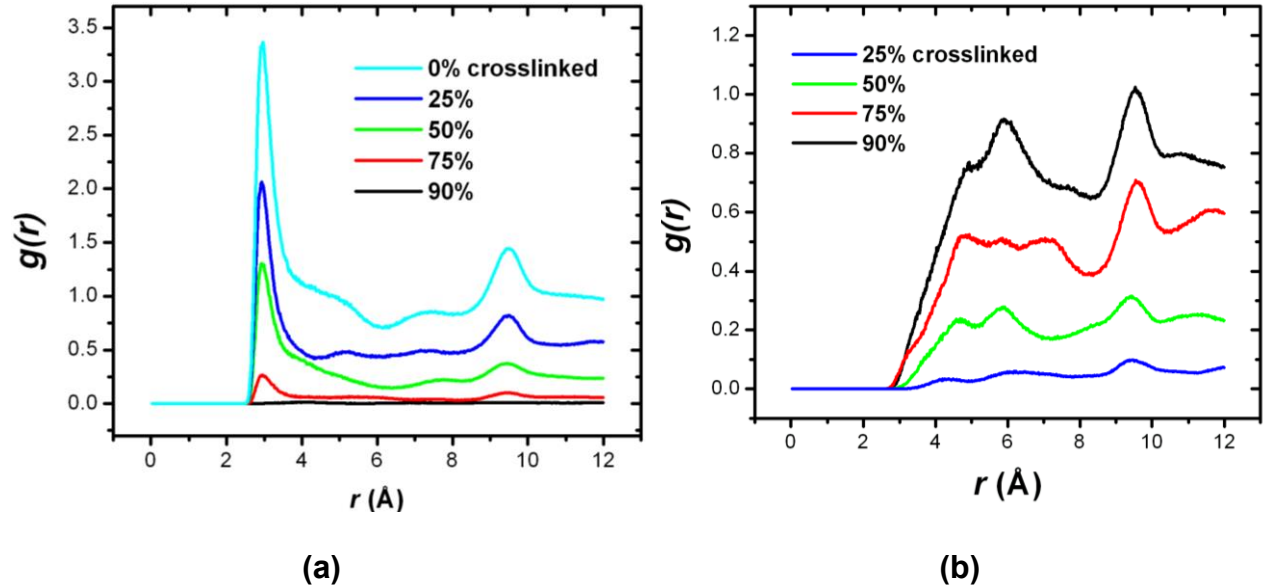


Figure 3-4. RDF's of reactive atoms at different conversion rates for (a) minus center-minus center pairs (b) plus center-plus center pairs



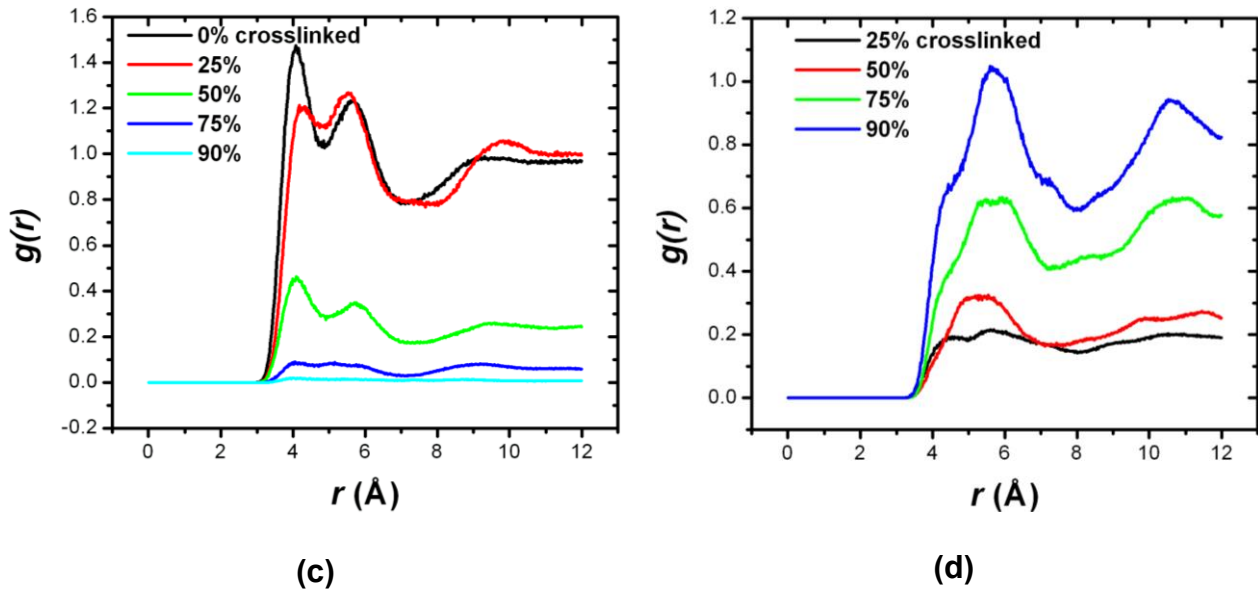


Figure 3-5. Contributions to the RDF from (a) reacted-reacted minus-center pairs, (b) unreacted-unreacted minus-center pairs, (c) reacted-reacted plus-center pairs and (d) unreacted-unreacted plus-center pairs

3.3.2 Cross-link Induced Shrinkage

Another effect of crosslinking is volume shrinkage or increase in density. To observe this shrinkage, systems generated along the trajectory of the polymerization simulation, with conversions of 0, 25%, 50%, 75% and 90%, were equilibrated at 300K following the same protocol described in Section II. The cell volume at the equilibration state for each conversion was obtained and shown in Figure 3-6, along with volumetric shrinkage with respect to the un-cross-linked state. For the highest cross-linked system (with conversion of 90%), a volume shrinkage of 4.24% is predicted.

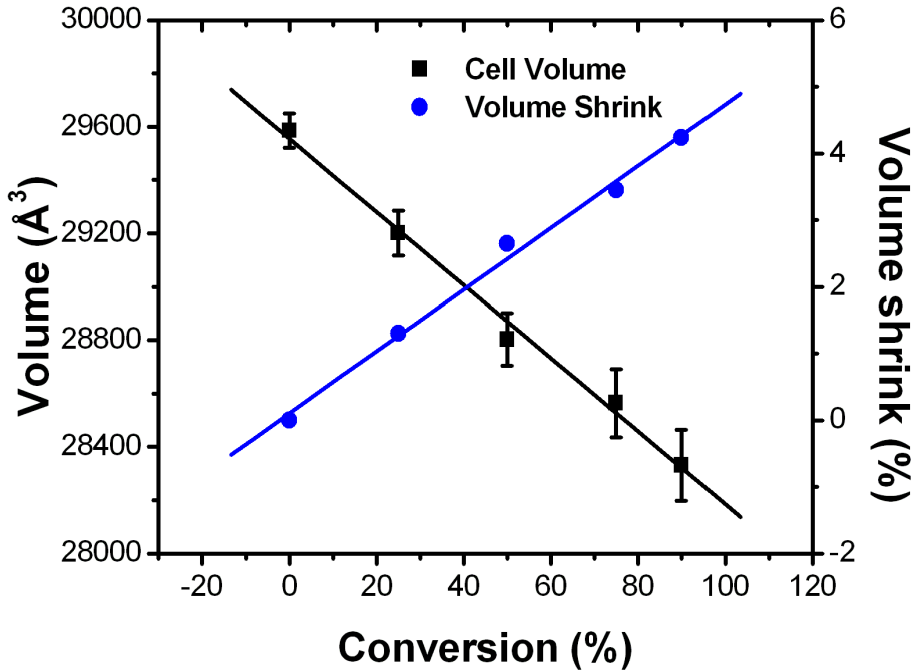


Figure 3-6. Volumetric shrinkage upon crosslinking

3.3.3 Thermal Expansion and Glass Transition

3.3.3.1 Glass Transition Temperature and CTE Determination

Once the system was sufficiently equilibrated, the atomistic model was ready for subsequent production runs for material property calculation. In order to study the temperature dependence of various thermodynamic quantities, a high temperature annealing protocol was followed. The temperature was first raised up to 500K and equilibrated for 500ps using a NPT ensemble under atmospheric pressure, and then dropped by 20K each time until it reached 200K. At each temperature, the system was equilibrated by a NPT MD simulation at atmospheric pressure for 200ps. Temperature and pressure were adjusted by the Nose-Hoover thermostat and baro-stat in all simulations. For each temperature, the volume of the simulation box V was sampled over the entire duration of the MD simulation and averaged. The duration over which

the volume is averaged at each temperature is an issue worth of discussion. Before cooling initiates the structure has been well equilibrated following the above mentioned procedure. Since each temperature drop is only 20K, the structure is re-equilibrated very quickly every time its temperature is decreased. Thus the error associated with the choice of the duration for averaging is negligible. Figure 3-7 plots the volume versus temperature relationship. It is seen that there is a discontinuity in the volume versus temperature slope, which gives the glass transition temperature T_g . The glass transition temperature T_g marks a second-order phase transition from glassy to rubbery state, and is one of the most important properties of polymeric materials since it determines the temperature range for processing and operating the material. To determine the glass transition from volume versus temperature data segmental linear regression needs to be conducted, which depends on the temperature range selected for fitting. Bandyopadhyay et al. [108] derived T_g as a temperature range based on five choices of temperature ranges for data fitting. We followed similar approach in our study by using temperature ranges $[T_{min}, T_1]$ and $[T_2, T_{max}]$, where T_{min} and T_{max} are fixed as 200K and 500K while T_1 and T_2 vary. Our predicted T_g is 402.6 ± 4.9 K and it compares well with the experimental data that range from 369K from dilatometric measurements to 396K from DMA measurements [92]. The fact that our predicted T_g is somewhat higher has to do with the higher cooling rate used in our MD simulations.

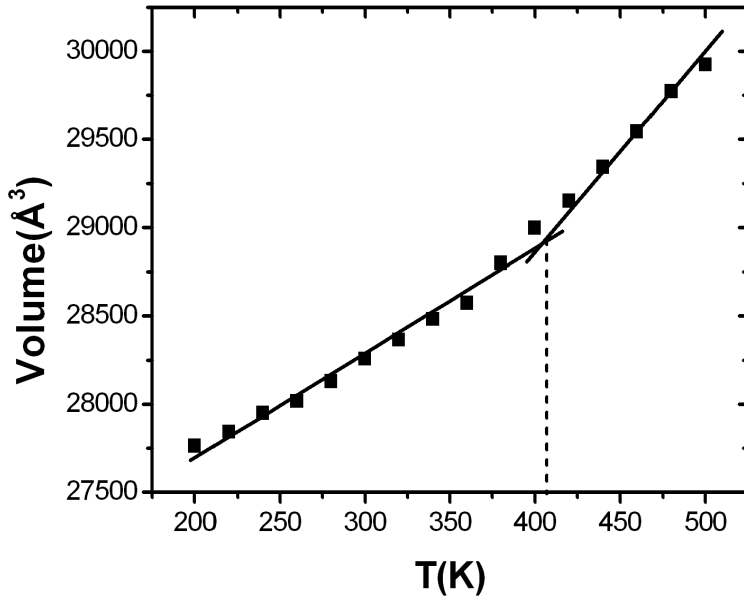


Figure 3-7. Volume versus temperature relationship for the 90% cured epoxy system, fitted by bilinear function. The intersection corresponds to T_g

The volumetric coefficient of thermal expansion (CTE) α is defined by

$$\alpha = \frac{1}{V_0} \left(\frac{\partial V}{\partial T} \right)_P \quad (3.3)$$

where V_0 is the equilibrated system volume before the cooling simulation starts. The fractional change of volume $\Delta V / V_0$ is obtainable from data shown in Figure 3-7 and its slope versus temperature is the coefficient of volume thermal expansion. CTE of the cured (90%) epoxy is calculated as 191.2 ± 14.7 ppm/K in the glassy state and 396.7 ± 28.072 ppm/K in the rubbery state, which are close to experimental measured values $\alpha_{g,\text{exp}} = 195$ ppm/K and $\alpha_{r,\text{exp}} = 579$ ppm/K [115], respectively. The error of CTE prediction is again associated with temperature range choice while doing segmental linear regression.

The glass transition temperature can also be obtained by calculating the free volume as a

function of temperature, since the free volume undergoes an abrupt change when the material goes through glass transition, according to Fox and Flory's theory of glass transition [116]. By probing the polymer cell with a spherical probe, using the "Atom Volume & Surfaces" tool of the Material Studio software, the free volume in the 90% cross-linked epoxy was calculated as a function of temperature during the annealing process. Several radii of the probe sphere ranging from 0.7Å to 1.4Å were used, and the results are almost identical regarding the temperature at which free volume experiences transition. Similar to the volume analysis, free volume was sampled and averaged over the MD trajectory at each temperature. Figure 3-8 plots the free volume versus temperature relationship using 0.7Å as the radius of the probe sphere. It is observed that below 400K, there is only a slight increase of free volume with temperature, while afterwards the rate of change of free volume rises abruptly. This significantly increased free volume facilitates higher molecule mobility and local structure transitions, leading to more rubber-like material behavior. Therefore, the intersection of the bi-linear function used to fit the raw data signifies the glass transition temperature. It is seen from Figure 3-8 that the T_g so obtained is 399K, almost the same as the T_g predicted by volume-temperature data.

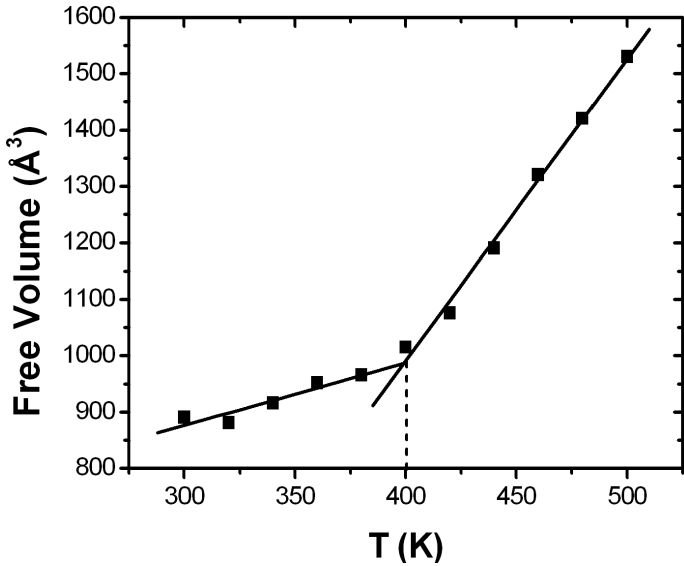


Figure 3-8. Free volume versus temperature relationship for the 90% cured system, fitted by bilinear function. The intersection corresponds to T_g .

3.3.3.2 Interaction Energies

MD simulations allow us to examine the role of different components of the potential energy near the glass transition temperature. Figure 3-9 plots variation of non-bond, bond stretching, angle bending and dihedral energies with temperature for the highest cross-linked system. It is observed that only the non-bond (Lennard-Jones plus Coulombic) potential energy exhibits a discontinuity in energy versus temperature slope at roughly 400K, quite close to the T_g predicted through volume-temperature relationship. All other energy components consistently increase linearly with temperature. One may conclude that the non-bond energy plays a vital role in the glass transition process of the epoxy system, while degrees of freedom associated with valence energies are in equilibrium both in glassy and rubbery states. A previous MD study [117] found that, in chain-wise polymeric materials, not only non-bond energy but also the torsional dihedral energy experiences a break in its slope versus temperature at T_g . This difference is due

to the fact that the network structure is more topologically constrained in the cross-linked epoxy system studied here than that in the chain-wise polymeric materials studied in [117].

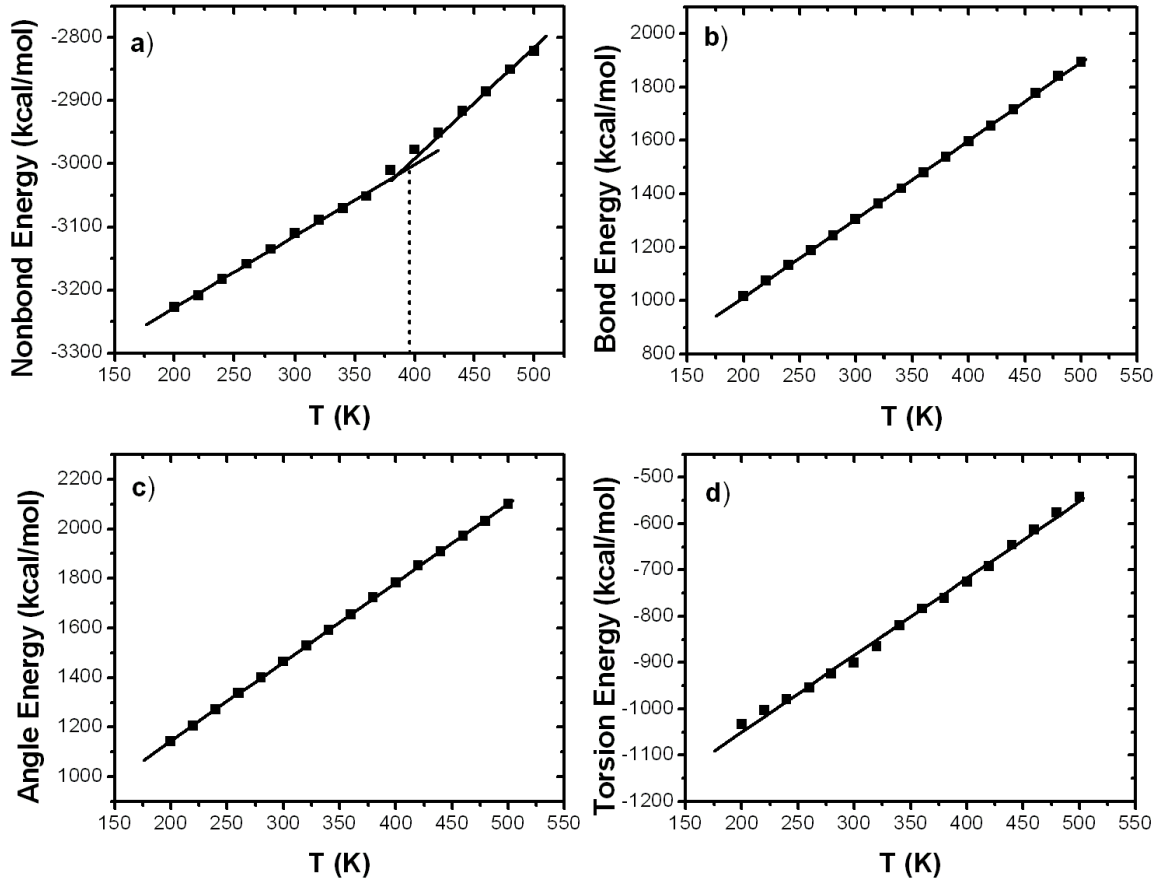


Figure 3-9. Temperature dependence of potential energy components for the system of 90% conversion. a). total non-bond energy, b) bond stretching energy, c) angle bending energy and d) dihedral torsion energy

3.3.3.3 Static Structure

Difference in molecular structure in rubbery and glassy states of polymers is of great interest, since it is likely to reveal deep insight regarding the origin of glass transition. In the current investigation we studied some structural aspects, namely radial distribution function

(RDF) and torsion distributions at temperatures below and above T_g . In Figure 3-10 we present the total RDF at 300K and 500K. Note that the total RDF shown here only considered the intermolecular contributions, i.e., RDF between atoms that are not directly bonded nor at the two ends of an angle/torsion. As far as the temperature effect is concerned, there is only slight variation of the total RDF, with peaks being higher at 300K than at 500K. This indicates the change in density of the studied epoxy system. We also paid special attention to the RDF between hydroxyl groups, since hydroxyl oxygens and hydroxyl hydrogens form H-bonds. Although there is no explicit term for hydrogen bonding in the PCFF force field, the interaction is implicitly considered by tuning LJ parameters of specific types of atoms. Figure 3-11 reveals a peak at 2.8Å associated with H-bonds, which is much sharper at 300K than at 500K. Therefore H-bonds decrease significantly with temperature. This finding is consistent with that of Wu and Xu's work [101] which applied COMPASS force field in studying DGEBA/IPD system.

Torsion distributions are investigated for torsions aligned along the epoxy monomers' backbones, and along newly created crosslinks. Their torsion angle distributions are plotted in Figure 3-12 (a) and (b). The temperature dependence of torsion distribution is trivial, due to the highly constrained network structure in the cross-linked system.

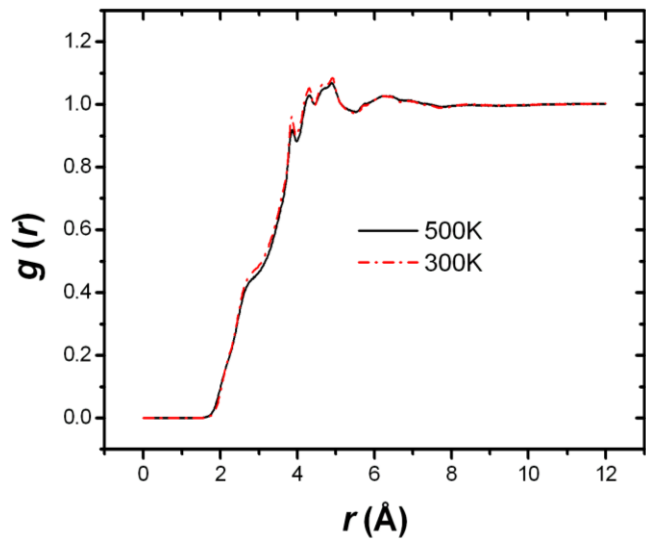


Figure 3-10. Total radial distribution function for the 90% crosslinked system at temperature of 300K and 500K

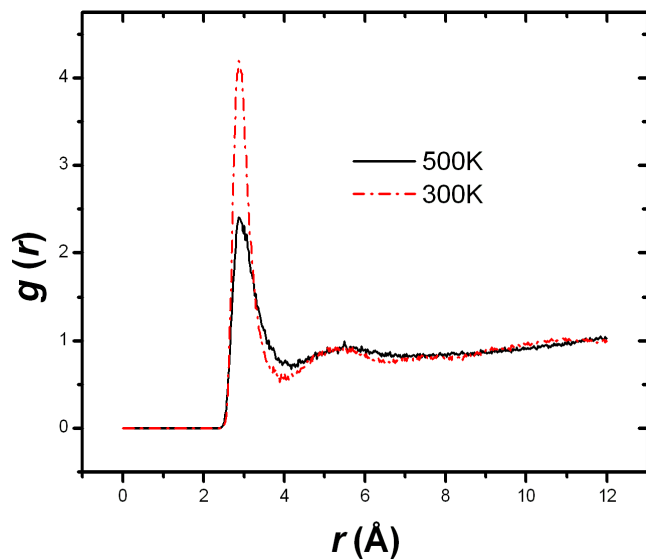


Figure 3-11. Radial distribution function between hydroxyl oxygens within the 90% crosslinked system at temperature of 300K and 500K

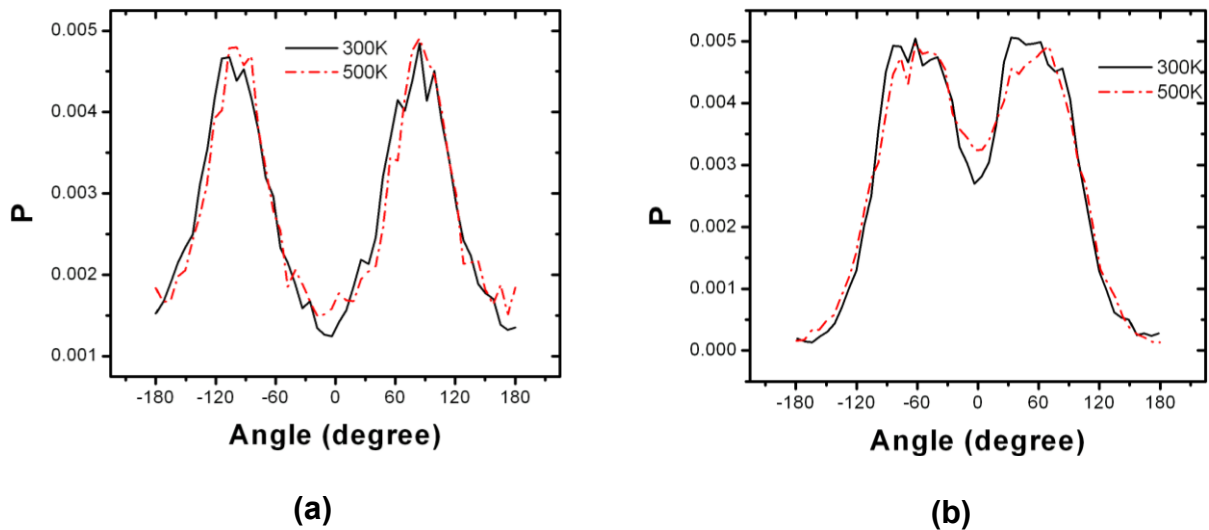


Figure 3-12. Torsion distributions for dihedrals aligned along (a) epoxy backbones, and (b) newly created crosslinks.

3.3.3.4 Translational Dynamics of Polymer Strands

Aside from static structure, we would like to study epoxy network strands' dynamic properties at temperatures below and above T_g . The translational dynamics of polymer chains is measured by the mean square displacement (MSD) of certain groups of atoms. MSD is defined as:

$$\text{MSD} = \frac{1}{3N} \sum_{i=0}^{N-1} \left\langle \left| \vec{R}_i(t) - \vec{R}_i(0) \right|^2 \right\rangle \quad (3.4)$$

where N is the number of particles studied, and the angle bracket stands for averaging over all choices of time origins. In the current investigation we chose to examine the MSD for epoxy backbone atoms, i.e. the methylene carbons connecting benzene rings in the epoxy monomers. Figure 3-13 plots this group of atoms' MSD versus time curves for the first 100ps, at various temperatures. As expected the diffusional behavior consistently increases with temperature.

Besides, the mobility of the epoxy back bone atoms shows transitional behavior at lower and higher temperatures, as can be seen in Figure 3-14 which presents MSD's at a specific time, 20ps in the current work, for different temperatures. The choice of the time for comparison of MSD is somewhat subjectively, but other choices have been tested and the results are close in terms of the temperature at which transition occurs. In Figure 3-14 it is clear that the slope of MSD versus temperature shows a discontinuity at roughly 381K. This is reasonably close to the glass transition temperature determined from volume versus temperature data. The abrupt increase of mobility of epoxy strands is consistent with free volume's transitional behavior around T_g , indicating it is the significantly increased free volume that facilitate higher polymer chain mobility and more rubbery material behavior.

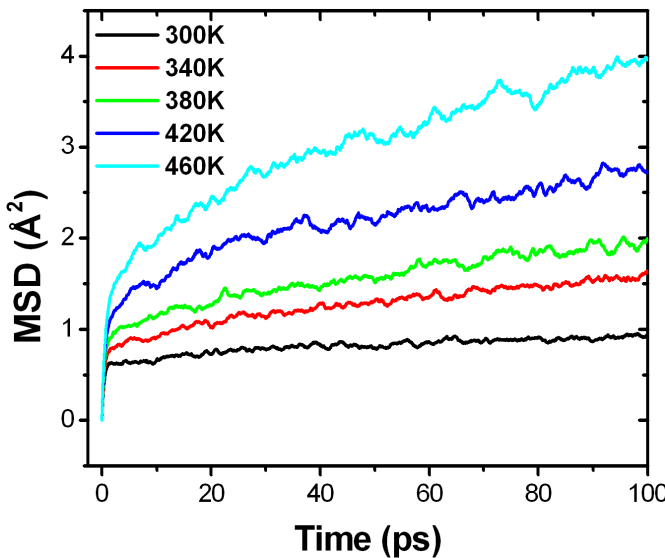


Figure 3-13. Mean square displacement versus time curves for epoxy backbone atoms at different temperatures.

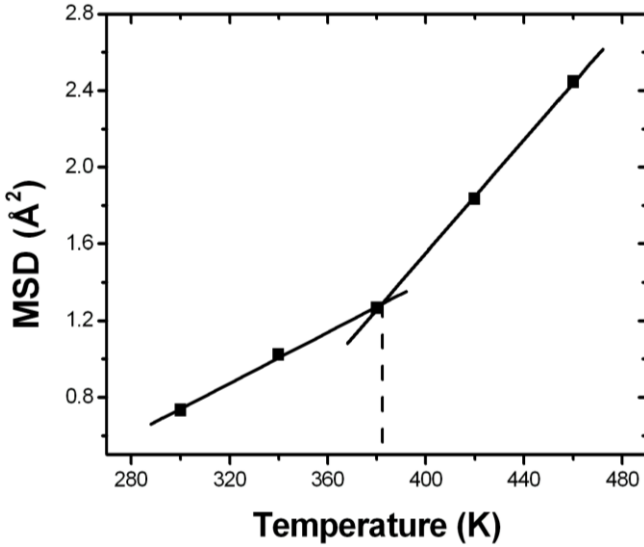


Figure 3-14. MSD at the time of 20ps at different temperatures.

3.3.3.5 Cross-link Density Dependency

It is well-known that the glass transition temperature increase with increasing crosslinking density. In order to investigate such dependence on crosslink density, the same high temperature annealing protocol was used to study systems with conversions of 0%, 25%, 50% and 75%. Figure 3-15 plots the volume versus temperature relationship for all cases. As expected, the less cured system with lower crosslink density has larger volume at given temperatures, the glass transition temperature increases with increasing crosslink density. The results are shown in Figure 3-16 (a). It shows that T_g increases from 309K for 0% conversion to 402K for 90% conversion. For comparison, the corresponding experimental measurements on the same epoxy compound [115] are presented in Figure 3-16 (a). Also shown is the fitting of experimental data to the Debenedetto equation [118]:

$$T_g(\alpha) = T_{g0} + \frac{(T_{g1} - T_{g0})\lambda\alpha}{1 - (1 - \lambda)\alpha} \quad (3.5)$$

where T_{g0} and T_{g1} are limiting glass transition temperatures and λ is an adjustable parameter, with the value of 0.54 [115] in this case. It is seen that our MD simulations predict the same dependence of T_g on conversion as the experimental data. However, T_g predicted here is about 30K higher than the experimental value at all conversions. This difference comes mainly from the fact that cooling rate used in the MD simulations is about 10 orders of magnitude higher than the cooling rate occurred in the experimental measurement. To account for the effect of cooling rate on T_g , the William-Landel-Ferry (WLF) equation [102] may be used, which describes the correlation between relaxation time and temperature measured from a reference value. For the system considered here, the WLF predicts an increase in T_g of 3K per decade [102] increase in cooling rate. Therefore, the T_g predicted by our MD simulation should be approximately 30K higher than that from experiment. This explains the roughly 30K shift between the MD and experimental curves shown in Figure 3-16 (a).

The dependence of CTE on conversion was also obtained. Figure 3-16 (b) plots the rubber and glassy state CTEs for all conversions. As expected, the rubbery CTE decreases with conversion while the glassy CTE stays almost constant as conversion increases.

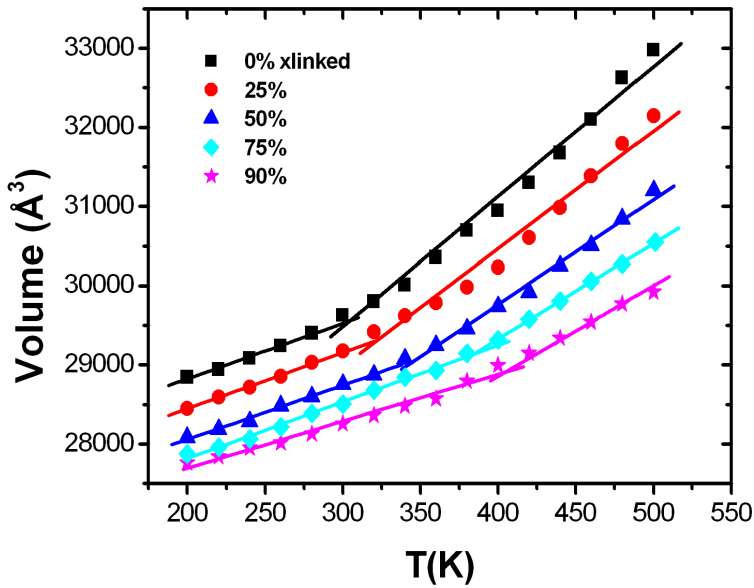


Figure 3-15. Volume versus temperature relationship for systems with different conversions:
black square: monomer mixture, red circle: 25%, blue triangle: 50%, cyan diamond: 75%,
magenta pentagon: 90%

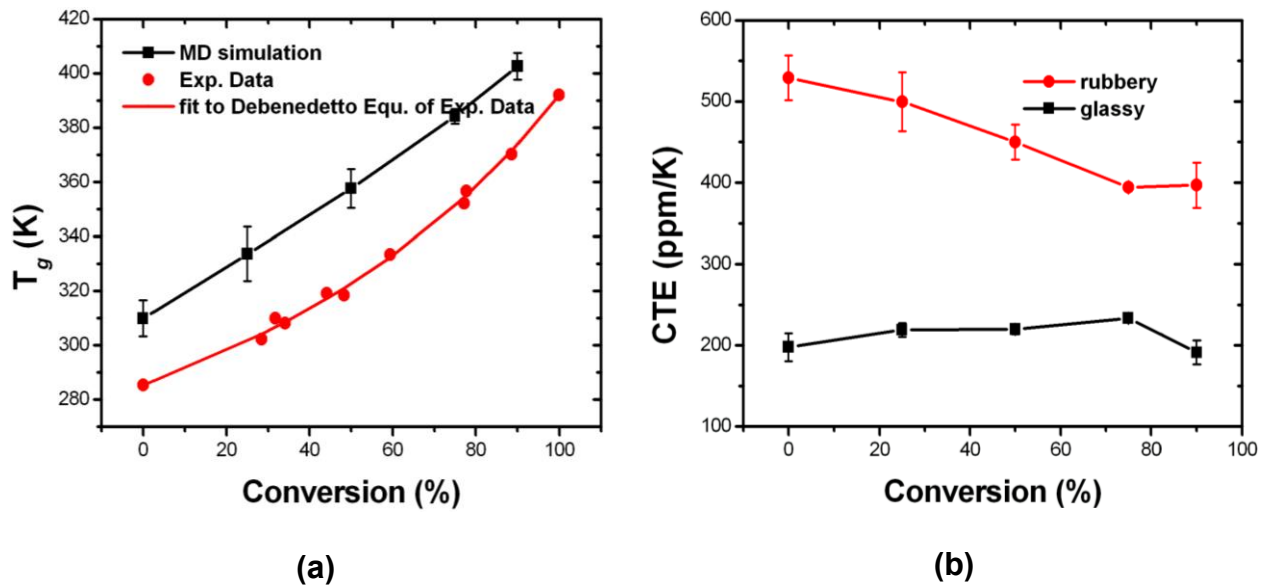


Figure 3-16. (a) T_g versus conversion relationship; (b) coefficient of thermal expansion (rubbery and glassy) versus conversion relationship

3.3.4 Mechanical Properties

3.3.4.1 Elastic Constants Determination

Calculation of mechanical properties through molecular simulations usually follows one of three methods, namely static, dynamic or fluctuation approaches. The static method loops over constant-strain energy minimization and produces stress-strain curves for the studied material at 0K. It is thus not appropriate if one wants to obtain elastic constants at finite temperatures. The fluctuation formula [119, 120] requires long simulation time, usually on the order of tens or even hundreds of nano-second, especially for polymers which are highly amorphous, thus is computationally expensive to perform. In this work, we applied the dynamic method, i.e., molecular dynamics simulation of tensile deformation, to study the elastic properties of our epoxy molding compound. We note that, to simulate tensile deformation, much large model is needed than that used for structural and thermal analyses, for the sake of reducing noises in the engineering stress data. Following the crosslinking and equilibration procedures described in Section II, a model having 240 3mers, 360 4mers and 1080 BPAs (corresponding to 82,992 atoms) was constructed. This corresponds to a cell length of $\sim 95.50\text{\AA}$. To simulate tensile deformation, the cell length along the loading direction is continuously elongated, while the atmospheric pressure is maintained on lateral surfaces. Due to the Poisson's effect, the simulation cell would shrink in the directions transverse to the tensile axis. The rate of deformation applied in MD simulation of tensile test was $1\times 10^9 \text{ s}^{-1}$. This rate is typical of MD simulations, albeit is much higher than those used in quasi-static tensile tests.

Figure 3-17 (a) plots the stress-strain curve of the 90% cured system at room temperature (300K). The lateral stress remains approximately zero. The longitudinal stress shows a linear

elastic regime up to approximately 5% strain. The Young's modulus was extracted by performing linear regression on the raw stress-strain data. The uncertainty is due to the different choices of strain range used for the linear regression. In this work, the strain range used is $[0, \varepsilon^u]$ with ε^u varying from 2% to 5%, which gives Young's modulus of 2.517 ± 0.168 GPa. The lateral versus longitudinal strain relationship is plotted in Figure 3-17 (b). Here the lateral strain stands for the average of compressive strains along x and y directions. The Poisson's ratio can then be extracted from data shown in Figure 3-17 (b) by linear regression. Following the same approach used for modulus, we found that the Poisson's ratio is 0.375 ± 0.0048 , falling in the range of 0.30~0.46 for typical glassy state thermosetting polymers.

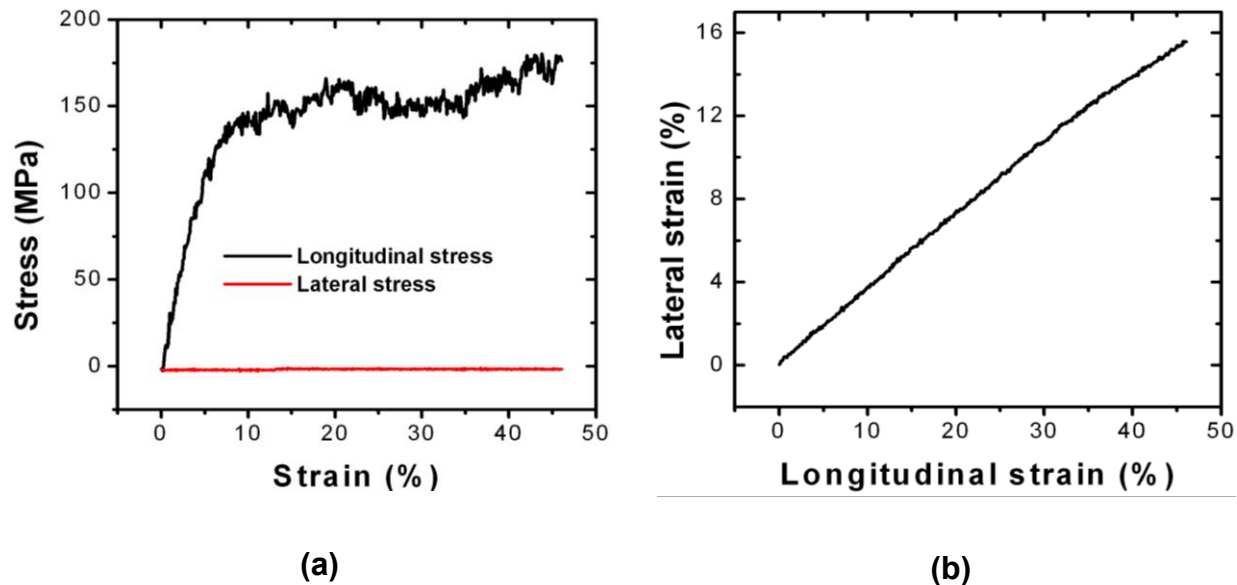
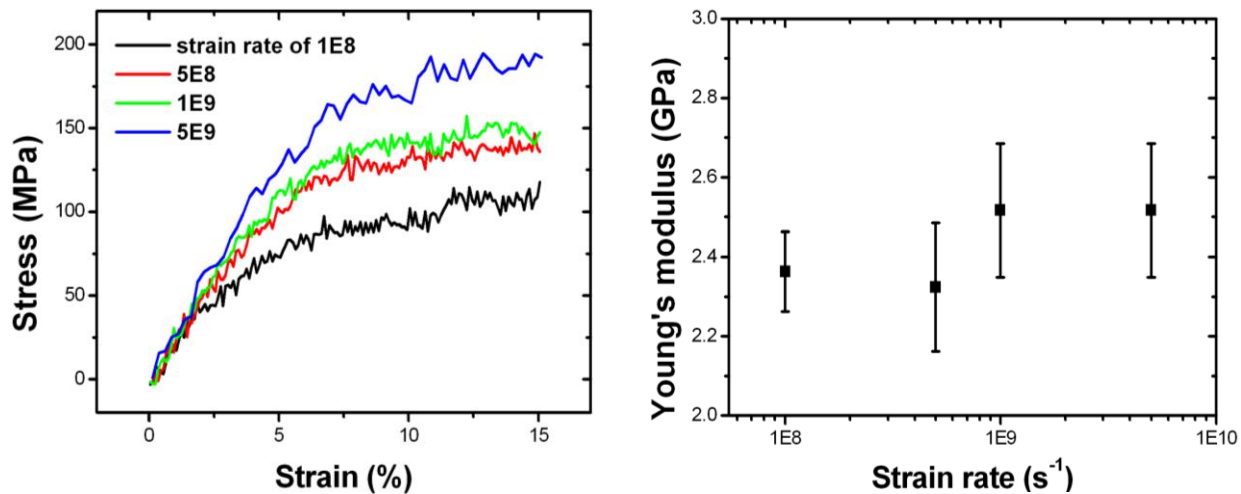


Figure 3-17. (a) Stress-strain response and (b) lateral versus longitudinal strain curve for the 90% cured epoxy model at 300K, using strain rate of 1×10^9 s $^{-1}$

3.3.4.2 Strain Rate Effect

To explore potential effect of strain rate on mechanical behavior, we examined three other rates of deformation and their stress-strain responses together with that for the rate of $1\times 10^9 \text{ s}^{-1}$ are plotted in Figure 3-18 (a). Our simulations show that yielding strongly depends on rate while the Young's modulus is less sensitive. This finding is consistent with the work by Li and Strachan [102]. Due to obviously more severe non-linearity in the stress-strain curve for the rate of $1\times 10^8 \text{ s}^{-1}$, we restrict our strain range for linear regression within 2%. For rates other than $1\times 10^8 \text{ s}^{-1}$, we followed the same fitting scheme mentioned above. Figure 3-18 (b) plots the modulus versus strain rate relationship. The error bars in the figure are associated with multiple choices of strain range. Within the range of strain rate ($10^8 \sim 5\times 10^9 \text{ s}^{-1}$) investigated, the modulus varies from 2.3 to 2.6GPa. From reference 33 [115], the experimental measured glassy plateau of the elongation modulus master curve is $2.1\pm 0.2\text{GPa}$, which is close to our simulation predicted values. Therefore, MD simulation is capable of predicting elastic properties in reasonably good agreement with experiments.



(a) **(b)**

Figure 3-18. (a) Stress-strain response of the 90% cross-linked system at 300K under various loading rates. (b) Young's modulus derived under different loading rates for the 90% cross-linked system at the temperature of 300K

3.3.4.3 Role of Conversion

The Young's modulus and Poisson's ratio depend on the crosslink density. Simulation cells with conversions of 75%, 50% and 25% were investigated at room temperature (300K). The dependence of modulus on conversion rate is shown in Figure 3-19 (a). Our simulations indicate a stiffening of the epoxy molding compound from 1.8GPa to 2.5GPa as degree of cross-linking increases from 25% to 90%. The decrease of room temperature modulus with conversion can be attributed to two factors. First, at lower conversions the epoxy molding compound possesses less network connectivity. Second, the lower glass transition temperature at lower conversions leads to an increase in temperature measured from T_g , i.e., $T-T_g$. As for the Poisson's ratio (shown in Figure 3-19 (b)), we do not observe a monotonically decreasing trend with increasing conversion. The too low Poisson's ratio for the 25% cross-linked system is likely due to numerical errors such as insufficient ensemble averaging. However, since room temperature is lower than T_g 's for all four systems, our MD computed values are within the range of typical glassy state epoxy's Poisson value.

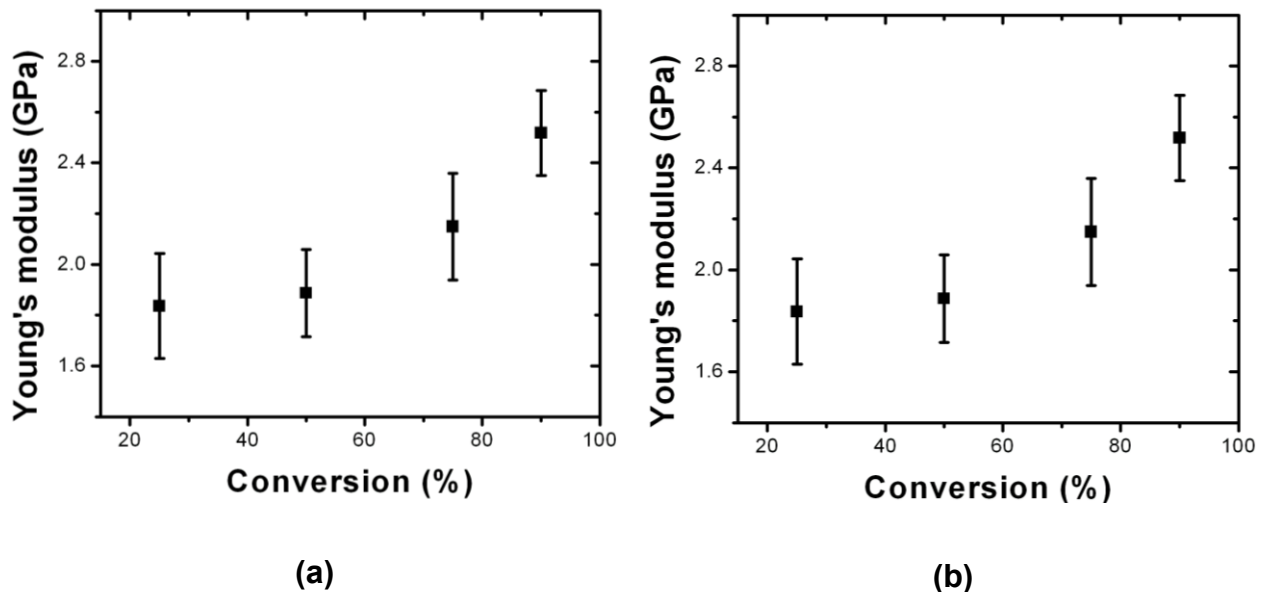


Figure 3-19. Young's modulus (a) and Poisson's ratio (b) at room temperature for structures with different conversion rates.

3.3.4.4 Role of Temperature

The role of temperature in the epoxy molding compound's mechanical behavior was examined by conducting the same MD simulation of uni-axial tension at various temperatures. Due to the significantly higher strain rate in MD tensile test than in experiment, and the well known rate-dependency of polymers' modulus at temperatures higher than the glass transition temperature, we restrict our MD study of mechanical properties in the glassy temperature range. Temperature's effect on modulus and Poisson's ratio for structures with different conversions are summarized in Figure 3-20 (a) and (b). Note that temperatures are measured from their respective T_g 's. Reduction of modulus is seen at higher temperatures, as expected. Another observation is that within the glassy temperature range, temperature affects moduli of structures with different conversions in a similarly linear fashion, evidenced by the fact that in Figure 3-20

(a) the data for various conversions stay readily aside a linear function. The Poisson's ratio scatters within the range from 0.36 to 0.41, falling in the range of 0.30~0.46 for typical glassy state thermosetting polymers.

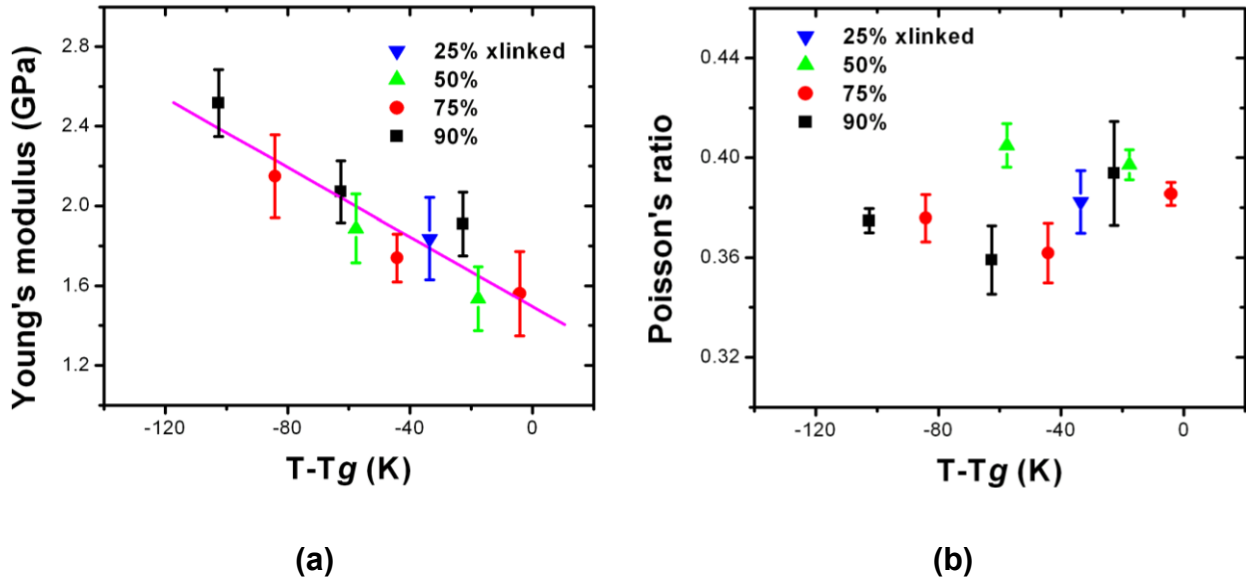


Figure 3-20. Young's modulus (a) and Poisson's ratio (b) versus temperature measured from T_g ($T-T_g$) relationships.

3.4 Summary of This Chapter

In this Chapter, we conducted molecular dynamics (MD) simulations to study the thermo-mechanical properties of a model epoxy molding compound. A multi-step crosslinking-relaxation methodology was developed to construct the simulation cell. This crosslinking-relaxation methodology allows the construction of highly cross-linked polymer network from a given set of monomers. Based in this computational algorithm, three-dimensional simulation cells were built for MD simulation. A polymer consistent force-field was used to describe the inter-atomic interactions during the MD simulation.

By conducting the MD simulations, we have computed several thermo-mechanical properties of the model epoxy such as curing induced shrinkage, gelation point, coefficient of thermal expansion, glass transition temperature, Young's modulus and Poisson's ratio. The dependence of these properties on crosslink density and temperature was also investigated. Simulated results were compared with existing theoretical or experimentally measured values when available. Good agreements are observed. For these compressions, we conclude that MD provides a useful tool to study the thermo-mechanical properties of cross-linked thermosetting materials, thus is a useful computational tool with predictive nature to help design more reliable materials in electronic packaging industry. Also, the success of MD in computing material properties of bulk epoxy validates using it to investigate the mechanical behaviors and properties of epoxy/Cu bimaterial, which will be presented in the next section, Chapter 4.

Before closing, we mention two limitations of using MD to simulate the thermo-mechanical behavior of polymeric materials. One of them is the long range forces in polymer. Unlike in crystalline materials, atoms in polymers interact through long range forces. Their interaction extends over a large distance. Therefore, the size of the simulation cell must be sufficiently large. This issue becomes even more pronounced when simulating failure. The other limitation is the extremely high strain rate used in MD. Although MD simulations of crystalline materials face the same issue, the problem is much more severe for polymer because of its visco-plastic nature.

CHAPTER 4 ATOMISTIC STUDY OF EPOXY/COPPER BIMATERIAL

In Chapter 3 we have shown the power of MD simulation of predicting epoxy molding compound's thermo-mechanical properties. The successful match with experimental measurements validates the force-field, the methodology of building atomistic model of epoxy, and the methodology of calculating material properties using MD simulation. This Chapter presents the full atomistic study based on classical molecular dynamics simulation to understand the deformation and failure behavior of the epoxy/copper bimaterial under pure tension normal to the interface. The epoxy considered is the same epoxy phenol novolac as studied in Chapter 3, and modeled using the cross-linking/equilibrating methodology developed in the previous section. The copper substrate is a standard face-center-cubic single crystal with its (1, 1, 1) surface as the epoxy/copper interface. Stress versus displacement/strain curves are obtained to understand the bimaterial behavior and to predict the epoxy/copper interfacial tensile strength. It is found that the interfacial failure is brittle caused by simultaneous detachment of epoxy atoms from the copper substrate, and the interfacial tensile strength is almost unaffected by the unloading and reloading before the failure strength is reached. Effects of temperature, epoxy cross-link density, and epoxy functionality are also investigated. Findings presented in this chapter provide significant insights into the deformation and failure behavior/mechanisms of the epoxy/copper bimaterial interface.

4.1 Introduction

As has been stated in 0, the interface/Cu interfaces are weak links in the material system in electronic packages, due to 1) intrinsic lack of chemical bonding, 2) thermal stresses caused

by the large mismatch of material properties such as coefficient of thermal expansion (CTE) and elastic constants, and 3) various other factors including surface treatment, humidity and formation of metal oxides. Thus there is urgent desire to characterize the interface's performance and in further search for approaches for improvement. The traditional destructive test based methods, such as, such as fracture of sandwiched double-cantilever beam [13, 14] and peeling-off of thin film bonded by epoxy adhesive to solid substrates [17], have the drawback of time/money consuming. In addition, they are often incapable of revealing the microstructure of the polymer network near the interface and how the microstructure affects the mechanical properties. On the other hand, molecular dynamics (MD) simulations are capable of describing material behavior at atomistic level and thus providing insights into the structure-property relationship. We present here the MD study of highly cross-linked epoxy resin bonded to a copper substrate. Using MD simulation, we are able to precisely control the structural and loading parameters and study their influence on the traction-displacement/strain behavior of the interface system. In fact, it has been extensively applied to study interfacial deformation/failure behavior between crystalline solids. For example, Gall et al. [39] studied tensile debonding at the interface between silicon and aluminum through MD simulations and obtained stress versus local opening displacement relationship. Spearot et al. [41] proposed an internal-variable based theoretical framework that uses interface separation constitutive laws motivated by MD simulations. Zhou et al. [42, 43] simulated crack propagation along the interface between two body-center-cubic metals and derived the traction-separation relationship.

In Chapter 3 we have reviewed the state of researches that have been done regarding using molecular modeling/simulation techniques to study bulk material properties of epoxy

based thermosetting polymers. In contrast to bulk materials, there are very few publications using MD simulations to study the interfaces between epoxy molding compounds and inorganics substrates. Stevens et al. [4, 121, 122] studied the deformation/failure behavior of highly cross-linked polymer network bonded by crystalline substrates. The stress-strain relationship and the failure mechanism were revealed. A number of factors including interfacial bond density, cross-linker functionality and cross-link density were considered to investigate their effects. Mukherji and Abrams [123, 124] also applied MD simulation to explore the mechanical behavior of cross-linked polymer network, and inspected the potential of improving ductility through blending thermosets with thermoplastics. These studies are for model material systems and the results are not in physical dimensions because their use of the coarse-grained approach. In the literature, full-atomic MD simulations have been used to study epoxy/substrate bimaterials. For example, Jia et al. [125] and Cheng et al. [126] studied interfacial energy and bonding strength between epoxy and self-assembly-monolayer coated Au surface using MD simulations. Li et al. [127] studied the mechanical behavior of multilayer graphene reinforced epoxy composites using full-atomic MD simulation and force-field. The effect of graphene layer orientation was focused on. The most relevant work to the present study is the MD simulation of the DGEBA-MDA epoxy/Cu bimaterial using the COMPASS force-field [128]. Besides simulating only a very small material volume ($3.53 \times 3.53 \text{ nm}^2$ in the x and y direction and a few thousand atoms), much of the epoxy network in their study is assumed rigid except atoms very close to the interface. As will be seen from our studies, such assumptions may not be appropriate for obtaining the strength or toughness of the interface due to the longer-range nature of the atomistic interaction in the epoxy network.

In order to investigate the deformation and failure behavior of the highly cross-linked epoxy/Cu interfaces, we carried out large scale MD simulations on an epoxy/Cu bimaterial. The epoxy/Cu bimaterial is made of a highly cross-linked epoxy molding compound attached to a Cu substrate. By applying velocity loading to the substrate during the MD simulation, the normal stress versus displacement/strain response was obtained. Effects of simulation cell size were studied to ensure that the results are independent of simulation cell size. In addition to the stress-strain relationship, we also investigated the effects of cyclic loading, temperature, conversion and epoxy monomer functionality on the stress-strain relationship. The rest of this chapter is organized as follows. In Section 4.2, the atomistic model and the loading set-up are presented. Simulation results and influence of various structural and loading parameters are discussed in Section 4.3. Finally, some conclusion remarks are summarized in Section 4.4.

To close this section, we note that the methodology developed here for modeling the epoxy modeling compound/Cu bimaterial is not restricted to the specific epoxy formulation in the current work, but can be extended to various other epoxy systems. Therefore, results from this study provide guidance to designing polymer/metal interfaces in the electronic packaging industry.

4.2 MD Simulation Method

In section 3.2 we have described in detail the molecular structure of the constitutive monomers (EPN and BPA) of the epoxy molding compound, as well as the mechanism of curing reaction through which the compound is synthesized (see Figure 3-1). To model the epoxy/Cu bimaterial, an orthogonal simulation cell of dimension $W \times D \times H$ was first created. Within the cell the same approach as in section 3.2 was followed to randomly seed EPN and BPA

monomers. The stoichiometric ratio of 2:3:9 among the tri- and tetra-functionalized epoxies and hardeners was maintained. The difference is that, the periodic boundary condition was applied to two directions while the third direction had a traction free boundary condition. This confined layer of EPN/BPA mixture was then placed on the (1 1 1) surface of a single crystal copper (Cu) substrate of dimension $W \times D \times h$. This formed the bimaterial consisting of Cu and un-cross-linked epoxy molding compound, see Figure 4-1. For convenience, a Cartesian coordinate system is attached to the bimaterial, where the x -axis and the y -axis are in the epoxy/Cu interface and the z -axis is perpendicular to the interface.

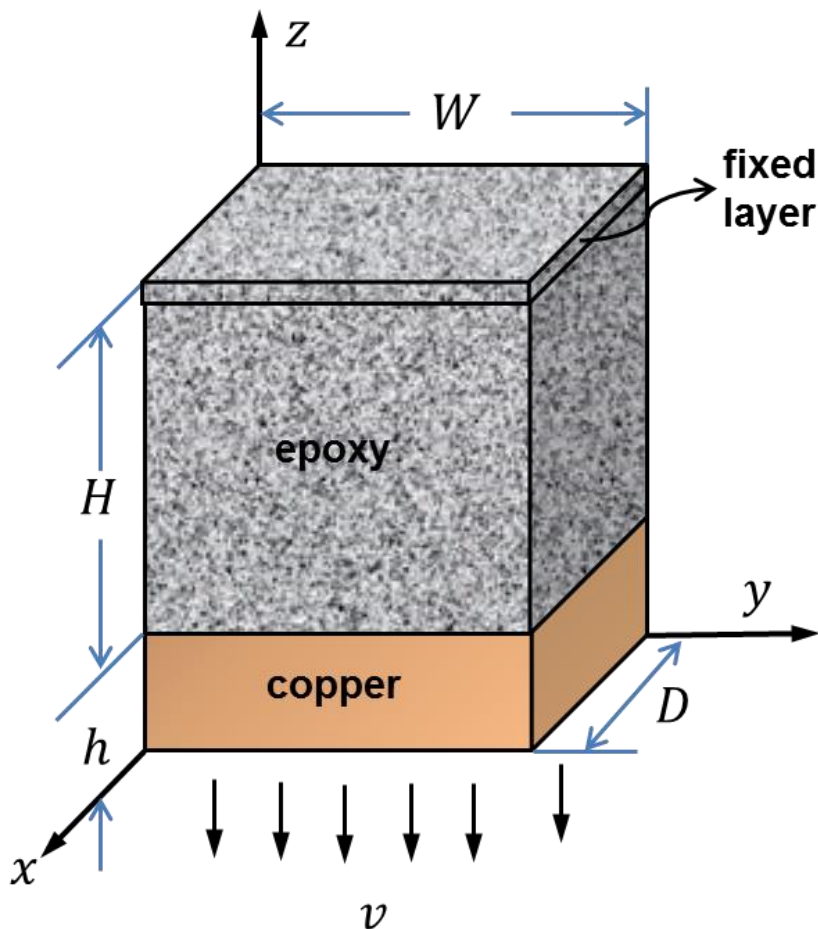


Figure 4-1. Schematic of the epoxy/Cu bi-material

The same force-field, namely the PCFF (Eq. (3.1)) was applied to describe the interatomic interactions in the bimaterial. Non-bond terms are the Coulombic forces between partially charged atoms and the Lennard-Jones (LJ) 9-6 potential representing the van der Waals forces. In the examples presented in this paper, the LJ potentials and the real-space contribution to the Coulombic energy were calculated with a cut-off distance of 12.5Å. The Coulombic term's reciprocal-space contribution was computed by the particle-particle-particle-mesh method, since it's much faster than the Ewald method yet maintains reasonable accuracy. For Cu the only term that applies to Cu is the Lennard-Jones potential, and the parameters have been written to the published force-filed database. Since the deformation in the Cu substrate is negligible, we assumed that the Cu substrate is rigid. Further, it is reasonable to assume [129] that the epoxy is bonded to the Cu substrate through van der Waals forces only (no covalent bond). Thus, the interaction between the polymer atoms and Cu atoms can be described by the LJ 9-6 potential whose parameter are obtained from the parameters of copper and epoxy atoms following the sixth-power mixing law [69],

$$\varepsilon_{ew} = \frac{2\sigma_e^3\sigma_w^3\sqrt{\varepsilon_e\varepsilon_w}}{\sigma_e^6 + \sigma_w^6} \quad \sigma_{ew} = \left(\frac{\sigma_e^6 + \sigma_w^6}{2} \right)^{1/6} \quad (4.1)$$

where the subscripts *e* and *w* stand for epoxy and copper substrate, respectively.

The bimaterial depicted in Figure 4-1 was then subjected to the simulated cross-linking process which is essentially the same as for bulk epoxy molding compound (described in section 3.2). The difference lies in two aspects: 1) the simulated cross-linking of epoxy was conducted on the Cu substrate, thus the effect of the substrate on the curing reaction's kinetics, and the microstructure of the final cross-linked was incorporated; 2) due to the in-plane periodic but out-

of-plane traction free boundary condition, the polymer network in the cross-linked epoxy percolates to infinity in the plane of the interface. The cross-linking was done at an elevated temperature of 500K. To speed up the process, the bond formation cut-off distance was increased from 3 to 10Å incrementally. At each cut-off, five crosslinking-equilibration loops were conducted. After reaching the desired conversion, the un-reacted reactive sites were saturated with hydrogen atoms and partial charges to make the entire system charge neutral. Finally, MD simulations were conducted to minimize the system energy and to equilibrate the atomistic structure under traction-free conditions.

To conduct simulation of uniaxial deformation of the epoxy/Cu bimaterial system, the very top layers of the polymer atoms are fixed, see Figure 4-1. The Cu substrate is assumed to be a rigid body moving downward with a prescribed velocity. A constant NVT MD simulation was conducted at 300K with the timestep of 1fs using the LAMMPS software [51]. The Nose-Hoover thermostat was applied to control the system's temperature. The virial stress tensor in the epoxy was calculated and outputted as a function of the total elongation of the epoxy/Cu bimaterial.

4.3 Results and Discussion

4.3.1 Effects of Simulation Cell Size and Strain Rates

We need to use a simulation cell that is large enough so that the results are independent of the cell size. To this end, three simulation cells of different sizes were considered, see Table 4-1. It was found that the overall stress-strain relationship for cell #1 changes significantly with the initial configuration before crosslinking, which indicates that the in-plane dimension is not

large enough to generate unique mechanical behavior. The two bigger cells do not suffer from this problem. The normal stress in the z -direction versus its corresponding strain for cells #2 and #3 are plotted in Figure 4-2. It is seen from Figure 4-2 that the stress-strain curve does not change much after doubling the cell size, indicating that the size of cell #2 is sufficient to study the normal stress versus strain behavior. Thus, cell #2 will be used in the rest of this article.

Table 4-1. Dimensions of the simulation cells

No.	Number of atoms	$W \times D (\text{\AA}^2)$	$H (\text{\AA})$
1	24194	44.48×44.48	110
2	96776	88.96×88.96	110
3	179552	88.96×88.96	220

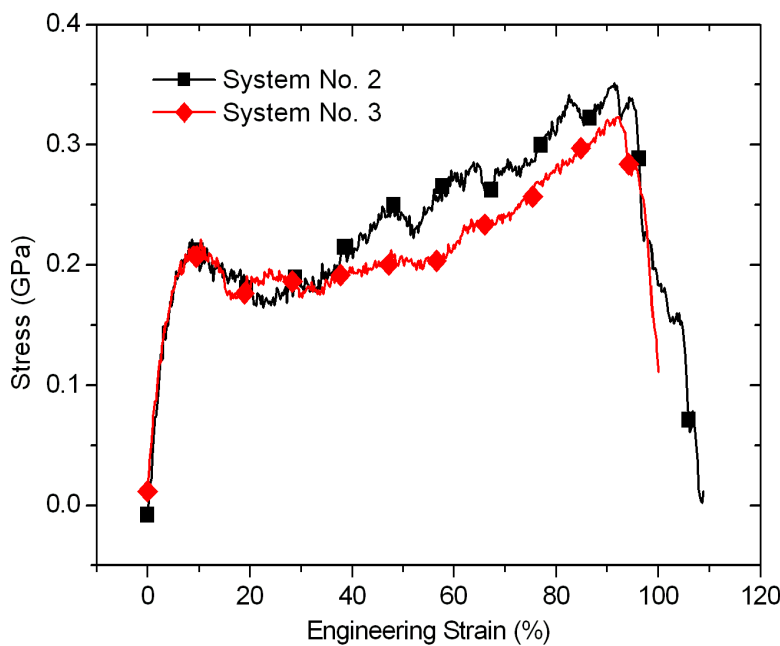


Figure 4-2. Stress versus strains curves for cells #2 and #3

We note that, in the above simulations, the prescribed velocity of the Cu substrate is $5 \times 10^{-5} \text{ \AA/fs}$ for cell #2, which corresponds to a strain rate of $\sim 5 \times 10^8 \text{ s}^{-1}$. The same strain rate was used in cell #3. The strain rate's effect on stress-strain behavior was investigated by applying three different rates to cell #2, and their results are shown in Figure 4-3. Stress-strain curves are very close among these three rates and the failure property does not show clear trend with respect to strain rate. Therefore we will use the rate $5 \times 10^8 \text{ s}^{-1}$ of throughout the rest of this article. This strain rate is obviously much higher than that used in quasi-static loading in realistic laboratory tests. Therefore, results given in the remainder of this paper must be interpreted with this high strain rate in mind.

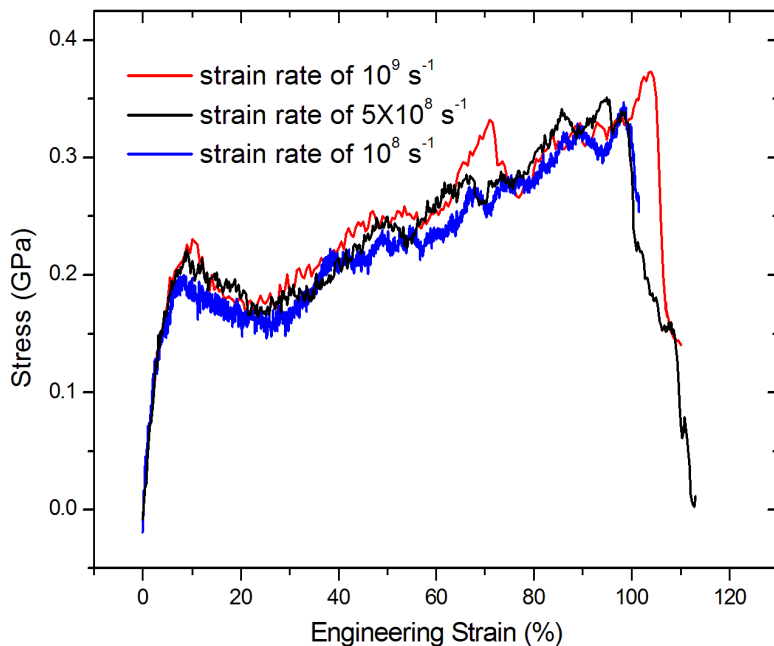


Figure 4-3. Stress versus strains curves for cells #2 using different strain rates

4.3.2 Deformation Behavior

It is seen from Figure 4-2 that that stress-strain relationship is almost linear initially until the yielding strength of 0.22GPa is reached at the strain of ~8.7%. Regarding the variation of the system's potential energy, Figure 4-4 (a) shows that the total and non-bond potential energies both increase with strain, while Figure 4-4 (b) shows slight decreases of bonding, angular and torsional energies within the elastic regime. This implies that the initial configuration represents a state in which valence degrees of freedom are constrained. Upon loading, constraints imposed on bonds, angles and torsions are released and so are their corresponding stored potential energies.

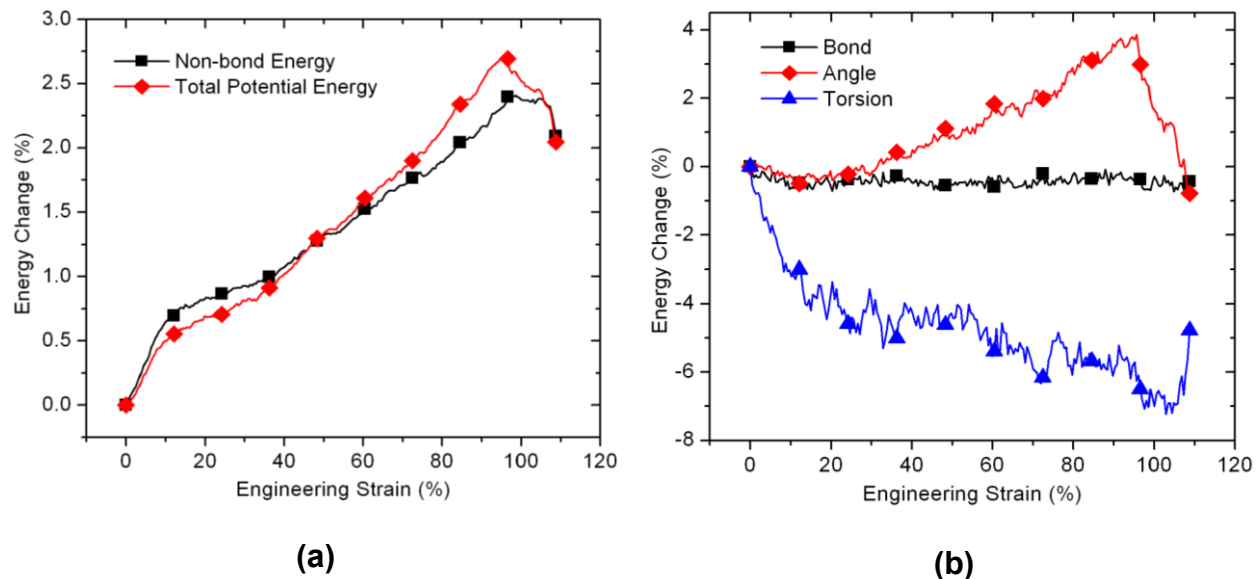


Figure 4-4. Variation of (a) total and non-bond, and (b) valence potential energies with respect to strain

Figure 4-5 shows snapshots of simulation cell #2 at different stages of the deformation. The first snapshot in the row is at yielding, in which no visible damage is observed. The post yielding behavior is characterized by strain softening from the yielding strength to 0.16GPa,

followed by strain hardening extending to the ultimate interfacial failure. At this stage, it is seen from the second snapshot that micro-voids are initiated in regions of the polymer network with lower connectivity, due to the tri-axial stress state within the epoxy layer. The tri-axial stress state is consistent with the zero in-plane strain condition in realistic adhesive layers which are highly constrained by adherends [130, 131].

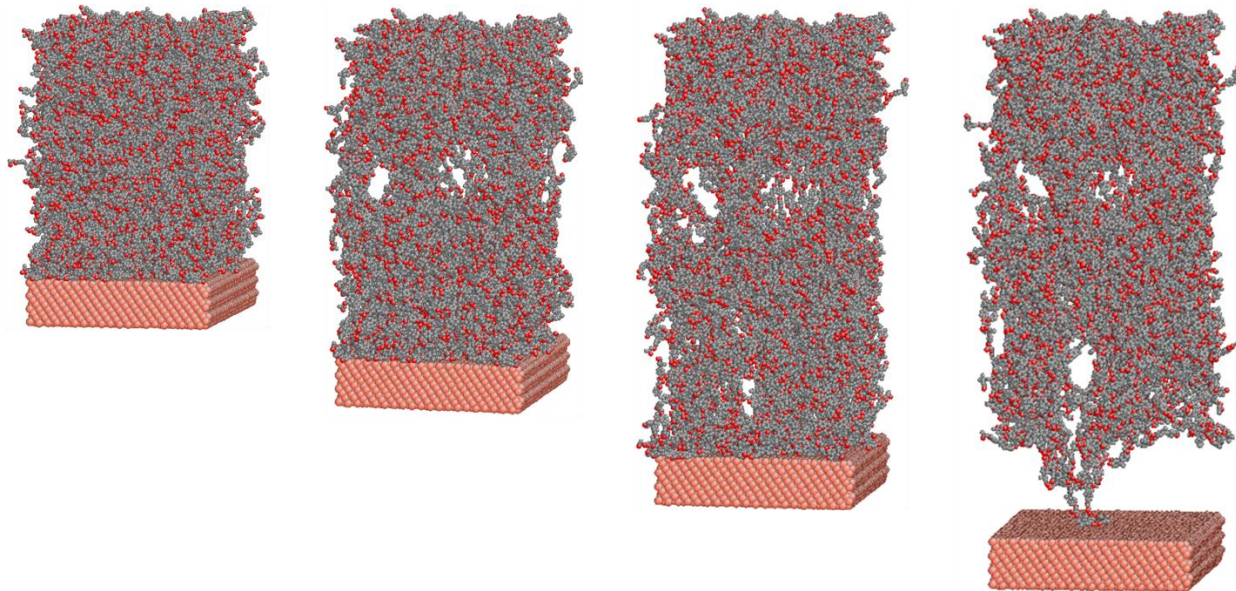


Figure 4-5. Snapshots of atomic configurations during the tensile simulation. The different figures in a row represent strains (from left to right): 8.7%, 38.5%, 77.1% and 107.9%.

These micro-voids enlarge and coalesce as the tensile deformation proceeds, as is shown in the third snapshot. At the meantime, polymer chains are being pulled taut from their initial configuration. This process, we argue, is accomplished via angle bending and dihedral torsion instead of direct bond stretching, because, as shown in Figure 4-4 (b), the bond energy experiences negligible post-yielding change, while the angular and torsional energy show significantly more drastic changes. The increase of angular energy is due to the change of angles.

The decrease in torsional energy indicates that the dihedrals were not in their equilibrium state, and tensile deformation moves them back to their equilibrium states.

At ~95% strain, the normal stress reaches the failure strength of approximately 0.34GPa and drops abruptly to zero. It is seen from the last snapshot in Figure 4-5 that failure is the result of debonding of the epoxy from the Cu substrate. Our simulations also show that immediately after the interfacial failure, the epoxy recoils back. Accordingly, angular/torsional energy drastically decreases/increases after reaching their maximum/minimum, as can be seen in Figure 4-4 (b).

4.3.3 Bulk versus Interfacial Deformation

The strain in the stress-strain curves shown in Figure 4-2 consists of the deformation occurred in the bulk of the epoxy and in the epoxy/Cu interface (the Cu substrate is assumed rigid). The bulk epoxy deformation is governed by the PCFF given in Eq.(3.1), and the interaction across the epoxy/Cu interface is the van der Waals force described by the LJ 9-6 potential given in Eq.(4.1). The potential well depth of copper is typically one or two orders of magnitude larger than that of epoxy atoms. Therefore, the van der Waals forces across the interface are strong attractions. Furthermore, the initial epoxy network is a fully relaxed one. Thus, at lower strain level, the bulk epoxy deforms relatively easily through the rearrangement of the polymer network (angles and torsion). Consequently, bulk deformation is predominant. However, since the epoxy has a highly constrained network microstructure, there is a limit for the rearrangement of strands to accommodate the deformation. Beyond that, valence forces within the polymer kick in. The bulk epoxy becomes significantly stiffer than the van der Waals

interaction at the epoxy/Cu interface. Thus, at higher strain level, the deformation occurring at the epoxy/Cu interface becomes non-negligible, which eventually fails the interface.

To demonstrate the above analysis, a numerical experiment was conducted, in which the bulk epoxy (with the Cu substrate removed) was subjected to tensile deformation by applying the same downward velocity to the bottom of the bulk epoxy as if the Cu substrate were present. The corresponding stress-strain curve is plotted in Figure 4-6 together with that of the epoxy/Cu bimaterial. It is seen that these two curves are almost identical at lower strain level (< 46%). At higher strain level (> 46%), they start to deviate. The difference between these two curves is due to the compliance of the interface. Another way of looking at this figure is by drawing a straight line of constant stress. Under the same stress, the bulk epoxy has smaller strain than the epoxy/Cu bimaterial. The additional strain in the epoxy/Cu bimaterial comes from the epoxy/Cu interface.

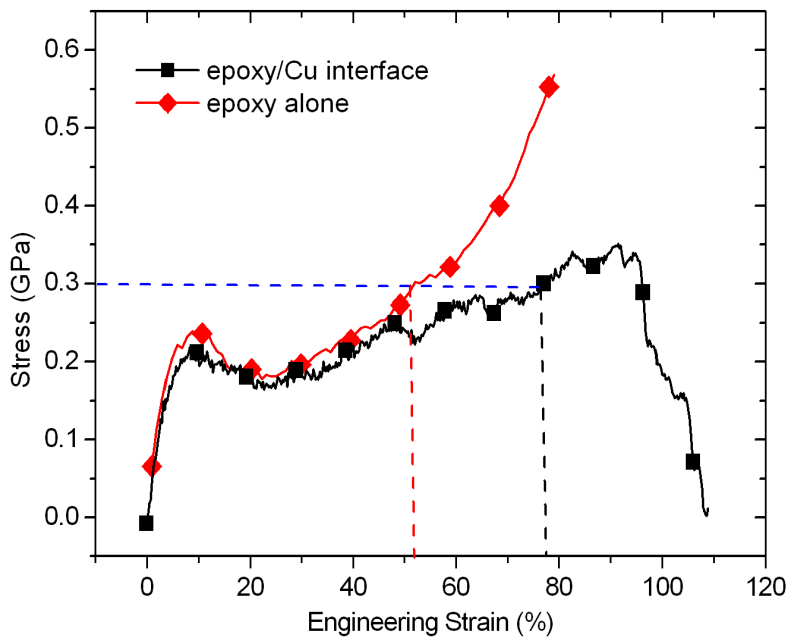


Figure 4-6. Stress-strain curves for the epoxy/Cu interface and the epoxy slab alone, respectively.

The large bulk deformation of the epoxy slab seems to contradict the brittle nature of epoxy observed in macroscopic mechanical tests. This contradiction can be explained by the different length scales of observation used. In comparison with the laboratory test samples, the material volume simulated in this study is extremely small. The deformation observed is, therefore, extremely localized. Such localized large deformation has been observed experimentally, such as in crazes [132], dilatation bands [133] and shear bands [134, 135] (images are shown in Figure 6-1 in Section 6.1). Regarding interfaces, local plastic deformation has been observed as ridges on epoxy fractured surface from glass [10] and sapphire [136] substrates.

The interfacial failure strength in our MD simulation is 340MPa, higher than experimental measured values ranging from ~50MPa for epoxy/steel [24, 137] to 120MPa for epoxy/bare-sapphire [136]. However, it is known that MD simulated local stresses could be much higher than macroscopically measured stress in typical laboratory test samples. For example, Gall et al. [39] reported the debonding strength of Al-Si bimaterial to be 20GPa, which contrasted sharply with the experimental measured ultimate tensile strength (~200MPa) of cast Al-Si alloy [138, 139]. In our case, the deformation within the MD simulated region is all due to the stretching of discrete molecular fibrils. Therefore, stress magnitude could be much higher. In fact, some analysis [4] of the self-assembled monolayer (SAM) revealed that the separation strength of two methyl-terminated alkylsiloxane SAM coated surfaces, which is solely due to van der Waals interaction, could be as high as 320MPa. This class of interactions (SAM-SAM) corresponds to those involved in epoxy bonded to silicon oxide substrate [4]. Therefore, our

computed strength of 340 MPa is reasonable as far as separation of atomic surfaces is concerned.

Clearly, more work is needed in order to use the MD results in macroscopic samples.

4.3.4 Unloading and Reloading Behavior

To understand how the bimaterial behaves under cyclic loading (loading-unloading-reloading), molecular dynamics simulations were conducted. First, a simulation cell was subjected to tensile loading up to the strain of 38.5%. The bimaterial is then unloaded by reducing the applied tensile deformation following the same rate of deformation as for the original tensile test. As shown in Figure 4-7, a residual strain of ~ 21% remains after the tensile load is completely removed (zero-tensile stress). In the fully unloaded bimaterial (snapshot not shown here), irreversible damages are seen in the epoxy slab as voids. Accordingly, the non-bond potential energy fails to restore to its original value, see Figure 4-8 (a). By reloading the system, the stress-strain response forms a hysteresis loop with that of the unloading process. The area encompassed by the loop corresponds to the energy dissipation during the strain cycle, indicating a visco-plastic nature of the material's post yielding constitutive behavior. Figure 4-8 (a) and (b) demonstrate that the non-bond energy's reloading curve is lower than the unloading curve, while for angular and torsional energies the two coincide. This implies that the energy dissipation in the unloading-reloading cycle is associated with the polymer chains' translational motion, rather than the changes of intra-chain rotational degrees of freedom, i.e., angle bending and dihedral torsion. Reloading of the interface system attains the same failure strength/strain as the original tensile test, which is expected since the failure is solely controlled by the copper-epoxy inter-atomic potentials. This also indicates that the interface deforms elastically and is not damaged until the ultimate failure occurs.

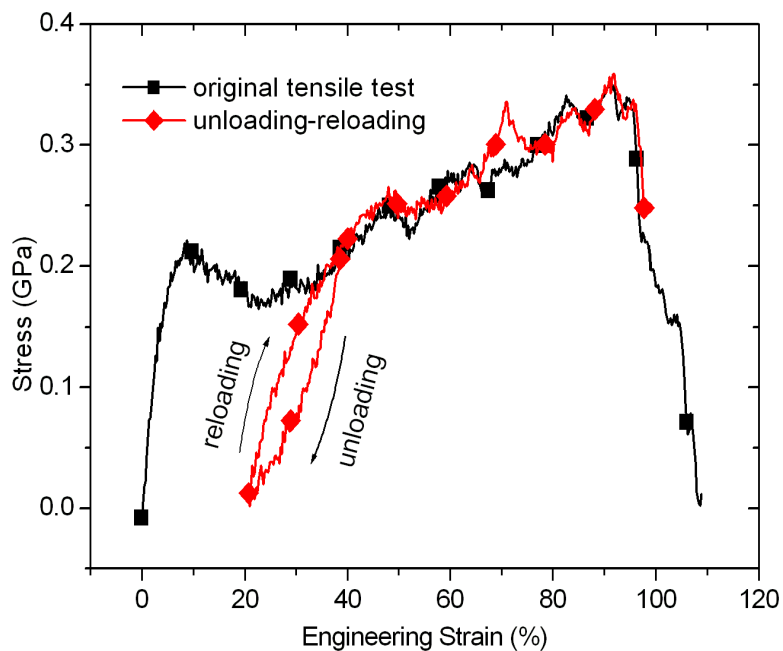


Figure 4-7. Unloading-reloading behavior of the epoxy/Cu interface system

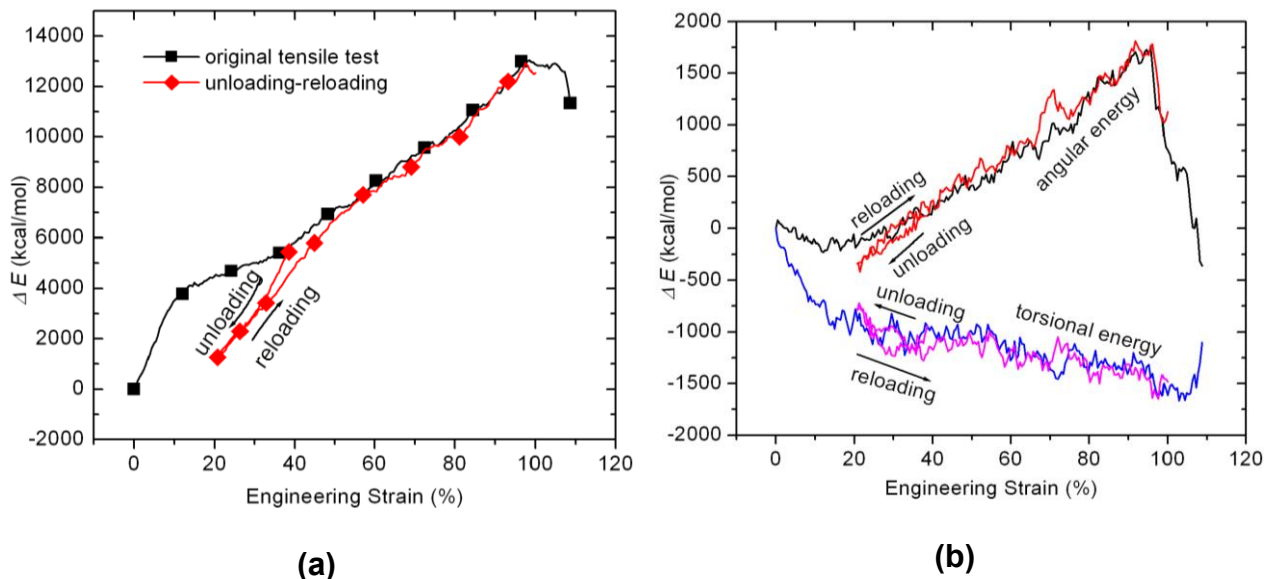


Figure 4-8. Variation of the (a) non-bond and (b) valence potential energy components during the unloading-reloading process

4.3.5 Effect of Temperature

To study the effects of temperature, MD simulations were conducted at several temperatures, $T = 340, 380, 440\text{K}$ and 500K . The resulted stress-strain curves are shown in Figure 4-9, and the corresponding yielding and failure strengths are shown in Figure 4-10. As expected, both the yielding and the failure strengths decrease with increasing temperature. In addition, there is a slight decrease in the yielding and failure strains as well. Note that, as discussed earlier, the yielding strength is predominately the bulk epoxy behavior, while the failure strength is the epoxy/Cu interface property. Therefore, the results shown in Figure 4-9 indicate that temperature affects both the bulk epoxy and the epoxy/Cu interface. In bulk epoxy, yielding is caused by the change in angular and torsional bonds facilitated by the relative sliding among the polymer chains. Higher temperature lowers the activation energy and makes the sliding easier, thus reducing the yielding strength, as well as the modulus [140]. The interface, on the other hand is mainly associated with the inter-atomic forces at the interface between epoxy and Cu atoms, governed by the LJ potential. At higher temperature, the increased mobility of near-surface polymer strands lowers the energy consumption to break interfacial (non-covalent) bonds. Thus the failure strength reduces.

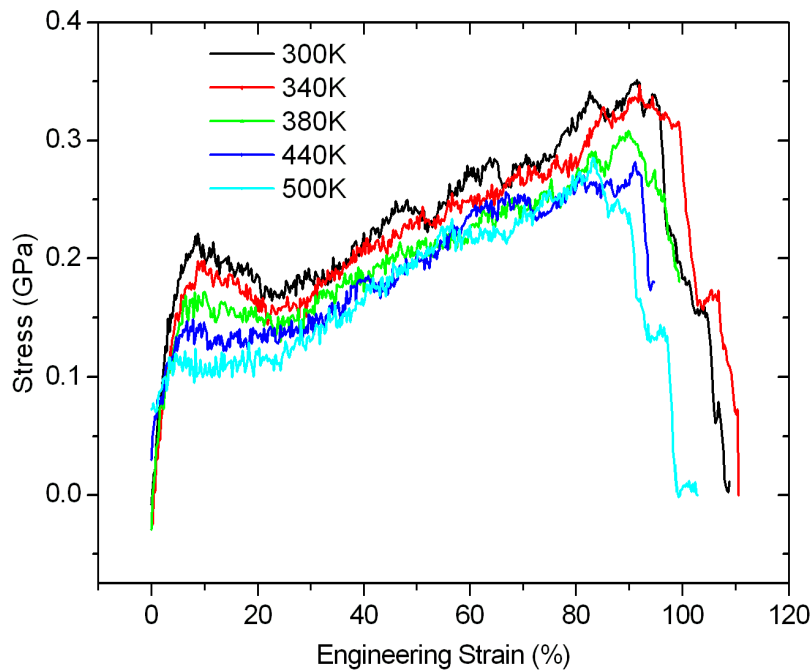


Figure 4-9. Stress-strain curves at different temperatures

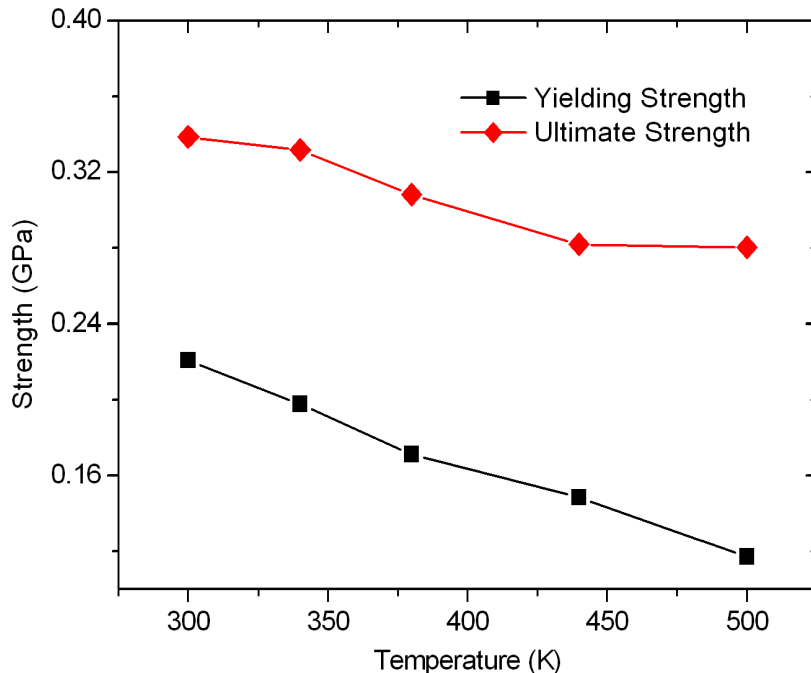


Figure 4-10. Yield and failure strengths of the bimaterial versus temperature

4.3.6 Effect of Conversion

The conversion, or the fraction of reactive sites that have been reacted, significantly influences the mechanical properties such as the Young's modulus of bulk epoxy [140]. All the results presented in the previous sections are for the case of 95% conversion. In this section, we are interested in how the conversation rate affects the epoxy/Cu interfacial strength.

As crosslinking proceeds, the polymer's microstructure experiences a transition from liquid mixture of monomers to loosely connected fragments, and to highly constrained network. Each of the three phases exhibits different mechanisms of deformation and failure when loaded. To investigate the effect of conversion, three additional bimaterials with different epoxy conversions, $c = 50\%$, 73% and 82% were constructed and were subjected to the same MD simulation of tensile deformation as described in previous sections. Figure 4-11 plots the stress versus strain curves for all four bimaterials. Prior to the occurrence of yielding, the four bimaterials exhibit similar elastic responses, indicating that the conversion does not affect the linear elastic behavior. However, the post-yielding behavior is strongly affected by the conversion. For the least cross-linked (50%) system, strain-softening occurs immediately after yielding, and the tensile stress decreases to zero almost exponentially. Snapshots of the atomic configuration shown in Figure 4-12 (a) indicate that failure initiates within the epoxy in the vicinity of interface, and progresses as the tensile load increases. Following Miller and Macosko's method [114], the theoretical gelation point of our particular epoxy formulation (E3+E4+H2, E for epoxy and H for hardener, number stands for functionality) is 62%. Since a conversion of 50% is lower than the gelation point, the atomistic model of epoxy comprised many loosely connected molecular fragments rather than a system-spanning cluster. Therefore,

the presence of a thin layer of molecules near the interface, which lacks sufficient covalent links to the epoxy bulk, is likely. Failure of the interface system is thus seen as the cohesive separation between this thin layer and the rest portion of epoxy. Fibrils vertically bridging the two parts are present at intermediate strains, but bounce back to epoxy bulk and return to coiled state as tensile deformation continuously proceeds. On the other hand, the thin layer in the vicinity of interface would remain attached to the substrate.

The systems with conversions of 73% and 82% exhibit deformation behaviors which are intermediate between extreme cases. For both bimaterials, the tensile stress decreases after reaching the yielding point and experiences strain hardening regime, followed by stress plateau until failure (green and red curves in Figure 4-11). Magnitudes of their post-yielding stress are lower than that of the 95% conversion. The reason lies in the fact that lower conversion facilitates more micro-voids to initiate, grow and coalesce, which can be evidenced by the larger average void size in the post-yielding atomic configurations shown in Figure 4-12 (b). The higher level of damage to the bulk epoxy leads to more drastic stress drop after yield.

In these lower conversion bimaterials, the ultimate failure occurs at larger strains but lower strengths, both can be attributed to the difference in microstructure. At lower conversions, the polymer chain network is less connected. This results in more not-crosslinked polymer strands in the epoxy. When deformed, these strands require larger overall strain to be stretched taut from their coiled state. Thus the failure strain is extended.

As discussed in previous sections, the failure strength of the bimaterial is related to the epoxy/Cu interface. Snapshots of the atomic configuration, see Figure 4-5, indicates that interfacial failure is caused by the simultaneous separation of all polymer atoms from the Cu

substrate that results in the brittle failure shown by the stress-strain curve, see Figure 4-11. It is also seen from Figure 4-11, that bimaterials with lower conversions, on the other hand, show a more ductile failure behavior. This ductile behavior is due to the gradual peeling-off of polymer chains from the Cu substrate, as observed in the snapshots shown in Figure 4-12 (b). Such gradual detachment of polymer chains from the Cu substrate decreases the interfacial strength, and increases the failure strain. To quantify this observation, we plotted in Figure 4-13 the number of epoxy atoms in the vicinity (van der Walls cutoff distance) of the epoxy/Cu interface as a function of tensile deformation. It is clear that lower conversion leads to more gradual interfacial separation of epoxy atoms from the Cu substrate.

Table 4-2 summarizes the failure strength and strain for different bimaterials. From 73% to 95%, strength and strain increases and decreases, respectively, with increasing conversion. The bimaterial with conversion of 50% (below the gelation point), fails cohesively instead of interfacially, thus need to be interpreted separately.

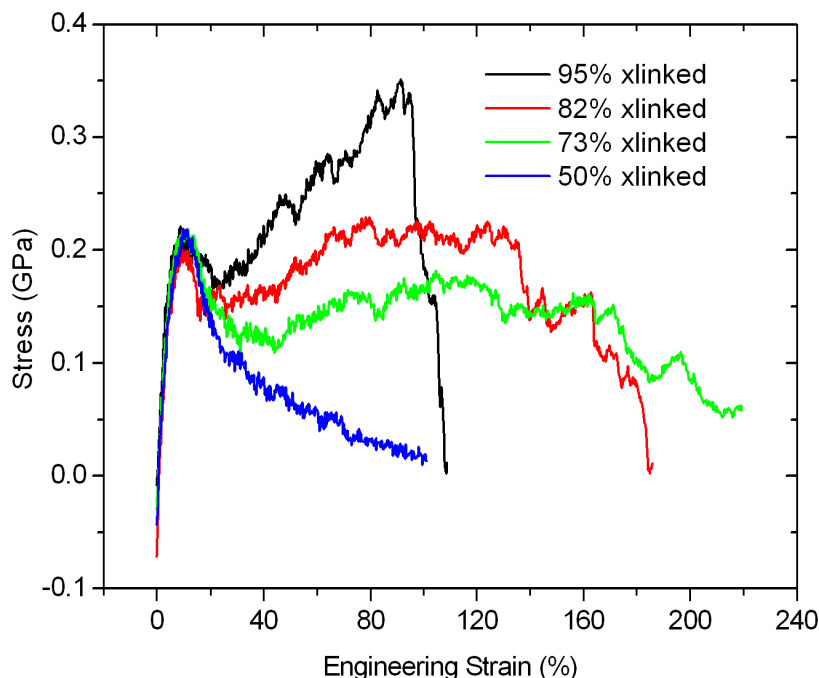
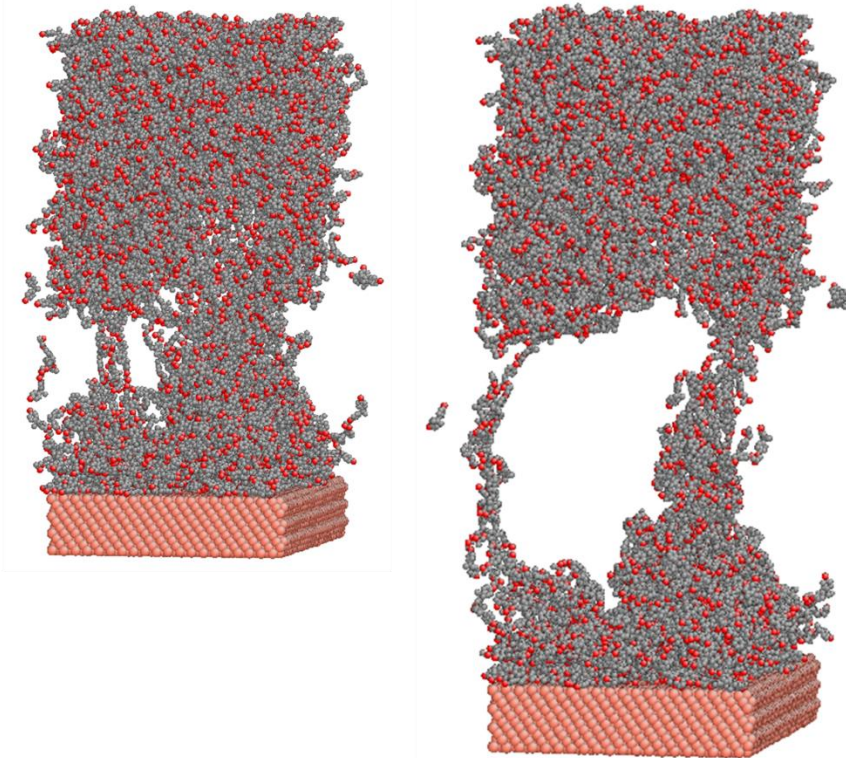


Figure 4-11. Stress-strain curves for bimaterials with different epoxy conversions



(a)

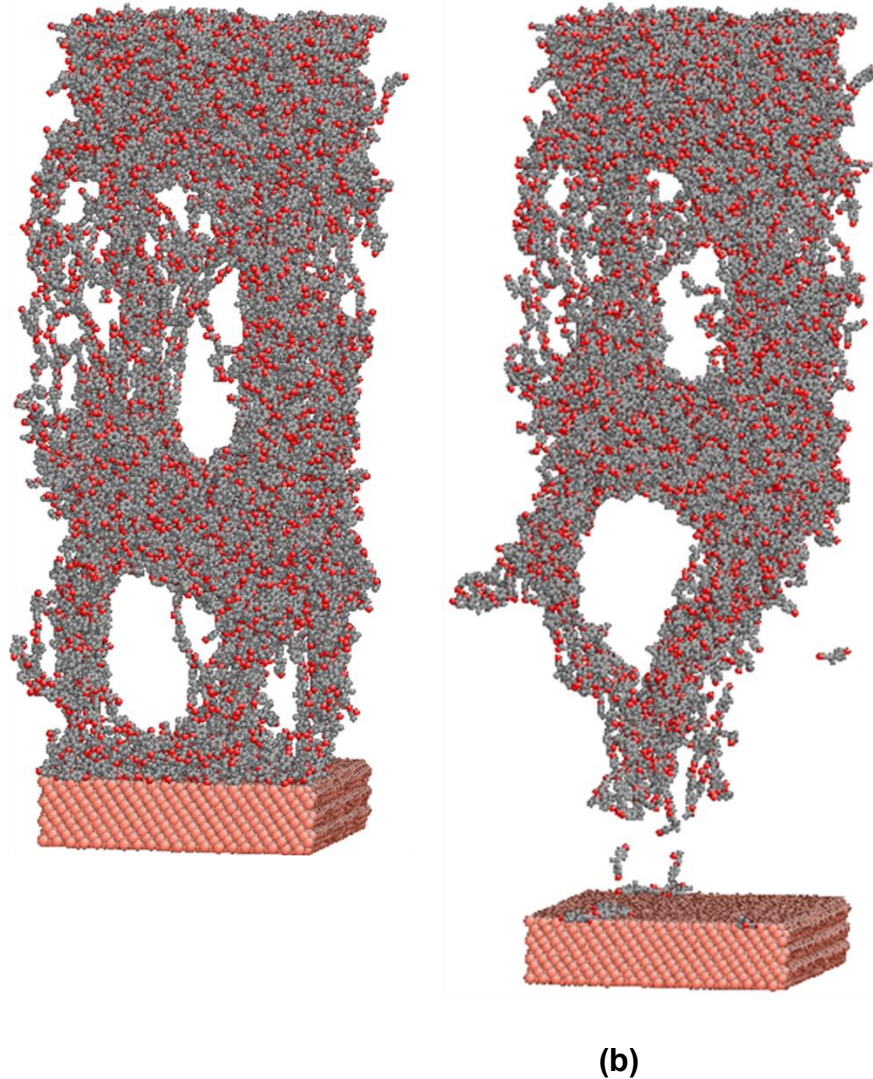


Figure 4-12. Atomistic configurations during tensile deformation for bimaterials with lower conversions at different strains: (a) 50% crosslinked; (b) 82% crosslinked. The different figures in each row represent strains (from left to right): (a) 56.6% and 98.1%; (b) 130% and 185.7%

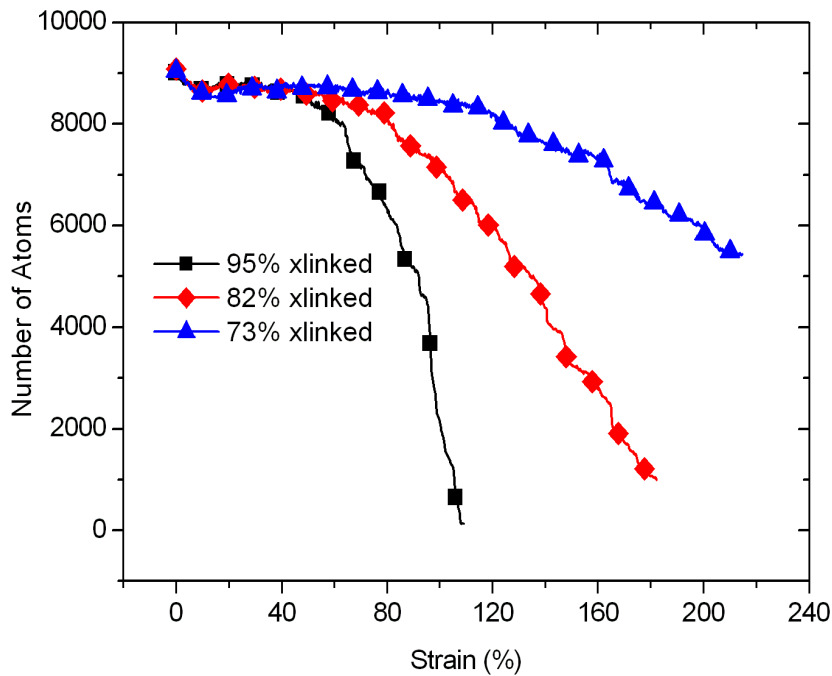


Figure 4-13. Number of epoxy atoms within the van der Waals cutoff distance from the epoxy/Cu

Table 4-2. Failure strength and strains for bimaterials with different conversions

Conversion (%)	Failure strength (GPa)	Failure strain (%)
50	0.2146	11.07
73	0.1470	170.48
82	0.2143	130.18
95	0.339	94.91

4.3.7 Effect of Epoxy Functionality

Results presented here so far are for the epoxy system containing tri- and tetra-functionalized epoxy monomers and the number-averaged functionality is 3.6. Different

functionality results in different microstructure of the cross-linked polymer network. Therefore, it is conceivable that the mechanical behavior of the epoxy/Cu bimaterial would be different for epoxies with different functionalities. To study the effects of epoxy monomer functionality (fn) on the mechanical behavior of the epoxy/Cu bimaterial, two additional MD simulations were conducted on epoxy/Cu bimaterials with $fn = 4$ and 6 , respectively. Figure 4-14 plots the corresponding stress-strain curves together with that of $fn = 3.6$. Points of interest on the stress-strain curves are extracted and tabulated in Table 4-3.

Several observations regarding the change of fn from 3.6 to 6 can be made from Figure 4-14 and Table 4-3. First, the yielding strength and yielding strain do not seem to change much, indicating that the bulk elastic properties are not sensitive to the epoxy functionality. Second, the failure strength does not seem to change much, indicating that interfacial strength is not sensitive to the epoxy functionality, since the failure strength of the bimaterial is dictated by the epoxy/Cu interfacial strength. Third, although the interfacial strength does not change much, the failure strain of the bimaterial reduces significantly with increasing fn . Note that the post-yielding (between the yielding and failure) is a consequence of the changes in angular and torsional bonds, or the relative sliding between the polymer chains, reduction of the failure strength implies that angular and torsional bonds are more constrained in epoxy with higher functionality. This is intuitively understandable, because $fn = 6$ means that (on average) each epoxy monomer in the polymer network has six sites to bond to other epoxy monomers, resulted in a more closely inter-connected network which limits the chain sliding and local voiding. Consequently, bulk epoxy with higher functionality is less deformable. This can be observed from Figure 4-15 where for $fn = 6$ the microstructure of the deformed epoxy/Cu bimaterial under

different strain is shown. In comparison to Figure 4-5 where the same is shown for $fn = 3.6$, it is clear that bulk epoxy with higher functionality has much less deformation, and much less and smaller voids.

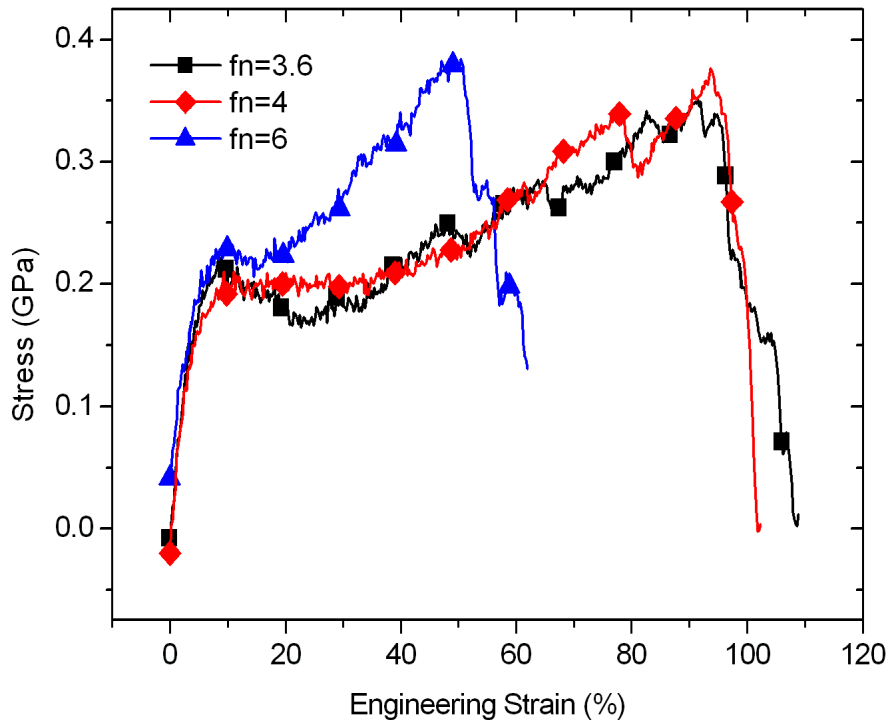


Figure 4-14. Stress-strain curves for models with different epoxy monomer functionalities

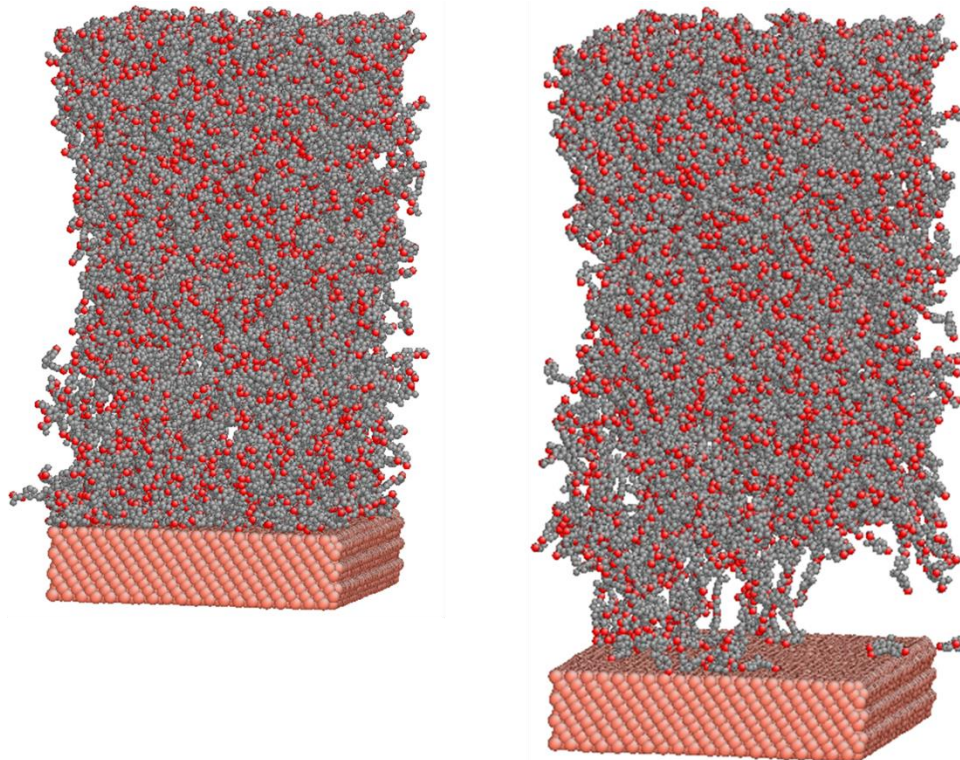


Figure 4-15. Deformed atomistic configurations for the $f_n = 6$ case. The different figures from left to right represent strains at 39.2% and 63.7%.

Table 4-3. Failure strength and strain for different functionalities

Functionality	Failure strength (GPa)	Failure strain (%)
3.6	0.339	94.91
4	0.376	93.78
6	0.384	50.45

4.4 Summary of This Chapter

To investigate the deformation/failure behavior of epoxy/Cu interface, we carried out

large scale classical molecular dynamics simulations on an epoxy/Cu bimaterial. The network structure of the epoxy was built through a simulated crosslinking process in which covalent bonds formation and MD equilibration of the system were performed iteratively. The crosslinked molecular network was applied on the Cu substrate to build the epoxy/Cu bimaterial. By applying velocity loading to the substrate on the fly of molecular dynamics simulations, the normal stress versus displacement/strain response was obtained. Effects of simulation cell size were studied to ensure that the results are independent of simulation cell size.

We found that normal stress versus strain curve exhibits a near linear elastic range, followed by yielding and post-yielding strain softening, and hardening regimes, ended with a brittle failure. The deformation between yielding and ultimate failure of the epoxy/Cu bimaterial is predominately due to micro-void initiation/growth and re-alignment of the epoxy network strands. The ultimate failure is predominantly interfacial and brittle caused by the (almost) simultaneous detachment of epoxy atoms from the Cu substrate.

In addition, we found that the linear range of the stress-strain curve is almost unaffected by the conversion of the epoxy. However, epoxy with lower conversion tends to have lower failure strength, but large failure strain. This is because at lower conversion, the polymer network is less connected, which facilitates void initiation and chain re-alignment leading to larger failure strain. The lower conversion also makes it easier for the epoxy atoms to be detached from the Cu substrate in a more gradual manner so that the ultimate interfacial failure becomes more ductile with a lower failure strength.

Further, the effects of epoxy functionality were also investigated. We found that epoxy with higher functionality tend to behave similarly to epoxy with higher conversion in that they

are more brittle and have higher failure strength.

Another interesting finding is that the failure strength is unaffected by the unloading and reloading before the failure strength is reached, because the epoxy/Cu interface is not damaged until the stress is very close to the failure strength. This is more so for epoxy with higher conversion.

In closing, we point out that in interpreting the above results/conclusions, one must keep in mind the limitations of the classical molecular dynamics simulations, most notably, the small material volume simulated, and the high strain rate used. We believe that relatively high yielding strength of the epoxy, and the failure strength of the epoxy/Cu interface are partially due to these limitations. In spite of these limitations, we believe that major findings of this study provide significant insights into the deformation and failure of the epoxy/Cu bimaterial. The basic mechanisms captured by our MD simulation remain valid for laboratory-size samples under quasi-static loading.

Another concern is the infinite cohesive strength of the epoxy predicted by the PCFF force field used in the MD simulations. We note, however, that numerous experimental observations of epoxy adhesive on Cu substrate have shown that the epoxy/Cu interface is indeed the weakest link in the bimaterial system, unless special treatment is applied to the Cu surface before bonding. This is because the epoxy forms no chemical bonds with copper without any modification. Only weak van der Waals force and hydrogen bonds are involved in the adhesion [129]. Thus the Cu-epoxy interface has poor intrinsic adhesion and is prone to interfacial delamination instead of cohesive failure in the polymer. Therefore, it is reasonable to assume in our MS studies that interfacial failure occurs prior to bulk failure. Consequently, the cohesive

strength of the bulk epoxy is not important as long as it is greater than the interfacial strength, since the stress in the bulk will never be high enough to reach the bulk strength. Thus, the use of PCFF is justified when interfacial failure is of the main interest.

CHAPTER 5 COARSE-GRAINED MODEL FOR EPOXY

In this chapter we present a coarse-grained model for molecular dynamics simulation of an epoxy resin used as adhesives and molding compound in electronic packaging industry. The epoxy and hardener molecules are represented as short chains of connected beads, and the curing of epoxy/hardener mixture to high cross-linked network is accomplished by continuously introducing bonds between reactive beads at the meantime of a MD simulation. The inter-bead potential, composed of Lennard-Jones, bond stretching and angle bending terms, is parameterized through an optimization process based on particle swarm optimization method to fit the key thermo-mechanical properties of the material from experiments and previous full atomistic simulations [140]. The derived coarse-grained model reproduces glass transition and thermal expansion related properties as well as elastic constants in good agreement with all-atomic simulation results. Temperature and/or conversion-degree dependencies of thermo-mechanical properties, i.e., the shifting phenomenon of glass transition temperature and the elastic response versus temperature relationship, which are not used for parameter fitting, are also well captured, indicating the good transferability of the coarse-grained model for epoxy. Also, the large deformation and failure behavior of the studied epoxy using the developed coarse-grained model is presented.

5.1 Introduction

In the previous two chapters we have demonstrated the capability of full-atomic MD simulation, equipped with rigorously parameterized force-field, to predict/reproduce the thermo-mechanical properties of highly cross-linked epoxy molding compound and mechanical behavior

of epoxy/Cu bimaterial. Albeit the success, there are stringent limitations of full-atomic MD models. The two most obvious limitations are rather restricted spatial and temporal scales, which originate from: 1) the large number-density of atoms within polymeric systems, which boosts the length of neighbor list and the time consumed on evaluating inter-atomic forces. This directly caps the size of the sample that can be simulated in full-atomic MD; 2) the expensive (yet necessary) force-field used to calculate inter-atomic energy and forces. Both Class I and Class II force-fields use a combination of various different terms, each of which is computed for large amount of bonds, angles and dihedrals (torsional/improper). The electro-static term needs special mention here. It is a long-range and conditionally convergent force and requires special technique such as Ewald summation (see section 2.2.2) which is quite expensive. Even with the less computational intensive PPPM method, the simulation can be rather inefficient for large systems; 3) the very short time-step used to integrate the equation of motions, due to inclusion of large number of light atoms, say hydrogen. The typical time-step of a full-atomic MD simulation for polymeric system is 1fs (10^{-15} s). These limitations prevent full-atomic MD simulation being applied in describing physical processes requiring larger length and time scales to correctly capture, e.g., mechanical responses of polymers.

As a consequence, methodology is urgently desired to achieve up-scaling. One such method is coarse-graining (CG), which by definition is to lump a group of atoms into a “super-atom” (see Figure 5-1 for an illustration). By doing this, one can not only reduce the system’s degree of freedom thus the computation load, but also apply larger time-step in the MD simulation, due to the softer inter-particle interactions and heavier weight of particles. Generally speaking, coarse-graining consists of two phases, namely partitioning the system into bigger

structural elements rather than single atoms, and building force-field to describe the inter-bead interactions. The second phase, which represents the major challenge in constructing a CG model, is highly material and application driven thus does not follow a universal rule. A class of methodologies in literature focuses on accurate matching the materials' structural aspects, such as distribution functions, through iteratively adjusting potential parameters starting from the potential of mean forces derived from Boltzmann inversion [141-144] or inverse Monte Carlo technique [145]. The inverse Boltzmann method relates the potential energy associated with a certain degree of freedom to the probability of that degree of freedom. For example, bond stretching potential can be expressed as $U_{bond}(b) = -k_B T \ln(P(b))$, where k_B and T are the Boltzmann constant and temperature, respectively, and $P(b)$ is the probability distribution of bond length between coarse-grained beads, but obtained from full-atomic simulation. Other potential terms, including angle bending, torsional dihedral and van der Waals forces, have similar formulations. Potentials obtained this way represent an initial guess of the true coarse-grained potential, and are optimized by iteratively improving the match between the full-atomic and coarse-grained generated probability distributions [144]:

$$\begin{aligned}
 U_{bond}^{i+1}(b) &= U_{bond}^i(b) + k_B T \frac{P^i(b)}{P^0(b)} \\
 U_{angle}^{i+1}(\theta) &= U_{angle}^i(\theta) + k_B T \frac{P^i(\theta)}{P^0(\theta)} \\
 U_{dihedral}^{i+1}(\psi) &= U_{dihedral}^i(\psi) + k_B T \frac{P^i(\psi)}{P^0(\psi)} \\
 U_{LJ}^{i+1}(r) &= U_{LJ}^i(r) + k_B T \frac{g^i(r)}{g^0(r)}
 \end{aligned} \tag{5.1}$$

where P^0 and g^0 are the target distribution functions (calculated from full-atomic simulations).

The iteration is terminated when the distribution functions computed from coarse-grained model is close enough to the target ones. The concern with the inverse Boltzmann conversion is that, as a configurational free energy in reduced space, the potential's transferability is an issue of questioning, in that it is required to be used in the simulation with identical thermodynamic conditions as the force field is fitted to. Furthermore, the resulting potentials are typically rather soft and lack the ability to mimic the mechanical response during large deformation compared to atomic simulations. Usually, when coarse-graining, it is impossible to accurately capture both the structural aspects and thermodynamic properties. Good agreement with one will inevitably lead to poor agreement with the other, thus compromises need to be made. In other words, the ideal CG method depends on what properties one is interested in. Alternatively, other researchers have developed their coarse-graining methodology based force matching [146]. The fundamental concept is to minimize the difference between the coarse-grained and full-atomic data on inter-(coarse-grained) particle forces. The third class of coarse-graining methods is based on the completely different philosophy. Unlike potentials of mean force and potentials matched to full-atomic force data, of which the mathematical formulation is unknown in priori, the expression is assumed in these methods and the parameters present are determined by matching the material properties of interest, calculated by coarse-grained MD simulation, to the available experimental or full-atomic data. For instance, the “MARTINI” force-field [147, 148], designed for lipid and surfactant systems, was parameterized by reproducing the partitioning free energy between polar and apolar phases of a number of chemical compounds. Similarly, Shinoda et al. [149] developed coarse-grained potential for surfactant/water systems by fitting density and surface/interfacial

tension. Our development for coarse-grained model is based on the latter methodology. As will be presented in the following sections, parameters of a few prescribed functional forms are iteratively optimized to reproduce material properties of interests. The versatility of the obtained potential is examined by applying it to structures with a broad range of cross-linking degrees, with emphasis on the ability of correctly capturing crosslink-density's effect on material behavior.



Figure 5-1. Illustration of Coarse-Graining of a Polymer Chain into Beads

Aside from achieving upscaling in spatial and temporal domains, a strong motivation to the current investigation is to incorporate bond rupture in the force-field, for the sake of modeling bulk material failure and possible cohesive fracture mechanisms in bimaterials composed of epoxy and in-organic substrates. This capability is missing in most of the fully atomistic models for polymer networks [102]. From purely mathematical point of view, the harmonic or quartic-polynomial bond stretching term present in consistent-valence force-field (CVFF) or consistent force-field (CFF, e.g, PCFF, COMPASS) inherently forbids smooth cutoff of bond energy. Also, simulation of valence bond breakage at atomistic level involves complex re-equilibration of partial charges thus is not practical to implement. On the other hand, a number

of works utilizing coarse-grained model with smooth bond cutoff have been conducted to study fracture of epoxy based materials or other types of polymer networks [4, 121, 122]. However, these are model materials without correspondence to any real system. Thus it is desired to have a methodology for efficient development of a failure-prediction-enabled potential for realistic epoxies or thermosetting polymers.

The rest of this chapter is organized as follows. In the next section, we will describe the partition scheme and inter-bead interactions, and the procedure to construct a highly cross-linked polymer network. In section 5.3, we give in detail the algorithm and implementation of the optimization scheme to obtain potential parameters. The parameterized potential is then applied to compute the epoxy molding compound's properties and their correlation to structure. Accompanied are some discussions. In the conclusion part, we describe the future application of the coarse-grained model for epoxy.

5.2 Model and Interactions

5.2.1 Mapping

To build the coarse-grained model for the cross-linked epoxy molding compound, it is a nature choice to start with the coarse-grained constitutive monomers, i.e., the tri-/tetra-functionalized EPN and BPA. Once the monomers are coarse-grained, one can randomly seed them into simulation box and cross-link them to the coarse-grained epoxy network. In building coarse-grained models for monomers, we do not follow the usual scheme of exact one-to-one mapping from a specific chemical moiety to certain bead type, which introduces a variety of different bead types, and thus a large pool of parameters for optimization. Instead, we represent

the monomer as chains which maintain similar geometry as their realistic atomistic configurations, of connected beads with unified parameters, i.e., identical mass M , Lennard-Jones potential-well depth ε and diameter σ . The bead-connector representations of the monomers are depicted in Figure 5-2. Epoxy monomers are simplified as chains of 3 or 4 backbone beads (colored blue in Figure 5-2 (a) and (b)), each of which has a reactive branching bead (brown) attached. The hardener monomer possesses two reactive beads (yellow) linked to one center bead (grey). During the cross-linking process, bonds are created continuously between reactive beads on EPNs and BPAs in the fly of an MD simulation to fulfill the percolation of polymer network throughout the entire system. The following sections of this article will show that, by iteratively tuning M , ε and σ , along with other potential parameters for bond and angle interactions, our simple coarse-graining approach is capable of generating model of which properties and behaviors resemble those of realistic the epoxy molding compound. Besides, since we have a relatively small number of parameters to fit, the time to reach convergence is significantly reduced.

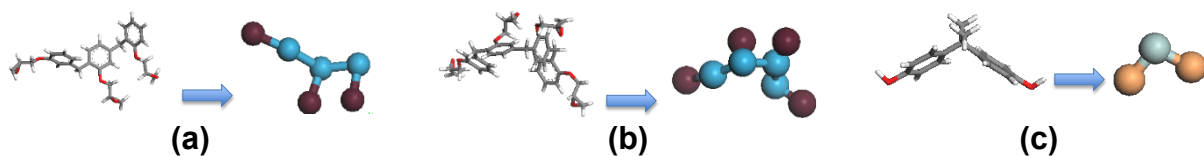


Figure 5-2. Bead-connector representations of monomers: (a). EPN-3mer; (b). EPN-4mer and (c). BPA

5.2.2 Inter-Bead Potential

In the coarse-grained system, beads interact via the Lennard-Jones (LJ) potential:

$$U_{LJ}(r) = 4\epsilon \left[\left(\frac{r}{\sigma} \right)^{12} - \left(\frac{r}{\sigma} \right)^6 \right] \quad (5.2)$$

The interaction is truncated at the distance of 2.5σ . As previously mentioned, ϵ and σ will be optimized, not only to correctly account for the non-bonded interactions but also to provide a good gauge of measurement of the system's real dimension and energy. Note the LJ interactions are only computed for beads which are not 1-2 (bond) or 1-3 (angle) neighbors of each other. Beads are bonded using a potential permitting bond breakage. It is a sum of the purely repulsive LJ interaction, with a cutoff at $2^{1/6}\sigma$, and a quartic bond potential:

$$\begin{aligned} U_b(r) = & U_0 + k_4(r - r_c)^2(r - b_1 - r_c)(r - b_2 - r_c)H(r_c - r) \\ & + 4\epsilon \left[\left(\frac{\sigma}{r} \right)^{12} - \left(\frac{\sigma}{r} \right)^6 + \frac{1}{4} \right] H(2^{1/6}\sigma - r)H(r_c - r) \end{aligned} \quad (5.3)$$

where $k_4 = 1434.3\epsilon / \sigma^4$, $b_1 = -0.7589\sigma$, $b_2 = 0$ and $U_0 = 67.2234\epsilon$ [121]. The bond extension cutoff r_c will be among the parameters to fit. Upon fixing other parameters, effect of r_c on the bond potential is illustrated in Figure 5-3. It indicates that the equilibrium distance decrease as smaller cutoff is used, so does the potential well depth. At r_c the potential is smoothly truncated, and the bond is removed from the system. Meanwhile pair potential (LJ) is turned on between the afore-bonded pair.

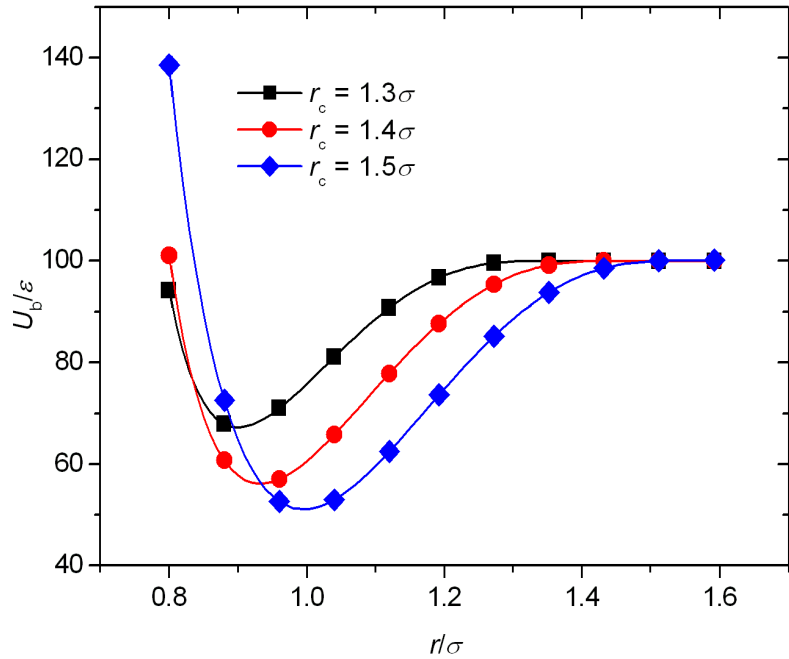


Figure 5-3. Bond Potential curves for different bond extension cutoffs

In addition to LJ and bond terms, angle bending interaction is introduced as a harmonic function:

$$U_a^{(i)}(\theta) = k_\theta^{(i)} (\theta - \theta_0^{(i)})^2 \quad (5.4)$$

Three angle types are defined. The angle formed by the 3 beads in a BPA monomer is called type 1, whose equilibrium angle is assumed to be $\theta_0^{(1)} = 100^\circ$. The angles formed by an reactive bead in an EPN and a reactive bead in a BPA is called type 2, whose equilibrium angle is assumed to be $\theta_0^{(2)} = 180^\circ$. All the angles formed by beads within each EPN are called type 3, whose equilibrium angle is assumed to be $\theta_0^{(3)} = 180^\circ$. The pre-factor, $k_\theta^{(i)}, i = 1, 2, 3$, will be subjected to iterative tuning through the optimization procedure.

5.2.3 Cross-linking Process

Epoxy based materials have percolating network structure formed by chemically curing epoxy and hardener monomers, starting from liquid mixture. A model for molecular dynamics simulation, either atomistic or coarse-grained, should mimic this unique structural characteristic. Upon simplifying constitutive monomers into bead-connector representations, as described in section 2.2, they are randomly seeded into a cubic simulation box with 3 dimensional periodic boundary conditions being assigned. The number of different types of monomers obeys the stoichiometric ratio, i.e., 2:3:9 for 3mer:4mer:BPA. The mixture of monomers is equilibrated under constant pressure ensemble at the temperature of $0.8 \varepsilon / k_B$ (k_B is the Boltzmann constant), with timestep of 0.005τ ($\tau = \sigma \sqrt{M / \varepsilon}$) for one million steps. What follows is the dynamic cross-linking process during the constant temperature/pressure MD simulation. Bond is conditionally formed, with the probability of 0.01, between an EPN reactive bead and a BPA reactive bead when their separation is less than 1.3σ . At the rate of one attempt of bond creation per 10 MD steps, the conversion degree of 90% typically takes 400,000~500,000 steps. Due to the 3D periodic nature of the simulation cell, the network is truly extending to infinity. Regarding the system size, we built a small simulation box containing 7752 beads, for the purpose of parameter fitting. Since iterative MD runs are involved at this stage, a smaller system is desired to speed up the process. In the later production runs, a larger system with 45689 beads is constructed.

5.3 Parameter Optimization

5.3.1 Particle Swarm Optimization

As described in the previous sections, a total of 7 adjustable parameters, namely $M, \varepsilon, \sigma, r_c, k_\theta^{(1)}, k_\theta^{(2)}$, and $k_\theta^{(3)}$, need to be determined for the potential of the coarse-grained potential. In this section, we present in detail the procedure used to obtain them simultaneously. The fundamental algorithm is the particle swarm optimization (PSO) method, which is a population based stochastic optimization method and originally attributed to Kennedy and Eberhart [150] for simulation of animal social behaviors in, e.g., a bird flock or fish school. Due to its simple algorithm and fast convergence, the PSO method has been successfully practiced in many other areas [151, 152]. Specifically for our purpose, the method has shown its applicability in parameterizing inter-atomic potentials for systems such as lithium-silicon alloys [153, 154].

In the PSO method, a population (swarm) of candidate solutions (particles) moves in the search-space following some simple mathematical formulae. Their movements are directed by each particle's and the entire swarm's best known positions in the search space. Formally, the method aims to find a solution \mathbf{x}_0 satisfying the condition that $f(\mathbf{x}) \leq f(\mathbf{x}_0)$ holds for any particle \mathbf{x} in the search-space. A typical PSO procedure is:

- 1). Initialize the i -th particle's position \mathbf{x}_i , and its own best known position \mathbf{p}_i to \mathbf{x}_i ; Update the global best position \mathbf{g} to \mathbf{p}_i if $f(\mathbf{p}_i) \leq f(\mathbf{g})$ holds, where f is the objective function; Initialize the i -th particle's velocity \mathbf{v}_i .

- 2). Update the i -th particle's velocity \mathbf{v}_i , and its position \mathbf{x}_i ($\mathbf{x}_i \leftarrow \mathbf{x}_i + \mathbf{v}_i$) accordingly; Set \mathbf{p}_i to \mathbf{x}_i if $f(\mathbf{x}_i) \leq f(\mathbf{p}_i)$ is satisfied, and \mathbf{g} to \mathbf{p}_i if $f(\mathbf{p}_i)$ is less than or equal to $f(\mathbf{g})$.
- 3). Repeat 2) until convergence criterion is met.

5.3.2 Implementation

In the current investigation, a particle corresponds to a set of candidate parameters for our coarse-grained potential, i.e., $\mathbf{x} = \{M, \varepsilon, \sigma, r_c, k_\theta^{(1)}, k_\theta^{(2)}, k_\theta^{(3)}\}$. The objective function is defined as:

$$f(\mathbf{x}) = \sum_{i=1}^N \left[\frac{g_i(\mathbf{x})}{y_i} - 1 \right]^2 \quad (5.5)$$

where $g_i(\mathbf{x})$ is the thermodynamic properties calculated by MD simulation using the coarse-grained potential with parameters \mathbf{x} , and y_i is the all-atomistic result of the properties [140]. The properties selected for fitting include the glass transition temperature, room temperature density, modulus and Poisson's ratio for the 90% cross-linked and pre-cured systems. Thus, a total of 8 properties are considered.

To start optimization, each parameter is given a random number uniformly distributed within a carefully chosen range. The range is empirically determined based on the observation of the properties' variation in a few trial optimizations. Afterwards, MD simulations over the two models (cross-linked and not cross-linked) are initialized. The two structures are first separately geometry optimized using energy minimization and equilibrated under constant pressure at the temperature of $0.8 \varepsilon / k_B$. MD simulated cooling process from 0.8 to $0.2 \varepsilon / k_B$ within 10^6 steps are conducted thereafter to generate their volume versus temperature relationships, from which the glass transition temperatures can be extracted by segmental linear regression, as is illustrated in

Figure 5-4 (a). Based on the glass transition temperature for the cross-linked model, the value of room temperature in LJ unit (ε / k_B) is estimated and what follows are MD simulations at this temperature. They include constant pressure equilibration at room temperature which produces values of density for the two systems (Figure 5-4 (b)), and uni-axial tension from which Young's modulus and Poisson's ratio are computed by linear regression over stress-strain and longitudinal-lateral strain data within the strain range of 0~3% (Figure 5-4 (c) and (d)). The strain rate of tensile simulation is $2 \times 10^{-4} \tau^{-1}$. Note that the calculated results are in the reduced (LJ) units, and are converted to numbers in real units using the values of M, ε and σ , following the rules of mapping expressed as:

$$\begin{aligned} T_g^{\text{real}} &= T_g^{\text{LJ}} \varepsilon / k_B, d^{\text{real}} = d^{\text{LJ}} M / d^3 \\ E^{\text{real}} &= E^{\text{LJ}} \varepsilon / d^3, \nu^{\text{real}} = \nu^{\text{LJ}} \end{aligned} \quad (5.6)$$

The objective function (Eq.(5.5)) can then be evaluated and used as criterion for update of local and/or global best known position of particle. The above described process repeats until a good set of parameters are found. The interaction among the MD engine (the LAMMPS software), post-processing of data to compute properties, and PSO algorithm is implemented by a code originally developed by Cui et al. for Li-Si system [153, 154], and modified to adapt to our problem. The iteration proceeds automatically.

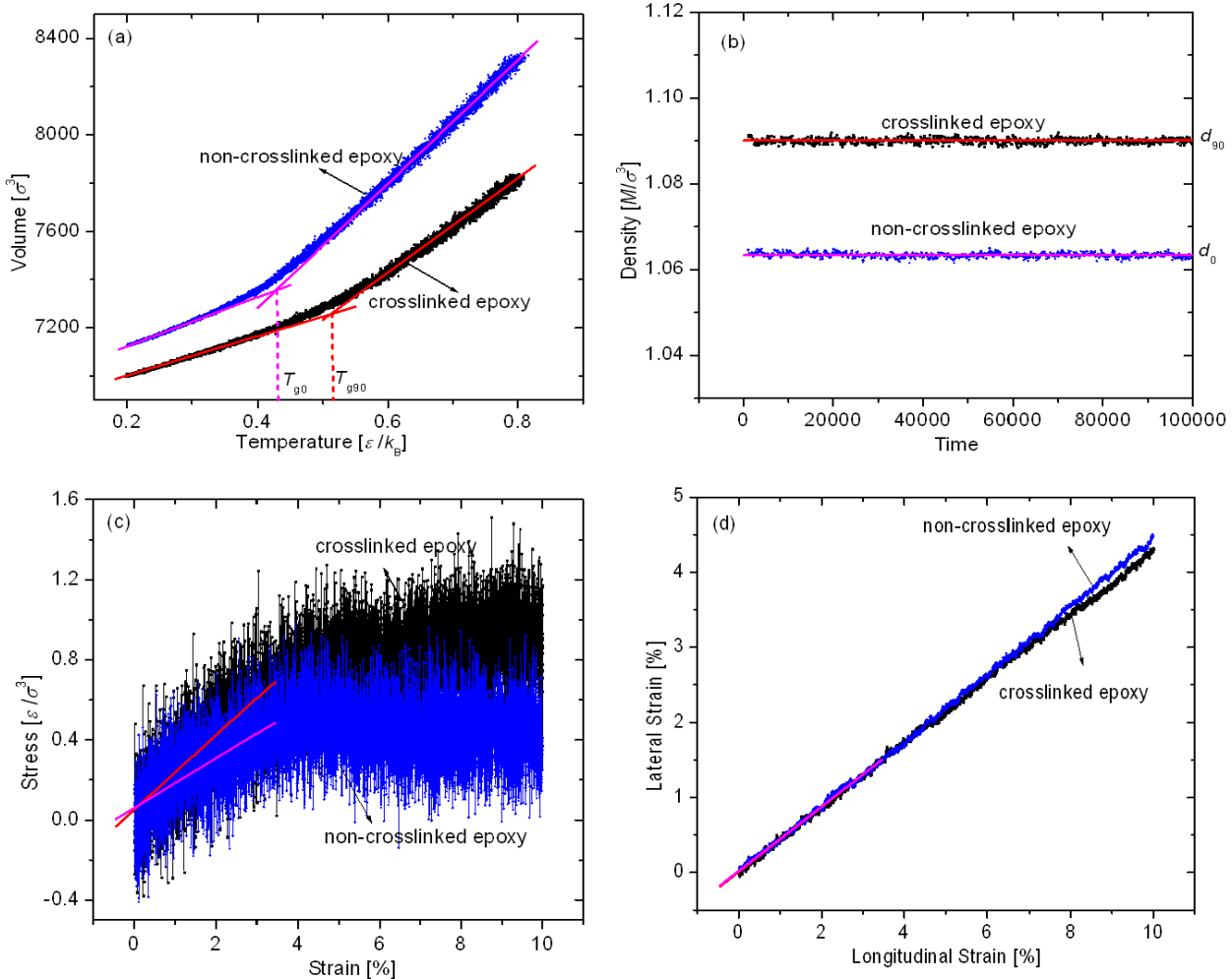


Figure 5-4. Demonstration of raw data from the phase of MD simulation in the optimization process and the derivation of material properties of the two systems (pre-cured and cross-linked with conversion of 90%): (a). T_g 's are obtained as the intersection of bi-linear functions used to fit volume versus temperature data; (b). Densities are obtained as the time averaged value over the time range [50,000~100,000]; (c). Elongation moduli are obtained as the slope of the linear function which fits the stress-strain data; (d). Poisson's ratios are obtained as the slope of the linear function fitting the lateral-longitudinal strain data.

Table 5-1 summarizes the range within which parameters are randomly initialized, and the values of the parameters obtained from the optimization process. In Table 5-2 we list the comparison between the properties calculated using the coarse-grained potential parameters and the all-atom MD simulation, along with the value of the objective function $f(\mathbf{x})$ (Eq.(5.5)). It should be pointed out that, for the current investigation, it is not practical to reach the global minimum within a reasonable amount of computation time. Thus we terminated the iteration process when the accumulated error (i.e. the objective function) was reduced to an acceptable level. Indeed a better solution is likely to be obtained if the optimization proceeds. However, since the current set of parameters is capable of generating target material properties in good agreement with atomistic force-field and simulation, we will accept it as the parameters for our coarse-grained model and apply the model for subsequent MD study of material properties as well as structure-property correlation.

Table 5-1. The lower and upper guess of the parameters and their optimized values (r_c is given as in the unit of σ . $k_\theta^{(1)}$, $k_\theta^{(2)}$ and $k_\theta^{(3)}$ are given in the unit of ε/rad^2)

	M (g/mol)	ε (kcal/mol)	σ (Å)	r_c (σ)	$k_\theta^{(1)}$ (ε/rad^2)	$k_\theta^{(2)}$ (ε/rad^2)	$k_\theta^{(3)}$ (ε/rad^2)
<i>Min</i>	50.0	1.50	4.0	1.25	0.2	1.25	1.6
<i>Max</i>	65.0	1.75	5.0	1.4	0.5	1.70	2.0
Optimized value	55.565	1.519	4.383	1.343	0.403	1.577	1.908

Table 5-2. Comparison between material properties calculated by coarse-grained and all-atom MD simulations (Superscript “(90)” stands for 90% cross-linked epoxy. Superscript “(0)” stands

for the non-cross-linked epoxy. Units for temperature, density, and modulus are Kelvin (K),

g/cm³ and GPa, respectively)

	$T_g^{(90)}$	$T_g^{(0)}$	$d^{(90)}$	$d^{(0)}$	$E^{(90)}$	$E^{(0)}$	$\nu^{(90)}$	$\nu^{(0)}$	$f(\mathbf{x})$
All-atom MD results	404	304	1.172	1.111	2.517	1.836	0.375	0.382	0.0216
CG MD results	402.8	317.6	1.183	1.156	2.489	1.868	0.412	0.416	

5.4 Results and Discussions

The coarse-grained potential parameters shown in Table 5-1 were applied to a system with edge length of ~152Å and 45689 beads, to conduct production MD runs for the investigation of thermo-mechanical properties and their correlations to degree of cross-linking. The pre-cured system containing fluidic mixture of monomers were dynamically cross-linked following the similar routine described in section 5.2.3. It was first equilibrated under constant pressure ensemble at the temperature of 610K for 10^6 steps with timestep of 5fs. During the subsequent one-million-step NPT simulation, bonds form conditionally with a probability of 0.01 between reactive beads on EPN and BPA monomers, provided they are within the bond-formation-cutoff of 5.7Å. The dynamic cross-linking process proceeded until the conversion of 90% was reached. Along the MD generated trajectory, structures with conversions of 25%, 50% and 75% were picked up for conversion-property relationship studies.

5.4.1 Glass Transition

The cross-linked epoxy molding compound was further equilibrated under NPT ensemble at high temperature (610K) before cooling simulation initiates. The MD cooling process decreases the temperature continuously from 610K to 150K within 4,000,000 steps. In Figure 5-5 we plot the specific volume versus temperature relationship for 90%, 50% and 0% cross-linked epoxies (other two conversions are not shown here). The black-square curve depicts the volume versus temperature relationship for the 90% cured system. T_g 's for the 90% and 0% cross-linked systems are identified as 401K and 312K, respectively, as the intersections of the bi-linear functions used to fit the data. Their good agreements with all-atomistic simulation results are expected since the optimization process took them into account. Between the two ends, the glass transition temperature indicates its trend of right-shifting, with the T_g –conversion correlation being shown in Figure 5-6. Note that the error bar is associated with different choices of temperature ranges while doing bi-linear regression. Compared to our previous all-atomistic studies, the coarse-grained MD predicts very close T_g –conversion relationship. This shows that our coarse-grained model and potential can correctly capture the property transition with the progress of cross-linking.

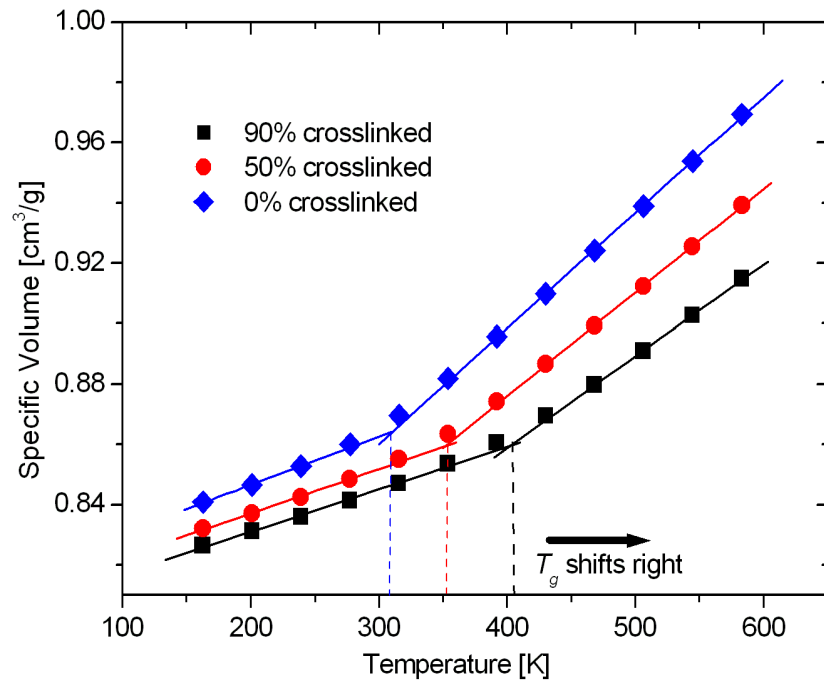


Figure 5-5. Specific volume versus temperature relationships for systems with different conversions using the optimized coarse-grained potential parameters

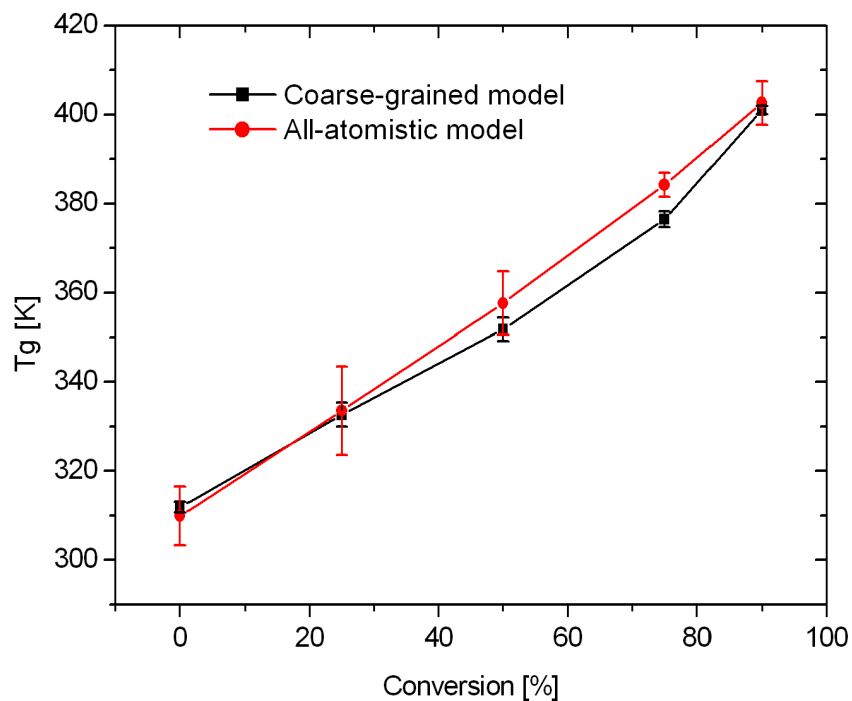


Figure 5-6. Glass transition temperature versus conversion relationships obtained from coarse-grained and all-atomistic simulations [140].

5.4.2 Elastic Constants

The elastic constants and their temperature as well as structural dependence based on the coarse-grained model and potential were investigated by the fluctuation method. The fluctuation formula gives stiffness matrix as [155, 156]:

$$C_{ijkl} = \langle \sigma_{ij} \varepsilon_{mn} \rangle \langle \varepsilon_{mn} \varepsilon_{kl} \rangle^{-1} \quad (5.7)$$

where σ_{ij} and ε_{ij} are the virial stress and strain tensors given by:

$$\sigma_{ij} = \frac{1}{V} \left[\sum_{\alpha} m_{\alpha} (v_{\alpha})_i (v_{\alpha})_j - \sum_{\beta > \alpha} \frac{\partial U}{\partial r_{\alpha\beta}} \frac{(r_{\alpha\beta})_i (r_{\alpha\beta})_j}{r_{\alpha\beta}} \right] \quad (5.8)$$

$$\varepsilon_{ij} = \frac{1}{2} \left[\langle h \rangle_{ik}^{-T} h_{kl}^T h_{lm} \langle h \rangle_{mj}^{-1} - \delta_{ij} \right] \quad (5.9)$$

In Eq. (5.8), subscripts α and β stand for α th and β th atoms. m , v , r and U are atomic mass, velocity, distance and system's potential energy. In Eq. (5.9) \mathbf{h} is the scaling matrix $\mathbf{h} = \{\mathbf{a}, \mathbf{b}, \mathbf{c}\}$ with \mathbf{a} , \mathbf{b} and \mathbf{c} being the basis vectors of the simulation cell.

In order to correctly calculate values of stiffness matrix and the elastic constants, the linear elastic assumption needs to be satisfied. That means the strains and their fluctuations should be sufficiently small. Nevertheless, it is well known that polymers become very soft when temperature goes above T_g since the material transits into rubbery phase. In MD simulations, strain tensor components go wild thus the elastic properties are not accurately obtainable. To solve this problem, we would like to adopt the elastic bath method to constraint the material in

the linear elastic state. The method immerses the MD simulation cell into an elastic bath with proper modulus. The system's Hamiltonian then can be formulated as [155]:

$$H = \sum_{\alpha} \frac{\vec{p}_{\alpha}^T G^{-1} \vec{p}_{\alpha}}{2m_{\alpha}} + U(\vec{q}, G) + \frac{1}{2} \langle V \rangle C_{ijkl}^b \varepsilon_{ij} \varepsilon_{kl} \quad (5.10)$$

The combined stiffness matrix is:

$$C_{ijkl}^t = \left\langle \left(\sigma_{ij} + C_{ijkl}^b \varepsilon_{kl} \right) \varepsilon_{mn} \right\rangle \left\langle \varepsilon_{mn} \varepsilon_{kl} \right\rangle^{-1} = \left\langle \sigma_{ij} \varepsilon_{mn} \right\rangle \left\langle \varepsilon_{mn} \varepsilon_{kl} \right\rangle^{-1} + C_{ijkl}^b \quad (5.11)$$

Therefore the real stiffness matrix is:

$$C_{ijkl} = \left\langle \sigma_{ij} \varepsilon_{mn} \right\rangle \left\langle \varepsilon_{mn} \varepsilon_{kl} \right\rangle^{-1} = C_{ijkl}^t - C_{ijkl}^b \quad (5.12)$$

where C_{ijkl}^t and C_{ijkl}^b are the total and elastic bath's stiffness matrix, respectively. In Voigt notation, an isotropic elastic bath can be described by its Lamé constants λ^b and μ^b ,

$$C_{11}^b = \lambda^b + 2\mu^b, C_{12}^b = \lambda^b, C_{44}^b = \mu^b \quad (5.13)$$

which can be arbitrarily chosen and even can be un-physical, e.g., negative, values, to ensure strains are small.

To implement the fluctuation method, NPT simulation using Nose-Hoover thermostat and Parrinello-Rahman baro-stat, which allow all 6 degrees of freedom of the simulation box to be independently adjusted, was conducted for 5×10^8 steps. The stress and strain tensor components were extracted from the MD run every 100 steps. At temperatures lower than 400K (T_g) the elastic bath method was not invoked, since the material is still glassy and strain was sufficiently small without additional constraints. At 400K and higher temperatures, elastic bath is added to ensure all strain components less than 1%. Figure 5-7 (a) and (b) plot the variation of moduli and Poisson's ratio with temperature for the 90% cross-linked epoxy model.

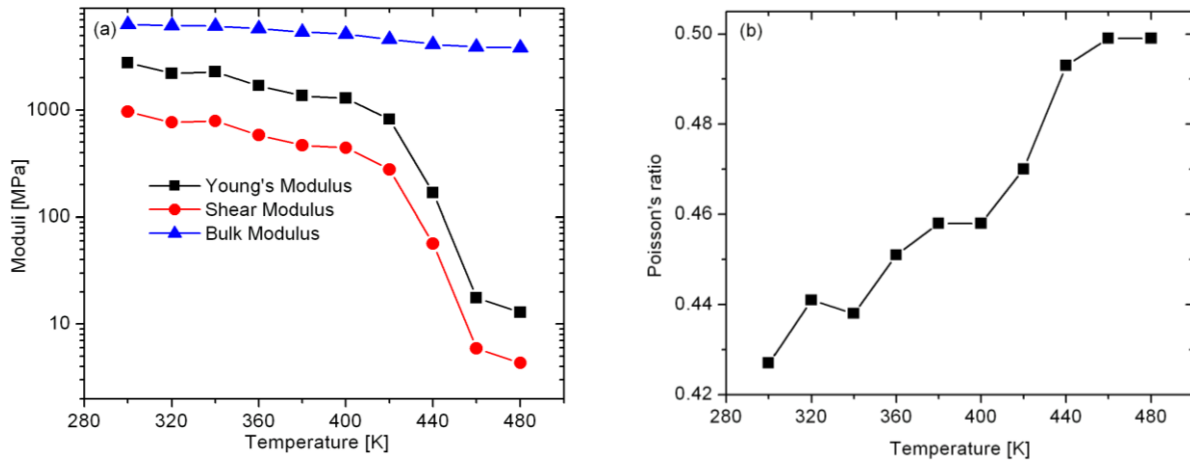


Figure 5-7. (a) Moduli and (b) Poisson's ratio versus temperature relationships for the 90% cross-linked epoxy using coarse-grained model and potential

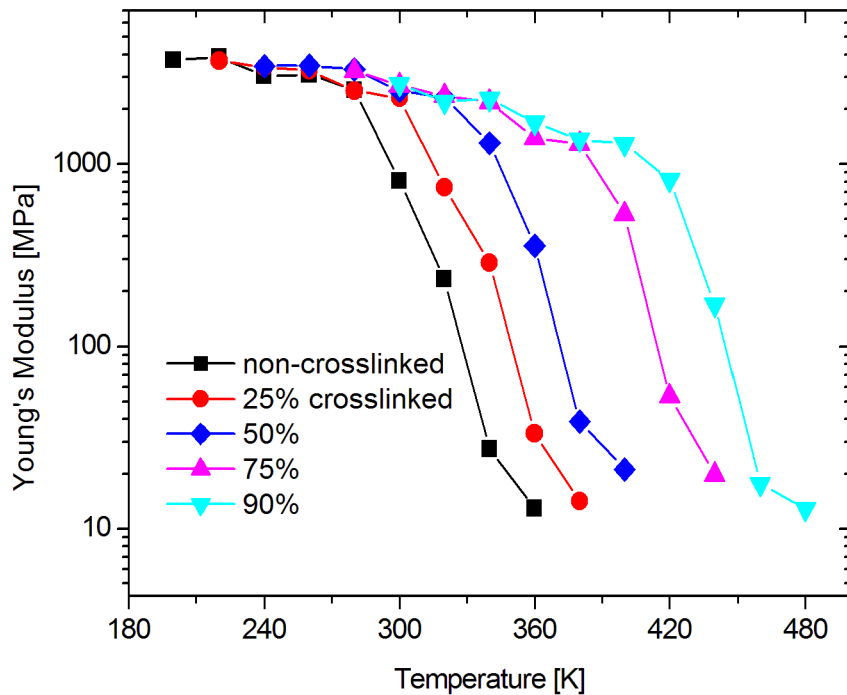


Figure 5-8. Young's modulus versus temperature relationships for epoxies with different conversion rates.

From Figure 5-7 one is able to observe the transition of moduli and Poisson's ratio around the glass transition temperature. Unlike the bulk modulus which stays above the GPa

level even at temperatures much higher than T_g , the Young's and shear moduli show drastic drop of two orders of magnitude starting from approximately 420K, indicating significant softening of the epoxy molding compound in its rubbery state. At the meantime, the Poisson's ratio rises up to approach to 0.5. At the highest two temperatures simulated (460 and 480K), the Poisson's ratio falls in the range of 0.49~0.5, which is typical value for rubbery-state thermosetting polymers. Compared to experiment results in which the Young's modulus drops at 400K, the transition temperature of Young's modulus is somewhat higher from MD prediction. The reason is still unclear and we would like to investigate in the future work. However, our MD simulation methodology is able to qualitatively reveal the elastic properties' dependence on temperature.

The temperature dependence of elastic properties was also investigated for epoxies with other conversion rates, to reveal the structural-property correlation. In Figure 5-8 we plot these dependencies, specifically the Young's modulus (E) versus temperature relationships. For all conversions investigated, a similar transitioning behavior of modulus was observed: E drops two orders of magnitude before and after T_g . A clear trend is the right shifting of the transition temperature of modulus. These temperatures are roughly consistent with the glass transition temperatures extracted from MD simulation of cooling (section 5.4.1). This further validated our coarse-grained model in terms of its capability to reproduce the correct thermo-mechanical properties for epoxies with a wide range of crosslink density.

5.4.3 Deformation and Failure Behavior of Bulk Epoxy

To investigate the deformation and failure behavior of the epoxy molding compound, CGMD simulations of uniaxial tension were conducted. For these simulations, we used a bigger simulation cell consisting 209,304 beads. The cubic cell measures 253Å in each direction. To

simulate uniaxial tension, the cell was stretched along one direction, while the pressure on the other two perpendicular directions was kept zero. Three different strain rates were used, $10^8/s$, $5 \times 10^8/s$, and $10^9/s$.

The simulated uniaxial stress-strain curves are presented in Figure 5-9. It is seen that the general behavior of the stress-strain curves is similar under different loading rates. They all show four distinct stages. In the first stage, the stress is almost linearly related to the strain up to the point of yielding, which will be called the yield strength. We see that the yield strength varies from 94MPa to 147MPa when the strain rate increases from $10^8/s$ to $10^9/s$. From yielding to about 50% strain is the second stage, where the material undergoes a slight strain-softening. The primary mechanism for such a phenomenon is the relaxation of polymer conformations as well as the reorientation of polymer strands, both intrinsically sluggish processes. During this stage, the polymer strands seek a more energetically favorable configuration in the conformational space that results in a softening behavior [157]. Following the strain-softening is the third stage, where the material experiences strain hardening. The hardening process is accompanied by orientating the polymer network strands along the loading direction. Strands are successively pulled taut and stress rises sharply until the ultimate strength is reached. In the fourth and final stage, the stress drops to zero almost instantaneously, indicating a brittle like failure.

To better understand mechanisms behind the stress-strain behavior, we show in Figure 5-10 the fraction of broken bonds (out of originally 217,457 bonds). It is clear that most of the bonds remain intact until the strain is more than 150%. Since the stress only experiences mild hardening before this strain, one may conclude that the deformation over this strain range is

mainly due to reorientation of polymer strands from their initial coiled state to a more linear state. After about 200% strain, bonds start to break as the deformation increases. The number of bonds rupture is almost linearly proportional to the strain, see Figure 5-10. In conjunction with the near liner stress-strain relationship in the third stage of the uniaxial tension shown in Figure 5-9, one may conclude that the load is primarily carried by the stretching of the bonds.

In addition, since the bond “strength” between two beads is characterized by the maximum distance between the beads, the linear relationship between the number of bond ruptures and the applied strain means that the polymer strands continue to realign themselves as the strain increases so that more and more bonds are reaching their “strength”. To illustrate the realignment of the polymer strands, snapshots of deformed configurations, with beads colored by virial stress along the loading direction, are presented in Figure 5-11. In the leftmost snapshot, some of the highly aligned polymer strands are seen as those chains with colors corresponding to the highest color-map scales. These strands experience large stress and are the most probable locations for bond ruptures. The accumulative bond rupture process will eventually lead to localization, as can be observed in the second snapshot of Figure 5-11. Roughly at the same strain, the epoxy reaches its strength. In this snapshot one can also find a bundle of deep colored, thus highly stressed, strands concentrated near the failure site. This stress concentration leads to rapid scission of a large number of strands near the failure surface. To quantify the localization, we plotted in Figure 5-12 the spatial distribution of percentage of broken bonds at different strain levels. It is seen that at lower strains, the bond rupture is almost uniformly distributed throughout the sample. As strain increases, localization occurs as more and more bond rupture happens at a single location ($z/L \approx 0.45$), while bond rupture ceases elsewhere. Comparison of

Figure 5-10 with Figure 5-12 shows that the rate of overall bond rapture remains almost constant in the strain range of 200% ~ 400%, but the increase occurs only locally near the failure surface.

The predicted ultimate failure strength is about 1GPa, which is an order of magnitude higher than experimentally measured strength of epoxy based thermosetting polymers. This discrepancy may come from several factors such as the pristine state of the CGMD sample (defect free), and the high strain rate used in the CGMD simulations. These drawbacks are intrinsic to such fine scale simulations. For example, Gall et al. [39] reported the debonding strength of Al-Si bimaterial to be 20GPa, which much higher than the experimentally measured ultimate tensile strength (~200MPa) of cast Al-Si alloy [138, 139]. In the work by Panico et al. [158] the authors also predicted very high ultimate strength for cross-linked polymers, $\sim 5.5 \frac{\varepsilon}{\sigma^3}$ in the LJ unit. In the LJ unit, our simulated the strength is $8.5 \frac{\varepsilon}{\sigma^3}$, consistent with [158].

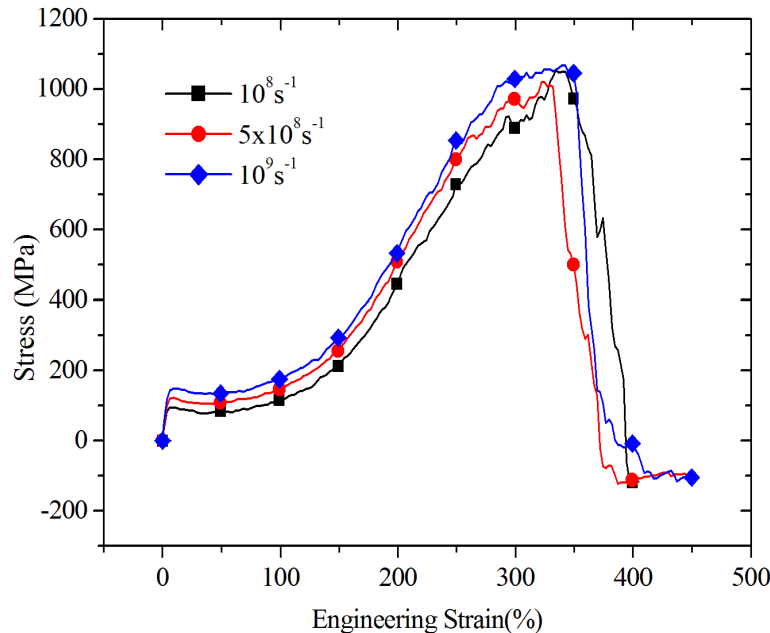


Figure 5-9. Stress-strain curves for the uni-axial tensile simulation using different strain rates.

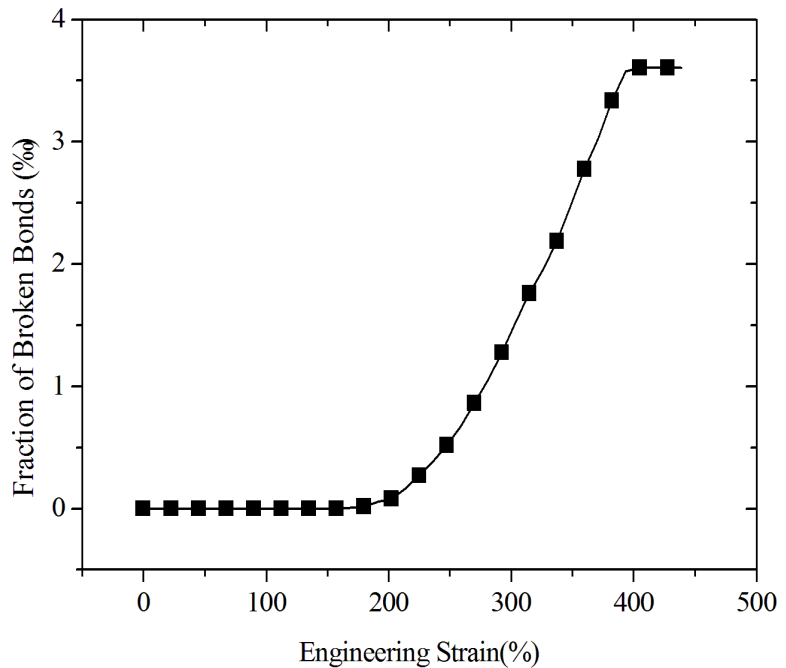


Figure 5-10. Number fraction of broken bonds versus strain

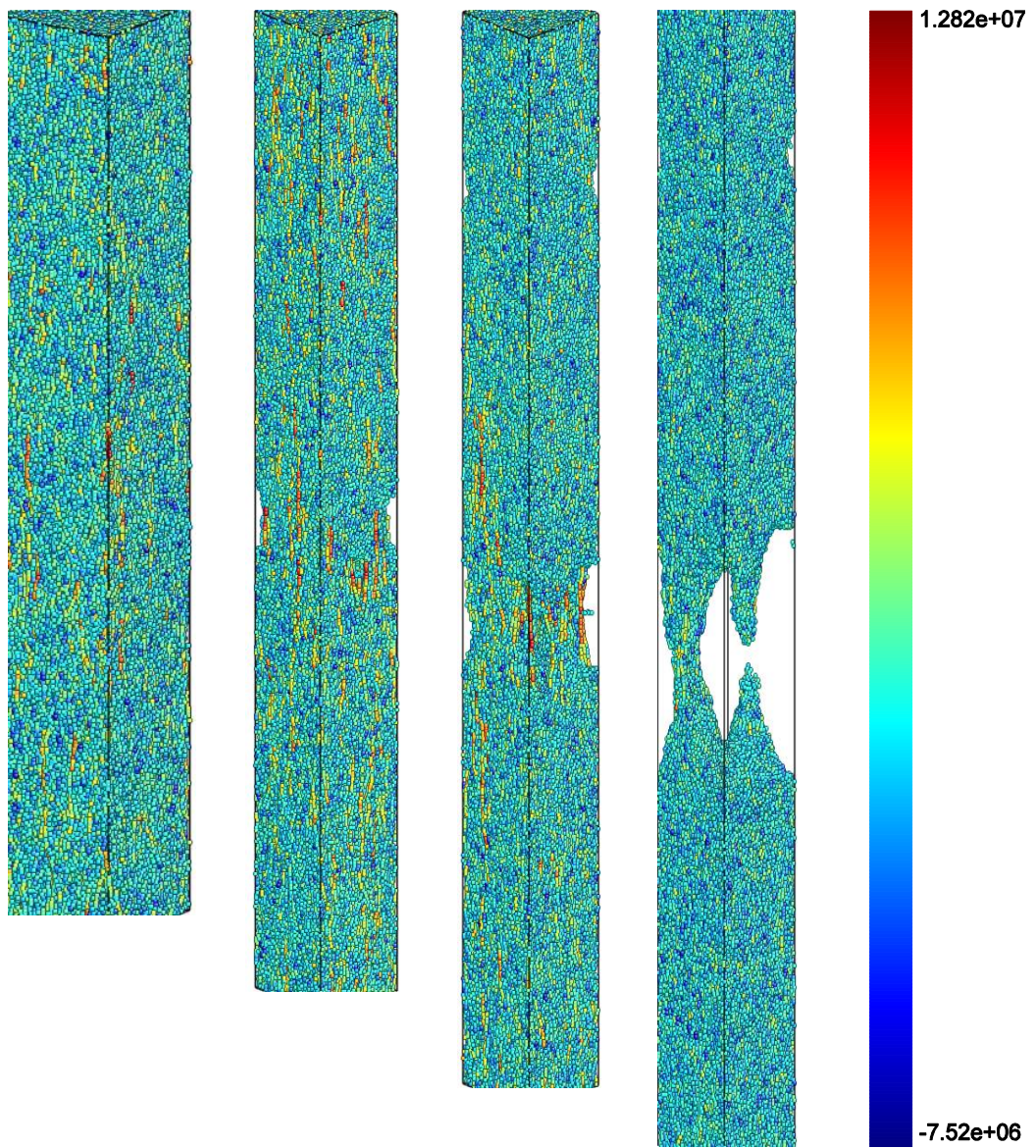


Figure 5-11. Snapshots of deformed configurations during the uniaxial tension for strains of (from left to right): 259%, 348%, 372% and 394%. Beads are colored according to their virial stress along the loading direction. The color bar is shown right to the last snapshot.

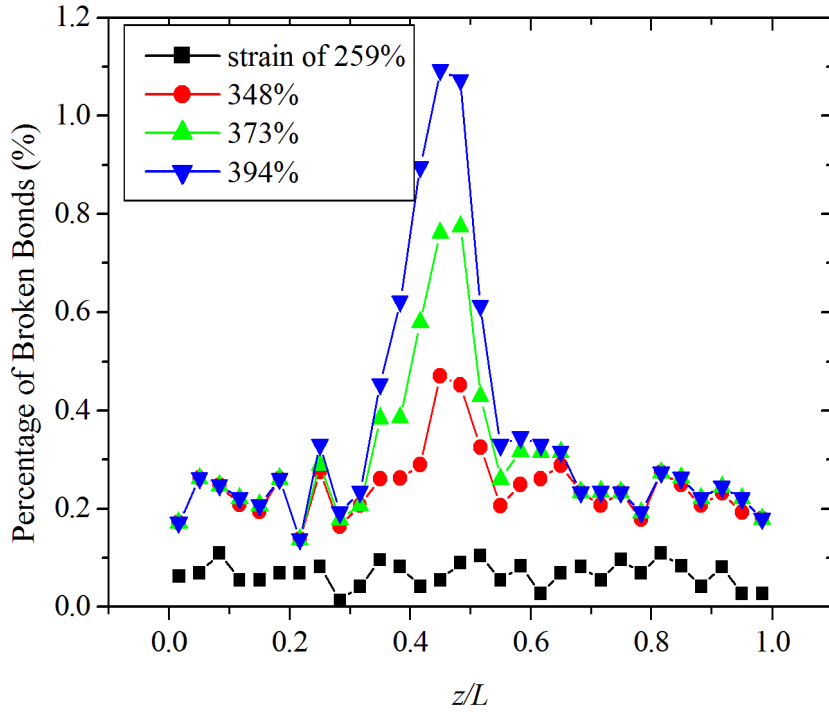


Figure 5-12. Spatial distribution of percentage of broken bonds at different strain levels.

5.5 Summary of This Chapter

In this chapter, we developed a coarse-grained model for an epoxy molding compound. The coarse-grained model is based on a bead-spring representation of the constitutive monomers of the epoxy system. The interactions between beads are represented by the inter-bead potentials consisting of a Lennard-Jones potential, a quartic function to capture bond stretch and strength, and harmonic functions to describe angle bonds. By using the particle swarm optimization technique, parameters in the inter-bead potential function were optimized through fitting certain key thermo-mechanical properties calculated from our previous atomistic MD studies. We demonstrated that the newly developed coarse-grained model is able to reproduce, in good agreement with atomic MD results, density, glass transition temperature and elastic constants, as well as these properties' temperature and structural dependence.

One significant advantage of the newly developed coarse-grain model is its ability to simulate bond breakage, which enables the simulation of polymer failure. No inter-atomic potential is currently available in the open literature that is capable of predicting failure of polymer materials. Taking advantage of the new capabilities, we simulated the uniaxial tension behavior of the epoxy compound. We found that, under the uniaxial stress condition, the polymer network experiences continuous orientation and scission of epoxy network strands, which eventually leads to localization of bond rupture and failure.

Finally, it is important to point out that the coarse-grain model significantly speeds up the simulation and allows us to simulate material size that is not feasible in conventional MD simulations. For example, for a simulation box of $250 \times 250 \times 250 \text{\AA}^3$, it takes our CG model about one minute of CPU time on a cluster of 108 Intel processors for each 10^4 time steps. On the other hand, even for a much smaller simulation box of $100 \times 100 \times 100 \text{\AA}^3$, it would take a conventional MD model more than 20 minutes of CPU to do the same.

CHAPTER 6 APPLYING LARGE SCALE CGMD TO STUDY BULK EPOXY FRACTURE

In this chapter, we used the coarse-grained (CG) model developed in Chapter 5 in large scale ($\sim 85 \times 85 \times 85 \text{ nm}^3$) Molecular Dynamics (MD) simulation of uniaxial-strain deformation to study the tensile failure mechanisms. Under the applied loading conditions, the material is found to exhibit cavity nucleation and growth, followed by stretching of the ligments separated by the cavities, until the ultimate failure through ligment scissions. However, the phenomenon of crazing as is typically observed for glassy thermoplastic polymers, does not set in, since chain entanglement/disentanglement is irrelevant in epoxy's chemically cross-linked polymer network. We detailedly discussed the size and microstructure of the cavities, the stress distribution and breakdown of the ligments. By comparing to other modeling investigations on glassy thermoplastics, our findings provide an interpretation of the relative brittleness of thermosets. Also, the simulated material behavior is related to the localized large deformation mechanisms observed for epoxy based thermosets in several experimental investigations.

6.1 Introduction

Epoxy based thermosets have shown superior mechanical and thermal properties and thus have found numerous applications as adhesives, molding compounds and composite matrices in such industries as electronic packaging, automotive manufacturing and aerospace. Nevertheless, fracture of epoxies has long been an issue of controversy. Despite of their macroscopically brittle behavior, there have been evidences of localized plastic deformation mechanisms in literatures for epoxy based thermosets. Morgan et al. [132] observed that epoxy films deform and fail by a crazing process, the predominant toughening mechanism in thermoplastics such as polystyrene.

Crazing phenomenon was also reported for a high-performance resin (AB-BCB-MI) [159, 160].

Similar to crazing but lacking the distinct fibrils, dilatation bands were found to form within a series of moderately cross-linked thermosets, and enhancable by toughening particles [133, 160]. Still, there lacks comprehensive understandings regarding the conditions and mechanisms of the initiation, growth and eventual failure of these localized plastic deformations. After all, direct tracking and measuring these sub-micron physical processes are extremely difficult, if not impossible.

Molecular Dynamics (MD) simulation has been demonstrated for its success in capturing the mechanical behaviors of polymers. For instance, yielding [161, 162] and strain hardening [163, 164] have been investigated for amorphous polymer glasses using the coarse-grained models. In a few other studies the authors examined the nucleation, growth, microstructure and failure of crazes formed in glassy thermoplastics [165, 166], and obtained fracture related properties based on MD simulation results [165]. Unlike thermoplastic polymers which have been extensively explored, the attention attracted by thermosets is limited, partially due to the complexity associated with modeling the chemically cross-linked network structure inherent to this type of materials. Highly cross-linked polymer networks were studied for their interfacial fracture versus solid substrate based on MD simulation with coarse-grained model [4, 122, 167]. The effect of monomer functionality, degree of curing and interfacial bond density was examined. However, these works focused on debonding of polymer networks from confining walls rather than the fracture within the bulk material. The detailed microstructure of the large plastic deformation was not carefully analyzed. Panico et al. [158] simulated the tensile failure of glassy polymers and discussed the distinction of mechanical behavior between thermoplastics

and thermosets, and concluded that chemical cross-linking embrittled polymer. None of the above investigations has physical dimension in their models, thus provides critical quantitative information, e.g., length scale and stress magnitude.

Using the coarse-grained model developed specifically for the epoxy molding compound of our interest, we will demonstrate in this chapter a large scale MD simulation to capture how thermosetting polymers fracture. As is shown in Figure 6-1, images of crazes and dilatation bands from experiments [132, 133, 159, 160] indicate that in epoxies, these localized plastic deformations occur with the width of a few microns or lower (several hundred nanometers) and length of tens microns. While including the entire crack tip is not realistic, the current MD model is approaching the length scale of crack opening and can be considered to serve as a representative volume to study cavity nucleation/growth and ligament scission. The rest of this chapter is organized as follows. In section 6.2 we describe the molecular model and the methodology of conducting non-equilibrium MD simulation. The results of the simulation are presented in section 6.3, with the correspondence between the stress-strain curve and the sequence of molecular deformation being given, and the micro-structure of the plastic deformation being thoroughly analyzed.

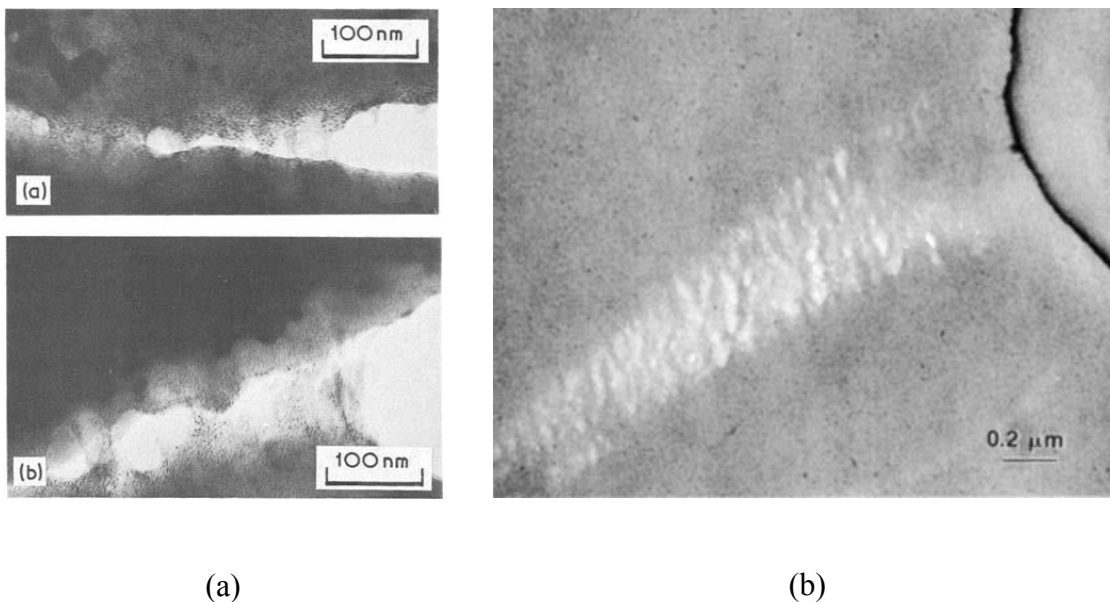


Figure 6-1. (a) Carbon-platinum surface replicas of craze structure in DGEBA-DETA epoxy films that were strained on metal substrate [132]; (b) TEM micrograph of dilatation bands of CTBN-modified DGEBA/piperidine taken inside the fatigue crack propagated damage zone [133]

6.2 Simulation Method

The coarse-grained model and potential (parameters) are the same as in Chapter 5. After reaching the conversion of 90%, which took typically 400,000~500,000 steps, the dynamic cross-linking process was followed by a quenching procedure from high curing temperature to 300K and additional one million steps of NPT simulation at 300K to reach the equilibrium density of 1.183 g/cm³. The simulation cell contains 7,834,220 beads, corresponding to its size of ~85×85×85nm³ at room temperature equilibrium.

The cross-linked and equilibrated polymer network was subjected to the tensile simulation with constrained lateral boundaries. The deformation was applied by elongating the

simulation cell along the loading axis with a strain rate of 10^8s^{-1} , while maintaining the temperature at 300K by using the Nose/Hoover thermo-stat coupled with SLLOD equation of motion [168]. This scheme of performing NVT MD simulation under non-equilibrium condition is accomplished by subtracting the each atom's position-dependent “stream velocity” to generate the thermo-velocity for temperature computing and adjusting, and has been built in LAMMPS [51]. The strain rate used is obviously much higher than that used in quasi-static loading in realistic laboratory tests. Therefore, results given in the remainder of this paper must be interpreted with this high strain rate in mind. This scheme of deformation provides a tri-axial stress state with strong dilatation component, and thus promotes cavity nucleation and growth. Indeed, crazes and dilatation bands are usually associated with high hydrostatic tensile stress components. Thus our simulated loading conditions are suitable.

6.3 Results and Discussions

6.3.1 Stress-strain Curve and Deformation Sequence

Figure 6-2 plots the stress strain curve. Upon reaching the yielding point, which is $\sim 298 \text{ MPa}$ at the strain of $\sim 7\%$, the material experiences a drastic relaxation of stress, down to $\sim 110 \text{ MPa}$. This is due to cavitation nucleation, shown in snapshot (a) in Figure 6-3. Note that beads are colored by their coordination number, defined as the number of one central bead's neighbors within the force-field (LJ potential) cut-off distance. This coloring scheme was adopted so as to visualize the cavities dispersed in a 3D cell. Those beads with colors corresponding to the highest color bar scales represent the undamaged matrix around the cavities, and beads with medium colors are on the boundaries of the cavities. Inside the cavities, one can

observe networks of strands connecting the inner walls, which are better illustrated in zoomed-in view of one specific cavity shown in Figure 6-4. Within the cavity the network strands have been converted from their initial closed-packed states to taut conformations. The taut network strands bear high stress and break upon further stretching, as will be discussed in detail later in this chapter.

The yielding and stress relaxation is followed by a relatively mild strain hardening process, extending to the strain of ~155%. This regime of the stress-strain behavior is accompanied by expansion of cavities. As is shown in Figure 6-3 (b), cavities grew both longitudinally and laterally. At the meantime, strands are continuously extended from their initial “zigzag” to linear configurations. After the entire simulation cell is converted to a network of ligments and cavities (snapshot (c) in Figure 6-3), the material experiences an even deeper strain hardening. During this process until the ultimate failure, the material deforms by pure stretch of the ligments. As will be presented in Section 6.3.4, most of strands have been pulled taut at this stage of deformation. What follows is rapid scission of a large amount of strands. Failure occurs at the stress of 206MPa and strain of 230%. From Figure 6-3 (d) to (e), failure is seen as breakdown of the ligments.

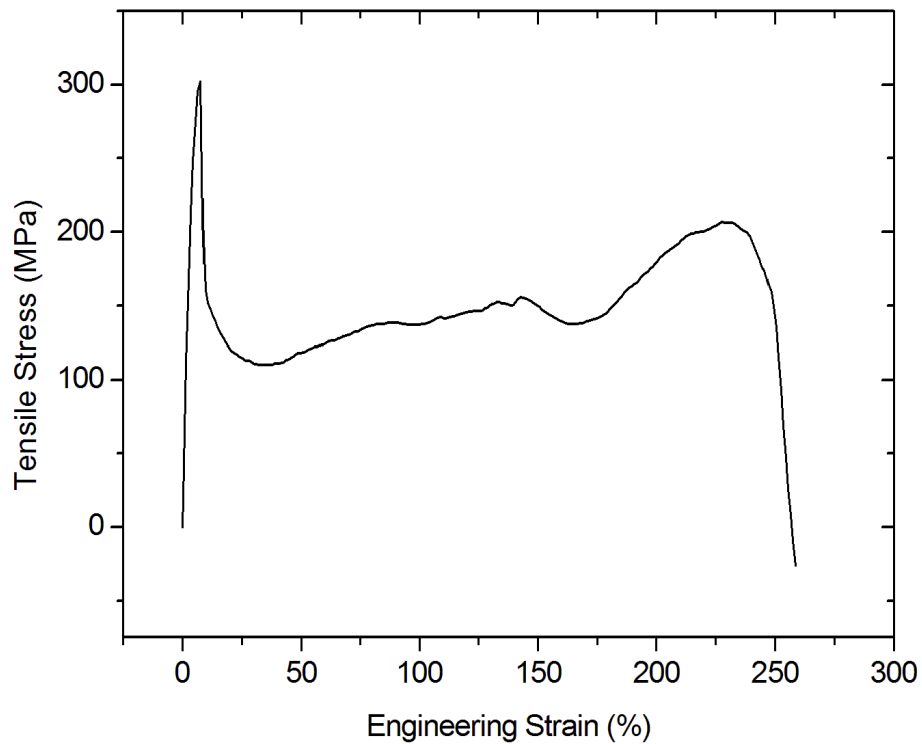


Figure 6-2. Stress-strain curve of the tensile deformations

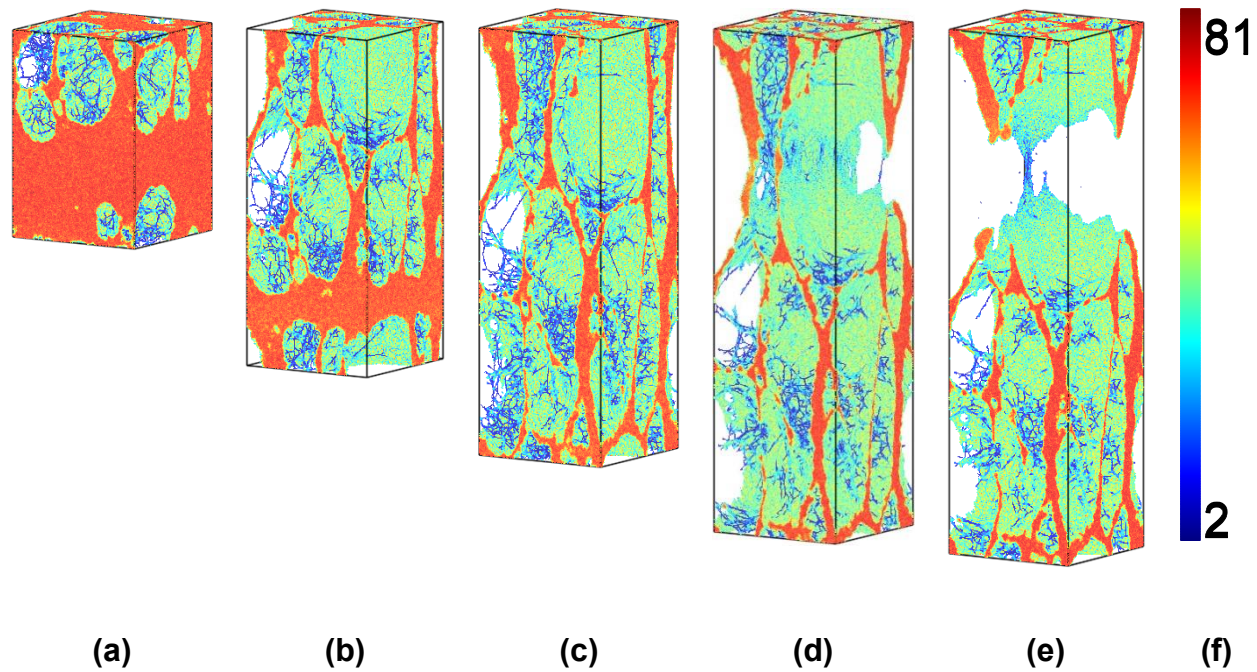


Figure 6-3. Snapshots of the deformation sequence. Strains are ((a) ~ (e)): 45%, 140%, 200%, 255% and 260%. (f) is the color bar. Snapshots are made by Atomeye [169].

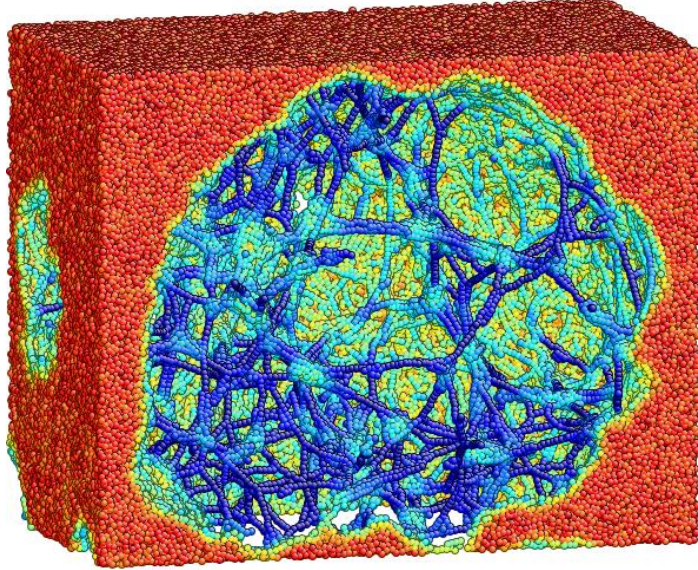


Figure 6-4. Zoomed-in view of one cavity from the configuration with strain of 45%. Beads are colored according to coordination number and the color map is the same as in Figure 6-3

6.3.2 Stress Criterion for Cavitation

In general glassy polymers yield through either shear yielding or cavitation/voiding. In our simulation the strong dilatation tensile stress component favors cavitation, while under other circumstances shear yield may occur. Thus it is desirable to investigate the stress criterion for both of the two yielding mechanisms. The pressure-modified von Mises yield criterion [170] is considered to be the most accurate shear yielding of polymers:

$$\tau_h^y = \tau_0 + \alpha p \quad (6.1)$$

where $\tau_h = \frac{1}{3} \sqrt{(\sigma_1 - \sigma_2)^2 + (\sigma_1 - \sigma_3)^2 + (\sigma_2 - \sigma_3)^2}$ is the octahedral shear stress with σ_i being the principal stresses. τ_0 and α are constants. Another way of interpreting this yielding criterion is to define a new octahedral shear stress, $\tau'_h = \tau_h - \alpha p$, so that Eq. (6.1) can be re-written as:

$$\tau'^y_h = \tau_0 \quad (6.2)$$

which is formally identical to the Mises yield criterion. Studies in [161, 166] found that for shear yielding and cavitation different values of the two constants hold. To study the criterion for our epoxy molding compound, several other loading conditions were conducted through MD simulation. Some of them are illustrated in Figure 6-5. For each of these loading conditions, tensile or compressive strain ε_i was applied to one or more axes following either the same rate as the rate used in section 6.3.1, or a fraction of the rate (e.g., the 4th loading condition illustrated in Figure 6-5). Along those directions that stress was controlled, the Nose-Hoover baro-stat was used to maintain the stress component at zero.

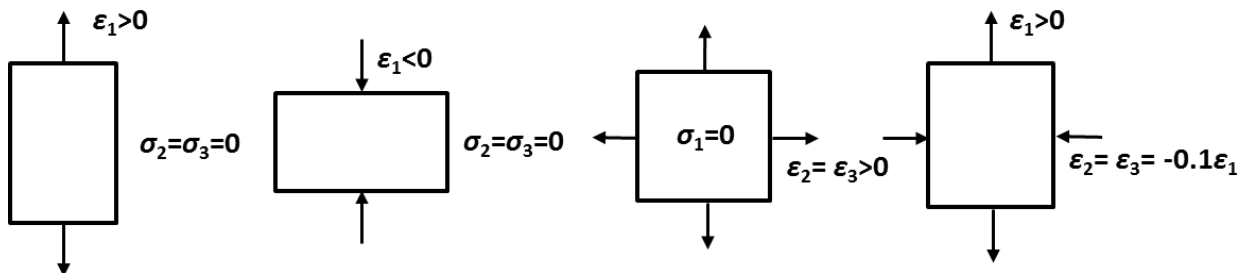


Figure 6-5. Some loading conditions for study of yield criterion

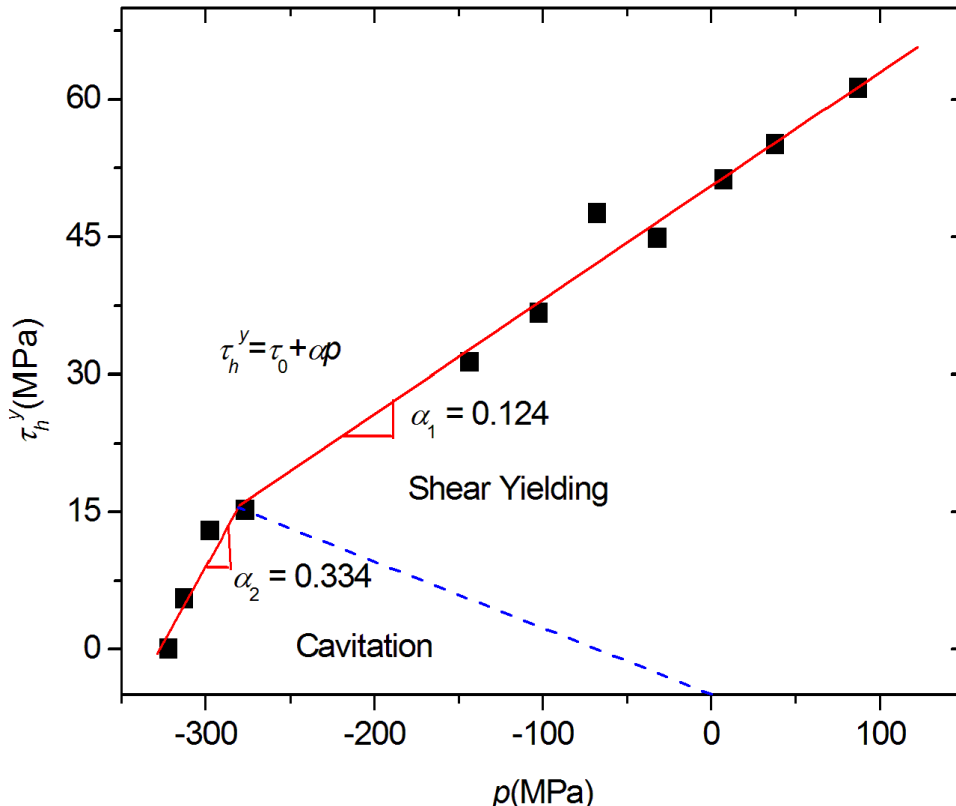


Figure 6-6. Relationship between the octahedral shear stress at yielding and the pressure

The octahedral shear stress and pressure at yielding for all the loading conditions were extracted from the stress-strain curves and Figure 6-6 presents the results. The choice of octahedral stress at yielding is worth discussing. In [161] the maximum octahedral shear stress was used. However, in our study it was found that for those loading conditions where cavitation sets in, cavitation does not occur at the maximum octahedral shear stress. Thus it was determined from the maximum of the individual tensile stress components, which were attained at the same strain. Figure 6-6 shows that the dependence of octahedral shear stress at yielding on pressure can be divided into two parts. Shear yielding was observed to the right of the dashed line, while to the left of the line, cavitation was seen as the yielding mechanism. The left most point corresponds to the loading condition in which the sample was elongated along three axes

isotropically, thus the octahedral stress is strictly zero. By fitting the data to linear functions, the value of α can be obtained and is shown in Figure 6-6 for both shear yielding and cavitation. Our results regarding α for shear yielding is in good agreement with the value reported in [161].

Albeit that Eq. (6.1) was originally proposed for shear yielding, our study and previous ones have shown that it can also serve as a stress criterion for cavitation, with the appropriate constants τ_0 and α being used.

6.3.3 Cavity Formation and Growth

An important aspect of the deformation and failure mechanism of the studied epoxy based thermoset is cavity nucleation/expansion. One may speculate that cavities appear at the locations where the epoxy has a less inter-connected network in its initial configuration. In order to find out whether the formation of cavities is related to the polymer network's topological structure, the spatial distribution of the cross-links was studied. The cross-links are defined as the beads having at least three strands reaching out and linking to other such beads in the cross-linked polymer network. The cross-links were found to be uniformly distributed in the simulation box, indicating that the cross-linked polymer network does not have inherent inhomogeneity that leads to cavitation upon loading. As a matter of fact, it was found that the tensile deformations using the same MD sample but starting with different equilibrium states result in different locations of cavity nucleation. However, the stress strain curve remains the same. This implies that the formation of cavities has a nature of randomness. However, different distributions of the cavity nucleating sites are statically similar, demonstrated by the same stress-strain behavior.

One piece of information of particular interest is the sizes of the cavities, as well as their evolution as the deformation proceeds. Since the cavities are usually not geometrically well defined, it is a formidable task to identify them and measure their volumes. To analyze cavity sizes, the simulation cell is decomposed according to Voronoi Tessellation. Upon this decomposition, each Voronoi cell contains a specific bead, as well as every point whose distance to that bead is less than or equal to its distance to any other beads. A cavity can be then identified as the cluster of those beads with Voronoi cell volume larger than a threshold volume. In Figure 6-7 such clusters are visualized and each cluster is a cavity. The cavity's volume can be calculated as:

$$V^{\text{cav}} = \sum_i V_i^{\text{voro}} \Big|_{V_i^{\text{voro}} > V_{\text{th}}^{\text{voro}}} \quad (6.3)$$

where $V_{\text{th}}^{\text{voro}}$ is the threshold Voronoi cell volume, and is determined such that the mass density of the cavity is less than 3% of the mass density of the surrounding matrix.

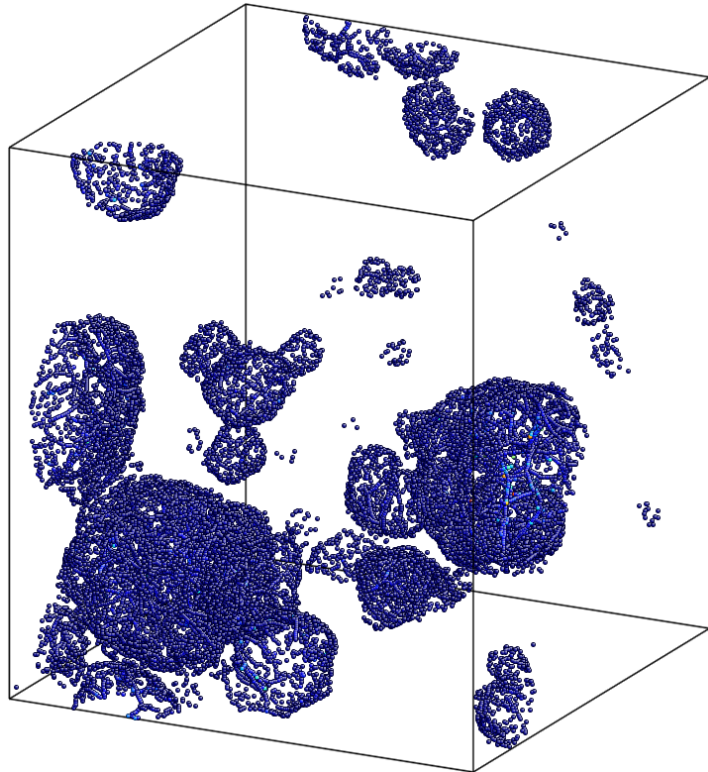


Figure 6-7. Visualization of clusters of beads with Voronoi cell volume larger than threshold volume. Beads are colored according to their Voronoi cell volumes.

Using the method described above, the cavities' sizes are measured for various deformed configurations. In the total volume of the cavities and its fraction over the simulation cell volume are plotted versus strain. It can be told from the plot that the total cavity volume increases linearly throughout the deformation process, and before the ultimate failure around 60% of the simulation box is occupied by cavities. Further investigation of the atomic configurations (not shown here) finds that the total cavity volume increases through: 1) expansion of the initially nucleated cavities, 2) formation of new cavities at various phases of the deformation.

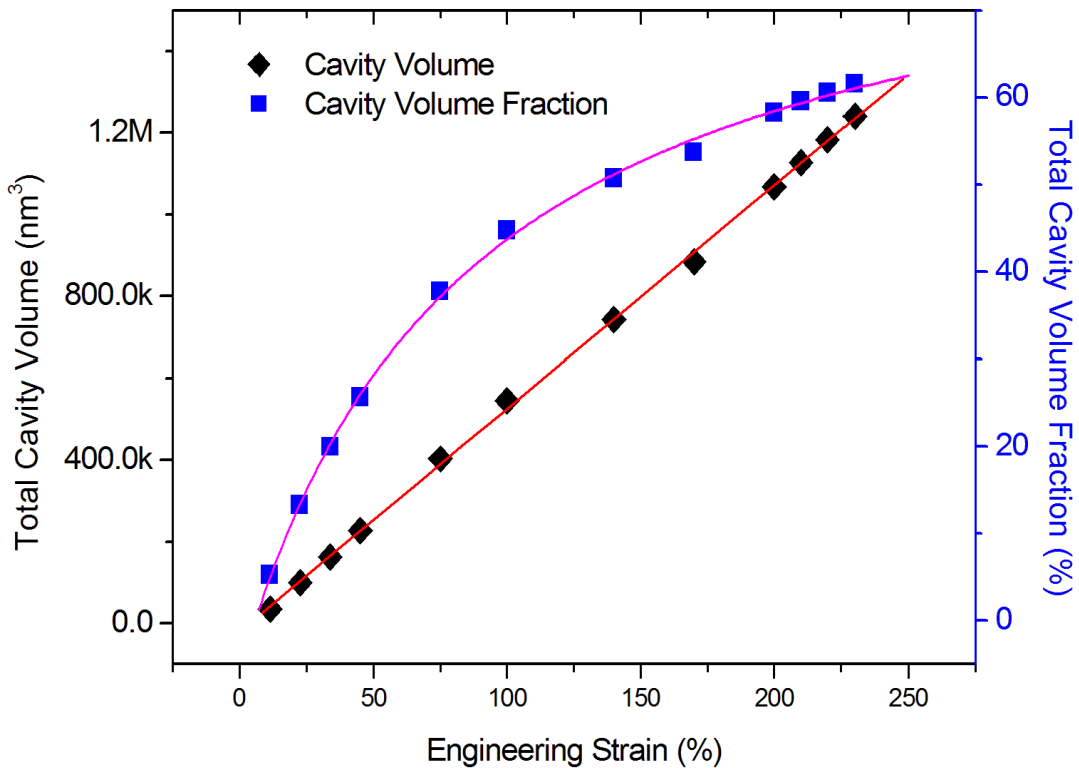


Figure 6-8. Total cavity volume and the fraction over the simulation cell volume, at different strains

6.3.4 Network Strand Scission

As mentioned in section 6.3.1, polymer network strands are continuously pulled taut and may break if bonds reach the cutoff length given by the potential. To quantitatively study this process, we measured the distances between cross-links linked by strands. Cross-links are defined as those beads having at least three strands reaching out and linking to other such beads in the cross-linked polymer work. In Figure 6-9 a pair of linked cross-links is shown. Here we define dr as the distance between the two cross-links, and $l = (N - 1)l_0$ as the length of the strands connecting them. Note that N and l_0 denote the number of beads on the strand and the equilibrium

bond length, respectively. In the initial configuration, N is either 7, 8 or 9, and may increase as the sample is deformed and some of the cross-links are no longer cross-links (due to bond breakage). Since strands are mostly coiled in the un-deformed configuration, dr is smaller than l , and approaches to l when strands are extended. Thus the ratio of dr over l , denoted here as ra , is a good measure of the degree to which strands are being pulled taut. The probability distribution of ra is studied for various deformed configurations and plotted in Figure 6-10. It is evident that ra is approaching to 1.0 as the overall strain increases. In the initial configuration, the peak of ra distribution is at ~ 0.47 . This peak right shifts and gets lower as deformation proceeds, and eventually vanishes. At the meantime, a second peak emerges at ~ 0.8 (45% strain) and shifts to ~ 0.9 (240% strain), with its height significantly increased. These trends clearly demonstrate that strands are continuously being converted from closed-packed to linear states.

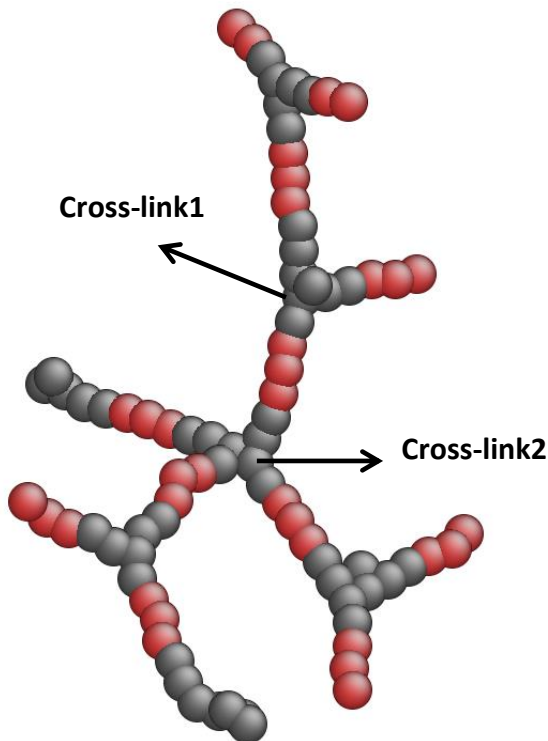


Figure 6-9. Illustration of one piece of cross-linked polymer network with linked two cross-links marked. Red beads are hardener molecule beads. Grey beads are epoxy molecule beads.

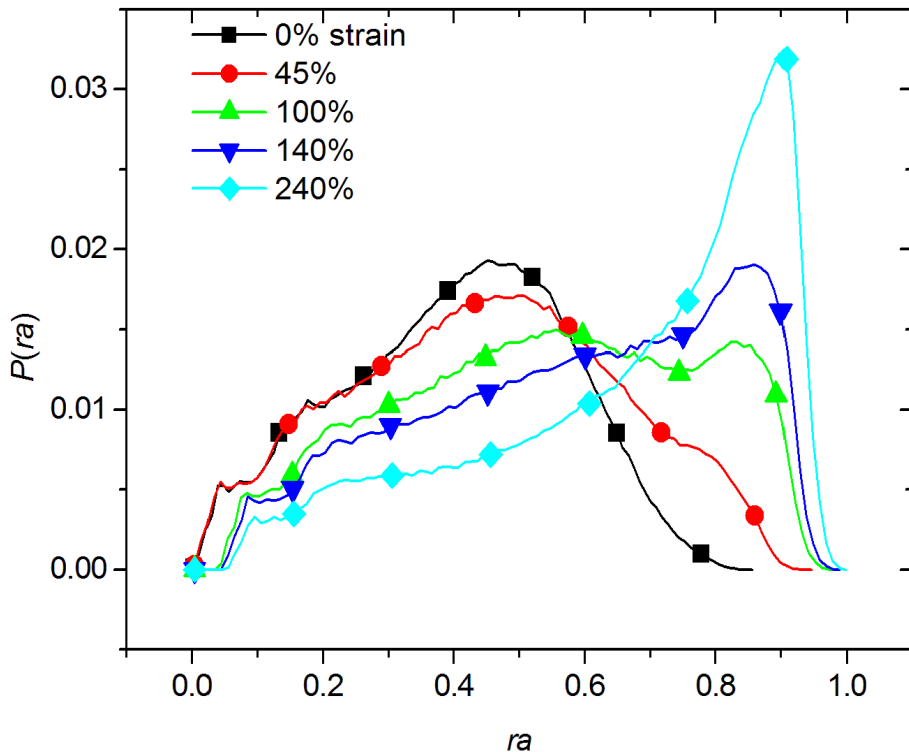


Figure 6-10. Probability distribution of ra for different deformed configuration

Covalent bond breakage occurs while strands are being pulled taut. Figure 6-11 plots the fraction of broken bonds (of the total ~ 8 million bonds) with respect to strain. It is evident from the plot that the rate of increase of the broken bonds shoots up after the strain of $\sim 150\%$. This finding is consistent with Figure 6-10 in that it is after most of strands are extended to taut configurations that the speed of bond breaking increases significantly. Also the strain of $\sim 150\%$ coincides with the starting point of the deep strain hardening regime of the stress-strain behavior, as mentioned in section 3.1, which indicates that the strain hardening is indeed accompanied by rapid scission of a large number of strands. Further investigation on stress distribution confirms this. In Figure 6-12 where beads are colored by their atomic stress along the loading direction, it

is seen that in snapshot (c) the chains bearing high stress can be found throughout the entire simulation box, while in (a) and (b) they are localized around the cavities. Therefore covalent bonds are expected to break much faster in the strain hardening process.

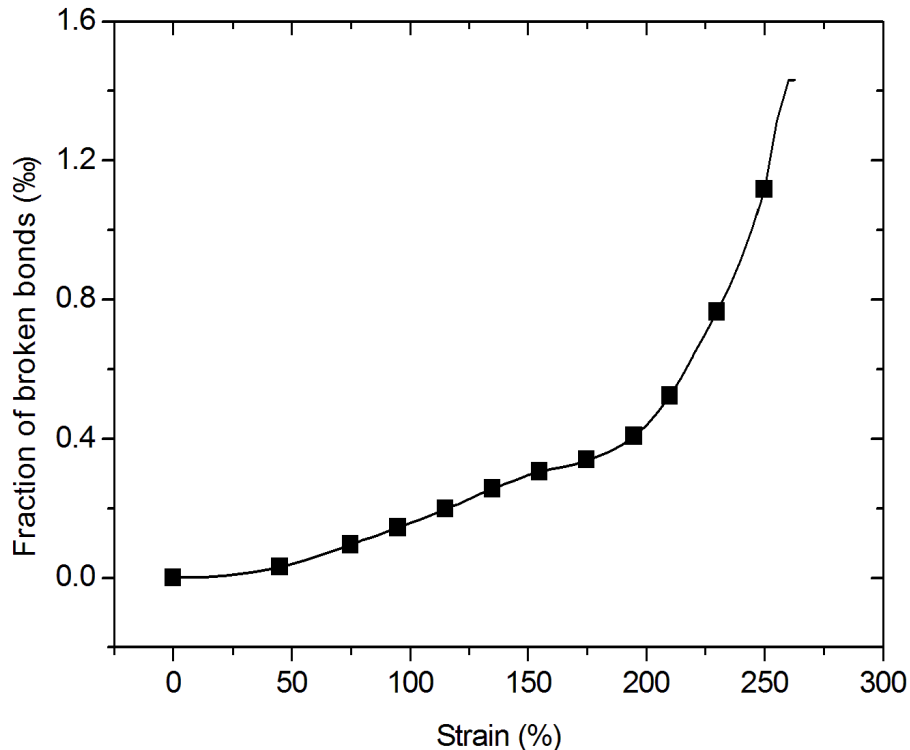


Figure 6-11. Fraction of broken bonds versus strain

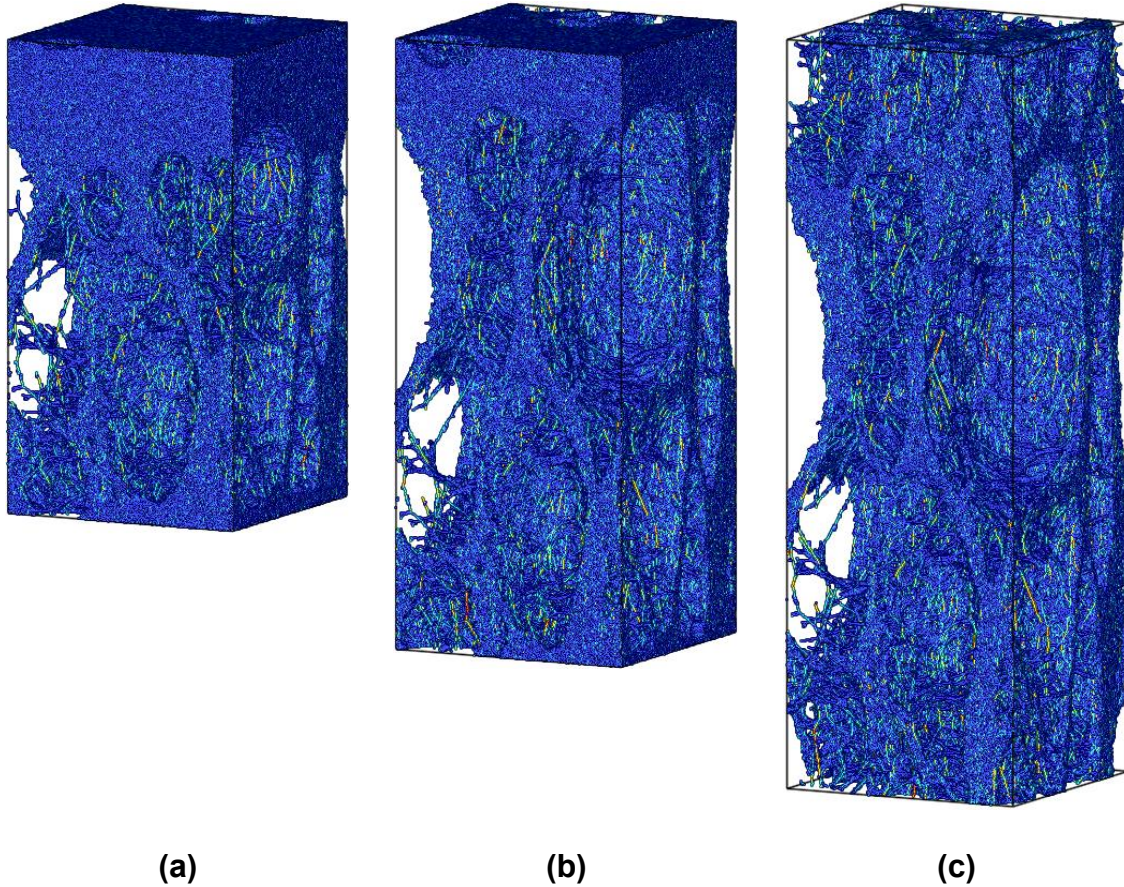


Figure 6-12. Atomic configurations with beads colored by their atomic stress along the loading direction. Corresponding strains are (a)~(c): 90%, 145% and 200%

6.3.5 Comparison to Thermoplastic Glassy Polymers

MD studies on thermoplastic glassy polymers [158, 166] reported similar phenomenon of cavitation, and accordingly, a drastic stress relaxation after yielding in the stress-strain behavior. Therefore, under high hydrostatic tensile stress, thermosets and thermoplastics both yield through cavitation. After the stress relaxation, for thermoplastic polymers stress stays on a plateau value, i.e., the “drawing stress”, and the range of this plateau regime, measured by the stretch ratio L_z / L_z^0 , is roughly 4 according to the results presented in [158, 166]. It has been well

understood that craze grows during this process, through void expansion and chain disentanglement. Stable crazes are characterized by a well-defined network of interconnecting voids and fibrils [158]. Although cavity growth also occurs during the post-yielding deformation process of the cross-linked thermosets, it's different than that of the thermoplastics in that stress increases. This is due to the continuous orientating and scission of rather short polymer network strands, as has been demonstrated in section 6.3.4 (Figure 6-10 and Figure 6-11). As can be seen from Figure 6-4, inside the cavities the network strands have been converted from their initial closed-packed states to taut conformations. Thus the further development of cavities involves more such transitions from coiled to linear states of strands.

In thermoplastics, crazes fails through disentanglement for shorter chains or chain scission for long chains ($N \geq 2N_e$) [166]. In thermosets neither of these two mechanisms plays a role. Instead, it is the scission of permanently cross-linked, much shorter chains, which occurs significantly more rapidly. In [166] the stretch ratio (L_z / L_z^0) required from the end of stress plateau to the ultimate failure is roughly 3, while in the current investigation it's less than 1.

Therefore, the highly cross-linked network structure of thermosetting polymers contributes to the more brittle mechanical behavior than thermoplastic polymers. Chemical cross-linking forbids chain disentanglement by which crazes stably thickens, and leads to faster breakage of chains thus earlier failure of the material.

6.3.6 Comparison to Experimental Observations

It has been found in experimental studies that in epoxies localized plastic deformations usually occur with the width of a few microns or lower (several hundred nanometers) and length

of tens of microns [132, 133, 159, 160]. The current MD model reaches a longitudinal dimension of ~300nm at full deformation, and is approaching to the crack opening displacement. Thus the MD simulated phenomenon can be understood as the behavior of a representative volume among the entire crack tip. In both crazes [132, 160] and dilatation bands [133, 160], it was observed that the crack tip consists parallel bands of coarse fibrils bridging the crack surfaces and cavities in between (see Figure 6-1). This resembles our simulated deformed configurations in which stretched ligaments are separated by cavities. The simulation results reveal the detailed micro-structure and quantitative aspects of the localized plastic deformation, including stretch ratio, strength and cavity volume fraction, which are not easily accessible through experiments. Therefore they provide valuable information in continuum mechanics based modeling of fracture of thermosetting polymers.

6.4 Summary of This Chapter

In the current investigation, a large scale MD simulation based on coarse-grained model was conducted to study the deformation/failure mechanisms of an epoxy molding compound. The coarse-grained potential was developed based on matching key thermo-mechanical properties of the epoxy molding compound. The crosslinked network structure of the epoxy was built by running a MD simulation of polymerization from the mixture of monomers. Major findings of the tensile deformation simulation are:

- 1). Yielding of the epoxy molding compound can be described by the pressure von Mises yield criterion. Two yielding mechanisms, namely shear yielding and cavitation, exist, each of which fits to the pressure von Mises criterion using a particular sets of constants (τ_0 and α).

Cavitation kicks in when strong dilatational stress states are present, otherwise the material yields by shear yielding.

2). Cavities nucleation has a nature of randomness, and grows thereafter from the nucleating sites. Using the technique of Voronoi Tessellation, cavities are identified and measured for their volume. It was found that cavity volume fraction increases throughout the tensile deformation. Near the ultimate failure, roughly 60% of the simulation box is occupied by cavities.

3). Polymer strands in the network are continuously extended to linear states and broken in the post-yielding strain hardening process. When most of the strands are stretched to their taut configurations, the material shows rapid scission of large amount of strands with short range of strain, which eventually leads to fracture.

4). The simulation results show much more brittle mechanical behavior as compared to similar studies on glassy thermoplastic polymers. This is attributed to the chemical crosslinking of very short chains, which forbids chain disentanglement and in further stable craze thickening.

The above findings provide valuable insights of the localized plastic deformation of thermosetting polymers. Future work based upon them can lead to MD-to-continuous multi-scale modeling framework for cracking in thermosetting polymers.

CHAPTER 7 STUDY OF TENSILE DEFORMATION AND FAILURE MECHANISMS OF
EPOXY/CU BIMATERIAL USING LARGE SCALE COARSE-GRAINED MD
SIMULATION

In this chapter, a coarse-grained model is developed for description of the interatomic interactions between the studied epoxy molding compound and the copper substrate. The CG potential is parameterized based on matching the free energy landscape reconstructed based on the Metadynamics algorithm, with the energy landscape obtained using the same approach, but from a full atomic model and force field. The CG model for the interfacial interaction, together with the CG model previously developed for the bulk epoxy molding compound, was applied to a large scale MD simulation to study the tensile deformation and failure mechanism of the bimaterial. Upon loading, the bimaterial's plastic deformation, including cavity nucleation/expansion and polymer network strand stretching/scission, is found to be localized to the epoxy molding compound within a zone with finite thickness near the substrate. This is not observed in the full atomic MD simulation due to rather small physical dimension that can be simulated in full atomic MD. The interfacial zone, or interphase, indicates that one can define an interfacial zone based on the deformation inhomogeneity and extract the cohesive law, i.e. the traction-separation relationship, as the stress versus opening displacement of the interfacial zone. The microstructure evolution, including cavitation and polymer chain stretching/scission, within the interfacial zone is analyzed in detail. In addition, effects of strain rate, temperature and epoxy molding compound's cross-link density are studied. With lower cross-link density, the epoxy/Cu bimaterial tends to fail cohesively within the epoxy, rather than fail adhesively as is the case for high cross-linked epoxy/Cu bimaterial.

7.1 Introduction

In Chapter 5 we have shown a coarse-grained model developed for the epoxy molding compound, based on the methodology of fitting key thermo-mechanical properties using iterative optimization algorithm. With the capability of simulating bond breaking and thus material failure, the coarse-grained model is then applied in Chapter 6 in a large scale MD simulation to study the deformation and fracture of the bulk epoxy molding compound. A nature next step to take is building the coarse-grained model for epoxy/Cu bimaterial. In Chapter 4, a full-atomic molecular dynamics study of tensile strength and deformation/failure mechanisms was conducted, based on the polymer consistent force field (PCFF). Valuable insights regarding the effects of strain rate, temperature, cross-link density and epoxy monomer functionality were provided. However, due to the rather expensive full-atomic MD simulation of polymeric materials, the length scale, including the in-plane area and out-of-plane thickness of the epoxy layer, is quite limited. It is unclear whether on a larger spatial scale the mechanical behavior of the epoxy/Cu bimaterial will be different. Thus, a coarse-grained model that enables exploration of the bimaterial's mechanical behavior on larger length scale is highly desired.

As has been reviewed in section 6.1, several methodologies have been developed by the MD simulation community to systematically construct coarse-grained models for bulk polymer. These methods focus on reproducing the material's either structural feature, force field information or properties of interest. In contrast, for polymer versus inorganic-substrate bimaterials, there has been relatively rare work existing about developing coarse-grained model to correctly describe the potential between polymer beads and substrate beads. Site et al. [171] studied adsorption of Bisphenol-A-polycarbonate (BPA-PC) on nickel (Ni) (111) surface using

coarse-grained MD simulation. The BPA-PC versus Ni interaction in the coarse-grained model is described by a planar Lennard-Jones 10-4 potential, in which the parameters are obtained from quantum mechanical calculations.

$$U_{10-4}(z) = 2\pi\varepsilon_w\sigma_w^2 \left[\frac{2}{5} \left(\frac{\sigma_w}{z} \right)^{10} - \left(\frac{\sigma_w}{z} \right)^4 + \frac{3}{5} \right] \quad (7.1)$$

where z is the distance from one polymer bead to the substrate surface. The coarse-grained model was later further developed to account for chain-end-orientation's effect on the adsorption [172]. In another work by Farah et al. [173] the authors also used planar Lennard-Jones potential, but with a 9-3 mathematical form, to calculate the interactions between coarse-grained beads and the planar surface. However, this work is a parametric study on the effect of tuning the potential well depth. No effect of rigorously determining the potential parameters is conducted. Wong et al. [174] studied the interaction energy and equilibrium distance between an epoxy molding compound and the copper substrate. It is not clear from their work how these quantities will be transferred to a coarse-grained MD simulation as potential parameters. The most relevant work to the current investigation is by Iwamoto [175-177], which establishes a meso-scale model for epoxy/Cu₂O bimaterial. The Cu₂O substrate is coarse-grained in such a way that a 2×2 super cell is used as a bead. However, it's not clear from their work how the potential parameters for epoxy/Cu₂O interactions are derived.

To sum up the above existing works in literature, there have been quite limited explorations about establishing coarse-grained model for polymer, especially epoxy based thermosets, versus in-organic substrate bimaterials. In the current investigation, we will show such a model and its application in large scale CG MD study of fracture of epoxy/Cu bimaterial.

The bulk epoxy will use the same coarse-grained potential previously developed, while the potential to capture epoxy/Cu interaction will be parameterized based on rebuilding, in a coarse-grained framework, the free energy landscape generated from full-atomic model. The rest of this chapter is organized as follows. In section 7.2 the concept and implementation of our potential derivation methodology are presented in detail. Section 7.3 and 7.4 present the method, results and discussions of CG MD study of tensile deformation/failure of epoxy/Cu bimaterials. The concluding remarks are made in section 7.5.

7.2 Coarse-Grained Model Development

To establish a coarse-grained model for epoxy/Cu bimaterial, the first task is to find approach of grouping Cu atoms into beads. The concept here is to use a virtual face-centered-cubic crystalline structure, with appropriate lattice constant, to represent the coarse-grained Cu substrate. The lattice constant should not be too small otherwise the advantage of reducing number of particles through coarse-graining is lost, nor should it be too big to prevent polymers from penetrating into the substrate, which is unphysical based on observations obtained from previous full atomic study [5]. In a previous investigation by Stevens [4] the nearest-neighbor distance between the FCC substrate beads is chosen to be 1.204σ where σ is the Lennard-Jones diameter of the epoxy beads. Here the same choice is adopted, which corresponds to a lattice constant of $1.204\sqrt{2}\sigma = 7.463\text{\AA}$. This choice of lattice constants is to certain degree arbitrary. However, since the key of building the coarse-grained bimaterial model is the correct parameters for epoxy/Cu interactions, we will use this scheme for subsequent parameter determination.

Our methodology of constructing the coarse-grained bimaterial potential is based on establishing the free energy surface of the epoxy/Cu system from attached to detached stage by the metadynamics method [178, 179]. The fundamental concept of this algorithm is to fill the system free energy using a series of Gaussian potentials, and to track the filled Gaussian to reconstruct the free energy landscape [180]. The definition of the Gaussian potential depends the selection of a set of collective variables (CV's), which are suitable to describe the physical process of interest. Let $s_i, i = 1, 2, \dots, d$ be d CV's, then the Gaussian potential applied on the system at time t can be written as:

$$V(s, t) = \omega \sum_{\substack{i=\tau_G, 2\tau_G, \dots \\ i < t}} \exp\left(-\sum_{i=1}^d \frac{(s_i(\mathbf{r}) - s_i(\mathbf{r}(t')))^2}{2\delta_i^2}\right) \quad (7.2)$$

where δ_i is the Gaussian width of the i -th CV. ω and τ_G are the Gaussian height and the frequency at which the Gaussian potential is added, respectively. Once the Gaussian potential is added to the system, forces due to this potential will be exerted to micro-coordinates, such as atom or bead positions. For example, let r_j be the system's j -th degree of freedom ($j \leq 3N$, N is the number of atoms), then the force on this degree of freedom is:

$$-\frac{\partial V(s, t)}{\partial r_j} = -\sum_{i=1}^d \frac{\partial V(s, t)}{\partial s_i} \frac{\partial s_i(\mathbf{r})}{\partial r_j} \quad (7.3)$$

By periodically adding the Gaussian potential, and the resulted forces to the molecule attached to solid substrate at the meantime of a MD simulation, the molecule will be forced to escape the attraction of from the substrate, during which the free energy surface will be constructed. The method has been applied in [180] to study the intrinsic strength between epoxy and silica.

In the current investigation, each of the 3mer-EPN, 4mer-EPN and BPA monomer is selected and linked to form a “representative” molecule of the epoxy molding compound. The representative molecule is attached to the Cu substrate, as is shown in Figure 7-1 (a). The Cu substrate has a surface area of $39.4 \times 38.7 \text{ \AA}^2$, and is periodic along both in-plane directions. It contains 6 layers (111) atomic planes. The polymer consistent force-field (PCFF) is used to describe full-atomic epoxy/Cu system. Between epoxy molecules and Cu substrate the Lennard-Jones (9-6) potential and the sixth-power mixing rule are applied to calculate the van der Waals forces. After the model geometry and force-field parameters are defined, the model is equilibrated using NVT MD simulation at 300K using the LAMMPS code.

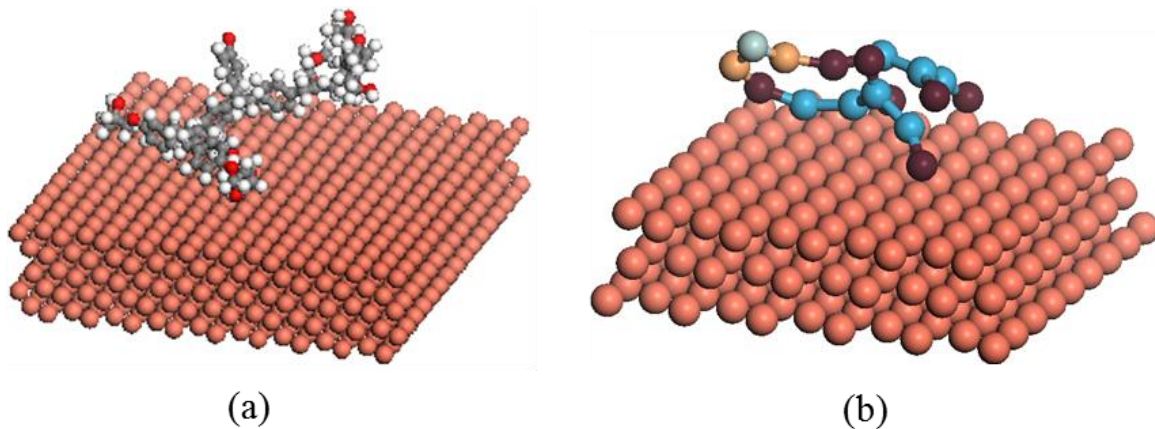


Figure 7-1. (a) full-atomic and (b) coarse grained models of the representative molecule attached to the Cu substrate

To implement metadynamics in MD simulation, the collective variable is chosen to be the distance between the Center of Mass (COM) of the representative molecule and Cu substrate surface. The plug-in package PLUMED [181] is used to conduct the metadynamics calculations. Also during a NVT MD simulation at 300K, Gaussian potential of height $\omega = 0.005$ and width $\delta = 0.35$ is added every 100 steps. These choices of parameters were also used in [180] and

found to be a good balance between precision and computation efficiency. Figure 7-2 shows the results of the metadynamics calculation. The convergence of the free energy surface takes a long simulation time, and is achieved at around 64ns. From the converged free energy surface (blue curve in Figure 7-2) the energy barrier between the attached and detached states is approximately 262kcal/mol, and the equilibrium distance between the epoxy molecule COM and the copper substrate surface is $\sim 3.68\text{\AA}$.

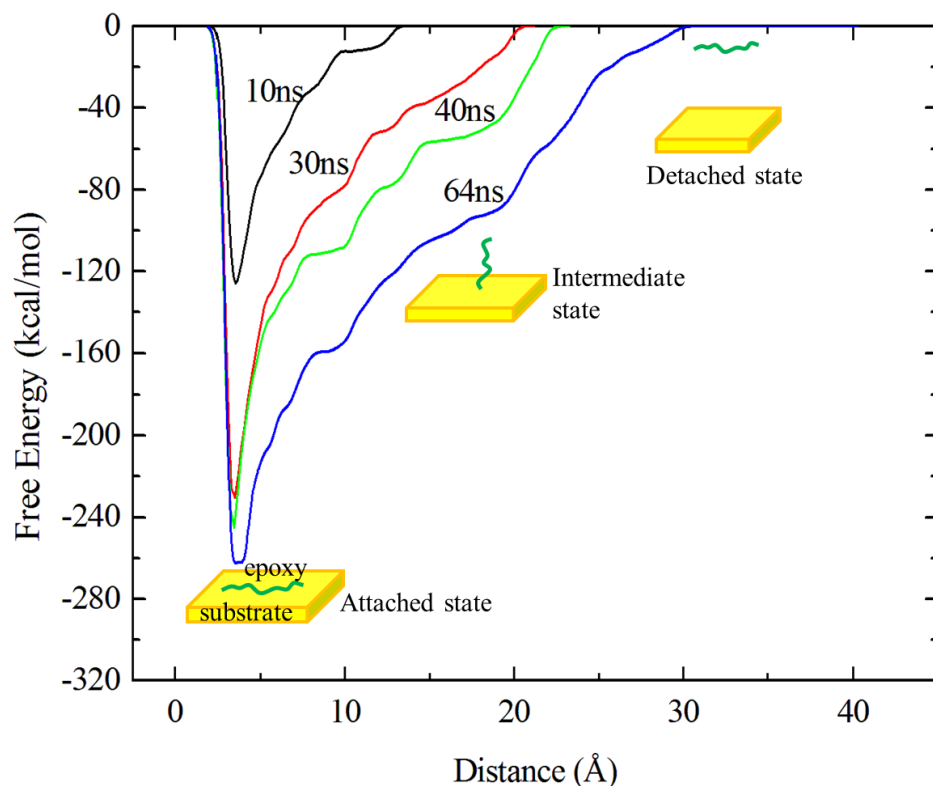


Figure 7-2. Metadynamics calculated free energy surface for the full-atomic model

In order to derive the coarse-grained model for epoxy/Cu bimaterial, the simplest Lennard-Jones 12-6 potential is used to describe the interactions between epoxy beads and the substrate beads. Let ε_{ew} and σ_{ew} be the two parameters of the potential function:

$$U_{ew} = 4\epsilon_{ew} \left[\left(\frac{\sigma_{ew}}{r} \right)^{12} - \left(\frac{\sigma_{ew}}{r} \right)^6 \right] \quad (7.4)$$

where superscripts *e* and *w* stand for epoxy and substrate. The task is then to determine the two parameters. To this end, we coarse-grain the full atomic epoxy molecule versus Cu substrate model, as shown in Figure 7-1 (b), and re-establish the free energy surface using the coarse-grained model. By varying the values of ϵ_{ew} and σ_{ew} , a series of different free energy surfaces can be obtained, and the one that can match the atomic result is believed to correspond to the correct potential (Eq. (7.4)) parameter. In our research it was found that taking σ_{ew} as the LJ diameter of the epoxy beads leads to the equilibrium distance close to the value in the full-atomic free energy surface. Thus we focus on tuning the parameter ϵ_{ew} to change the energy barrier. Figure 7-3 plots the free energy surfaces using the coarse-grained bimaterial model with different Lennard-Jones potential parameters. The clear trend is the increase of energy barrier from attached to detached states with respect to the potential depth ϵ_{ew} . The equilibrium distance between COM of the epoxy molecule and the substrate surface maintains almost unchanged with very slight increase with respect to ϵ_{ew} . It is seen that with the parameter $\epsilon_{ew} = 3\epsilon$, $\sigma_{ew} = \sigma$, the coarse-grained model generates very close free energy surface to the full-atomic result. Thus this set of parameters will be used for the MD modeling and simulation of epoxy/Cu bimaterial at coarse-grained level.

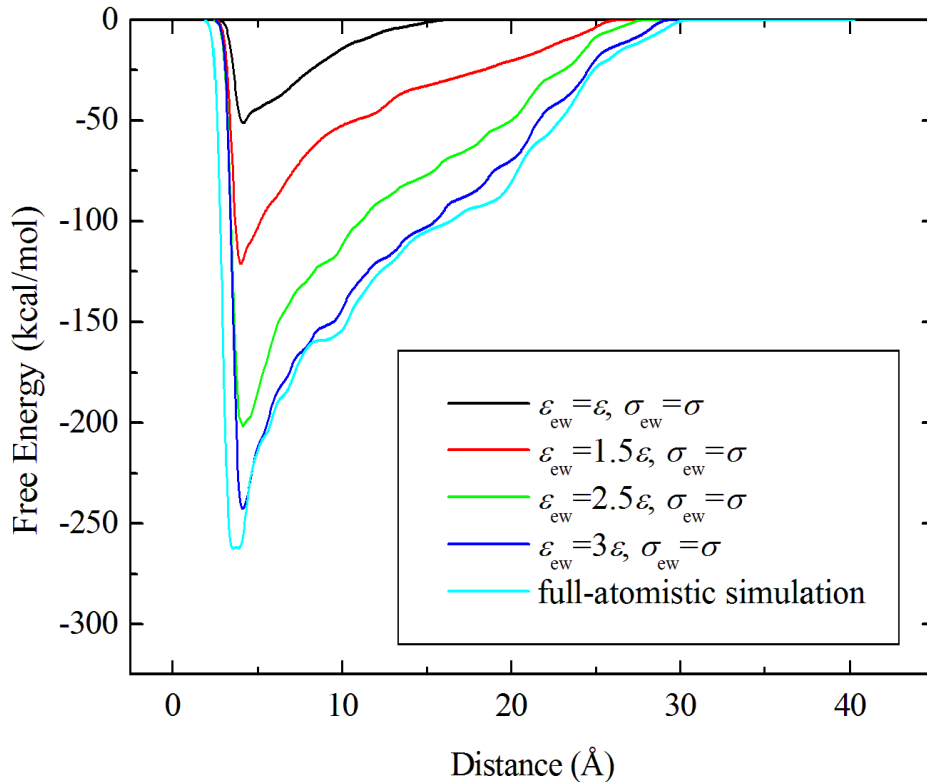


Figure 7-3. Free energy surfaces using different coarse-grained potential parameters, compared to the full-atomic free energy surface. ε and σ are LJ parameters for epoxy beads.

7.3 Coarse-Grained Study of Tensile Deformation of Bimaterial

In Section 7.2 we have derived the coarse-grained potential for epoxy/Cu interaction. Together with the coarse-grained potential for bulk epoxy, it is ready to study the mechanical property/behavior of epoxy/Cu bimaterial at the length scale which is inaccessible by full-atomic simulation. In the coarse-grained bimaterial model, a Cu substrate containing 4 (111) atomic planes sits at the bottom of an orthogonal simulation cell, with periodic boundary condition along the in-plane directions, and traction-free boundary condition along the direction normal to the interface. The rest space of the cell is then randomly seeded with coarse-grained epoxy and

hardener monomers, the numbers of which obey the stoichiometry ratio 3mer-EPN: 4mer-EPN: BPA = 2: 3: 9. In total there are 7,964,588 beads, corresponding to its physical dimension of $\sim 89 \times 89 \times 79 \text{ nm}^3$ (at 300K). After the random seeding of monomers, the system is heated up to 500K, and a dynamic cross-linking process starts and continues at that temperature. It should be pointed out that since we do not have a potential for interactions between Cu substrate beads, we link each substrate bead to its FCC lattice site using a spring with spring constant of $1000\varepsilon / \sigma^2 = 79.04 \text{ kcal}/(\text{mol}\cdot\text{\AA}^2)$. This is to maintain the crystalline structure of the substrate during the MD simulation. During the 500K MD simulation with timestep of 5fs, we specify that if an EPN reactive bead is within a 5.7Å radius of a BPA reactive bead, there is a chance of 1% that this EPN bead will form a bond with the BPA. For every 10 MD steps, the system is checked for potential bond formations. In this way, it typically takes 400,000~500,000 MD steps to reach 90% conversion. Due to the 2D periodic boundary condition, the epoxy network percolates to infinity 2 dimensionally. It mimics the geometry of a thin film. The epoxy layer interacts with the Cu substrate purely via the Lennard Jones potential Eq. (7.4).

The tensile deformation of the bimaterial is simulated by assigning a downward rigid-body velocity, normal to the interface, to the Cu substrate while fixing the very top layer ($\sim 1 \text{ nm}$ thick) of the epoxy layer. The velocity corresponds to a strain rate of 10^8 s^{-1} . At the meantime of translating the Cu substrate, the epoxy layer is maintained at constant temperature, namely 300K, using the Langevin thermostat, with the equation of motion being formulated as:

$$m\ddot{\mathbf{r}}_i = \mathbf{f}_i - m\Gamma\dot{\mathbf{r}}_i + \mathbf{W}_i(t) \quad (7.5)$$

where Γ is the damping constant and \mathbf{W} is a random noise term, and they satisfy the relation:

$$\langle \mathbf{W}_i(t) \mathbf{W}_j(t') \rangle = 6k_B T m \Gamma \delta_{ij} \delta(t-t') \quad (7.6)$$

The two additional terms (other than the force due to potential) couple the system to a heat bath which maintains constant temperature.

7.4 Results and Discussions

7.4.1 Microstructure Near Surface

The microstructure of the epoxy molding compound near the substrate surface is always of interest. The geometric and energetic constraints may cause structural inhomogeneity than the bulk part of the epoxy slab. Upon full equilibrium at room temperature, the near-surface microstructure is analyzed. Figure 7-4 presents a zoomed-in view of the near-surface part of the bimaterial. Note that, to clearly demonstrate structural features, the epoxy and BPA beads are made in-proportionally small. A clear characteristic is that epoxy beads tend to be dense-packed into a few distinctive layers. The further away from the substrate surface, the layer becomes less distinctive and tends to “dissolve” itself to the bulk. This structural feature is due to the rather planar geometry of the substrate surface, and the Lennard-Jones interactions between epoxy and substrate beads. It has been shown in literature, using *ab initio* calculations, that Benzene has a strong adsorption to metal, e.g., Ni, surfaces [171], and prefers to align itself parallel with the surface. In our previous full-atomic study of the same epoxy molding compound versus Cu bimaterial [5], the use of PCFF which itself is rigorously parameterized against *ab initio* data, also leads to dense packing of benzene rings, which serve as the backbones of all constitutive monomers (EPN and BPA), near the substrate surface. Therefore, the coarse-grained model for the bimaterial is able to reproduce the structural characteristics of its full atomic counterpart. This is not surprising, since the potential is derived through matching the entire free energy

surface during a process (metadynamics simulation) which explores all possible configurations of the epoxy molecule on the Cu substrate.

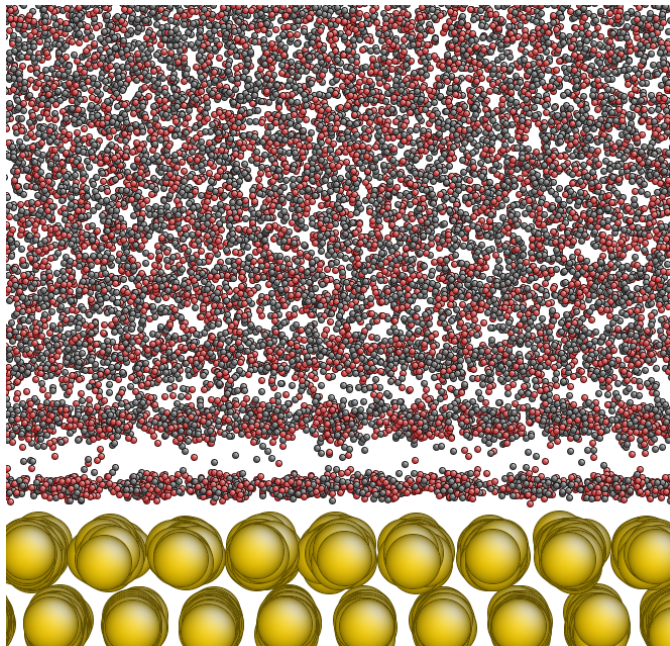


Figure 7-4. Zoomed-in view near the interface. Grey and red beads are EPN beads and BPA beads, respectively. Yellow beads are substrate beads.

To quantify the above observed structural inhomogeneity and also to determine how far it extends from the substrate surface, we studied the variation of few properties of the epoxy with respect to the z (normal direction) coordinate. In Figure 7-5 (a) we plot the density's change along the perpendicular direction. It clearly shows an oscillating trend within the range of 0~2nm from the substrate surface. Beyond 2nm the density of the epoxy maintains at the bulk value, $\sim 1.18\text{g/cm}^3$. The oscillating behavior of density agrees with the structural feature shown in Figure 7-4, i.e. a few distinctive layers of dense-packed epoxy beads exist near the substrate surface. In Figure 7-5 (b) another quantity, the projection on z axis of the average end-end distance of polymer network strands, $\langle z_{E-E} \rangle$, is plotted against the z coordinate. This quantity

indicates how “flat” a polymer strand is. If the strand is aligned parallel to the surface, then the two ends sit roughly on the same plane and $\langle z_{E-E} \rangle$ tends to be zero, which is situation of the near-surface network strands. Figure 7-5 (b) agrees with what is expected: $\langle z_{E-E} \rangle$ increases from 0 to $\sim 6.7\text{\AA}$, which is the bulk value, within the range of 0~2nm. The results shown in Figure 7-5 (a) and (b) are consistent in that they indicate the same range of structural inhomogeneity near the substrate surface.

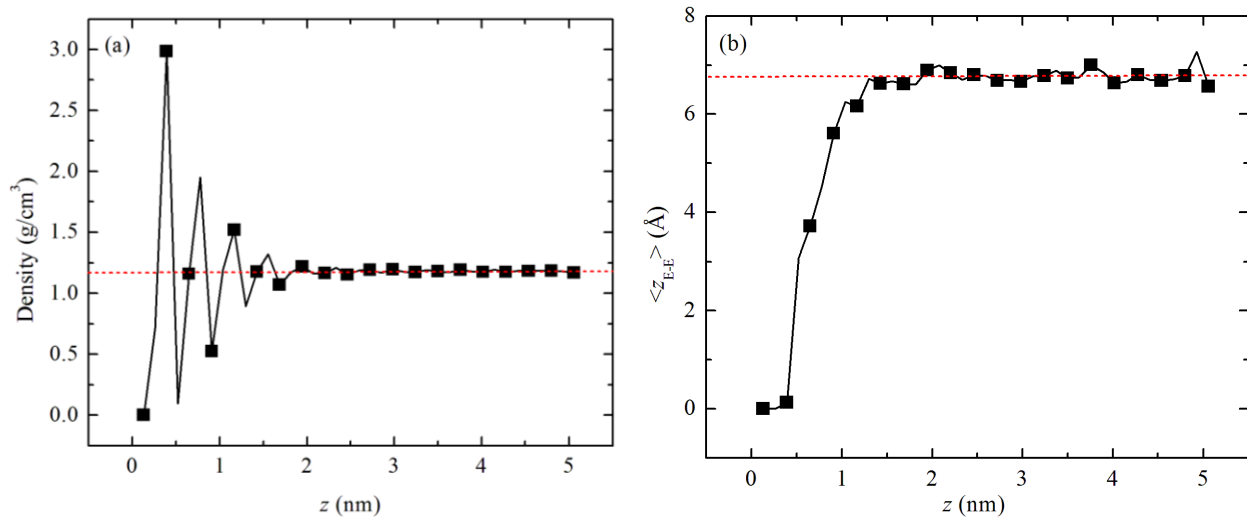


Figure 7-5. Variation of (a) density and (b) end-to-end distance (projection to the normal axis) of network strands along the normal direction. The dashed line represents the bulk value.

7.4.2 Stress-strain Curve and Deformation Behavior

Using the tensile simulation described in section 7.3, the stress-strain curve is obtained and shown in Figure 7-6 for the strain rate of 10^8s^{-1} . The stress-strain behavior shows an elastic response until reaching the yielding strength $\sim 260\text{MPa}$ at the strain of $\sim 5.4\%$. Beyond that, the epoxy material experiences a drastic relaxation of stress down to $\sim 125\text{MPa}$, which is due to the nucleation of cavitation. This yielding mechanism is related to the tri-axial stress state with

strong dilatational component. The tri-axial stress state is consistent with the zero in-plane strain condition in realistic adhesive layers which are highly constrained by adherends. In Figure 7-7 the snapshots of configurations are shown for the tensile simulation. The configuration of the strain 15% indicates that the initial cavities initiate within the epoxy near the substrate surface, while the bulk part of the epoxy (far away from surface) remains intact. The reason why cavitation starts near substrate is due to the relatively weaker force-field. The epoxy and substrate are only connected by the van der Waals forces described by the Lennard-Jones potential (Eq.(7.4)), while within the bulk epoxy across an inner surface there are additional valence forces (bond stretching and angle bending). The cavitation is also accompanied by extension of the polymer network strands from their coiled states to taut conformations. Zoomed-in view (not shown here) demonstrates that networks of strands connecting the inner walls are observable.

The yielding and stress relaxation is followed by a strain hardening process, extending to the strain of ~25%. This behavior is accompanied by expansion of cavities. The second snapshot of Figure 7-7 shows both longitudinally and laterally enlarged voids compared to the first snapshot. At the meantime, strands are continuously converted from their closed-packed to linear configurations. Upon reaching the ultimate failure strength, which is ~137MPa at the strain of 25%, the near-surface region of epoxy is fully stretched. Further deformation is restricted by the highly cross-linked network which applies stringent topological constraints. Therefore it starts a debonding process from the substrate. As is shown in the configuration with strain of 30% (third snapshot in Figure 7-7), during the debonding process those epoxy network strands initial aligned along the surface are being peeling off from the substrate. This eventually leads to a

rather clean interfacial separation between the epoxy and the substrate, shown in the configuration with strain of 40%.

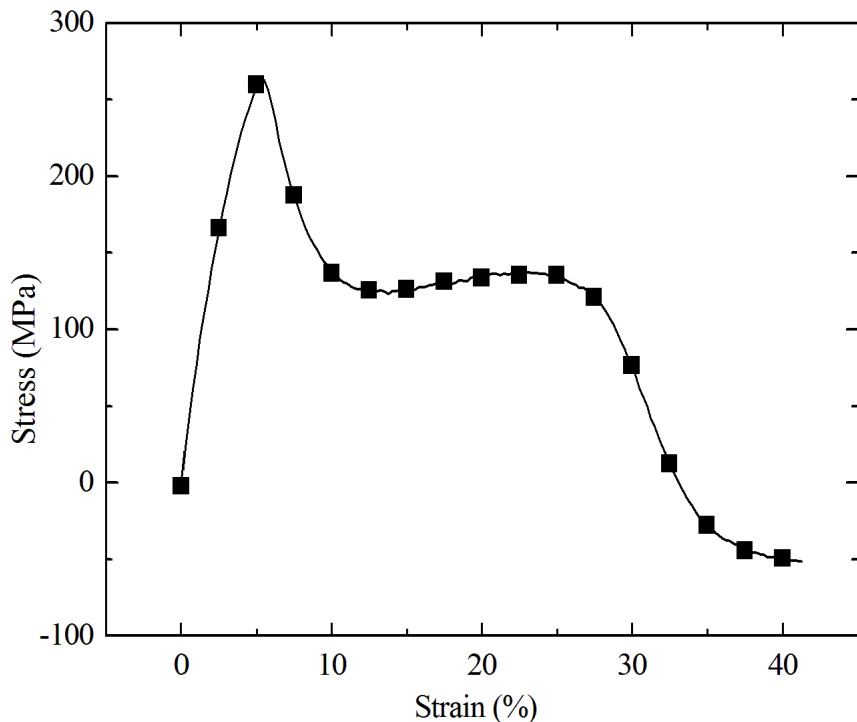
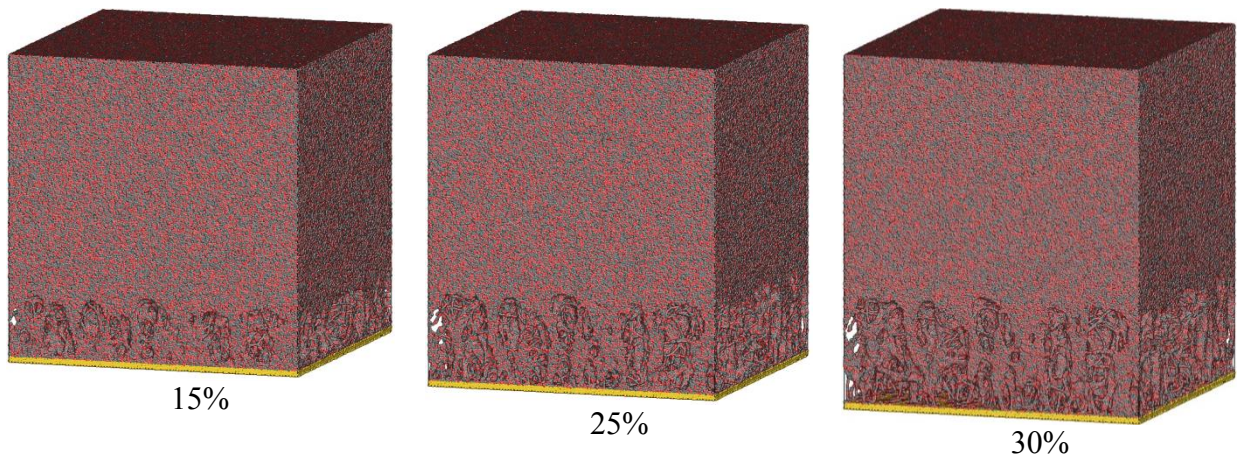


Figure 7-6. Stress-strain curves for the tensile simulation of epoxy/Cu bimaterial



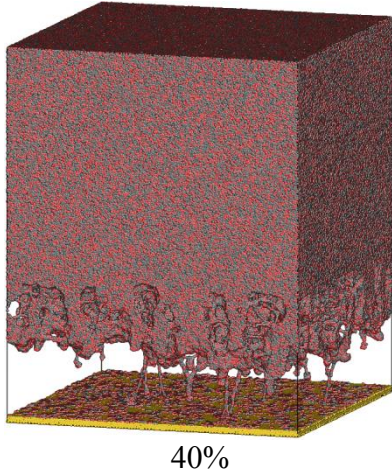


Figure 7-7. Snapshots of the configurations of the 90% cross-linked epoxy/Cu bimaterial during the tensile deformation using the strain rate of 10^8s^{-1}

An important characteristic of the epoxy/Cu bimaterial's deformation/failure behavior is that the plastic deformation mechanisms, including cavity nucleation/expansion and polymer chain stretching/breaking, are restricted to a zone with finite thickness near the substrate surface. The thickness of this "interfacial zone" can be determined by investigating the variation of displacement with respect to the Lagrangian z coordinates, which is plotted in Figure 7-8 (a). The displacement profiles shown in this Figure for two strains, 15% and 25%, both show a "kink" at $z = 10\text{nm}$, below which the displacement is much larger than above. Moreover, there is no additional deformation within the bulk epoxy (above the kink) with increase of overall strain. This confirms the localization of plastic deformation within an interfacial zone near the substrate, and indicates a thickness of $\sim 10\text{nm}$. With this in mind, one is able to extract the traction-separation relationship as such: define the separation as the opening displacement of the interfacial zone, and the traction as the stress within the interfacial zone. The extracted traction-separation relationship is shown in Figure 7-8 (b). It also shows an elastic response, followed by drastic drop of stress and strain hardening, until reaching the cohesive strength and critical

separation. The critical separation is approximately 20nm, and the cohesive strength is roughly 155MPa, which is slightly higher than the strength in stress-strain curve (Figure 7-6). This is because that within the more restricted volume of interfacial zone there is concentration of stress.

In the previous full atomic study of the same epoxy/Cu bimaterial, such localization of plastic deformation was not observed, due to the too small length scale ($\sim 10\text{nm}$ thickness) of the full atomic model. It is the coarse-grained model that enables one to model the bimaterial's mechanical behavior on a much larger length scale and uncover the existence of interfacial zone. This demonstrates the necessity of accessing the correct length scale to fully understand the mechanical behavior of polymeric materials.

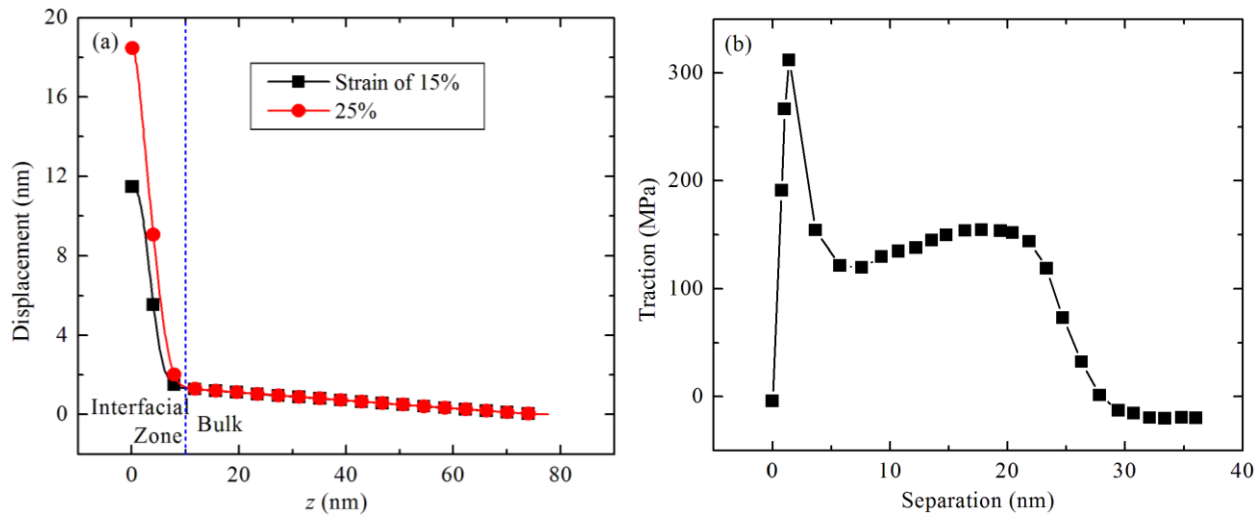


Figure 7-8. (a) Displacement profile along the normal direction for the 90% cross-linked epoxy/Cu bimaterial, for two different overall strains. (b) The extracted traction-separation relationship based on the definition of the interfacial zone.

The change of conformations of epoxy network strands within the interfacial zone, during the tensile deformation, is of our interest and worth of thorough investigation. From the Figure

7-5 (b) one has already known that in the configuration $\langle z_{E-E} \rangle$ has the uniform value of 6.7 Å except for strands very close the substrate (up to 2nm from the surface). Upon tensile deformation, it is expected that this quantity for near-surface strands increases, since from snapshots shown above strands tend to be oriented along the loading direction. This is confirmed in Figure 7-9, which plots $\langle z_{E-E} \rangle$ versus Lagrangian z coordinates for different overall strains. For the configuration with 15% strain the $\langle z_{E-E} \rangle$ profile shows a peak at 3.4 nm with the value of 15.7 Å, and decays to the bulk value when z approaches to 10 nm, which is the interfacial zone/bulk boundary obtained from the displacement profile. Upon further deformation, the maximum $\langle z_{E-E} \rangle$ shifts to 1.4 nm with the value of 16.8 Å. This is consistent with the observation that those network strands initial aligned along the surface are being peeling off from the substrate. After the bimaterial has failed, the interfacial zone separates with the substrate and bounces back to the bulk, thus $\langle z_{E-E} \rangle$ decreases within the interfacial zone, as is shown in Figure 7-9 (blue curve with triangle marker). Although polymer strands are being continuously re-orientated along the loading direction, and peeled off from the substrate, the broken of chains occurs quite rarely. Even within the mostly deformed interfacial zone, the number fraction of broken bonds is less than 0.05%. Therefore, the failure mechanism is dominantly adhesive rather than cohesive.

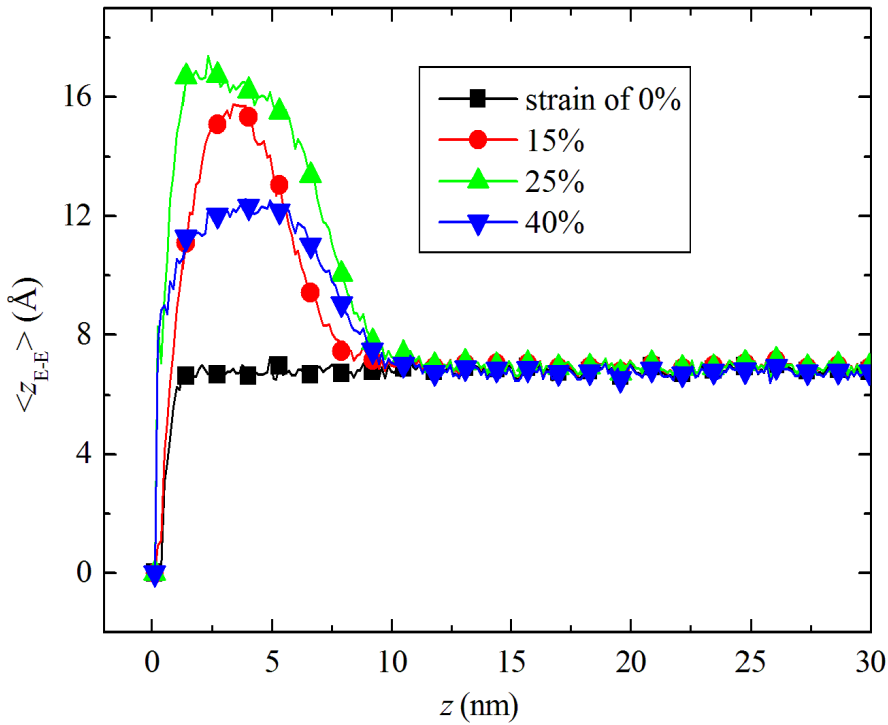


Figure 7-9. End-end distance (projection to the normal axis) of network strands along the normal direction for different overall strains.

7.4.3 Effects of Strain Rate and Temperature

The epoxy/Cu bimaterial's mechanical behavior can be affected by a number of factors. In terms of loading condition, strain rate and temperature are the major parameters to consider. Due to the large number of particles (~ 8 million) of the current model, our available computational power only allows us to simulate very high strain rate. Other than 10^8s^{-1} , a smaller strain rate of $2 \times 10^7 \text{s}^{-1}$, is used in the simulated tensile deformation. In Figure 7-10 the red curve with circle markers shows the stress-strain curve. Compared to the higher rate, the stress-strain behavior contains a similar elastic response, but a wider post-yielding strain hardening regime with lower stress magnitude. The failure strain and strength are 43% and 126 MPa, respectively.

These all indicate a more ductile mechanical behavior of the epoxy/Cu bimaterial at lower strain rate, which is expected. In section 4.2 we have described the localization of plastic deformation in an interfacial zone near the substrate, and extracted the traction-separation relationship based on the definition of this interfacial zone. For the lower strain rate situation, the same localization behavior is also observed. However, the thickness of the interfacial zone is bigger. The snapshot in Figure 7-11 for the strain of 18% shows that the initial cavitation occurs further away from the substrate than in the higher strain rate situation. The reason can be understood as that, when the substrate is moved away with lower velocity, the epoxy material further away from the substrate is given time to respond to the applied deformation, i.e. releasing the stress beyond yielding strength through nucleating cavities. The displacement profile (red curve with circle marker) shown in Figure 7-12 (a) indicates that the thickness of the interfacial zone is roughly 20nm. Accordingly, the traction-separation relationship can be obtained and shown in Figure 7-12 (b). It has a larger critical separation, ~37nm, and higher cohesive strength, 135MPa.

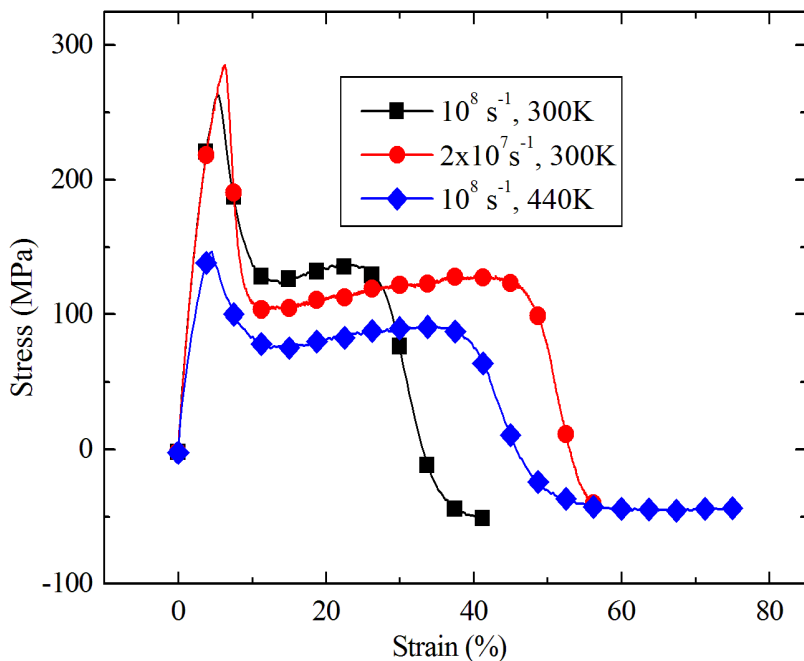


Figure 7-10. Stress-strain curves for lower strain rate and higher temperature

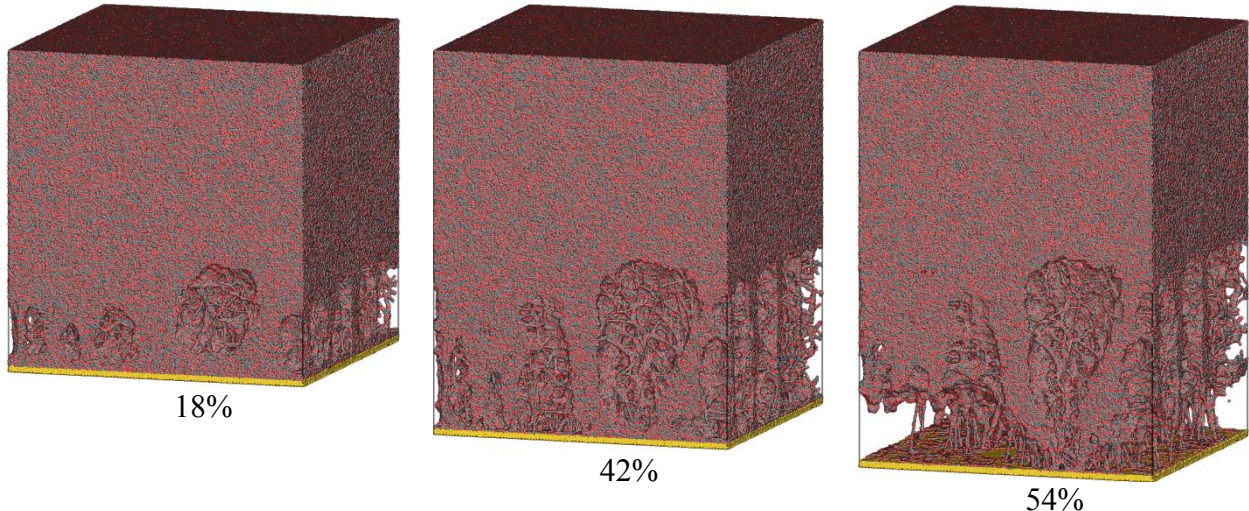


Figure 7-11. Snapshots of the configurations of the 90% cross-linked epoxy/Cu bimaterial during the tensile deformation using the strain rate of $2 \times 10^7 \text{ s}^{-1}$

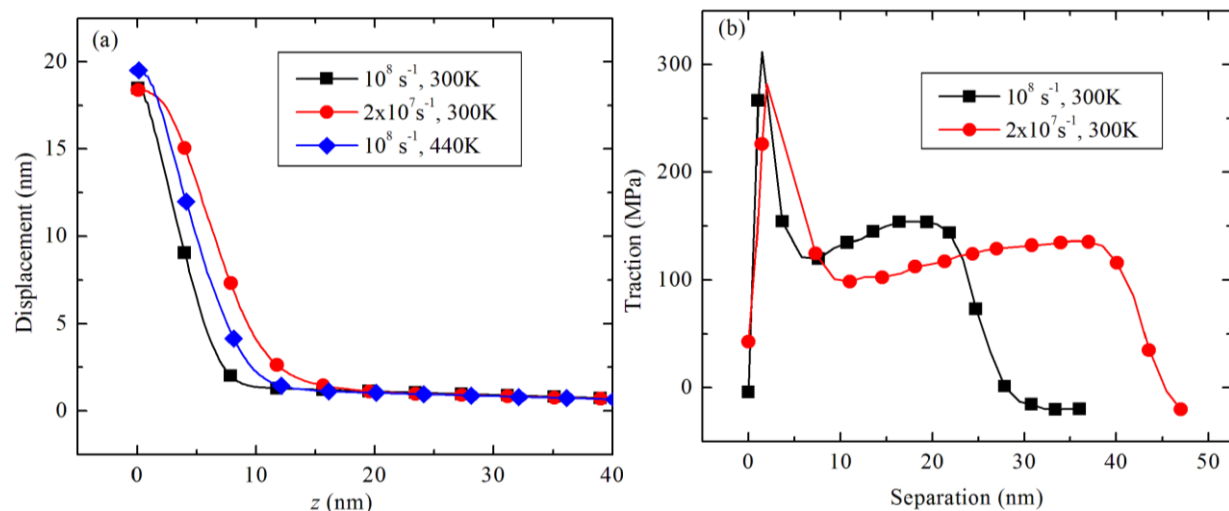


Figure 7-12. (a) Displacement profile for lower strain rate and higher temperature. (b) Traction-separation relationship for lower strain rate and higher temperature.

From the second and third snapshots in Figure 7-11 one can observe that the same plastic deformation mechanisms, namely cavity growth and polymer chain stretching/breaking, occur during the strain hardening process of the lower rate tensile deformation. The failure is also

through peeling off of near-surface polymer strands, and then interfacial debonding. However, since the interfacial zone is thicker, one would expect cavities with larger sizes, which can be seen in Figure 7-11, and bigger probability for bond breakage since more polymer strands experiences re-orientation along the loading axis. The latter is demonstrated in Figure 7-13, which confirms that for lower rate the number broken bonds is significantly larger than that for higher rate.

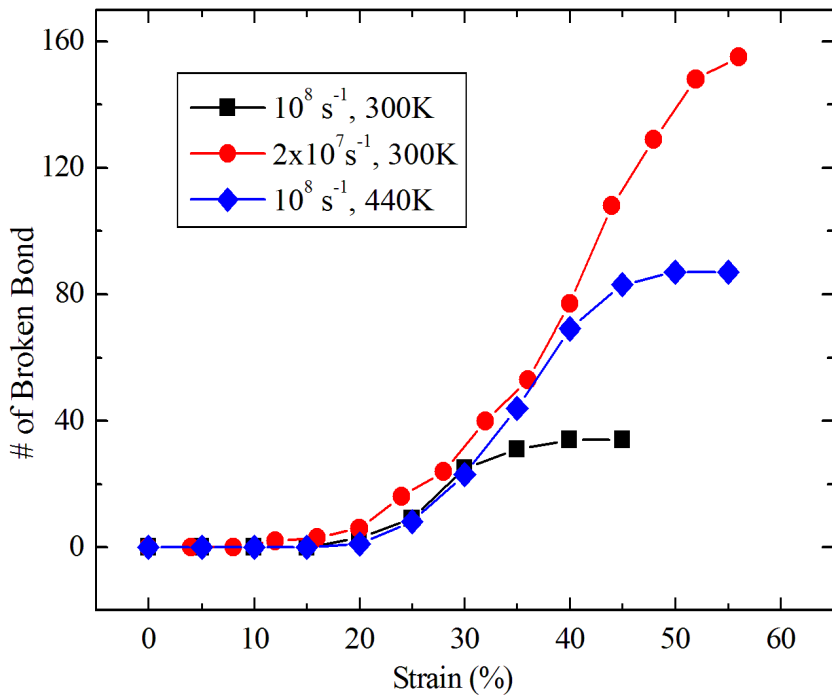


Figure 7-13. Number of broken bonds versus strain for different strain rates and temperatures

Temperature's effect is investigated by conducting the tensile simulation at 440K. Since previous MD calculations and experimental measurements all gave the epoxy molding compound's T_g to be $\sim 400\text{K}$, 440K is picked here to study the bimaterial's mechanical behavior in the epoxy's rubbery state. Before the tensile simulation starts, it is necessary to re-conduct the cooling process from the curing the curing temperature (500K) to 440K and the subsequent equilibration at this temperature. The obtained stress-strain curve is presented in Figure 7-10 as

the blue curve. It is seen that the high temperature significantly lowers the yielding strength, to $\sim 145\text{ MPa}$. Since yielding of the bimaterial is due to the yielding of the epoxy molding compound, this is a reflection of the temperature dependency of the epoxy's yielding strength. Beyond yielding, the bimaterial experiences similar strain hardening, until reaching the failure strength of $\sim 90\text{ MPa}$ at the strain of $\sim 36\%$. In general high temperature has similar effects with low strain rate on the mechanical behavior of the bimaterial. Figure 7-12 (a) indicates that a thicker interfacial zone, $\sim 14\text{ nm}$, is associated with the deformation process with higher temperature. Also Figure 7-13 shows that more bond breaking occurs than in the low temperature simulation.

7.4.4 Effects of Conversion

Previous sections of this article have been focused on the bimaterial with highly cross-linked epoxy molding compound, and its failure mode has been shown as interfacial rather than cohesive. It is not clear that the failure mechanism will change with epoxies of lower cross-link density. To study this issue, another bimaterial model with 73% conversion of epoxy is built and equilibrated using the same procedure for the 90% cross-linked model. In Figure 7-14 the stress-strain curve is plotted. It is seen that after yielding there is no strain hardening regime in the stress-strain behavior. Instead, the stress drastically drops to $\sim 43\text{ MPa}$, maintains at a plateau for a short range of strain, and gradually decays to zero thereafter. Figure 7-15 presents the atomic configurations during the tensile deformation. The first snapshot (with strain of 20%) demonstrates that microstructures which resemble "crazing" in thermoplastics are formed: an array of vertical ligaments is observed to bridge the bulk epoxy to a thin layer of epoxy attached to the substrate surface. The reason why this microstructure forms is that the epoxy molding

compound with lower conversion tends to have less cross-linked network structure. This is can be demonstrated by the difference in the number density of elastically effective chains, defined as the network strands between two cross-links (a cross-link is a bead that has at least three strands reaching out to other such beads). For the highly cross-linked epoxy molding compound, the number density of elastically effective chains is roughly $1.4 \times 10^{21}/\text{cm}^3$, while for the epoxy with conversion of 73% the density is approximately $7.9 \times 10^{20}/\text{cm}^3$, almost one order of magnitude lower. The much lower cross-link density makes it easier to form ligments that lack links among each other, i.e. the crazing-like microstructure shown in the first snapshot of Figure 7-15. The much lower stress magnitude in the post-yielding regime of the stress-strain curve can be explained by the larger volume fraction of cavities in the lower conversion epoxy molding compound, which is again related to the lower density of elastically effective chains. Further deformation involves the opening up of this band of crazing. This process can be visualized by the second snapshot in Figure 7-15, in which the ligments are significantly stretched as compared to the first snapshot. Stretching of the ligments can be confirmed by studying the number of broken bonds with deformation, which is shown in Figure 7-16. It is seen that from the strain of 20% to 80%, there is sharp increase of number of broken bonds. Since there is very limit bond breaking event occurring in the bulk epoxy, the bond breakings are concentrated in the interfacial zone, and represent stretching and scission of the ligments. Beyond the strain of 80%, the number of broken bonds tends to saturate, indicating that all the ligments have been broken and the bimaterial completely fails. This corresponds to the configuration shown as the third snapshot in Figure 7-15. In the failed bimaterial, the substrate is observed to be fully covered by epoxy

material residues. Therefore, the failure mode of the bimaterial with lower conversion is cohesive rather than adhesive.

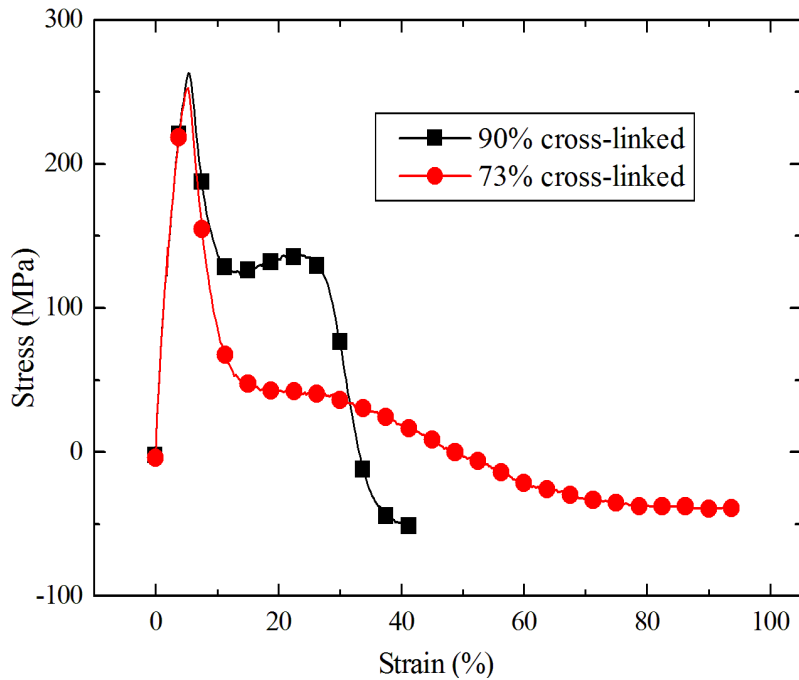


Figure 7-14. Stress-strain curve for bimaterial with lower epoxy conversion

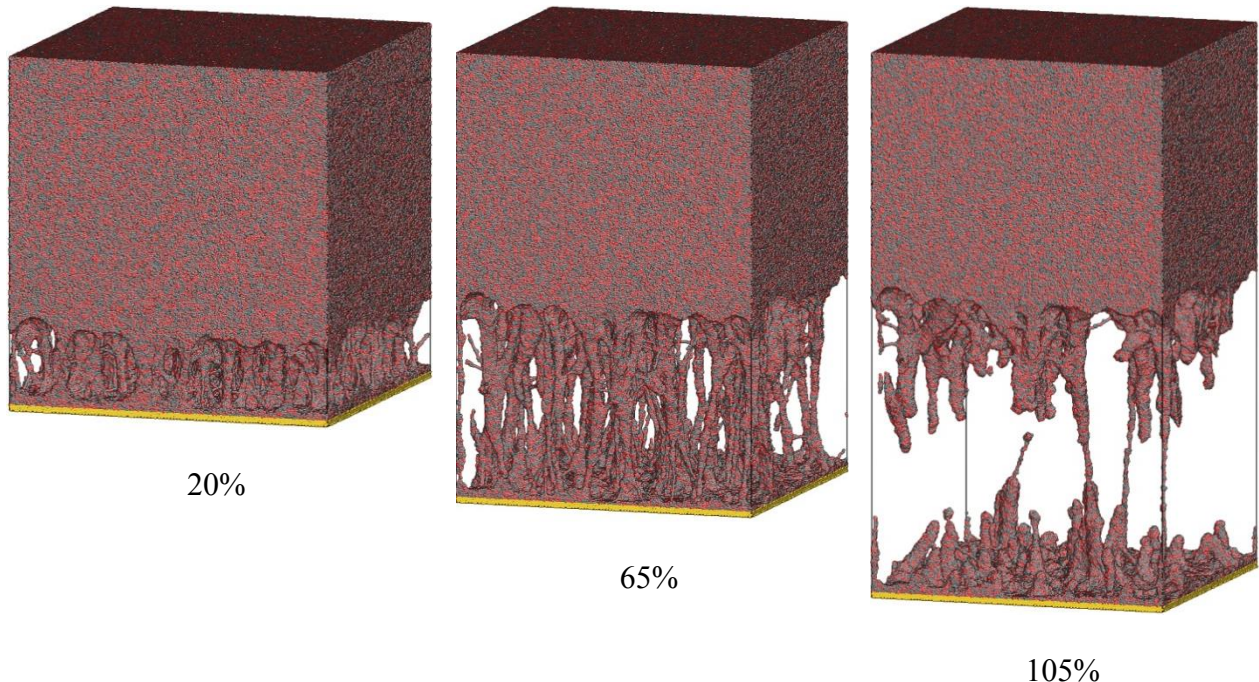


Figure 7-15. Snapshots of the configurations of the 73% cross-linked epoxy/Cu bimaterial during the tensile deformation

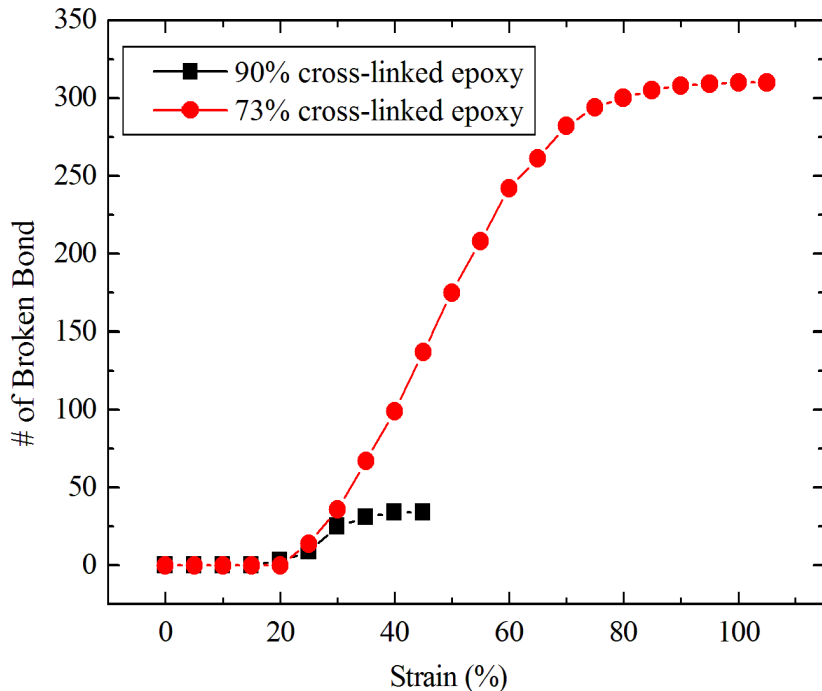


Figure 7-16. Number of broken bonds versus strain for different conversions

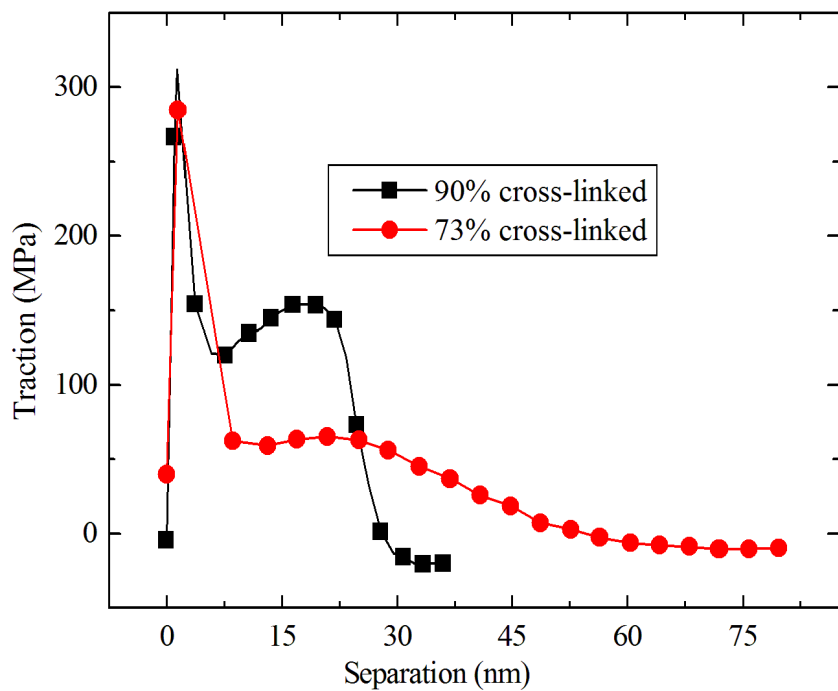


Figure 7-17. Traction-separation relationship for different conversions

As can be observed in Figure 7-15 the plastic deformation mechanisms, specifically the formation of the band of ligments and the subsequent stretching/scission of the ligments, is localized in the interfacial zone. Through analyzing the displacement profile, the thickness of the interfacial zone is found to be ~10nm. Following the same method, the traction-separation relationship of the bimaterial with lower epoxy conversion can be extracted and is presented in Figure 7-17. The cohesive strength is ~65MPa at the separation of ~21nm. However, due to the ductile mechanical behavior of the interfacial zone, the traction decays gradually after reaching the strength and does not vanishes until ~54nm. Therefore the critical separation at which the interfacial zone completely fails is 54nm.

7.5 Conclusions

In this chapter, a coarse-grained study of the interface between an epoxy molding compound and the Cu substrate is presented. The coarse-grained model for the epoxy molding compound is the previously developed one based on fitting the key thermo-mechanical properties using iterative optimization algorithm. The coarse-grained potential for epoxy/Cu bimaterial is parameterized through matching the free energy landscape calculated using the full atomic model using the Metadynamics algorithm. The Metadynamics method is found to be a powerful tool to obtain the intrinsic energy barrier, equilibrium distance and the entire free energy landscape for organic molecules attached to solid substrate. Using the coarse-grained bimaterial model, a large scale MD simulation with nearly 8 million particles and up to $100 \times 100 \times 100 \text{ nm}^3$ physical dimension is conducted to study the tensile deformation/failure behavior. For highly cross-linked epoxy molding compound, it is found to interfacially fail with respect to Cu substrate. The plastic deformation mechanisms, including cavity nucleation/expansion and polymer chain

stretching/breaking, are found to be localized within an interfacial zone with thickness of roughly 10nm. This finding enables the extraction of traction-separation relationship as the stress within the interfacial zone versus its normal opening displacement. The dependency of the bimaterial's mechanical behavior on loading rate and temperature is investigated. Lowering the strain rate and raising the temperature are found to result in a thicker interfacial zone and more ductile traction-separation relationship. The conversion's effect is also studied. The bimaterial with lower epoxy conversion, specifically 73%, is found to fail cohesively rather than adhesively. Similarly, the plastic deformation mechanisms, formation of the band of ligaments and the subsequent stretching/scission of the ligments, are highly localized within the interfacial zone. The traction-separation relationship is also extracted following the same method.

The contribution of the current investigation consists of two aspects. One is the development of the methodology of building coarse-grained model for bimaterial using the Metadynamics algorithm used with rigorously parameterized full atomic force field. The second contribution is the study of the epoxy/Cu bimaterial's mechanical behavior at large length scale, which is not accessible to full atomic MD simulation. This unveils the interfacial zone, or interphase, near the substrate surface. The cohesive law can then be defined and obtained, which can be feed up to continuum mechanics based finite element simulations as the constitutive relationship of the interface.

CHAPTER 8 CONCLUSIONS AND RECOMMENDATIONS

8.1 Summary of Contributions

The work presented in this dissertation demonstrates a fundamental and innovative research into the interface between engineering materials that have important application in electronic packaging industry. The epoxy/Cu interface is studied from the very bottom: atomistic model in which each atom's motion is governed by equation of motion and rigorously parameterized and validated full-atomic force field. Towards the aim of extracting failure related properties and constitutive relationships applicable in continuum mechanics based modeling, a coarse-grained model is built to extend the capability of MD simulation to larger length scale. Not only have we obtained useful information regarding this particular epoxy molding compound and its interface with Cu, we have also developed methodologies that can be extended to modeling and simulation of other material systems including epoxy based thermosetting polymers and in-organic substrate, which are prevalent not only electronic packaging, but also in automobile, aerospace and a number of other industries. This will significantly expedite material design. Below we summarize the scientific and technical contributions:

- 1) A multi-step crosslinking-relaxation algorithm is developed to build the cross-linked network structure of the epoxy molding compound from given monomers. This solves the issue of representing in MD simulation the molecular structure of epoxy resins, which used to be challenging since one cannot assume *a priori* how monomers are linked. The full-atomic model thus constructed is subjected to MD simulation with the polymer consistent force-field for the prediction/reproduction of crucial thermo-mechanical

properties, including curing induced shrinkage, gelation point, coefficient of thermal expansion, glass transition temperature, and elastic constants, and their dependency on temperature and/or cross-link density. MD simulation is able to yield good agreement with available experimentally measured data. These accomplishments demonstrate that MD simulation can serve as a powerful tool to calculate the thermo-mechanical properties of cross-linked thermosetting materials, thus is a useful predicitve computational alternative other than experimental testing to help design more reliable materials.

2) Using the developed crosslinking-relaxation algorithm, the epoxy molding compound is cross-linked on Cu substrate to model the bimaterial at the full atomic length scale. By applying MD simulated tensile deformation, its stress-strain curve and deformation/failure behavior are revealed. For highly cross-linked epoxy molding compound, the plastic deformation is mainly due to micro-void initiation/growth and re-alignment of epoxy network strands, and the failure occurs through simultaneous detachment from the substrate therefore is brittle in nature. With larger epoxy monomer functionality, the interfacial failure is even more brittle. For epoxy with lower conversion thus lower cross-link density, the ultimate interfacial failure becomes more ductile with lower failure strength and larger failure strain. These findings uncover the basic mechanisms of deformation/failure of epoxy/Cu interface which are difficult, if not impossible, for experiment to observe. They also clearly show the influence of structural and loading parameters, which is again useful in design interfaces with better performances.

3) A coarse-grained model is developed for the epoxy molding compound. The coarse-grained model consists of bead-spring representation of the constitutive monomers, and inter-bead potentials with prescribed mathematical formulations for non-bond, bond and angle interactions. The parameters of the coarse-grained model are determined from iterative optimization towards good match between coarse-grained and full atomic calculated thermo-mechanical properties, which is rooted in the Particle Swarm Optimization algorithm and implemented by a self-developed code. We demonstrated that the newly developed coarse-grained model is able to reproduce, in good agreement with atomic MD results, density, glass transition temperature and elastic constants, as well as these properties' temperature and structural dependence. It also can simulate bond breakage and thus material failure, which is not possible by the full atomic model due the restriction of force-field.

To build the coarse-grained of bimaterial, the method of Metadynamics is applied to construct the free energy surface of epoxy molecules attached to the Cu substrate. The free energy surface is extracted on both full atomic level and coarse-grained and matched in order to determine the potential parameters that describe the interactions between epoxy beads and substrate beads in the coarse-grained model. Our methodology of building the coarse-grained model is effective and efficient, and can be transplanted to other material systems.

4) The coarse-grained model is applied to study the deformation/failure behaviors of both bulk epoxy and epoxy/Cu bimaterial. Thanks to the coarse-grained model which significantly extends the physical dimension that can be simulated, we are able to study

mechanical behavior on length scale of nearly $100 \times 100 \times 100 \text{ nm}^3$. For the bulk epoxy it is found that two yielding mechanisms, shear yielding and cavitation, exist, and both of them fit to pressure modified von Mises criterion using a particular set of constants. Cavitation kicks in when strong dilatational stress states are present. During the post-yielding plastic deformation, the nucleated cavities continuously grow while polymer strands in the epoxy network are extended to taut configurations and broken in the strain hardening process. The material fails through rapid scission of large amount of strands within short range of strain. It is also found that the highly cross-linked network strands forbids chain disentanglement and the further stable craze thickening, thus leads to much more brittle mechanical behavior of thermosets than thermoplastics.

For epoxy/Cu bimaterial, the failure is found to be interfacial for highly cross-linked epoxy molding compound. The key finding is that the plastic deformation mechanisms, including cavity nucleation/expansion and polymer chain stretching/breaking, are localized in an interfacial zone with finite thickness. This finding enables the extraction of traction-separation relationship as the stress within the interfacial zone versus its normal opening displacement. On the other hand, for epoxy with lower conversion, the failure is found to be cohesive within epoxy. The bimaterial fractures within epoxy and leaves a layer of epoxy beads attached to the substrate. The dependency of the bimaterial's mechanical behavior on loading rate and temperature is investigated. Lowering the strain rate and raising the temperature are found to result in a thicker interfacial zone and more ductile traction-separation relationship.

8.2 Recommendations to Future Work

8.2.1 On the Atomic End

Cu based leadframes are prone to thermal oxidation due to their working environment.

Researchers observed growth of Cu oxides as pebble-like Cu_2O followed by needle-shaped CuO (shown in Figure 8-1) [14, 15, 17]. Oxidation would significantly affect inter-atomic interactions and interface morphology, thus failure mechanisms of the epoxy molding compound versus leadframe interface. The acicular CuO precipitates acts as surface roughness thus strengthen the interface through asperity interlocking. Therefore, down to the atomic end, it is worth studying the traction-separation behavior of epoxy/ Cu_2O and CuO interfaces, following the atomic and coarse-grained modeling/simulation methodologies described in this dissertation.

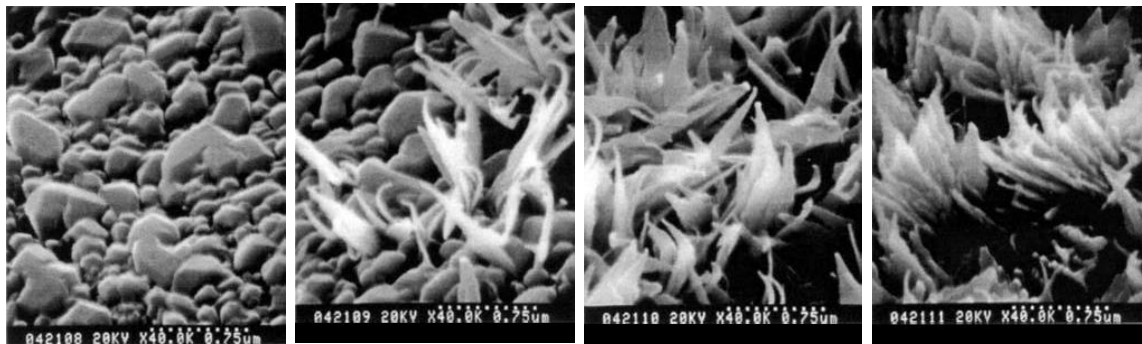


Figure 8-1. SEM images of Cu leadframe being oxidized [17]

8.2.2 Transition From Atomic to Macroscopic Cohesive Law

Although the coarse-grained model has been developed to model and simulation the epoxy/Cu bimaterial on the order of a hundred nanometers, there is still gap of length scale. In experimental studies of fracture of bulk epoxies and epoxy/solid substrates interfaces, crack opening displacement (COD) is often observed as on the order of micron. This contrasts to the

opening displacement of tens of nano-meters in our coarse-grained MD simulation. One of the sources for the difference is that in reality we have surface roughness which “magnifies” COD to the characteristic length of the surface profile. For instance, when the surface is modeled to a sinusoidal profile, as depicted in Figure 8-2, the critical separation that interface fails to sustain stress would be close to the peak-to-peak of the waveform, due to mechanical interlocking. Therefore, a potential approach of upgrading length scale is to mesh the interface with cohesive elements characterized by MD obtained traction-separation law, and derive stress versus opening displacement relationship through computational homogenization within the interfacial zone that encompasses the roughness. The above cohesive zone law will be directly used in a realistic polymer/metal interface models for FEA simulations.

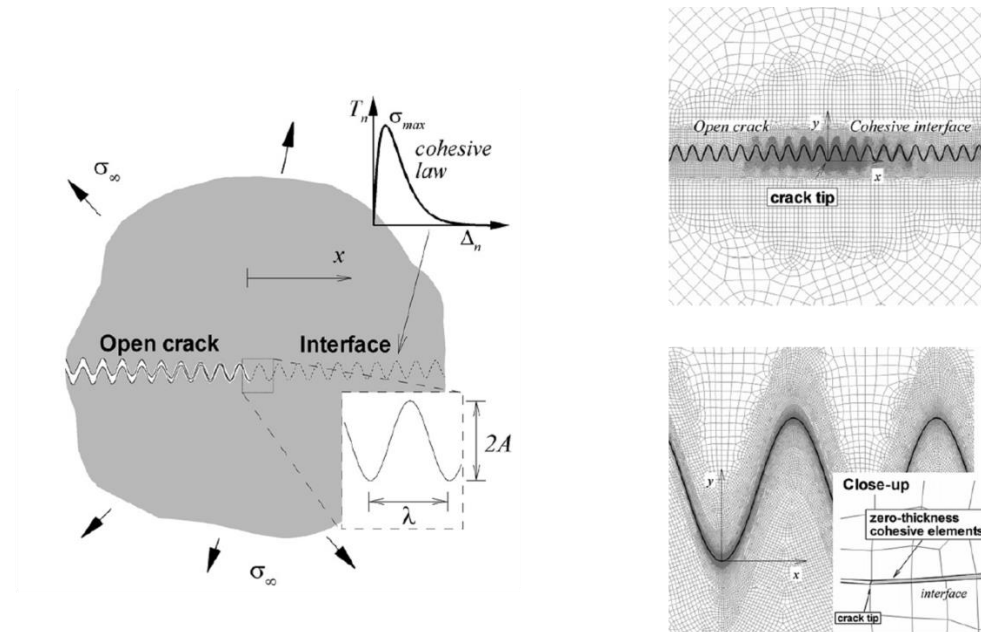


Figure 8-2. schematic illustration of how a roughened interface is modeled and meshed in FEM [182]

Compared to the length scale issue, the extreme loading rate ($10^7 \sim 10^9 \text{ s}^{-1}$) in MD seems to be a more fundamental challenge, considering that in experiments strain rates are usually less than 1 s^{-1} . High strain rate results in elevated yield strength, and since modulus is relatively insensitive to strain rate, yield strain is extended. There have been theories that correlate yielding stresses at different rates. For example, an implicit expression for dislocation nucleation stress under constant temperature and strain rate was presented in Zhu's work [183]:

$$\frac{Q(\sigma, T)}{k_B T} = \ln \frac{k_B T V_0}{E \dot{\epsilon} \Omega(\sigma, T)} \quad (8.1)$$

The authors assumed linear dependence of activation energy and activation volume on temperature. By calculating and inputting to Eq. (8.1) the activation energy on the zero- T potential energy surface, $Q_0(\sigma)$, through the free-end nudged elastic band method, at different stress levels, the nucleation stress as function of temperature and strain rate can be numerically solved. $\sigma \sim T$ relationship for high strain rate (10^8 s^{-1}) agrees quite well with MD generated results. The solution for $\dot{\epsilon} = 10^{-3} \text{ s}^{-1}$ was also given and showed significant drop of nucleation stress. For amorphous polymers, however, the lack of long range structural orders prohibits the use of theories based on dislocation motions. Built on the notion that polymers' plastic deformation is associated with localized transformations, such as dihedral angle transitions, some theoretical models have been proposed to relate the yield stress to state transition rate. The Eyring model [184] postulates that the energy barrier to transitions can be lowered or raised by application of stress, and it leads to an expression of strain rate as [185]:

$$\dot{\epsilon} = \dot{\epsilon}_0 \exp\left(-\frac{E - \sigma V^*}{k_B T}\right) \quad (8.2)$$

where V^* is the activation volume and E is the activation energy independent of stress. Capaldi and Boyce et al. [185] conducted MD simulation of PE-like polymers experiencing compressive loading. The yielding stress was determined as a function of strain rates from 10^8 to $5\times10^{10} \text{ s}^{-1}$. Even within this range of extreme rates, the consistent linearity between yielding stress and logarithm of strain rate is broken since a bi-linear function is the best fit to MD data. Besides, extrapolation to experimental strain rate (10^{-2}) gives un-physical yield stress of -74MPa. These all indicates that a single process Eyring model may not be enough and additional yielding mechanisms need be uncovered to decrease the slope of yield stress versus logarithm of strain rate [185]. One thought would be to consider collaborative motion, such as diffusion, of polymer chains instead of localized state transitions.

REFERENCES

1. Pecht, M.G., L.T. Nguyen, and E.B. Hakim, *Plastic-Encapsulated Microelectronics*. 1995, New York: John Wiley & Sons, Inc.
2. Fowkes, F.M., *Physico-Chemical Aspects of Polymer Surfaces*. 1983, New York: Plenum Press.
3. Good, R.J., *Treaties on Adhesion and Adhesive*. 1967, New York: Marcel Dekker.
4. Stevens, M.J., *Interfacial fracture between highly cross-linked polymer networks and a solid surface: Effect of interfacial bond density*. Macromolecules, 2001. **34**(8): p. 2710-2718.
5. Yang, S., F. Gao, and J. Qu, *A molecular dynamics study of tensile strength between a highly-crosslinked epoxy molding compound and a copper substrate*. Polymer, (0).
6. Wong, K.Y., *Molecular Design of Thiol Based Nano Network For Copper-Epoxy Interfacial Adhesion*, in *Department of Mechanical Engineering*2008, Hong Kong University of Science and Technology.
7. Miller, J. and H. Ishida, *Adhesive—Adherend Interface and Interphase*, in *Fundamentals of Adhesion*, L.-H. Lee, Editor. 1991, Springer US. p. 291-324.
8. Müller, R., et al., *New Adhesion Promoters for Copper Leadframes and Epoxy Resin*. The Journal of Adhesion, 2000. **72**(1): p. 65-83.
9. Boiziau, C. and G. Lecayon, *Adhesion of Polymers to Metals - a Review of the Results Obtained Studying a Model System*. Surface and Interface Analysis, 1988. **12**(1-12): p. 475-485.
10. Swadener, J.G., K.M. Liechti, and A.L. de Lozanne, *The intrinsic toughness and adhesion mechanisms of a glass/epoxy interface*. Journal of the Mechanics and Physics of Solids, 1999. **47**(2): p. 223-258.
11. Agrawal, R.K. and L.T. Drzal, *Adhesion mechanisms of polyurethanes to glass surfaces I. Structure-property relationships in polyurethanes and their effects on adhesion to glass*. Journal of Adhesion, 1995. **54**(1-2): p. 79-102.

12. Agrawal, R.K. and L.T. Drzal, *Adhesion Mechanisms of Polyurethanes to Glass Surfaces .2. Phase-Separation in Polyurethanes and Its Effects on Adhesion to Glass*. Journal of Adhesion Science and Technology, 1995. **9**(10): p. 1381-1400.
13. Lee, H.Y., *Failure paths of the Cu-based leadframe/EMC joints*. Materials Science and Engineering a-Structural Materials Properties Microstructure and Processing, 2001. **311**(1-2): p. 217-225.
14. Lee, H.Y. and J.M. Qu, *Microstructure, adhesion strength and failure path at a polymer/roughened metal interface*. Journal of Adhesion Science and Technology, 2003. **17**(2): p. 195-215.
15. Lee, H.Y. and J. Yu, *Adhesion strength of leadframe/EMC interfaces*. Journal of Electronic Materials, 1999. **28**(12): p. 1444-1447.
16. Yao, Q.Z. and J.M. Qu, *Interfacial versus cohesive failure on polymer-metal interfaces in electronic packaging - Effects of interface roughness*. Journal of Electronic Packaging, 2002. **124**(2): p. 127-134.
17. Yu, J., J.Y. Song, and I.S. Park, *Analyses of the practical adhesion strengths of the metal/polymer interfaces in electronic packaging*. Journal of Electronic Materials, 2002. **31**(12): p. 1347-1352.
18. Cho, K.W. and E.C. Cho, *Effect of the microstructure of copper oxide on the adhesion behavior of epoxy/copper leadframe joints*. Journal of Adhesion Science and Technology, 2000. **14**(11): p. 1333-1353.
19. Wei, Y. and J. Hutchinson, *Interface strength, work of adhesion and plasticity in the peel test*. International Journal of Fracture, 1998. **93**(1-4): p. 315-333.
20. Chung, P.W.K., et al. *Effect of copper oxide on the adhesion behavior of Epoxy Molding Compound-copper interface*. in *Electronic Components and Technology Conference, 2002. Proceedings. 52nd*. 2002.
21. Ma, Q., et al. *Measurement of Low-k Polymerimetal Interfacial Toughness Using 4-point Bending Method*. in *MRS Proceedings*. 1996.
22. Swadener, J.G. and K.M. Liechti, *Asymmetric shielding mechanisms in the mixed-mode fracture of a glass/epoxy interface*. Journal of Applied Mechanics-Transactions of the Asme, 1998. **65**(1): p. 25-29.

23. Rice, J.R., *A Path Independent Integral and the Approximate Analysis of Strain Concentration by Notches and Cracks*. Journal of Applied Mechanics, 1968. **35**(2): p. 379-386.
24. Ji, G.F., et al., *Effects of adhesive thickness on global and local Mode-I interfacial fracture of bonded joints*. International Journal of Solids and Structures, 2010. **47**(18-19): p. 2445-2458.
25. Sorensen, B.F., *Cohesive law and notch sensitivity of adhesive joints*. Acta Materialia, 2002. **50**(5): p. 1053-1061.
26. Sorensen, B.F. and T.K. Jacobsen, *Determination of cohesive laws by the J integral approach*. Engineering Fracture Mechanics, 2003. **70**(14): p. 1841-1858.
27. Barenblatt, G.I., *The Mathematical Theory of Equilibrium Cracks in Brittle Fracture*, in *Advances in Applied Mechanics*. 1962, Elsevier. p. 55-129.
28. Dugdale, D.S., *Yielding of Steel Sheets Containing Slits*. Journal of the Mechanics and Physics of Solids, 1960. **8**(2): p. 100-104.
29. Needleman, A., *A Continuum Model for Void Nucleation by Inclusion Debonding*. Journal of Applied Mechanics-Transactions of the Asme, 1987. **54**(3): p. 525-531.
30. Xu, X.P. and A. Needleman, *Void Nucleation by Inclusion Debonding in a Crystal Matrix*. Modelling and Simulation in Materials Science and Engineering, 1993. **1**(2): p. 111-132.
31. Camacho, G.T. and M. Ortiz, *Computational modelling of impact damage in brittle materials*. International Journal of Solids and Structures, 1996. **33**(20-22): p. 2899-2938.
32. Tvergaard, V. and J.W. Hutchinson, *Toughness of an Interface Along a Thin Ductile Layer Joining Elastic Solids*. Philosophical Magazine a-Physics of Condensed Matter Structure Defects and Mechanical Properties, 1994. **70**(4): p. 641-656.
33. Tvergaard, V. and J.W. Hutchinson, *On the toughness of ductile adhesive joints*. Journal of the Mechanics and Physics of Solids, 1996. **44**(5): p. 789-800.
34. Wei, Y.J. and L. Anand, *Grain-boundary sliding and separation in polycrystalline metals: application to nanocrystalline fcc metals*. Journal of the Mechanics and Physics of Solids, 2004. **52**(11): p. 2587-2616.

35. Zavattieri, P.D., P.V. Raghuram, and H.D. Espinosa, *A computational model of ceramic microstructures subjected to multi-axial dynamic loading*. Journal of the Mechanics and Physics of Solids, 2001. **49**(1): p. 27-68.
36. Andersson, T. and U. Stigh, *The stress-elongation relation for an adhesive layer loaded in peel using equilibrium of energetic forces*. International Journal of Solids and Structures, 2004. **41**(2): p. 413-434.
37. Farkas, D., H. Van Swygenhoven, and P.M. Derlet, *Intergranular fracture in nanocrystalline metals*. Physical Review B, 2002. **66**(6).
38. Yamakov, V., E. Saether, and E.H. Glaessgen, *Multiscale modeling of intergranular fracture in aluminum: constitutive relation for interface debonding*. Journal of Materials Science, 2008. **43**(23-24): p. 7488-7494.
39. Gall, K., et al., *Atomistic simulations on the tensile debonding of an aluminum-silicon interface*. Journal of the Mechanics and Physics of Solids, 2000. **48**(10): p. 2183-2212.
40. Kubair, D.V., et al., *Multiscale mechanics modeling of direct silicon wafer bonding*. Scripta Materialia, 2009. **60**(12): p. 1125-1128.
41. Spearot, D.E., K.I. Jacob, and D.L. McDowell, *Non-local separation constitutive laws for interfaces and their relation to nanoscale simulations*. Mechanics of Materials, 2004. **36**(9): p. 825-847.
42. Zhou, X.W., et al., *Molecular-dynamics-based cohesive zone law for brittle interfacial fracture under mixed loading conditions: Effects of elastic constant mismatch*. Acta Materialia, 2009. **57**(16): p. 4671-4686.
43. Zhou, X.W., et al., *Molecular dynamics simulation based cohesive surface representation of mixed mode fracture*. Mechanics of Materials, 2008. **40**(10): p. 832-845.
44. Lloyd, J.T., et al., *Finite element analysis of an atomistically derived cohesive model for brittle fracture*. Modelling and Simulation in Materials Science and Engineering, 2011. **19**(6).
45. Yamakov, V., et al., *Molecular-dynamics simulation-based cohesive zone representation of intergranular fracture processes in aluminum*. Journal of the Mechanics and Physics of Solids, 2006. **54**(9): p. 1899-1928.

46. van Duin, A.C.T., et al., *ReaxFF: A reactive force field for hydrocarbons*. Journal of Physical Chemistry A, 2001. **105**(41): p. 9396-9409.
47. Verlet, L., *Computer Experiments on Classical Fluids .I. Thermodynamical Properties of Lennard-Jones Molecules*. Physical Review, 1967. **159**(1): p. 98-&.
48. Hockney, R.W. and J.W. Eastwood, *Computer simulations using particles*. 1988, Bristol: Adam Hilger.
49. Swope, W.C., et al., *A Computer-Simulation Method for the Calculation of Equilibrium-Constants for the Formation of Physical Clusters of Molecules - Application to Small Water Clusters*. Journal of Chemical Physics, 1982. **76**(1): p. 637-649.
50. Gear, C.W., *The Numerical Integration of Ordinary Differential Equations*. Mathematics of Computation, 1967. **21**(98): p. 146-156.
51. Plimpton, S., *Fast Parallel Algorithms for Short-Range Molecular-Dynamics*. Journal of Computational Physics, 1995. **117**(1): p. 1-19.
52. Allen, M.P., *Introduction to Molecular Dynamics Simulation*, in *Computational Soft Matter: From Synthetic Polymers to Proteins, NIC Series*. 2004: John von Neumann Institute for Computing. p. 1-28.
53. Lennard-Jones, J.E., *Cohesion*. Proc. Phys. Soc., 1931 **43** (5).
54. Daw, M.S. and M.I. Baskes, *Embedded-Atom Method - Derivation and Application to Impurities, Surfaces, and Other Defects in Metals*. Physical Review B, 1984. **29**(12): p. 6443-6453.
55. Zope, R.R. and Y. Mishin, *Interatomic potentials for atomistic simulations of the Ti-Al system*. Physical Review B, 2003. **68**(2).
56. Mishin, Y. and A.Y. Lozovoi, *Angular-dependent interatomic potential for tantalum*. Acta Materialia, 2006. **54**(19): p. 5013-5026.
57. Mayer, J.E., *Dispersion and polarizability and the van der Waals potential in the alkali halides*. Journal of Chemical Physics, 1937. **1**(4): p. 270-279.
58. Huggins, M.L. and J.E. Mayer, *Interatomic distances in crystals of the alkali halides*. Journal of Chemical Physics, 1933. **1**(9): p. 643-646.
59. Stillinger, F.H. and T.A. Weber, *Computer-Simulation of Local Order in Condensed Phases of Silicon*. Physical Review B, 1985. **31**(8): p. 5262-5271.

60. Tersoff, J., *New Empirical-Approach for the Structure and Energy of Covalent Systems*. Physical Review B, 1988. **37**(12): p. 6991-7000.
61. Cornell, W.D., et al., *A second generation force field for the simulation of proteins, nucleic acids, and organic molecules (vol 117, pg 5179, 1995)*. Journal of the American Chemical Society, 1996. **118**(9): p. 2309-2309.
62. MacKerell, A.D., et al., *All-atom empirical potential for molecular modeling and dynamics studies of proteins*. Journal of Physical Chemistry B, 1998. **102**(18): p. 3586-3616.
63. Dauber-Osguthorpe, P., et al., *Structure and energetics of ligand binding to proteins: Escherichia coli dihydrofolate reductase-trimethoprim, a drug-receptor system*. Proteins, 1988. **4**(1): p. 31-47.
64. Sun, H., et al., *An Ab-Initio Cff93 All-Atom Force-Field for Polycarbonates*. Journal of the American Chemical Society, 1994. **116**(7): p. 2978-2987.
65. Sun, H., *Ab-Initio Calculations and Force-Field Development for Computer-Simulation of Polysilanes*. Macromolecules, 1995. **28**(3): p. 701-712.
66. Sun, H., *Force-Field for Computation of Conformational Energies, Structures, and Vibrational Frequencies of Aromatic Polyesters*. Journal of Computational Chemistry, 1994. **15**(7): p. 752-768.
67. Sun, H., P. Ren, and J.R. Fried, *The COMPASS force field: parameterization and validation for phosphazenes*. Computational and Theoretical Polymer Science, 1998. **8**(1-2): p. 229-246.
68. Mayo, S.L., B.D. Olafson, and W.A. Goddard, *DREIDING: a generic force field for molecular simulations*. The Journal of Physical Chemistry, 1990. **94**(26): p. 8897-8909.
69. Sun, H., *COMPASS: An ab initio force-field optimized for condensed-phase applications - Overview with details on alkane and benzene compounds*. Journal of Physical Chemistry B, 1998. **102**(38): p. 7338-7364.
70. Sutmann, G., *Classical Molecular Dynamics*, in *Quantum Simulations of Complex Many-Body Systems: From Theory to Algorithms, NIC Series*. 2002: John von Neumann Institute for Computing. p. 221-254.

71. Ewald, P.P., *Die Berechnung optischer und elektrostatischer Gitterpotentiale*. Annalen der Physik, 1921. **369**(3): p. 253-287.
72. Lee, H. and W. Cai *Ewald Summation for Coulomb Interactions in a Periodic Supercell*. 2009.
73. Eastwood, J.W., R.W. Hockney, and D.N. Lawrence, *P3M3DP-The three-dimensional periodic particle-particle/ particle-mesh program*. Computer Physics Communications, 1980. **19**: p. 215-261.
74. Kremer, K. and G.S. Grest, *Dynamics of Entangled Linear Polymer Melts - a Molecular-Dynamics Simulation*. Journal of Chemical Physics, 1990. **92**(8): p. 5057-5086.
75. Berendsen, H.J.C., *Transport-Properties Computed by Linear Response through Weak-Coupling to a Bath*. Computer Simulation in Materials Science, 1991. **205**: p. 139-155.
76. Berendsen, H.J.C., et al., *Molecular-Dynamics with Coupling to an External Bath*. Journal of Chemical Physics, 1984. **81**(8): p. 3684-3690.
77. Hoover, W.G., *Canonical Dynamics - Equilibrium Phase-Space Distributions*. Physical Review A, 1985. **31**(3): p. 1695-1697.
78. Nose, S., *A Unified Formulation of the Constant Temperature Molecular-Dynamics Methods*. Journal of Chemical Physics, 1984. **81**(1): p. 511-519.
79. Schneider, T. and E. Stoll, *Molecular-dynamics study of a three-dimensional one-component model for distortive phase transitions*. Physical Review B, 1978. **17**(3): p. 1302-1322.
80. Groot, R.D. and P.B. Warren, *Dissipative particle dynamics: Bridging the gap between atomistic and mesoscopic simulation*. Journal of Chemical Physics, 1997. **107**(11): p. 4423-4435.
81. Andersen, H.C., *Molecular dynamics simulations at constant pressure and/or temperature*. The Journal of Chemical Physics, 1980. **72**(4): p. 2384-2393.
82. Parrinello, M. and A. Rahman, *Polymorphic Transitions in Single-Crystals - a New Molecular-Dynamics Method*. Journal of Applied Physics, 1981. **52**(12): p. 7182-7190.
83. Abraham, F.F., et al., *Simulating materials failure by using up to one billion atoms and the world's fastest computer: Brittle fracture*. Proceedings of the National Academy of Sciences of the United States of America, 2002. **99**(9): p. 5777-5782.

84. Lee, B.-J., J.-H. Shim, and M.I. Baskes, *Semiempirical atomic potentials for the fcc metals Cu, Ag, Au, Ni, Pd, Pt, Al, and Pb based on first and second nearest-neighbor modified embedded atom method*. Physical Review B, 2003. **68**(14): p. 144112.
85. Mishin, Y., et al., *Structural stability and lattice defects in copper: Ab initio, tight-binding, and embedded-atom calculations*. Physical Review B, 2001. **63**(22): p. 224106.
86. Park, H.S. and J.A. Zimmerman, *Modeling inelasticity and failure in gold nanowires*. Physical Review B, 2005. **72**(5).
87. Leach, A.M., M. McDowell, and K. Gall, *Deformation of top-down and bottom-up silver nanowires*. Advanced Functional Materials, 2007. **17**(1): p. 43-53.
88. Cheng, K.C. and W.Y. Chiu, *Monte-Carlo Simulation of Polymer Network Formation with Complex Chemical-Reaction Mechanism - Kinetic Approach on Curing of Epoxides with Amines*. Macromolecules, 1994. **27**(12): p. 3406-3414.
89. Shy, L.Y., Y.K. Leung, and B.E. Eichinger, *Critical Exponents for Off-Lattice Gelation of Polymer-Chains*. Macromolecules, 1985. **18**(5): p. 983-986.
90. Schulz, M. and H.L. Frisch, *Monte-Carlo Studies of Interpenetrating Polymer Network Formation*. Journal of Chemical Physics, 1994. **101**(11): p. 10008-10022.
91. Mijovic, J. and H. Zhang, *Molecular dynamics simulation study of motions and interactions of water in a polymer network*. Journal of Physical Chemistry B, 2004. **108**(8): p. 2557-2563.
92. Liao, N.B., et al., *Investigation on Thermal Properties of Crosslinked Epoxy Resin by MD Simulation*. Eurosime 2009: Thermal, Mechanical and Multi-Physics Simulation and Experiments in Micro-Electronics and Micro-Systems, 2009: p. 546-549.
93. Ford, D.M. and J.L. Tack, *Thermodynamic and mechanical properties of epoxy resin DGEBF crosslinked with DETDA by molecular dynamics*. Journal of Molecular Graphics & Modelling, 2008. **26**(8): p. 1269-1275.
94. Fan, H.B. and M.M.F. Yuen, *Material properties of the cross-linked epoxy resin compound predicted by molecular dynamics simulation*. Polymer, 2007. **48**(7): p. 2174-2178.

95. Komarov, P.V., et al., *Highly cross-linked epoxy resins: an atomistic molecular dynamics simulation combined with a mapping/reverse mapping procedure*. Macromolecules, 2007. **40**(22): p. 8104-8113.
96. Yarovsky, I. and E. Evans, *Computer simulation of structure and properties of crosslinked polymers: application to epoxy resins*. Polymer, 2002. **43**(3): p. 963-969.
97. Wu, C.F. and W.J. Xu, *Atomistic molecular modelling of crosslinked epoxy resin*. Polymer, 2006. **47**(16): p. 6004-6009.
98. Varshney, V., et al., *A molecular dynamics study of epoxy-based networks: Cross-linking procedure and prediction of molecular and material properties*. Macromolecules, 2008. **41**(18): p. 6837-6842.
99. Lin, P.H. and R. Khare, *Local Chain Dynamics and Dynamic Heterogeneity in Cross-Linked Epoxy in the Vicinity of Glass Transition*. Macromolecules, 2010. **43**(15): p. 6505-6510.
100. Bermajo, J.S. and C.M. Ugarte, *Influence of Cross-Linking Density on the Glass Transition and Structure of Chemically Cross-Linked PVA: A Molecular Dynamics Study*. Macromolecular Theory and Simulations, 2009. **18**(6): p. 317-327.
101. Wu, C.F. and W.J. Xu, *Atomistic molecular simulations of structure and dynamics of crosslinked epoxy resin*. Polymer, 2007. **48**(19): p. 5802-5812.
102. Strachan, A. and C.Y. Li, *Molecular dynamics predictions of thermal and mechanical properties of thermoset polymer EPON862/DETDA*. Polymer, 2011. **52**(13): p. 2920-2928.
103. Varshney, V., et al., *Heat transport in epoxy networks: A molecular dynamics study*. Polymer, 2009. **50**(14): p. 3378-3385.
104. Lin, P.H. and R. Khare, *Molecular Simulation of Cross-Linked Epoxy and Epoxy-POSS Nanocomposite*. Macromolecules, 2009. **42**(12): p. 4319-4327.
105. Fan, H.B., et al., *Investigation of moisture diffusion in electronic packages by molecular dynamics simulation*. Journal of Adhesion Science and Technology, 2006. **20**(16): p. 1937-1947.
106. Lin, Y.C., *Investigation of the moisture-desorption characteristics of epoxy resin*. Journal of Polymer Research, 2006. **13**(5): p. 369-374.

107. Bermejo, J.S. and C.M. Ugarte, *Chemical Crosslinking of PVA and Prediction of Material Properties by Means of Fully Atomistic MD Simulations*. Macromolecular Theory and Simulations, 2009. **18**(4-5): p. 259-267.
108. Bandyopadhyay, A., et al., *Molecular modeling of crosslinked epoxy polymers: The effect of crosslink density on thermomechanical properties*. Polymer, 2011. **52**(11): p. 2445-2452.
109. Jansen, K.M.B., *Structure of Delft Molding compound. (private communication)*.
110. Hill, J.R. and J. Sauer, *Molecular Mechanics Potential for Silica and Zeolite Catalysts Based on Ab-Initio Calculations .1. Dense and Microporous Silica*. Journal of Physical Chemistry, 1994. **98**(4): p. 1238-1244.
111. Sun, H., *Ab initio calculations and force field development for computer simulation of polysilanes*. Macromolecules, 1995. **28**(3): p. 701-712.
112. Sun, H., et al., *An ab Initio CFF93 All-Atom Force Field for Polycarbonates*. Journal of the American Chemical Society, 1994. **116**(7): p. 2978-2987.
113. Theodorou, D.N. and U.W. Suter, *Detailed Molecular-Structure of a Vinyl Polymer Glass*. Macromolecules, 1985. **18**(7): p. 1467-1478.
114. Miller, D.R. and C.W. Macosko, *A New Derivation of Post Gel Properties of Network Polymers*. Macromolecules, 1976. **9**(2): p. 206-211.
115. Jansen, K.M.B., et al., *Constitutive modeling of moulding compounds*. 54th Electronic Components & Technology Conference, Vols 1 and 2, Proceedings, 2004: p. 890-894.
116. Fox, T.G. and S. Loshaek, *Influence of Molecular Weight and Degree of Crosslinking on the Specific Volume and Glass Temperature of Polymers*. Journal of Polymer Science, 1955. **15**(80): p. 371-390.
117. Yu, K.Q., Z.S. Li, and J.Z. Sun, *Polymer structures and glass transition: A molecular dynamics simulation study*. Macromolecular Theory and Simulations, 2001. **10**(6): p. 624-633.
118. Nielsen, L.E., *Cross-Linking-Effect on Physical Properties of Polymers*. Journal of Macromolecular Science-Reviews in Macromolecular Chemistry, 1969. **C 3**(1): p. 69-&.
119. Gusev, A.A., M.M. Zehnder, and U.W. Suter, *Fluctuation formula for elastic constants*. Physical Review B, 1996. **54**(1): p. 1-4.

120. Parrinello, M. and A. Rahman, *Strain Fluctuations and Elastic-Constants*. Journal of Chemical Physics, 1982. **76**(5): p. 2662-2666.
121. Lorenz, C.D., M.J. Stevens, and R.P. Wool, *Fracture behavior of triglyceride-based adhesives*. Journal of Polymer Science Part B-Polymer Physics, 2004. **42**(18): p. 3333-3343.
122. Tsige, M. and M.J. Stevens, *Effect of cross-linker functionality on the adhesion of highly cross-linked polymer networks: A molecular dynamics study of epoxies*. Macromolecules, 2004. **37**(2): p. 630-637.
123. Mukherji, D. and C.F. Abrams, *Mechanical behavior of highly cross-linked polymer networks and its links to microscopic structure*. Physical Review E, 2009. **79**(6): p. -.
124. Mukherji, D. and C.F. Abrams, *Anomalous ductility in thermoset/thermoplastic polymer alloys*. Physical Chemistry Chemical Physics, 2009. **11**(12): p. 2113-2115.
125. Jia, J., et al., *Molecular dynamics simulation of the interface between self-assembled monolayers on Au(111) surface and epoxy resin*. Applied Surface Science, 2009. **255**(13-14): p. 6451-6459.
126. Cheng, H.C., et al., *Molecular dynamics study of interfacial bonding strength of self-assembled monolayer-coated Au-epoxy and Au-Au systems*. Applied Surface Science, 2011. **257**(20): p. 8665-8674.
127. Li, C.Y., et al., *Atomistic simulations on multilayer graphene reinforced epoxy composites*. Composites Part a-Applied Science and Manufacturing, 2012. **43**(8): p. 1293-1300.
128. Fan, H.B., C.K.Y. Wong, and M.M.F. Yuen, *A Multiscale Method to Predict Delamination in Cu-Epoxy Systems in Electronic Packages*. 2009 Ieee 59th Electronic Components and Technology Conference, Vols 1-4, 2009: p. 246-250.
129. Wong, C.K.Y., *Molecular design of thiol based nano network for copper-epoxy interfacial adhesion*. PhD Thesis, The Hong Kong University of Science and Technology, 2008.
130. Carlberger, T., K.S. Alfredsson, and U. Stigh, *Explicit FE-Formulation of Interphase Elements for Adhesive Joints*. International Journal for Computational Methods in Engineering Science and Mechanics, 2008. **9**(5): p. 288-299.

131. Stigh, U., et al., *Some aspects of cohesive models and modelling with special application to strength of adhesive layers*. International Journal of Fracture, 2010. **165**(2): p. 149-162.
132. Morgan, R.J. and J.E. O'Neal, *The microscopic failure processes and their relation to the structure of amine-cured bisphenol-A-diglycidyl ether epoxies*. Journal of Materials Science, 1977. **12**(10): p. 1966-1980.
133. Sue, H.J., et al., *Characterization and Promotion of Dilatation Bands in Toughenable Thermosetting Resins*. Journal of Polymer Science Part B-Polymer Physics, 1995. **33**(14): p. 2003-2017.
134. Liu, J., et al., *Nanocavitation in Self-Assembled Amphiphilic Block Copolymer-Modified Epoxy*. Macromolecules, 2008. **41**(20): p. 7616-7624.
135. Liu, J., et al., *Strain rate effect on toughening of nano-sized PEP-PEO block copolymer modified epoxy*. Acta Materialia, 2009. **57**(9): p. 2691-2701.
136. Mello, A.W. and K.M. Liechti, *The effect of self-assembled monolayers on interfacial fracture*. Journal of Applied Mechanics-Transactions of the Asme, 2006. **73**(5): p. 860-870.
137. Marzi, S., A. Biel, and U. Stigh, *On experimental methods to investigate the effect of layer thickness on the fracture behavior of adhesively bonded joints*. International Journal of Adhesion and Adhesives, 2011. **31**(8): p. 840-850.
138. Samuel, A.M. and F.H. Samuel, *A Metallographic Study of Porosity and Fracture-Behavior in Relation to the Tensile Properties in 319.2 End-Chill Castings*. Metallurgical and Materials Transactions a-Physical Metallurgy and Materials Science, 1995. **26**(9): p. 2359-2372.
139. Dighe, M.D. and A.M. Gokhale, *Relationship between microstructural extremum and fracture path in a cast Al-Si-Mg alloy*. Scripta Materialia, 1997. **37**(9): p. 1435-1440.
140. Yang, S.R. and J.M. Qu, *Computing thermomechanical properties of crosslinked epoxy by molecular dynamic simulations*. Polymer, 2012. **53**(21): p. 4806-4817.
141. Fukunaga, H., J. Takimoto, and M. Doi, *A coarse-graining procedure for flexible polymer chains with bonded and nonbonded interactions*. Journal of Chemical Physics, 2002. **116**(18): p. 8183-8190.

142. Vettorel, T. and H. Meyer, *Coarse graining of short polyethylene chains for studying polymer crystallization*. Journal of Chemical Theory and Computation, 2006. **2**(3): p. 616-629.
143. Shelley, J.C., et al., *A coarse grain model for phospholipid simulations*. Journal of Physical Chemistry B, 2001. **105**(19): p. 4464-4470.
144. Li, Y., et al., *A predictive multiscale computational framework for viscoelastic properties of linear polymers*. Polymer, 2012. **53**(25): p. 5935-5952.
145. Murtola, T., et al., *Coarse-grained model for phospholipid/cholesterol bilayer*. Journal of Chemical Physics, 2004. **121**(18): p. 9156-9165.
146. Izvekov, S. and G.A. Voth, *A multiscale coarse-graining method for biomolecular systems*. Journal of Physical Chemistry B, 2005. **109**(7): p. 2469-2473.
147. Marrink, S.J., et al., *The MARTINI force field: Coarse grained model for biomolecular simulations*. Journal of Physical Chemistry B, 2007. **111**(27): p. 7812-7824.
148. Marrink, S.J., A.H. de Vries, and A.E. Mark, *Coarse grained model for semiquantitative lipid simulations*. Journal of Physical Chemistry B, 2004. **108**(2): p. 750-760.
149. Shinoda, W., R. Devane, and M.L. Klein, *Multi-property fitting and parameterization of a coarse grained model for aqueous surfactants*. Molecular Simulation, 2007. **33**(1-2): p. 27-36.
150. Kennedy, J. and R. Eberhart. *Particle swarm optimization*. in *Neural Networks, 1995. Proceedings., IEEE International Conference on*. 1995.
151. Begambre, O. and J.E. Laier, *A hybrid Particle Swarm Optimization - Simplex algorithm (PSOS) for structural damage identification*. Advances in Engineering Software, 2009. **40**(9): p. 883-891.
152. Lee, W.S., Y.T. Chen, and T.H. Wu, *Optimization for ice-storage air-conditioning system using particle swarm algorithm*. Applied Energy, 2009. **86**(9): p. 1589-1595.
153. Cui, Z.W., et al., *Developing a second nearest-neighbor modified embedded atom method interatomic potential for lithium*. Modelling and Simulation in Materials Science and Engineering, 2012. **20**(1).
154. Cui, Z.W., et al., *A second nearest-neighbor embedded atom method interatomic potential for Li-Si alloys*. Journal of Power Sources, 2012. **207**: p. 150-159.

155. Li, J., et al., *Least square method for the calculation of elastic constants*. Computer Physics Communications, 2011. **182**(7): p. 1447-1451.
156. Cui, Z.W., et al., *Combination method for the calculation of elastic constants*. Physical Review B, 2007. **75**(21).
157. Cui, Z.W. and L.C. Brinson, *Thermomechanical properties and deformation of coarse-grained models of hard-soft block copolymers*. Physical Review E, 2013. **88**(2).
158. Panico, M., S. Narayanan, and L.C. Brinson, *Simulations of tensile failure in glassy polymers: effect of cross-link density*. Modelling and Simulation in Materials Science and Engineering, 2010. **18**(5).
159. Sue, H.J., et al., *Crazing in High-Performance Thermoset Resins*. Journal of Materials Science Letters, 1993. **12**(18): p. 1463-1466.
160. Sue, H.J., et al., *Crazing and dilatation-band formation in engineering thermosets*. Toughened Plastics Ii, 1996. **252**: p. 161-175.
161. Rottler, J. and M.O. Robbins, *Yield conditions for deformation of amorphous polymer glasses*. Physical Review E, 2001. **64**(5).
162. Rottler, J. and M.O. Robbins, *Shear yielding of amorphous glassy solids: Effect of temperature and strain rate*. Physical Review E, 2003. **68**(1).
163. Hoy, R.S. and M.O. Robbins, *Strain hardening of polymer glasses: Entanglements, energetics, and plasticity*. Physical Review E, 2008. **77**(3).
164. Hoy, R.S. and M.O. Robbins, *Strain hardening in polymer glasses: Limitations of network models*. Physical Review Letters, 2007. **99**(11).
165. Rottler, J., S. Barsky, and M.O. Robbins, *Cracks and crazes: On calculating the macroscopic fracture energy of glassy polymers from molecular simulations*. Physical Review Letters, 2002. **89**(14).
166. Rottler, J. and M.O. Robbins, *Growth, microstructure, and failure of crazes in glassy polymers*. Physical Review E, 2003. **68**(1).
167. Tsige, M., C.D. Lorenz, and M.J. Stevens, *Role of network connectivity on the mechanical properties of highly cross-linked polymers*. Macromolecules, 2004. **37**(22): p. 8466-8472.

168. Tuckerman, M.E., et al., *Modified nonequilibrium molecular dynamics for fluid flows with energy conservation*. Journal of Chemical Physics, 1997. **106**(13): p. 5615-5621.
169. Li, J., *AtomEye: an efficient atomistic configuration viewer*. Modelling and Simulation in Materials Science and Engineering, 2003. **11**(2): p. 173-177.
170. Raghava, R., R. Caddell, and G.Y. Yeh, *The macroscopic yield behaviour of polymers*. Journal of Materials Science, 1973. **8**(2): p. 225-232.
171. Delle Site, L., et al., *Polymers near Metal Surfaces: Selective Adsorption and Global Conformations*. Physical Review Letters, 2002. **89**(15): p. 156103.
172. Abrams, C.F., L. Delle Site, and K. Kremer, *Dual-resolution coarse-grained simulation of the bisphenol-A-polycarbonate/nickel interface*. Physical Review E, 2003. **67**(2): p. 021807.
173. Farah, K., et al., *Interphase Formation during Curing: Reactive Coarse Grained Molecular Dynamics Simulations*. The Journal of Physical Chemistry C, 2011. **115**(33): p. 16451-16460.
174. Wong, C.K.Y., et al., *Establishment of the coarse grained parameters for epoxy-copper interfacial separation*. Journal of Applied Physics, 2012. **111**(9): p. 094906-7.
175. Iwamoto, N. *Mechanical properties of an epoxy modeled using particle dynamics, as parameterized through molecular modeling*. in *Thermal, Mechanical & Multi-Physics Simulation, and Experiments in Microelectronics and Microsystems (EuroSimE), 2010 11th International Conference on*. 2010.
176. Iwamoto, N. *Molecularly derived mesoscale modeling of an epoxy/Cu interface (part III*): Interface roughness*. in *Thermal, Mechanical and Multi-Physics Simulation and Experiments in Microelectronics and Microsystems (EuroSimE), 2012 13th International Conference on*. 2012.
177. Iwamoto, N., *Developing the stress-strain curve to failure using mesoscale models parameterized from molecular models*. Microelectronics Reliability, 2012. **52**(7): p. 1291-1299.
178. Laio, A. and F.L. Gervasio, *Metadynamics: a method to simulate rare events and reconstruct the free energy in biophysics, chemistry and material science*. Reports on Progress in Physics, 2008. **71**(12).

179. Laio, A. and M. Parrinello, *Escaping free-energy minima*. Proceedings of the National Academy of Sciences of the United States of America, 2002. **99**(20): p. 12562-12566.
180. Lau, D., O. Buyukozturk, and M.J. Buehler, *Characterization of the intrinsic strength between epoxy and silica using a multiscale approach*. Journal of Materials Research, 2012. **27**(14): p. 1787-1796.
181. Bonomi, M., et al., *PLUMED: A portable plugin for free-energy calculations with molecular dynamics*. Computer Physics Communications, 2009. **180**(10): p. 1961-1972.
182. Zavattieri, P.D., L.G. Hector, and A.F. Bower, *Cohesive zone simulations of crack growth along a rough interface between two elastic-plastic solids*. Engineering Fracture Mechanics, 2008. **75**(15): p. 4309-4332.
183. Zhu, T., et al., *Temperature and strain-rate dependence of surface dislocation nucleation*. Physical Review Letters, 2008. **100**(2).
184. Eyring, H., *Viscosity, plasticity, and diffusion as examples of absolute reaction rates*. Journal of Chemical Physics, 1936. **4**(4): p. 283-291.
185. Capaldi, F.M., M.C. Boyce, and G.C. Rutledge, *Molecular response of a glassy polymer to active deformation*. Polymer, 2004. **45**(4): p. 1391-1399.